DESIGN AND MODULATION OF ADENINE BASED METAL-ORGANIC FRAMEWORKS AND EXPLORATION OF THEIR NEW PROPERTIES

by

Tao Li

B.S., Fudan University, 2008

Submitted to the Graduate Faculty of

The Kenneth P. Dietrich School of Arts and Sciences

in partial fulfillment

of the requirements for the degree of

Doctor of Philosophy

University of Pittsburgh

2013

UNIVERSITY OF PITTSBURGH

KENNETH P. DIETRICH SCHOOL OF ARTS AND SCIENCES

This dissertation was presented

by

Tao Li

It was defended on

October 15th, 2013

and approved by

Geoffrey R. Hutchison, PhD, Assistant Professor, Department of Chemistry

Alexander Star, PhD, Associate Professor, Department of Chemistry

J. Karl Johnson, PhD, William Kepler Whiteford Professor, Department of Chemical and Petroleum Engineering

Dissertation Advisor: Nathaniel L. Rosi, PhD, Associate Professor, Department of Chemistry

Prof. Nathaniel L. Rosi

DESIGN AND MODULATION OF ADENINE BASED METAL-ORGANIC FRAMEWORKS AND EXPLORATION OF THEIR NEW PROPERTIES

Tao Li, PhD

University of Pittsburgh, 2013

This dissertation describes the development of adenine-based biomolecular metal-organic frameworks (Bio-MOFs). Four specific topics are presented: 1) design of new bio-MOFs for CO_2 capture; 2) preparation of core-shell bio-MOFs with enhanced properties; 3) development of new synthetic strategies for increasing bio-MOF porosity; and 4) exploration of new applications of mesoporous bio-MOFs.

Specifically, Chapter 2 reports the preparation of an isoreticular series of cobalt-adeninate bio-MOFs (bio-MOFs-11-14). The pores of bio-MOFs-11-14 are decorated with linear aliphatic pendant groups (acetate, propionate, butyrate, and valerate). The new materials exhibit higher CO_2/N_2 selectivity and greatly improved water stability. Based on the findings in Chapter 2, Chapter 3 describes the design of a core-shell material comprising a porous bio-MOF-11/14 mixed core and a less porous bio-MOF-14 shell. The resulting core-shell material successfully combined the merits of bio-MOF-11 and 14 and exhibits higher CO_2 capacity, the ability to exclude N_2, and improved water stability. Chapter 4 demonstrates the use of *in situ* ligand exchange as a synthetic strategy for the preparation of an isoreticular series of zinc-adeninate bio-MOFs (bio-MOFs-100-103) exhibiting exclusive mesoporosity. Following the work in Chapter 4, Chapter 5 presents the use of these exclusively mesoporous bio-MOFs for the separation of thiolated gold nanoclusters. This is the first demonstration of large species separation using MOFs.

TABLE OF CONTENTS

LIST OF TABLES

LIST OF FIGURES

PREFACE

ACKNOWLEDGMENTS

Advisors and Co-workers

I would like to express my deepest gratitude to my PhD advisor Prof. Nathaniel L. Rosi for instructing and helping me in every aspect of my graduate research. He is always being supportive whenever I have new ideas and allows me to conduct my research with maximum degree of freedom. I would not have achieved that much without his high standards.

I would like to specially thank Dr. Steven Geib for teaching me single crystal X-ray techniques and helping me on difficult structures throughout the past four years. His effort is reflected in each single one of my publications so far.

I would also like to thank my thesis committee, Prof. J. Karl Johnson, Prof. Alex Star, and Prof. Geoffrey Hutchison, for all of their time and helpful suggestions.

I thank my collaborators Prof. J. Karl Johson, Prof. Rongchao Jin, Prof. Stephane Petoud, Chong Liu, Dr. De-li Chen, Anindita Das, Chenjie Zeng, Husain Kagalwala, and Kristy A. Gogick for their great work and contribution to the publications. I also thank former group member Prof. Jihyun An for teaching me the basics of MOF research and other group members Dr. Leekyoung Hwang, Dr. Chengyi Song, Chen Zhang, Chong Liu, Alex Spore, Jessica Sammons, Ryan Ruenroeng, and Andre Merg for their help over the past several years.

I also thank Prof. Allen Oliver and Prof. Jeanette Krause for their help on synchrotron data collection.

Particularly, I would like to thank undergraduate researchers Mark Kozlowski, Jeanne Sullivan, Eric Peterson, Catherine Madden, Evan Doud, Maike Blakely, and Wendy Jiang who worked for me on many of my projects.

Family Members

My parents, Xiong Li and Liqin Tao, have been providing great, endless support for the longest time. They deserve the most credits.

Last but most importantly, I would like to thank my wife Rui Zuo for keeping my company during most of my graduate school life. Thank you for being considerate whenever I am super busy.

1.0 INTRODUCTION

1.1 METAL-ORGANIC FRAMEWORKS

Metal-organic frameworks (MOFs), as a subgroup of coordination polymers, are defined as crystalline materials constructed by interlinking nodes (metal ions or metal containing clusters) and spacers (organic linker molecules) through strong bonds (Figure 1).[1,2,3] The combination between metals/metal clusters and the huge library of organic ligands has led to the discovery of thousands of MOF structures.

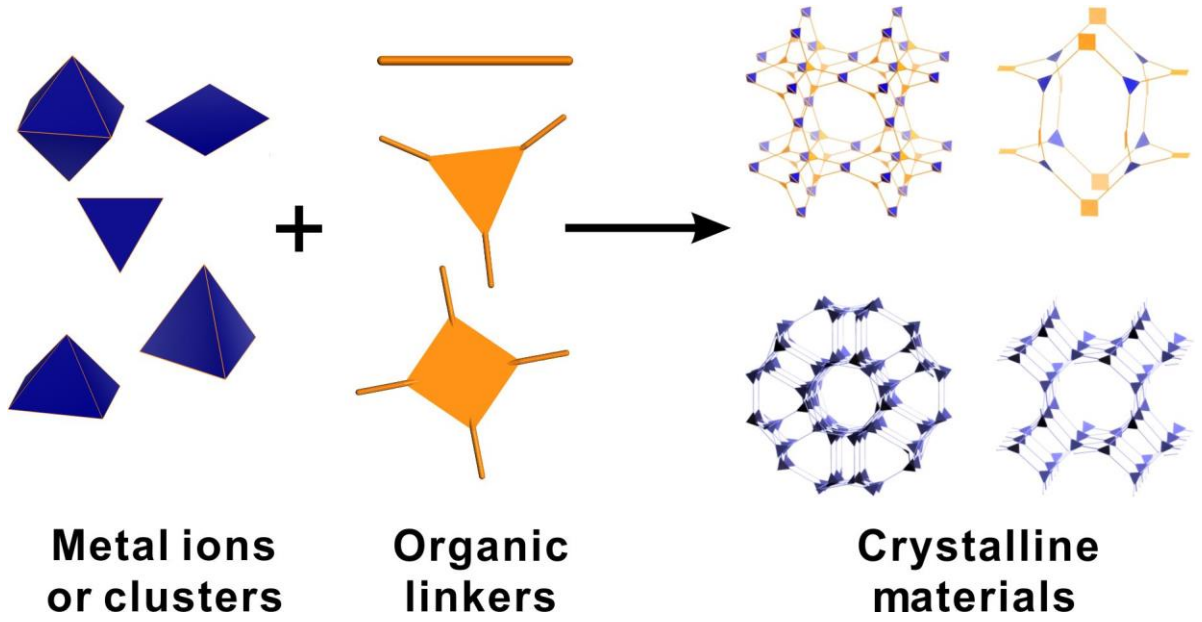

Figure 1. Scheme of typical MOF assemblies.

Unlike zeolites and porous carbon materials, most MOFs can be obtained as single crystals. Through single crystal X-ray diffraction analysis, complete structural information of the material, including the precise location of each atom, coordination environment around the metal center, ligand arrangement, and bond length can be determined. Correlating structural features with experimental properties not only allows us to better interpret experimental observations, but also to predict new properties through modeling and simulation.

A typical MOF synthesis involves a reaction between a metal salt and organic linkers under elevated temperature. Therefore, both pore metrics and functionality of a MOF can be readily tuned. For instance, changing the length of the linker in MOF-5 resulted in a series of MOFs with the same underlying topology.[4] Replacing the ditopic linker in MOF-5 with a tritopic linker (1,3,5-Tris(4-carboxyphenyl)benzene, H_3BTB) lead to a new topology.[5]

To endow MOFs with specific functions for desired applications requires the introduction of functional moieties into MOFs. This can be achieved during the synthesis. Yaghi et al. demonstrated the use of mixtures of pre-functionalized ligands to construct MOFs with up to 8 functional moieties.[6] This can also be achieved after the synthesis via post-synthetic modification (PSM).[7,8] These two methods of MOF functionalization are complementary.

Permanent porosity is one of the most important features of MOFs. High surface area and adequate pore volume are two key features that lead to high capacity gas storage. Large accessible voids are also a prerequisite for the encapsulation of large species. Currently, some MOFs exhibit surface area as high as 7000 m^2/g [9] and pore volume exceeding 4 cc/g.[9,10,11] Pore sizes can be tailored from a few angstroms up to 9.8 nm.[12] These values make MOFs the most promising nanoporous material for a variety of applications.

1.2 POTENTIAL APPLICATIONS OF METAL-ORGANIC FRAMEWORKS

The periodic pore arrangement and structural tailorability of MOFs prompted their exploration for a variety of potential applications. These include gas storage (H_2, CH_4, C_2H_2, and CO_2 etc.),[13,14,15] gas separation (CO_2/CH_4, O_2/N_2, and hydrocarbons etc.),[16] heterogeneous

catalysis,[17,18,19,20] biological imaging,[21] sensing,[22] and drug delivery[23,24]. Here, two applications, separation and carbon dioxide capture, are selected and discussed in detail because of their relevance to my research projects.

1.2.1 Separation

From light gases and organic molecules to stereoisomers and nanoparticles, mixture separations are a major challenge, yet they are extremely important process in the chemical industry. Among current commercial techniques, distillation accounts for 90-95% of all separation processes.[16] However, it is limited to low molecular weight species, since high temperature can decompose the desired products. Moreover, distillation cannot separate mixtures of similar boiling points and in most cases it is highly costly, requiring much energy input. Adsorptive separation is a potential alternative to distillation. It relies on the differential adsorption behaviors of adsorbates on a porous media. This difference is a consequence of the physical and chemical properties of the porous materials including pore size, pore shape, pore flexibility and functional groups on the pore surface. The designability and tunability of MOFs allow precise control over each of the aforementioned parameters to meet the criteria of different separation processes. Systematic study of the relationship between pore parameter and separation selectivity and efficiency also gives us fundamental understanding of porous materials.

In recent years, MOFs have been shown to be very successful in separating gases and small organic molecules.[16] However, there is no demonstration of separation of large species such as nanoparticles using MOFs. The main challenge is pore size limitation. Despite the fact that several mesoporous MOFs have been reported so far,[25] few exhibits exclusive mesoporosity, which is a requirement for the separation of nanoscale (>2 nm diameter) species.[12,26]

1.2.2 Carbon dioxide capture

CO_2 separation attracts great attention due to the realization of global warming. Improving energy efficiency, using carbon-neutral energy sources, and carbon capture and sequestration[27] are three principle options for reducing and stabilizing CO_2 levels and global temperatures. Carbon capture and sequestration from post-combustion is currently considered the most viable means of reducing CO_2 emissions from point sources.

At a coal-fired power plant, a typical post-combustion flue gas contains approximately 15-16% CO_2, 73-77% N_2 and 5-7% H_2O.[13] Therefore, there are two basic requirements for CO_2 capture. First, high CO_2/N_2 selectivity is critical for efficient removal of CO_2 from flue gases. Second, the material should be stable enough to withstand the presence of moisture.

Currently, elimination of CO_2 from flue gases emitted from fossil fuel power plants mainly relies on gas scrubbing using aqueous amine solutions or amine based organic solvents. However, this industrially mature technology has a few major limitations. First, the amine solution reacts with CO_2 through a chemisorptive mechanism. Although this strong interaction ensures the complete removal of CO_2, the regeneration process requires large energy input which significantly increases the cost of energy. Second, liquid amines are corrosive and highly volatile. Maintenance of the equipment becomes very expensive.[28] Therefore, seeking alternative materials for CO_2 capture is of great interest.

Nanoporous materials are great candidates for future CO_2 capture since solids are much easier to handle than corrosive liquids. As a new type of CO_2 adsorbent, MOFs interact with CO_2 via a physisorptive mechanism and require much less energy for regeneration. Their structural attributes can be tuned via proper selection of organic linker and network topologies

which allows for the optimization of their interactional potential with CO_2. MOF pores can also be post-synthetically modified to modulate the selectivity for CO_2 over other flue gases.[29,30,31]

1.3 BIOMOLECULE-BASED METAL-ORGANIC FRAMEWORKS

Many applications of MOFs depend not only on the performance of the material but also their environmental and biological safety aspects. These include biological applications such as drug delivery and bio-imaging that requires that the materials be biocompatible and non-toxic. One way to construct MOFs that meet these standards is to use biomolecules as building blocks and nontoxic metal ions as nodes. In fact, apart from their biocompatibility, there are multiple benefits to using biomolecules as basic components in MOFs. First, many biomolecules have more than two metal coordination sites which can potentially lead to multiple coordination modes and diverse MOF structures. Second, biomolecules such as amino acids and nucleobases are readily available at low price. Third, MOFs constructed from therapeutically active biomolecules can be used for drug delivery. Fourth, hydrogen bonding among biomolecules can potentially direct and facilitate the self-assembly of MOFs. Last, the inherent chirality of biomolecules can lead to chiral MOFs that are potentially useful in molecular recognition and chiral separations.[32]

The construction of biomolecule based MOFs with permanent porosity can potentially lead to new properties or applications that cannot be achieved with other MOFs. For example, porous biomolecule based MOFs may serve as vehicles for drug delivery. Their pores can also be decorated with fluorescent molecules for cell imaging.[33] When a large quantity of

biomolecule based MOFs are used for environmental remediation such as CO_2 sequestration, the environmental concerns raised from the disposal of the MOFs are minimized.

However, compared to other small organic ligands, biomolecules are less explored in MOF synthesis. One of the reasons is because of the flexibility and asymmetry of many biomolecules (amino acids, peptides and proteins) prevent them from forming structurally rigid and 3-D MOFs.[32,34] In order to increase the dimensionality of the resulting structure, additional treatments such as employing a secondary linker molecule along with amino acids or chemical modification of the amino acids with more potential coordination sites are often times required.[32] Within the existing examples of 3-D biomolecule based MOFs, few exhibit permanently porosity due to the flexibility of biomolecules. In contrast to flexible and irregularly-shaped amino acids and peptides, nucleobases are more rigid. Therefore, using nucleobases as organic linkers can potentially lead to permanently porous MOFs. The work in this thesis solely focuses on MOFs constructed from one of the nucleobases, adenine.

1.4 ADENINE BASED METAL-ORGANIC FRAMEWORKS

Over the past seven years, our group has explored adenine, a nucleobase, as a simple biomolecule for constructing MOFs.[24,31,33,35,36,37,38,39] These MOFs are termed 'bio-MOFs'. There are a number of reasons to choose adenine as a linker molecule. First, unlike other biomolecules such as amino acids, adenine is a rigid, planar molecule due to π conjugation. Rigidity of the linker molecule is often a prerequisite for the construction of permanently porous MOFs. Second, the asymmetry of adenine molecule creates complexity and can potentially lead to more sophisticated structures. Third, there are four heterocyclic nitrogens (N1, N3, N7, and

N9 as shown in Figure 2) and one amino group on each adenine which can potentially bind to metal ions via a number of coordination modes (Figure 2). In Mode I, two imidazolate nitrogens coordinate to metal ions while N1 along with the amino group form hydrogen bonds with a secondary adenine. In Mode II, N3, N7 and N9 bind to metal centers leaving N1 and the amino group uncoordinated. In Mode III, all four heterocyclic nitrogens coordinate to metal centers (Figure 2). These diverse coordination modes in combination with judicious selection of metal center and a secondary carboxylate linker can in theory yield a large library of new structures with unprecedented topologies and properties. In addition to the reasons above, a recent *ab initio* computational study evaluated the interaction potentials between CO_2 and various N-containing heterocycles[40]. These heterocycles were potential ligand molecules for constructing MOFs. According to this study, compared with many other N-heterocyclic species (e.g. imidazole, tetrazole, triazole), adenine has one of the highest interaction energies with CO_2 (5.9 kcal/mol). This result suggests that adenine-based MOFs should have good performance in CO_2 uptake and separation applications [40].

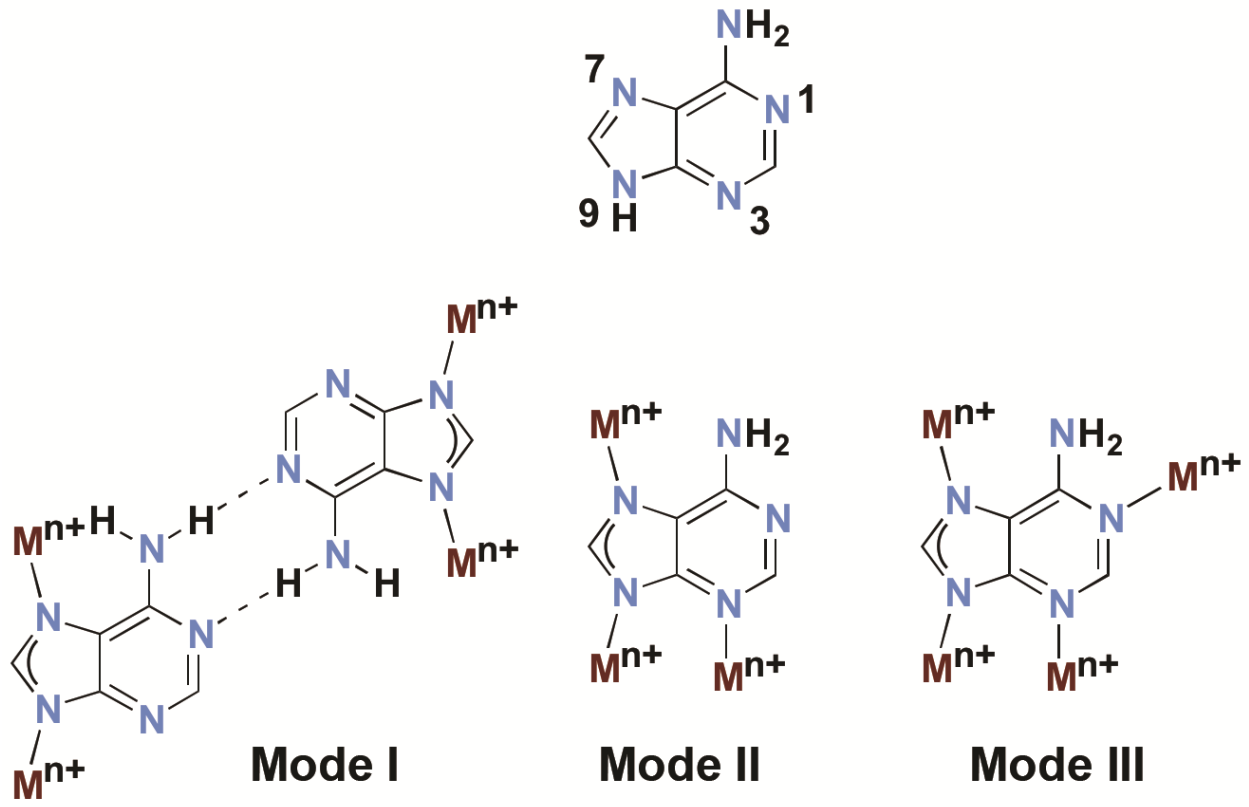

Figure 2. Coordination modes of adenine.

Previous work by An demonstrated fruitful results on metal-adeninate based MOFs.[11,24,31,33,35,36] The first discovery was a 0-D macrocycle-based structure. This porous material consists of Zn^{2+}, adeninate, pyridine and nitrate and is constructed based on coordination mode I (Figure 3A). It contains tubular cavities and exhibits permanent porosity as well as good CO_2 uptake capacity.[35] When cobalt acetate was employed as a metal source, a 3-D microporous MOF named bio-MOF-11 was obtained (Figure 3B).[36] Adenines are linked to each other via coordination mode II while N1 and amino groups are exposed to the cavity. This periodic alignment of Lewis basic sites along the pore walls allows bio-MOF-11 to interact with CO_2 strongly and exhibit very high CO_2 capacity (6.0 mmol/g at 273 K and 4.1 mmol/g at 298K)

and selectivity over N_2 (81:1 at 273 K and 75:1 at 298 K).[36] Bio-MOF-11 exhibited the second highest CO_2 capacity of any MOF at the time it was reported and remains near the top of the list to this date.[13]

When linear dicarboxylic acids were introduced as secondary linker molecules, a 1-D microporous MOF, bio-MOF-1 (Figure 3C),[24] and a 3-D mesoporous MOF, bio-MOF-100 (Figure 4C),[11] were discovered. Interestingly, bio-MOF-1, $Zn_8(ad)_4(BPDC)_6O^{2-} \bullet 2(Me_2NH_2)^+$ (BPDC = 4,4'-biphenyldicarboxylic acid, ad = adenine) exhibits an anionic framework. Extra framework cations, dimethylammonium (DMA), reside in the pore and can be easily replaced by other cations via cation-exchange. Utilizing this property, An et al. demonstrated a cation-triggered drug release process from a cationic drug loaded bio-MOF-1.[24] On the other hand, bio-MOF-1 can serve as a platform to display, and examine the properties of specific cations. For example, organic ammonium cations of various sizes were exchanged into bio-MOF-1 to study the influence of pore confinement on CO_2 adsorption capacity.[31] Lanthanides were encapsulated in bio-MOF-1 to yield luminescent lanthanide MOFs.[33]

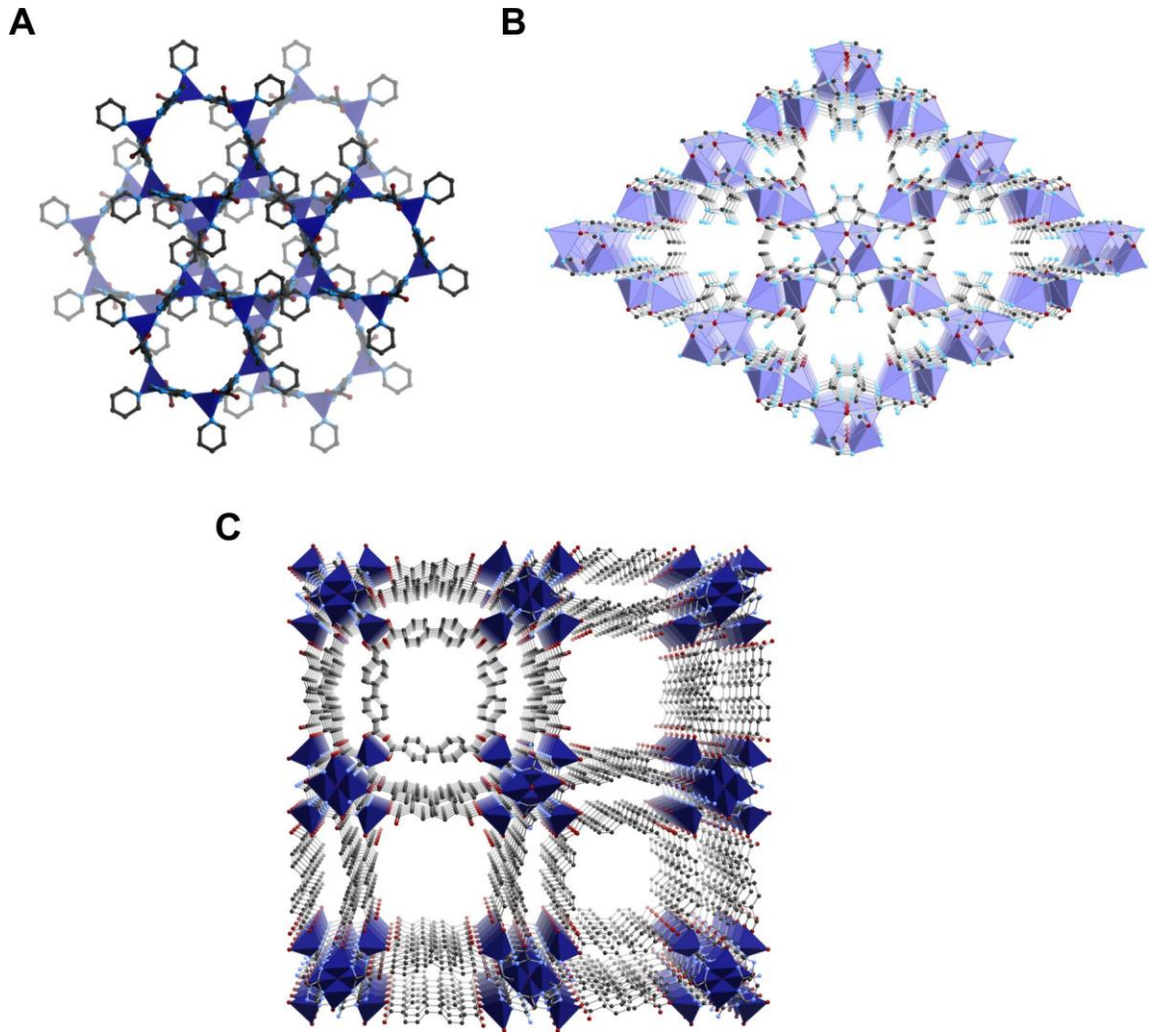

Figure 3. Crystal structures of zinc-adeninate macrocycle (A), bio-MOF-11 (B), and bio-MOF-1 (C). Navy polyhedra: zinc; purple polyhedral: cobalt; light blue: nitrogen; grey: carbon; red: oxygen.

The structure of bio-MOF-100 reveals a discrete octahedral-shaped secondary building unit (SBU), namely Zn-adeninate octahedral cages (Figure 4A).[11] Each cage is composed of eight zinc atoms and four adeninates where zinc atoms occupy six vertices (four on the equatorial plane and four at the apical positions) and adeninates locate on four alternating faces of the octahedron. A total of twelve dicarboxylates connect each cage through four faces to four

other cages to form a 3-D framework having the *lcs* network topology (Figure 4B).[41] Compared to conventional zinc-acetate and copper paddle-wheel building units, Zn-adeninate cages are much larger in size and can potential lead to more porous structures. In fact, bio-MOF-100 exhibits pore volume up to 4.3 cc/g which was the most porous MOF at the time it was published, based on the pore volume metric.[11]

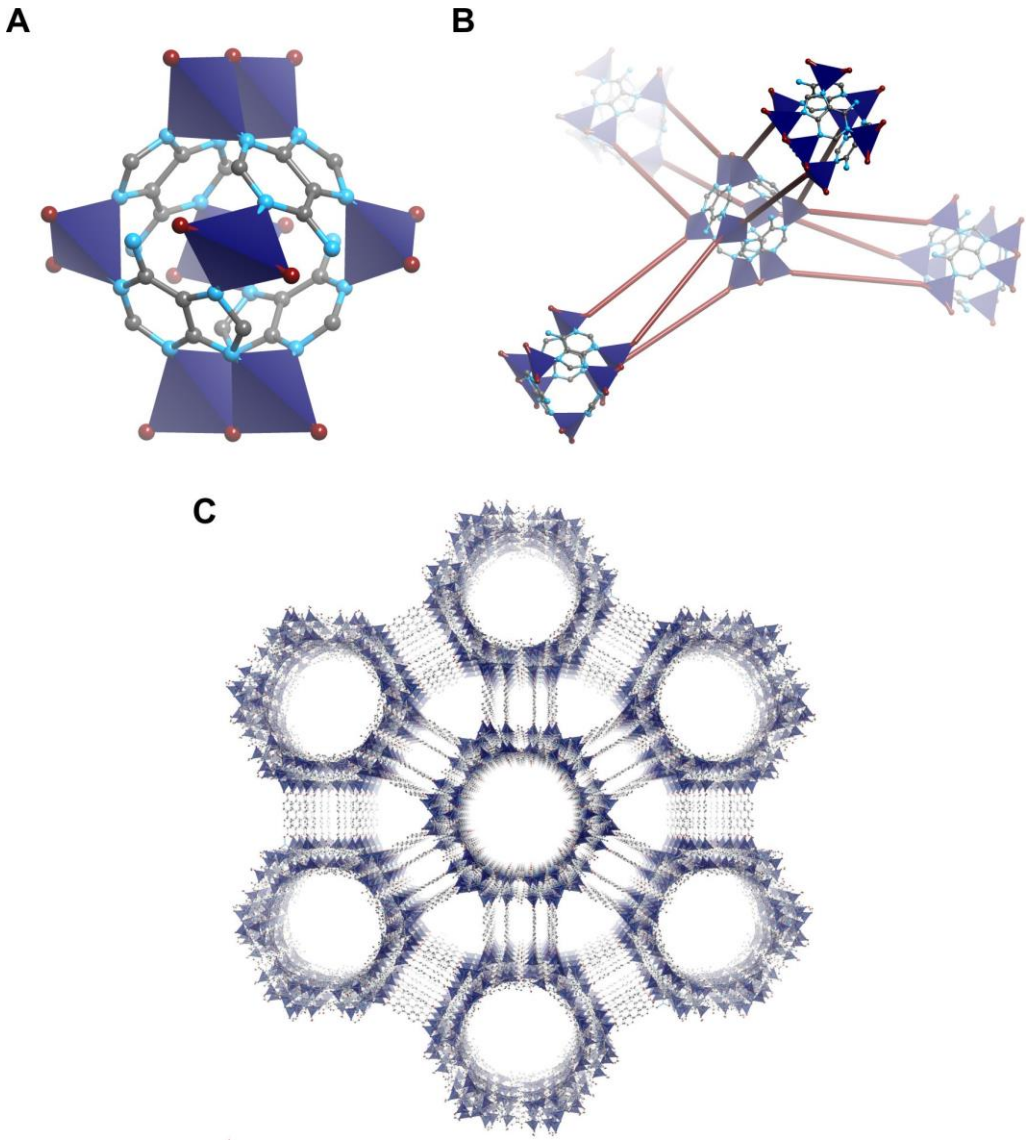

Figure 4. Zinc-adeninate building units (A) are connected through four faces on the octahedron through linear dicarboxylate linkers (illustrated as red rods) (B) resulting in a 3-D mesoporous MOF, bio-MOF-100 (C). Navy polyhedra: zinc; light blue: nitrogen; grey: carbon; red: oxygen.

As described above, adenine based MOFs have established themselves as an important branch in the MOF field. Compared to the rest of the MOF materials, metal-adeninate MOFs have many unique features. For instance, bio-MOF-11 exhibits promising CO_2 adsorption capacity, and bio-MOF-100 is the first example of an exclusively mesoporous MOF. These features allow us to explore new strategies and new applications that cannot be achieved using other MOFs. This thesis focuses on two members of bio-MOFs: bio-MOF-11 and bio-MOF-100, and explores four different aspects of MOF chemistry:

- Modulation of water stability and CO_2 adsorption properties of bio-MOFs
- Increasing CO_2 adsorption performance via crystal design
- Development of a new MOF synthetic methodology
- Design of a series of bio-MOFs for nanoparticle separation

2.0 SYSTEMATIC MODULATION AND ENHANCEMENT OF CO_2:N_2 SELECTIVITY AND WATER STABILITY IN AN ISORETICULAR SERIES OF BIO-MOF-11 ANALOGUES

This work, written in collaboration with De-Li Chen, Jeanne E. Sullivan, Mark T. Kozlowski, J. Karl Johnson, and Nathaniel L. Rosi*, was published in *Chem. Sci.*, **2013**, 4, 1746-1755.[42]

De-Li Chen and J. Karl Johnson performed the theoretical modeling work. Jeanne E. Sullivan and Mark T. Kozlowski helped with the synthesis and characterization of bio-MOFs.

2.1 INTRODUCTION

CO_2 capture from flue gas of coal-fired power plants is recognized as an important clean energy goal, and the development of new adsorbent materials for selective CO_2 capture is central to this pursuit.[43,44] Metal-organic frameworks (MOFs) are being intensively studied as CO_2 adsorbents because of their tailorable structures and chemical functionality and their physisorptive property, an aspect that is expected to decrease adsorbent regeneration energy and therefore net energy costs.[13,45]

To first be considered for CO_2-capture applications, a MOF adsorbent must meet several important criteria: i) it should have a high capacity for CO_2 at flue gas temperatures; ii) it should

selectively adsorb CO_2 over N_2; and iii) its structure should be able to withstand the moisture present in flue gas. Numerous MOFs meet at least one of these criteria, yet few meet all of these criteria.[16,26,29,30,36,46,47,48,49,50,51,52,53,54,55,56,57,58,59,60]

We have introduced and developed a strategy for preparing CO_2-phillic MOFs that utilizes the nucleobase adenine as a linker molecule. Adenine is an ideal linker because it has multiple Lewis-basic sites that can interact with CO_2. In principle, by controlling the adenine coordination mode, one should be able to control the number of Lewis-basic sites exposed to the pore space within the MOF. In our work[11,24,31,36], we identified three principle coordination modes (Figure 2) for deprotonated adenine (adeninate) within finite and infinite periodic coordination assemblies. Mode I, observed in 0-D macrocyclic structures,[35] and Mode III, observed in **bio-MOF-1**[24,31] and **bio-MOF-100**[11], have only one free Lewis-basic site (N3 and the amino group, respectively) , while Mode II, observed in **bio-MOF-11**,[36] has two free Lewis-basic sites (N1, and the amino group). Of these reported materials, **bio-MOF-11**, as expected, had the highest capacity for CO_2 and a high selectivity for CO_2 over N_2. In fact, compared to other reported MOFs, **bio-MOF-11** remains one of the best adsorbents for CO_2 in terms of capacity and selectivity.[13] However, despite its favorable CO_2 capacity and selectivity, it degrades rapidly in water and therefore would not withstand the moisture present in flue gas (5~7 % water[13]). In this report, we present a strategy for tuning the CO_2 adsorption properties and the water stability of a series of new isostructural **bio-MOF-11** analogues, hereafter named **bio-MOF-12**, **13**, and **14**. We modulate the porosity and hydrophobicity within this series by decorating the pores with different aliphatic monocarboxylates. Importantly, we demonstrate that one member of this series, **bio-MOF-14**, is highly stable in water and exhibits exceptional selectivity for CO_2 over N_2, due to a molecular sieving effect.

2.2 RESULTS AND DISCUSSION

2.2.1 Design Approach, Preparation, and Structural Characterization.

As described in a previous report,[36] **bio-MOF-11**, $Co_2(ad)_2(CH_3\ CO_2)_2$, crystallizes in the $I4_1/a$ space group (a = b = 15.4355(18) Å, c = 22.775(5) Å; α = β = γ = 90 °). It consists of cobalt-adeninate-acetate 'paddle-wheel' building blocks that are periodically linked together through the N7 of the adeninate to form a 3-D structure with the augmented ***lvt*** topology.[41] This arrangement of building blocks affords channels that run parallel to the *a* and *b* crystallographic axes. These channels are densely functionalized with Lewis-basic groups: the top and bottom wall of each channel is decorated, in a zig-zag fashion, with amino groups spaced 5 Å apart as well as pyrimidal nitrogen groups spaced 4.7 Å apart. In addition, the channels are lined with methyl groups from the acetates of the building blocks.

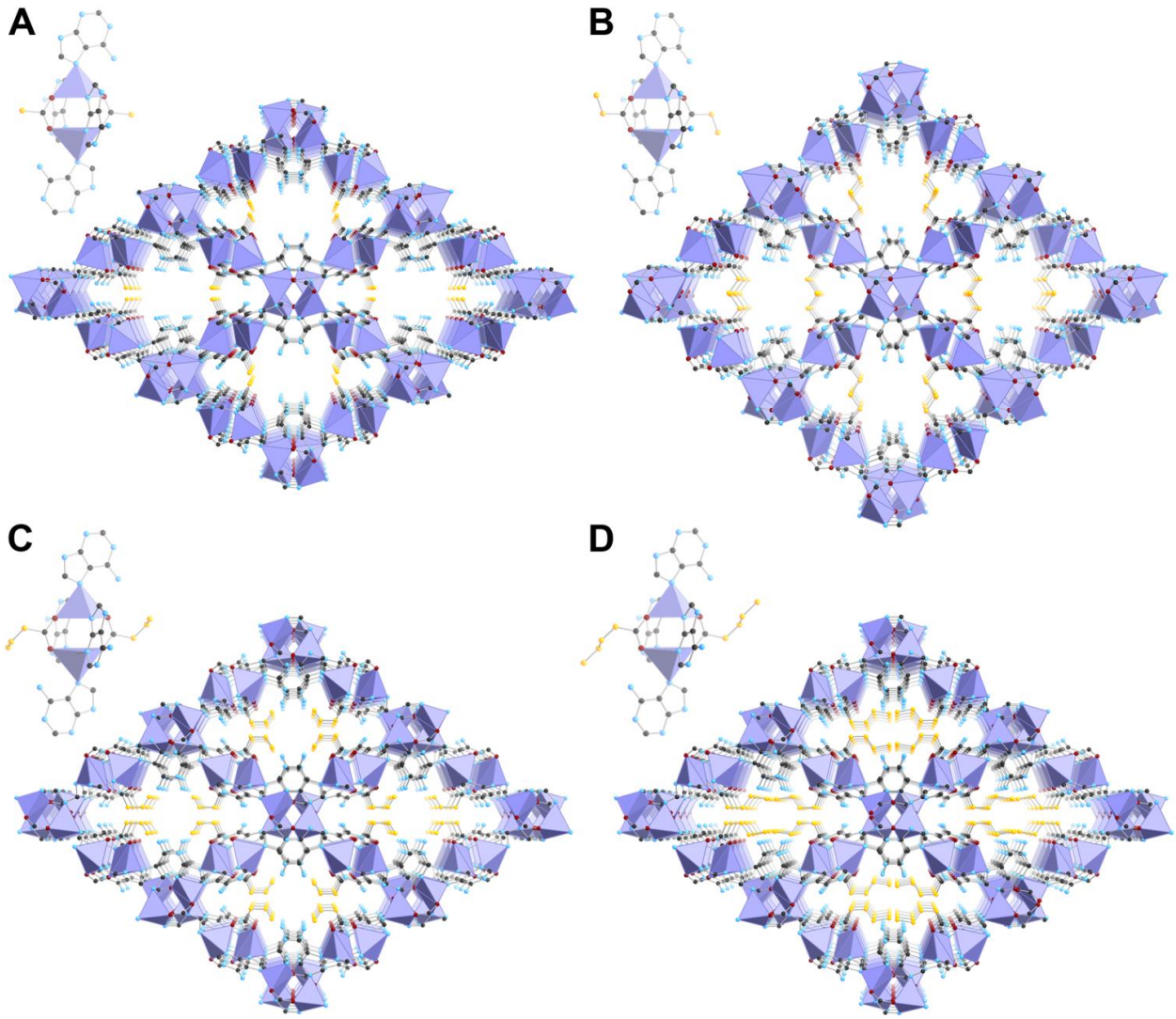

Figure 5. Secondary building units (SBUs) (upper left quadrant) and crystal structures of **bio-MOF-11**, **12**, **13**, and **14** (A, B, C, and D, respectively (Co^{2+}, light purple polyhedra; C, dark gray spheres; O, dark red spheres; N, light blue spheres. H atoms have been omitted for clarity. Aliphatic carbon atoms are represented by orange spheres).

After studying the structure of **bio-MOF-11**, we decided to fabricate an isoreticular series of MOFs by replacing the acetate groups with monocarboxylates having longer aliphatic chains, such as propionate, butyrate, and valerate. These small modifications to the **bio-MOF-11** structure would allow us to carefully modulate both the cavity size and the pore hydrophobicity. To realize this design strategy, we prepared the cobalt monocarboxylate salts (cobalt propionate, cobalt butyrate, and cobalt valerate) and then reacted these salts with adenine under solvothermal conditions. Each reaction yielded crystalline product. Collection and subsequent refinement of single crystal X-ray diffraction data for each product MOF, **bio-MOF-12** ($Co_2(ad)_2(C_2H_5CO_2)_2$), **bio-MOF-13** ($Co_2(ad)_2(C_3H_7CO_2)_2$), and **bio-MOF-14** ($Co_2(ad)_2(C_4H_9CO_2)_2$) (Figure 5, A1-A3; Tables A1-A15), confirmed that they were isostructural to **bio-MOF-11**.[60,61,62] The complete compositions of the solvated samples were determined via elemental analysis. **Bio-MOFs-12**, **13**, and **14** each crystallize in the tetragonal space group ($I4_1/a$), and the unit cells are similar to each other and to **bio-MOF-11** (Table 1). Compared to the other members of the series, the unit cell of **bio-MOF-12** is slightly elongated along *a* and *b* but compressed along *c*. These differences derive from close interactions (3.55 Å nearest neighbor distance) between the propionate methyl group and the six-member pyrimidal ring of the adeninate. The alkyl chains of each bio-MOF extend into the channel space with either single or multiple conformations, each of which was crystallographically resolved; these chains serve to modulate the accessible void space. Given this observation, we were keen to explore the gas adsorption properties of this series of bio-MOFs.

Table 1. Unit cell parameters of **bio-MOF-11** to **14**

	Unit cell parameters			
	a (Å)	b (Å)	c (Å)	$\alpha = \beta = \gamma$
Bio-MOF-11	15.44	15.44	22.78	90^o
Bio-MOF-12	17.24	17.24	20.16	90^o
Bio-MOF-13	15.79	15.79	22.33	90^o
Bio-MOF-14	15.85	15.85	22.35	90^o

2.2.2 Porosity and N_2 Adsorption Studies.

Thermogravimetric analysis (TGA) data for as-synthesized **bio-MOFs 11-14** each exhibited a weight loss step below 200 ℃ which corresponds to the loss of DMF and water guest molecules, as determined via comparison to the elemental analysis data (Table 2). The percentage weight of included solvent decreases with the extension of the aliphatic chains: **bio-MOF-11**, 22.4 % (2.25 DMF, 0.6 H_2O); **bio-MOF-12**, 21.7 % (2.25 DMF, 0.3 H_2O); **bio-MOF-13**, 12.0 % (1.1 DMF, 0.6 H_2O); and **bio-MOF-14**, 8.7 % (0.6 DMF, 0.6 H_2O) (Figure 6, Table 2). For each material, no additional weight loss was observed until the onset of framework decomposition at approximately 280 ℃.

Table 2. Correlation of EA and TGA data.*

	EA of as-synthesized MOF	wt % of solvent in as-synthesized MOF	Weight loss in TGA at 200 ℃
Bio-MOF-11	$Co_2(ad)_2(CH_3CO_2)_2$ • 2.25 DMF, 0.6 H_2O	25.8	22.4
Bio-MOF-12	$Co_2(ad)_2(C_2H_5CO_2)_2$ • 2.25 DMF, 0.3 H_2O	24.2	21.7
Bio-MOF-13	$Co_2(ad)_2(C_3H_7CO_2)_2$ • 1.1 DMF, 0.6 H_2O	14.0	12.0
Bio-MOF-14	$Co_2(ad)_2(C_4H_9CO_2)_2$ • 0.6 DMF, 0.6 H_2O	8.5	8.7

*We note that there exist small discrepancies between the calculated solvent content from EA and the observed solvent content from TGA. Such discrepancies are not uncommon for MOF samples, and they could be caused by several factors that may influence the amount of surface solvent, including drying time and crystallite size.

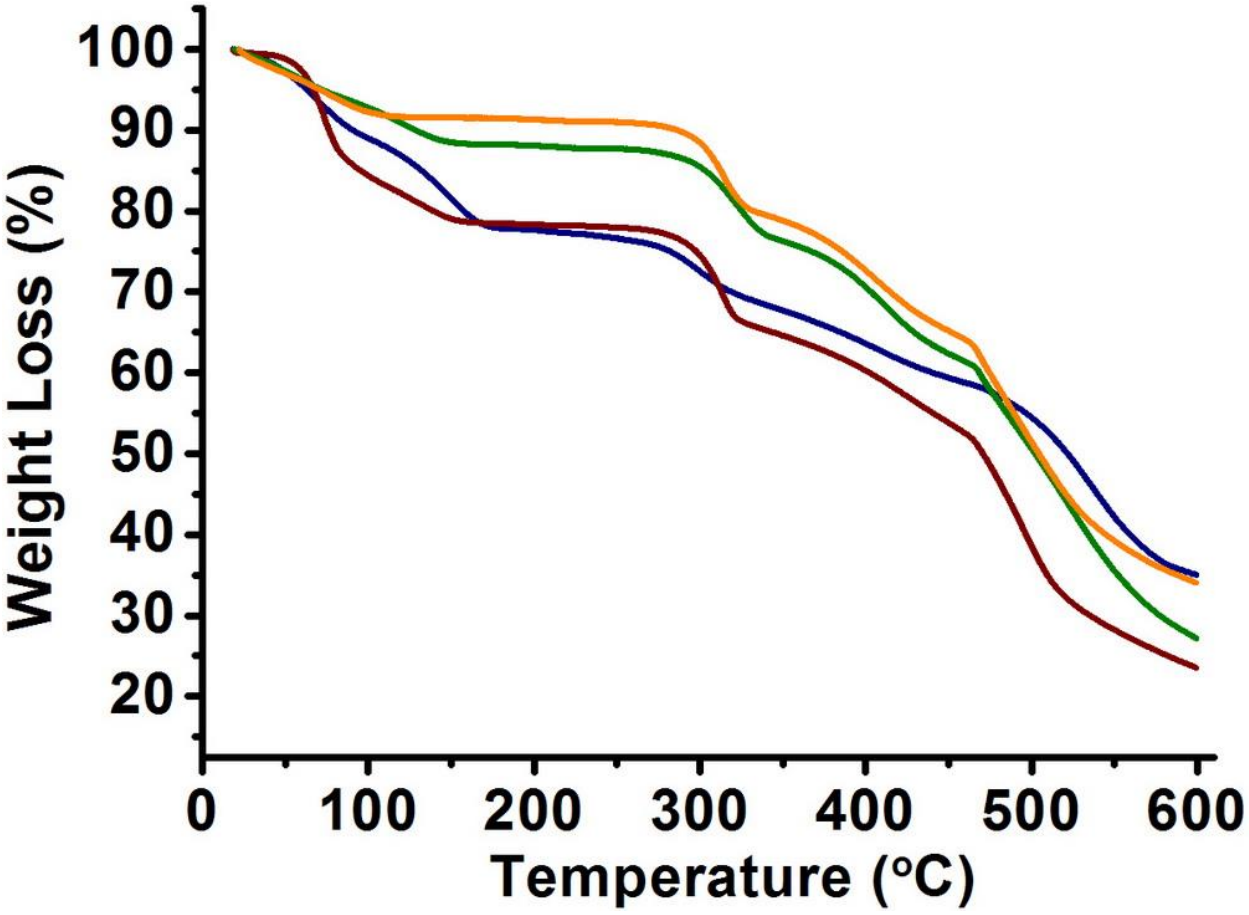

Figure 6. TGA of as-synthesized **bio-MOF-11** (navy), **bio-MOF-12** (dark red), **bio-MOF-13** (green), and **bio-MOF-14** (orange).

N_2 adsorption experiments verified the permanent porosity of **bio-MOFs 11**, **12**, and **13**. Each MOF exhibited a Type I isotherm characteristic of a microporous material (Figure 7). As expected, the surface area and pore volume decreased as the length of the aliphatic chains increases (Table 3). Surprisingly, although **bio-MOF-14** includes 8.7 wt% solvent, its N_2 uptake under the conditions studied was very low compared to the other analogues (Figure 7).

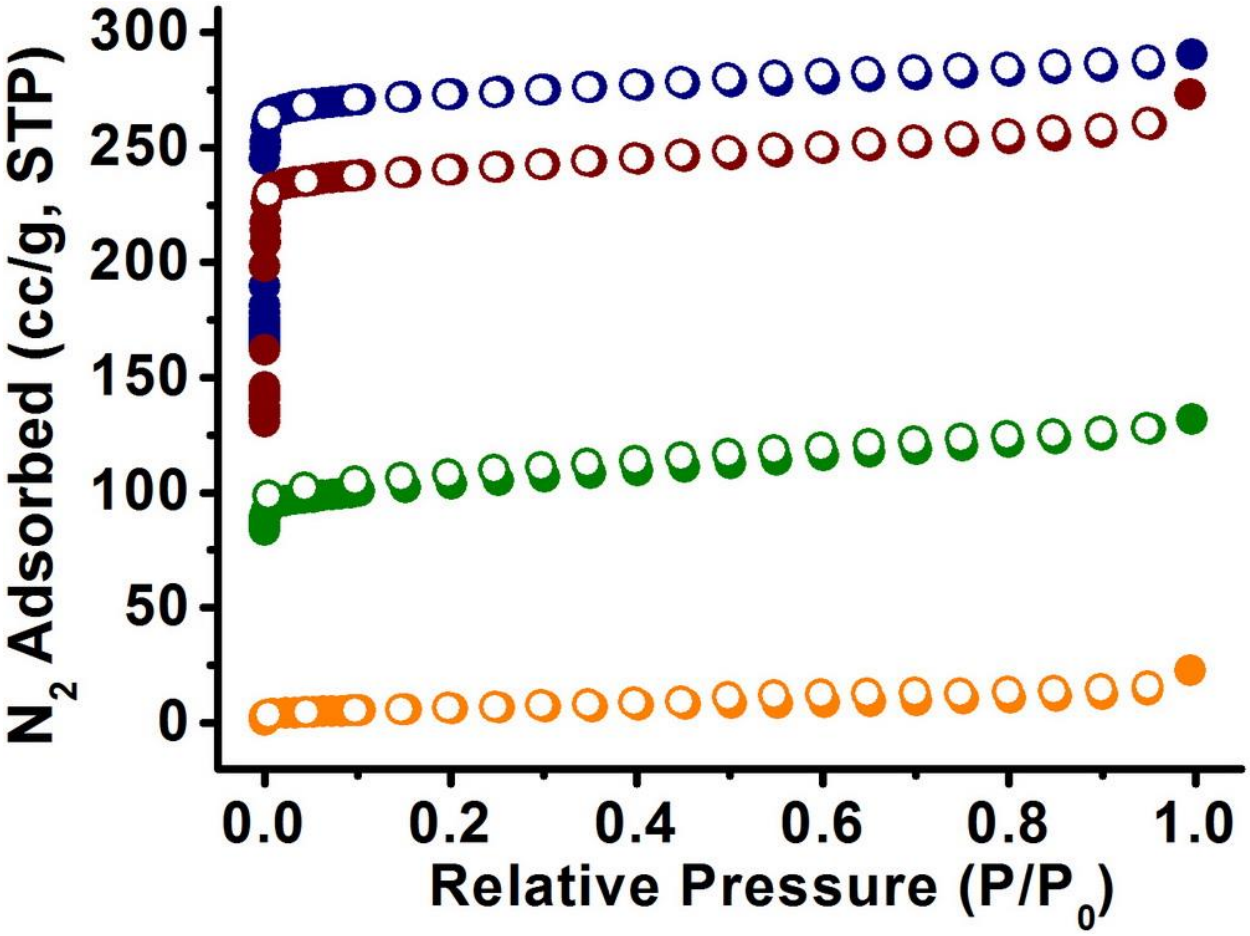

Figure 7. N_2 adsorption isotherms of **bio-MOF-11** (navy), **bio-MOF-12** (dark red), **bio-MOF-13** (green), and **bio-MOF-14** (orange) at 77 K.

Table 3. BET surface area and total pore volume of **bio-MOFs 11-14** based on N_2 adsorption isotherms at 77K (pressure range from 0.001 to 0.009 bar was selected for BET calculation; Pore volume was calculated based on amount of N_2 adsorbed at 0.995 bar).

	BET surface area (m^2/g)	Total pore volume (cc/g)
Bio-MOF-11	1148	0.45
Bio-MOF-12	1008	0.42
Bio-MOF-13	412	0.20
Bio-MOF-14	17	0.035

2.2.3 CO_2 Adsorption Studies.

We measured CO_2 isotherms for each material at multiple temperatures (Tables A18-A21). At 273 K, we found that the total CO_2 capacity at 1 bar decreased with increasing aliphatic chain length (Figure 8, Table 4). Notably, the CO_2 isotherm for **bio-MOF-14** at 273 K does not exhibit typical Langmuir behavior. Rather, it has three distinct regions: an initial gradual rise to 13 cc/g between 0 and 0.15 bar, a second steeper adsorption step to 29 cc/g between 0.15 and 0.25 bar, and a third gradual increase to 44.8 cc/g between 0.25 and 1 bar (Figure 8). Such stepwise adsorption behavior has been observed for flexible MOFs at room temperature[56,63,64,65,66,67,68,69] and for rigid MOFs at low temperatures[55]. To the best of our knowledge, this behavior is unique among rigid MOFs at ambient temperature.

We collected CO_2 isotherms at higher temperatures (298, 303, 308, and 313 K) (Figure 9-12) and used these data to calculate the isosteric heats of adsorption (Q_{st}) for **bio-MOFs 11-13**; **bio-MOF-14** Q_{st} values were not calculated because we could not fit its isotherms to the dual-

site Langmuir model. **Bio-MOF-12** and **13** each have noticeably higher Q_{st} values at low loading than **bio-MOF-11** (33.1 kJ/mol for bio-MOF-11, 38.4 kJ/mol for **bio-MOF-12** and 40.5 kJ/mol for **bio-MOF-13**) and remain appreciably higher throughout the whole adsorption range (Figure 13; Table 4). The high Q_{st} values for **bio-MOF-12** and **bio-MOF-13** correlate well with the high CO_2:N_2 selectivity values computed from IAST (*vide infra*).

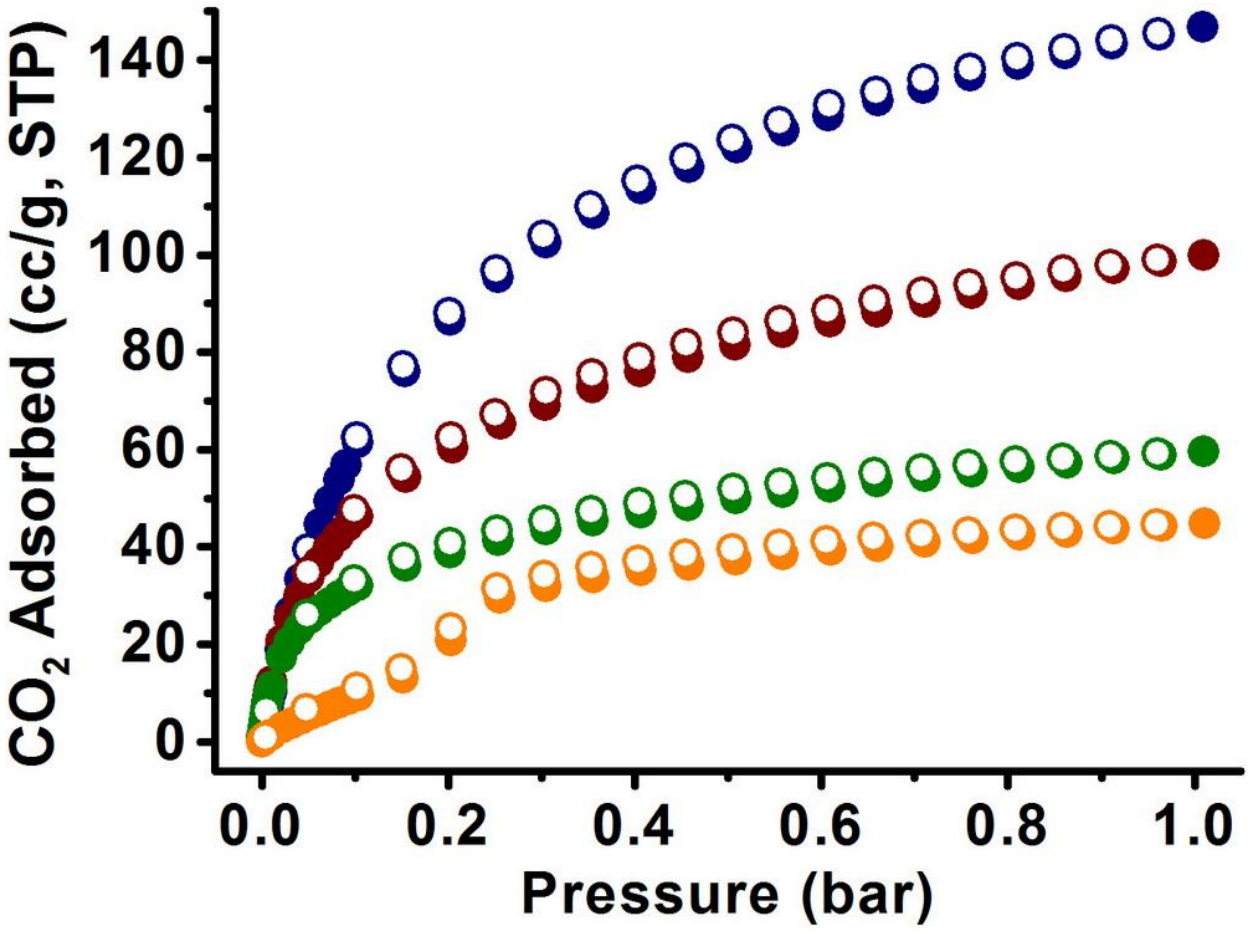

Figure 8. CO_2 adsorption isotherms of **bio-MOF-11** (navy), **bio-MOF-12** (dark red), **bio-MOF-13** (green), and **bio-MOF-14** (orange) at 273 K.

Table 4. CO_2 adsorption data and isosteric heats of adsorption at low loadings, given in parentheses.

	CO_2@273K[a]	CO_2@298 K[b]	Q_{st}[c] (loading, cc/g)
Bio-MOF-11	147	105	33.1(2.18)
Bio-MOF-12	100	71	38.4(2.91)
Bio-MOF-13	60	45	40.5(3.01)
Bio-MOF-14	45	31	N/A

[a] Amount of CO_2 absorbed (cc/g) at 273 K, 1 bar. [b] Amount of CO_2 absorbed (cc/g) at 298 K, 1 bar. [c] kJ/mol.

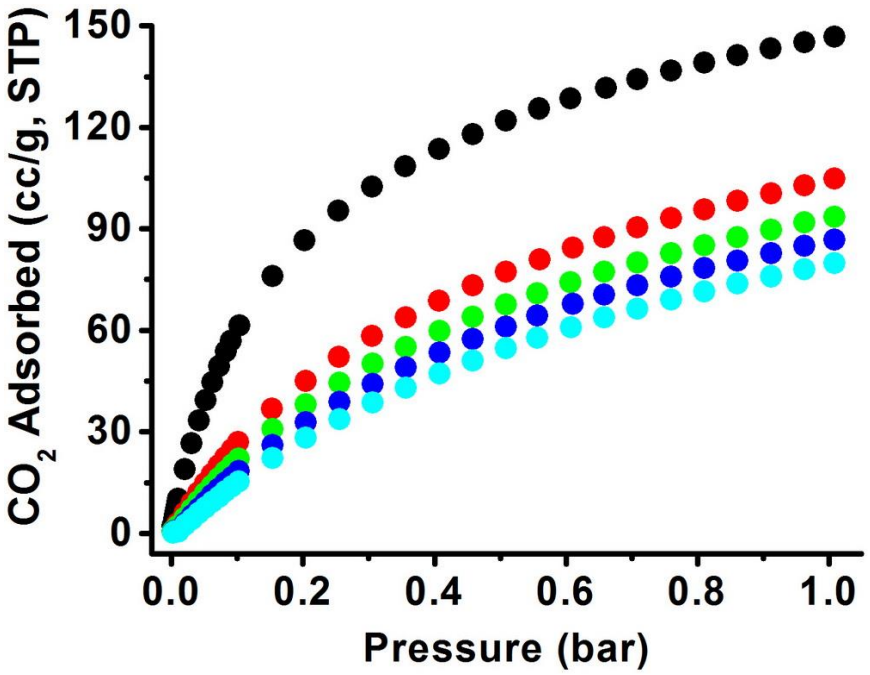

Figure 9. CO_2 adsorption isotherms of **bio-MOF-11** at 273 K (black), 298 K (red), 303 K (green), 308 K (blue), and 313 K (cyan).

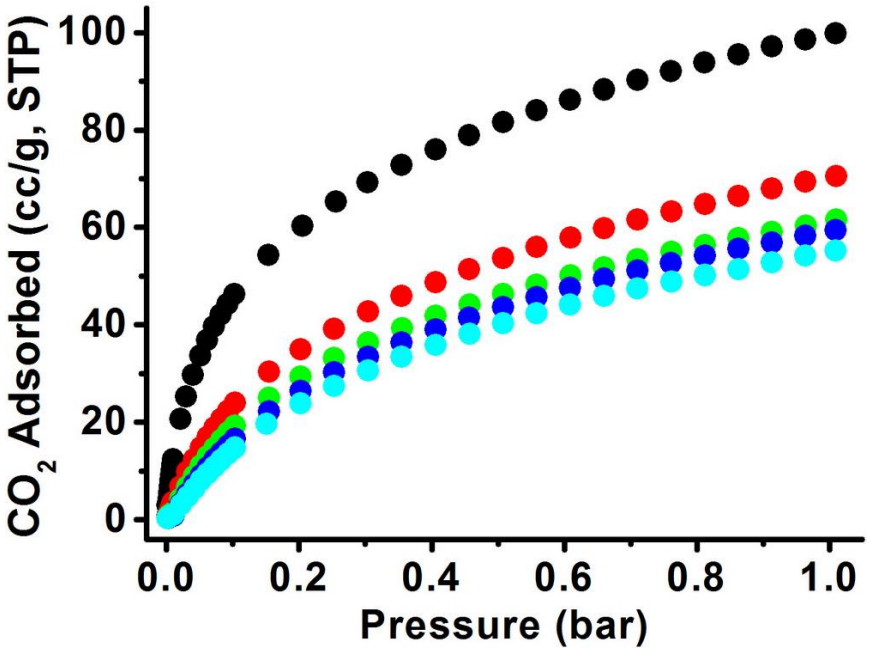

Figure 10. CO_2 adsorption isotherms of **bio-MOF-12** at 273 K (black), 298 K (red), 303 K (green), 308 K (blue), and 313 K (cyan).

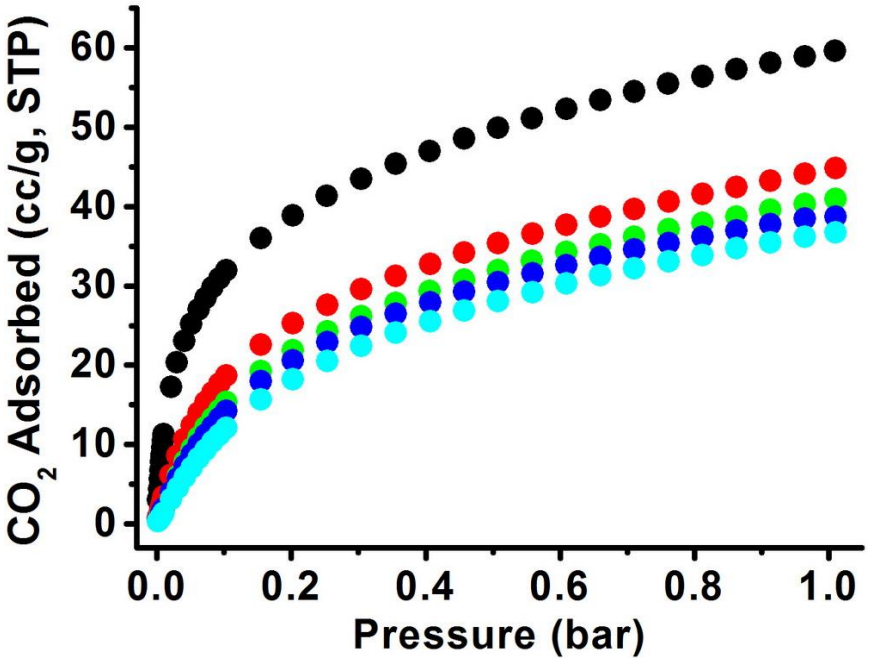

Figure 11. CO_2 adsorption isotherms of **bio-MOF-13** at 273 K (black), 298 K (red), 303 K (green), 308 K (blue), and 313 K (cyan).

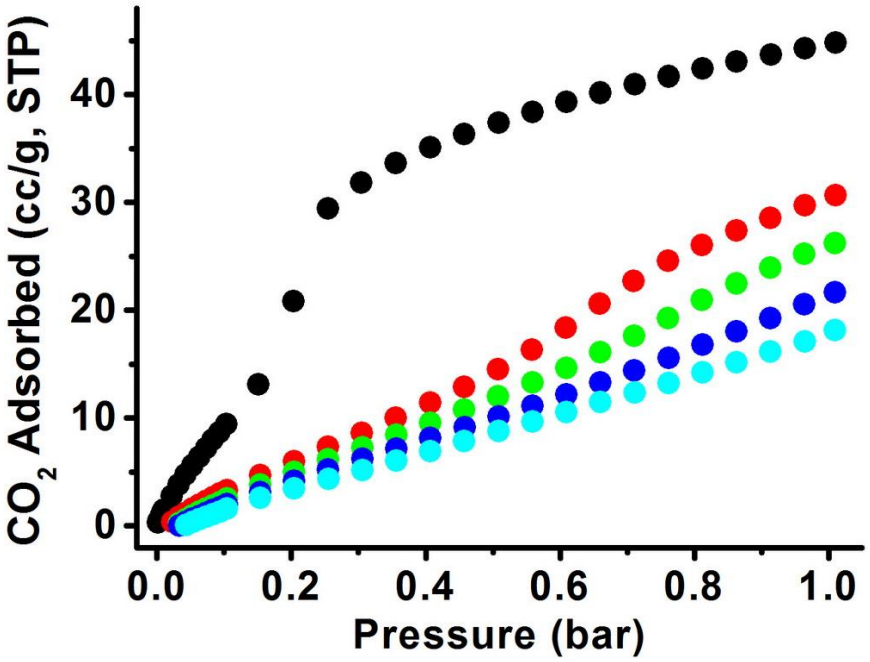

Figure 12. CO_2 adsorption isotherms of **bio-MOF-14** at 273 K (black), 298 K (red), 303 K (green), 308 K (blue), and 313 K (cyan).

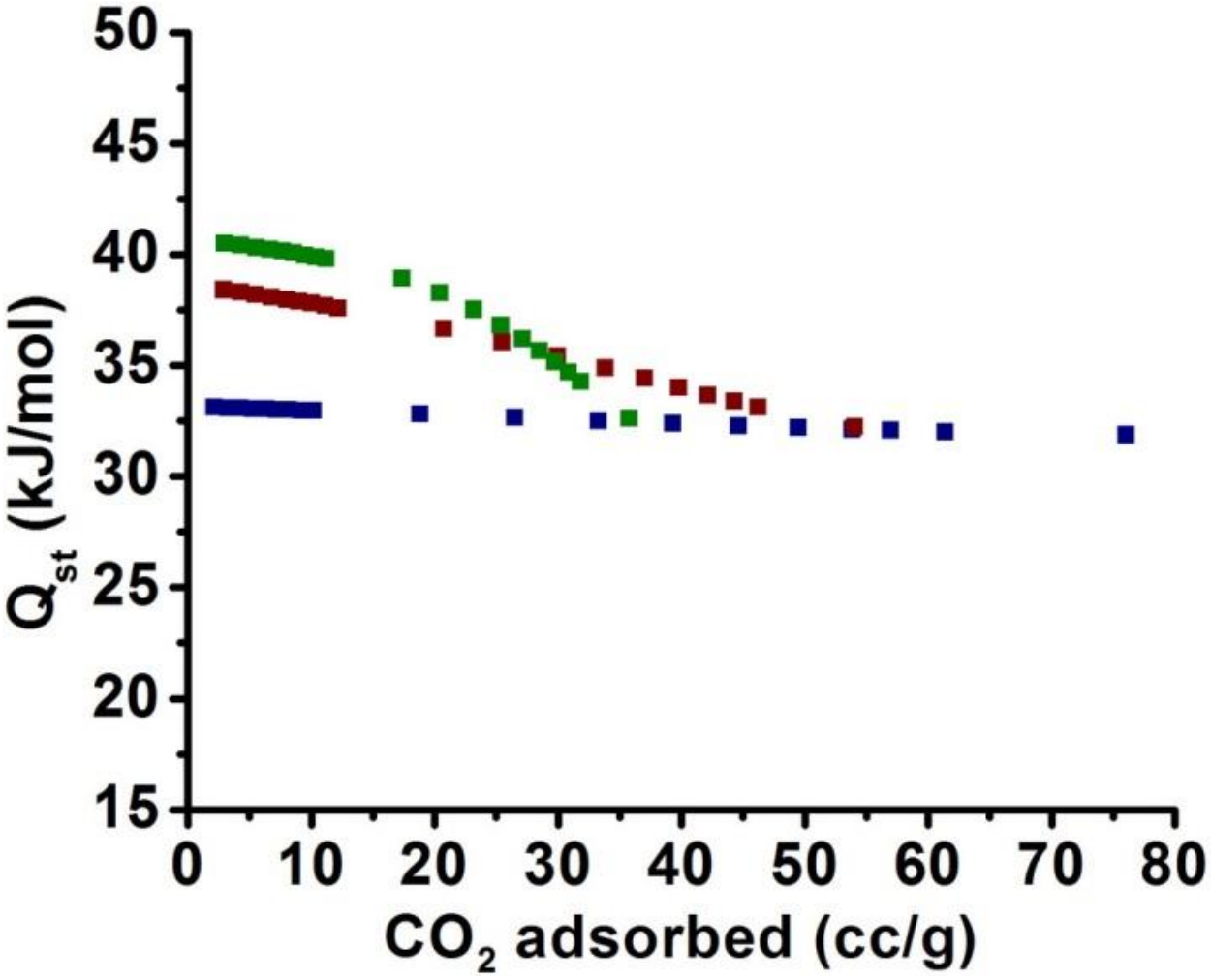

Figure 13. Isosteric heat of adsorption of **bio-MOF-11** (navy), **bio-MOF-12** (dark red), and **bio-MOF-13** (green). The absolute average errors in the Q_{st} are 0.3, 1.7, and 1.7 kJ/mol for **bio-MOF-11**, **bio-MOF-12**, and **bio-MOF-13**, respectively (details provided in the Supporting Information).

2.2.4 CO_2:N_2 Selectivity.

We first estimated the CO_2:N_2 selectivity for each bio-MOF using the single component CO_2 (Figure 9-12) and N_2 isotherms (Figure 14 and Figure 15). Specifically, we divided the amount of CO_2 adsorbed at 0.15 bar by the amount of N_2 adsorbed at 0.75 bar.[13] **Bio-MOF-11**, **12**, and **13** show similar selectivity ranging from 52 to 59 at 273 K and from 44 to 46 at 298 K (Figure 16). Since **bio-MOF-14** shows essentially no N_2 uptake (Figure 14 and Figure 15), the CO_2:N_2 selectivity is predicted to be extremely high.

IAST was used to estimate the CO_2:N_2 selectivities for CO_2/N_2 gas mixtures.[70] The experimental CO_2 and N_2 isotherms collected at 273 and 298 K for **bio-MOF-11** to **13** were fitted to the dual site Langmuir model (Table 5; Figure 31-33). We computed the IAST predicted adsorption selectivity of CO_2 over N_2 for a 10:90 CO_2/N_2 mixture (Figure 17). At 273 K, **bio-MOF-12** and **13** exhibited much higher initial CO_2:N_2 selectivity (163:1 and 290:1 respectively) than **bio-MOF-11** (102:1); they remain more selective than **bio-MOF-11** over the whole pressure range (0 - 1 bar) (Figure 17A). At 298 K, **bio-MOF-12** still exhibits an appreciably higher CO_2:N_2 selectivity (52:1) than **bio-MOF-11** (43:1) while **bio-MOF-13** exhibits a slightly lower selectivity (40:1) (Figure 17B).

It is important to understand that the inherent CO_2:N_2 selectivities for **bio-MOFs 11-13** derive principally from their Q_{st} values for CO_2 at moderate loading (*vide supra*). Indeed, the Q_{st} values (Figure 13) and the IAST selectivities (Figure 17) follow a similar trend. On the other hand, the CO_2:N_2 selectivity for **bio-MOF-14** likely derives from a molecular sieving effect (*vide infra*).

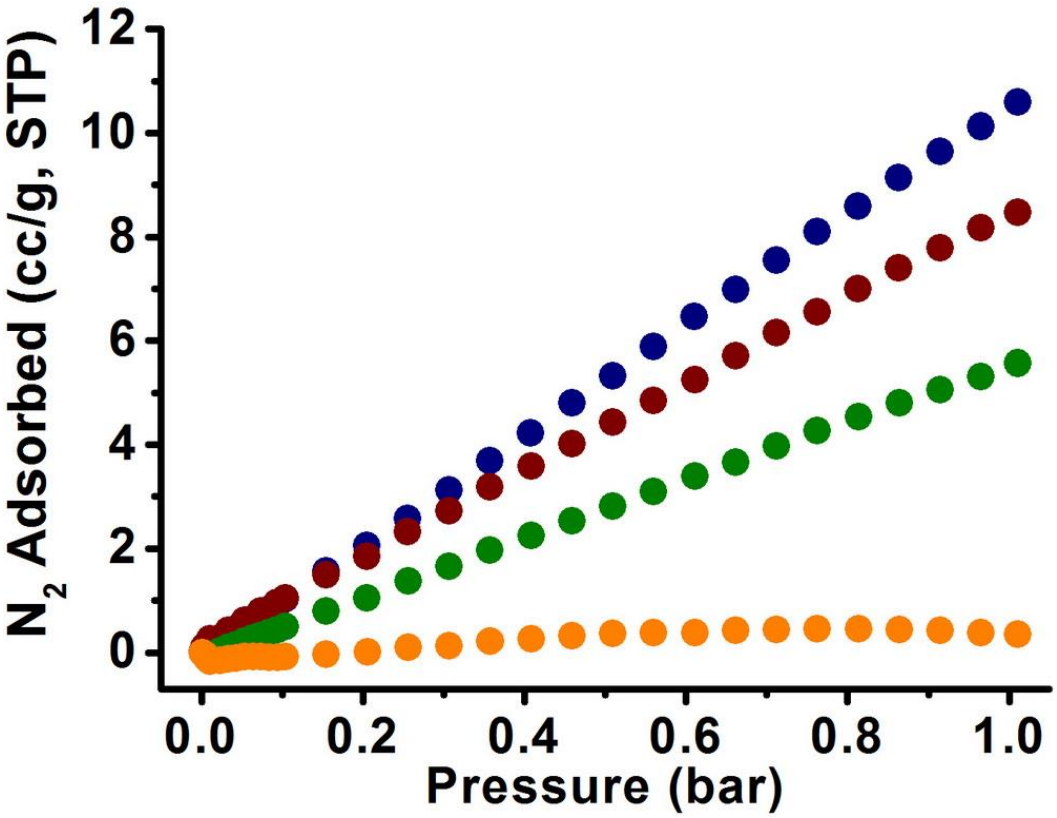

Figure 14. N_2 adsorption isotherms of **bio-MOF-11** (navy), **bio-MOF-12** (dark red), **bio-MOF-13** (green), and **bio-MOF-14** (orange) at 273 K. The isotherm data for **bio-MOF-14** reflects the instrument noise, because no measurable amount of N_2 was adsorbed.

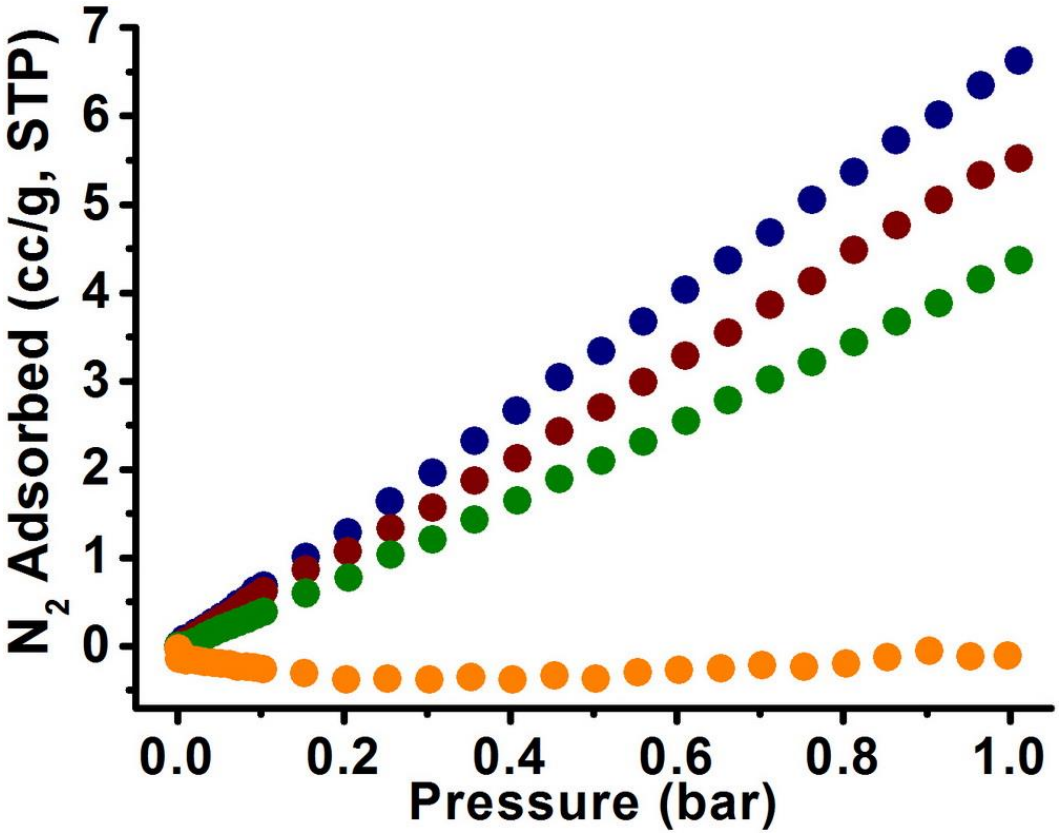

Figure 15. N_2 adsorption isotherms of **bio-MOF-11** (navy), **bio-MOF-12** (dark red), **bio-MOF-13** (green), and **bio-MOF-14** (orange) at 298 K. The isotherm data for **bio-MOF-14** reflects the instrument noise, because no measurable amount of N_2 was adsorbed.

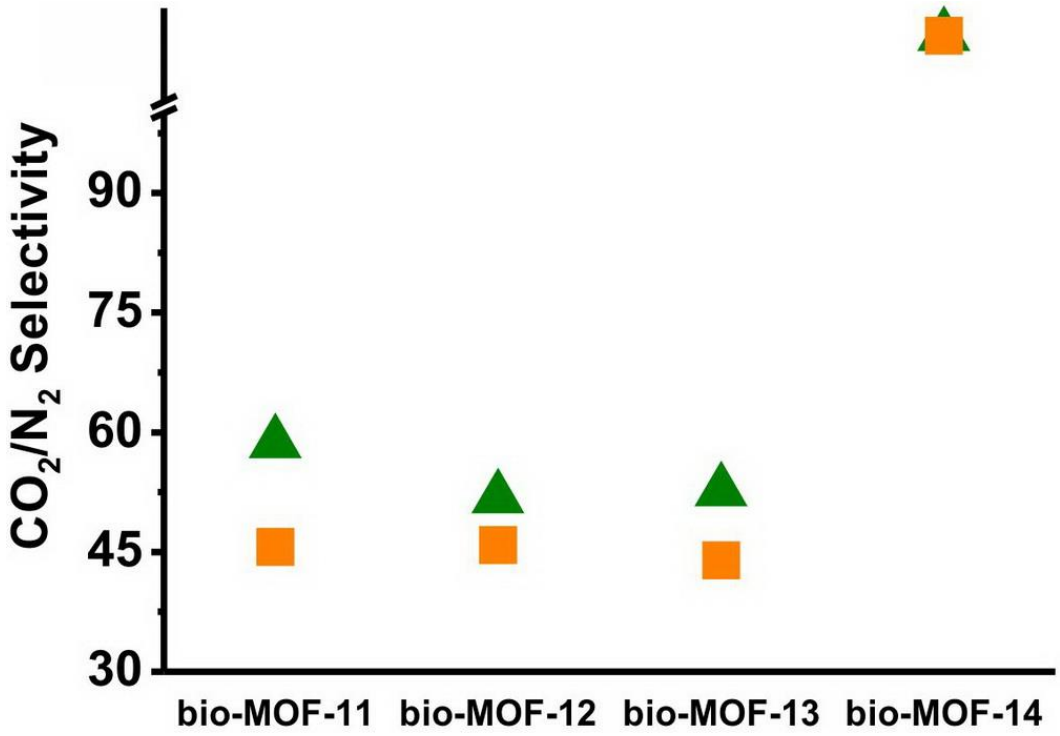

Figure 16. CO_2:N_2 selectivity of **bio-MOF 11-14** at 273 K (green) and 298 K (orange) calculated from single component isotherms. Note that the selectivity for **bio-MOF-14** is inferred to be extremely high.

Table 5. Fitting equations, constants and estimated error of CO_2 isotherms for isosteric heats of adsorption calculations.*

Bio- MOF	Temp. K	Constants			
		a	*b*	*c*	*d*
11	273	4.31907	1.05872	4.93959	0.113029
	298	4.8926	0.371175	4.77658	3.40143
	303	2.92966	1.53268	4.39239	0.465668
	308	2.37393	0.67473	4.36922	0.795414
	313	4.03048	0.90846	2.76736	0.923252
12	273	2.06284	0.033473	4.30731	0.769994
	298	4.7187	2.39924	1.97776	0.131818
	303	6.05072	6.40008	2.33383	0.22117
	308	2.66924	0.31853	23.8319	37.9556
	313	2.57505	0.352666	10.0766	17.4637
13	273	2.32496	0.797528	1.37895	0.019962
	298	1.36656	0.087907	3.83663	4.2019
	303	1.48023	0.146465	5.75071	9.86365
	308	1.41326	0.153541	4.15856	7.16274
	313	4.38588	8.48581	1.40738	0.200442

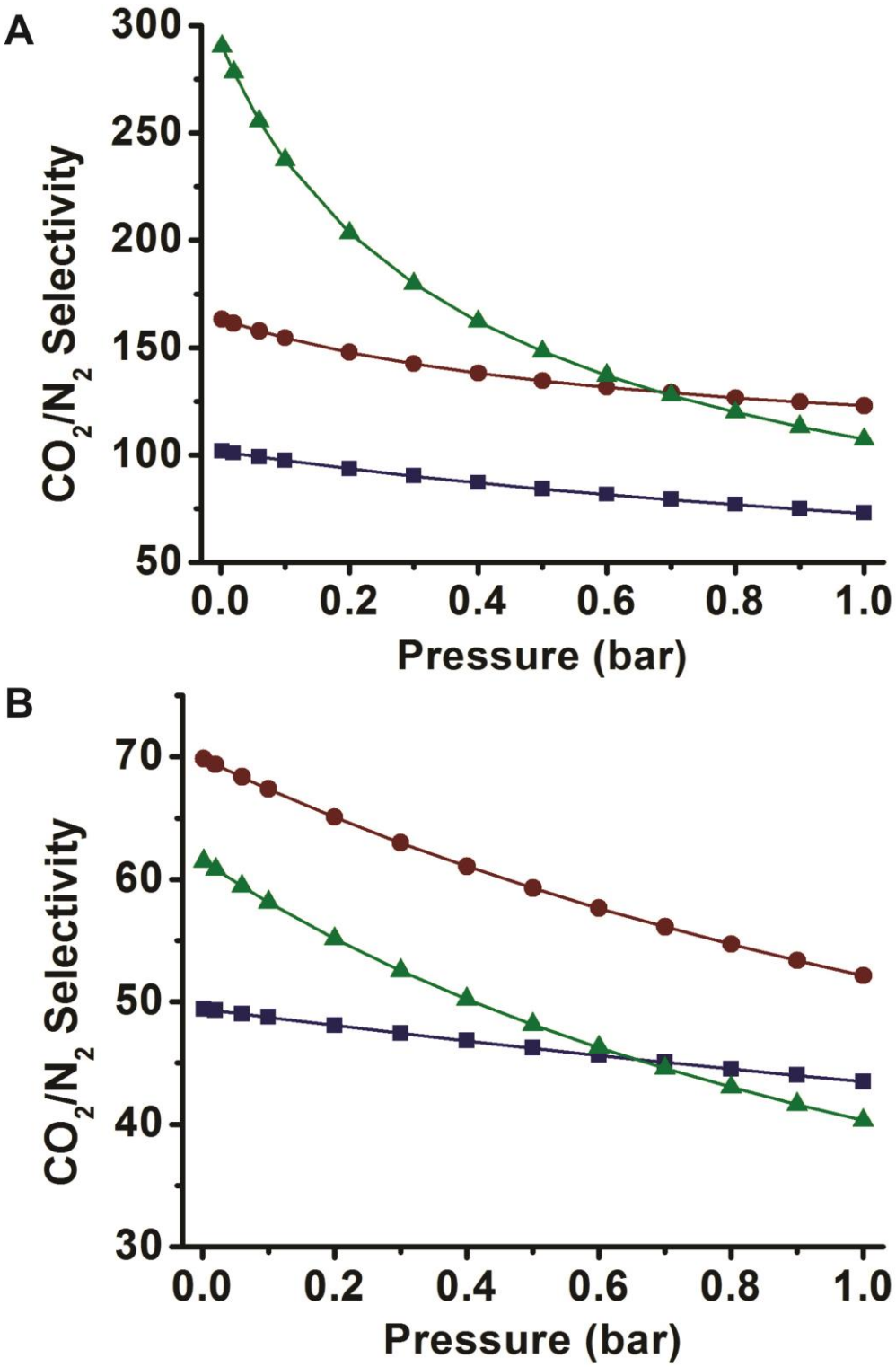

Figure 17. IAST selectivity for CO_2:N_2 (10:90 mixture) of **bio-MOF-11** (navy), **bio-MOF-12** (dark red), and **bio-MOF-13** (green) at 273 K (A) and 298 K (B).

2.2.5 Molecular Modeling and Simulation.

To more completely understand the adsorption behavior for this series of bio-MOFs, we used Materials Studio software to generate Connolly surface diagrams for each bio-MOF. In cases where multiple aliphatic chain conformations were possible, we generated multiple diagrams. The diagrams (Figure 18-21) were generated using a probe radius of 1.82 Å (half the kinetic diameter of a N_2 molecule). These diagrams reveal several important pieces of information. First, they show that the cavities in **bio-MOFs 11-12** are completely interconnected and thus allow passage of N_2 molecules (Figure 18 and Figure 19). Second, they show that when the butyrate chains in **bio-MOF-13** adopt conformation I (42.6 % occupancy), its cavities are isolated from each other; however, when they adopt configuration II (57.4 % occupancy), its cavities are interconnected (Figure 20), which leads to appreciable N_2 adsorption at 77 K (165 cc/g). Third, they show that two out of the three possible conformation of the valerate chain in **bio-MOF-14** (configuration II and III with total occupancy of 65.3 %) result in isolated cavities that would prevent passage of N_2 throughout the structure, while configuration I (34.7 %) for **bio-MOF-14** results in interconnected cavities (Figure 21). As a result, **bio-MOF-14** adsorbs a comparatively small amount of N_2 at 77 K (29 cc/g) (Figure 7) and a negligible amount at 273 and 298 K (Figure 14-15). CO_2, on the other hand, has a smaller kinetic diameter (3.30 Å) than N_2 (3.64 Å)[13] and interacts more strongly with the framework. In the case of **bio-MOF-14**, a possible pressure-induced configuration change allows CO_2 to access the inner cavities after the breakthrough point (Figure 8, 0.15 bar), resulting in the observed unusual CO_2 adsorption behavior. Our molecular modeling results support this conclusion. We have quantified the effects of conformations of the valerate chains on the adsorption isotherms by comparing adsorption isotherms computed from GCMC simulations using two different valerate

conformations generated from our DFT molecular dynamics calculations that were then relaxed to their local minima. These isotherms are plotted in Figure 22. The energy difference between the two configurations is 0.065 eV per unit cell (496 atoms), with the configuration having the largest uptake having the lower energy. The conformations of the chains were held fixed in the GCMC simulations. The isotherms in Figure 22 indicate that chain conformations in **bio-MOF-14** can have a profound effect on the adsorption capacity. Moreover, the adsorption of CO_2 could influence the chain conformation because the energy differences between the configurations are not large. Hence, it is likely that the step in the isotherm for **bio-MOF-14** seen in Figure 8 is the result of configurational changes of the valerate chains induced by the presence of CO_2. In contrast, our simulations found that the conformations of the aliphatic chains in **bio-MOFs 11-13** had little effect on the computed adsorption isotherms. Note that the modeling results from the Connolly surface diagram and the GCMC simulations complement one another. The former indicates pore entrance blocking, which limits adsorption on reasonable time-scales, while the latter indicates that the chain conformations also dramatically impact equilibrium loading. To summarize, N_2 cannot access the pores of **bio-MOF-14** at any of the studied elevated temperatures (273 and 298 K) due to a molecular sieving effect, whereas CO_2 can access the pores through a gating process.[67,71] As a result, **bio-MOF-14** exhibits extremely high selectivity for CO_2 over N_2, as inferred from single component isotherms.

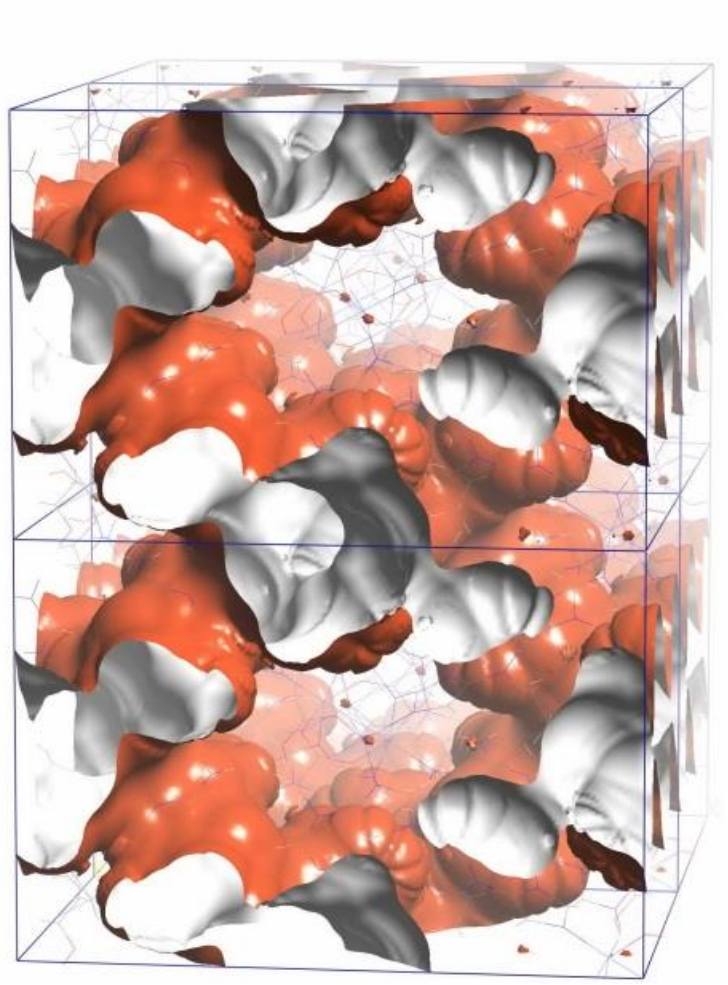

Figure 18. Connolly surface diagram of **bio-MOF-11** using N_2 as a probe molecule (probe radius 1.86 Å). The inner surfaces of the cavities have been shown in white, while the outer surfaces are represented in orange.

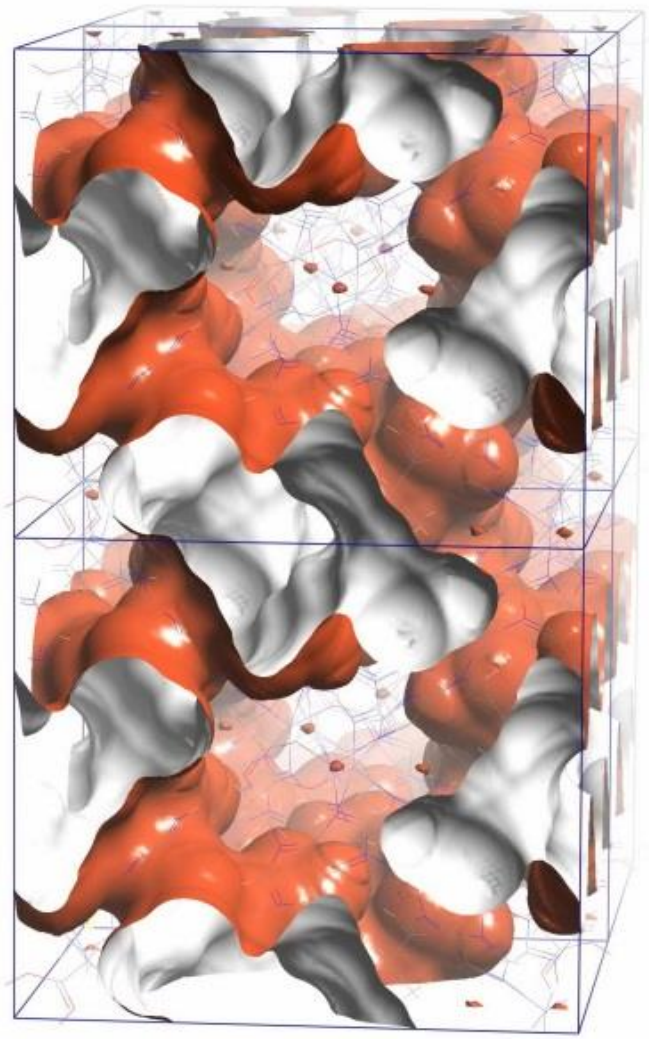

Figure 19. Connolly surface diagram of **bio-MOF-12** using N_2 as a probe molecule (probe radius 1.86 Å). The inner surfaces of the cavities have been shown in white, while the outer surfaces are represented in orange.

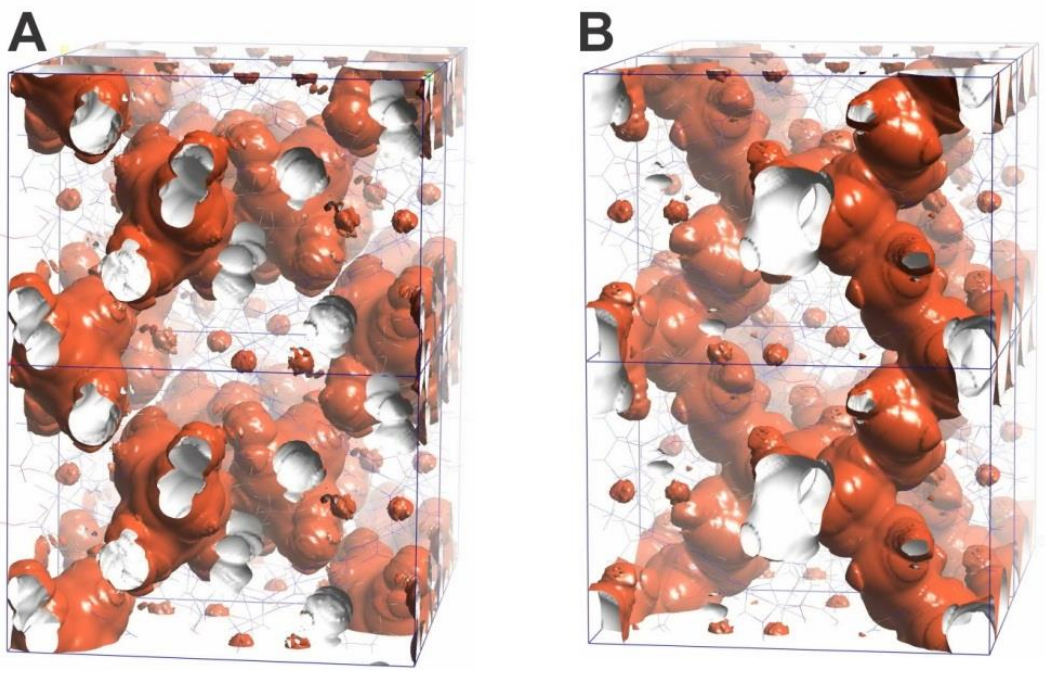

Figure 20. Connolly surface diagram of **bio-MOF-13** using N_2 as a probe molecule (probe radius 1.86 Å). The inner surfaces of the cavities have been shown in white, while the outer surfaces are represented in orange. A and B represent configuration I and II respectively.

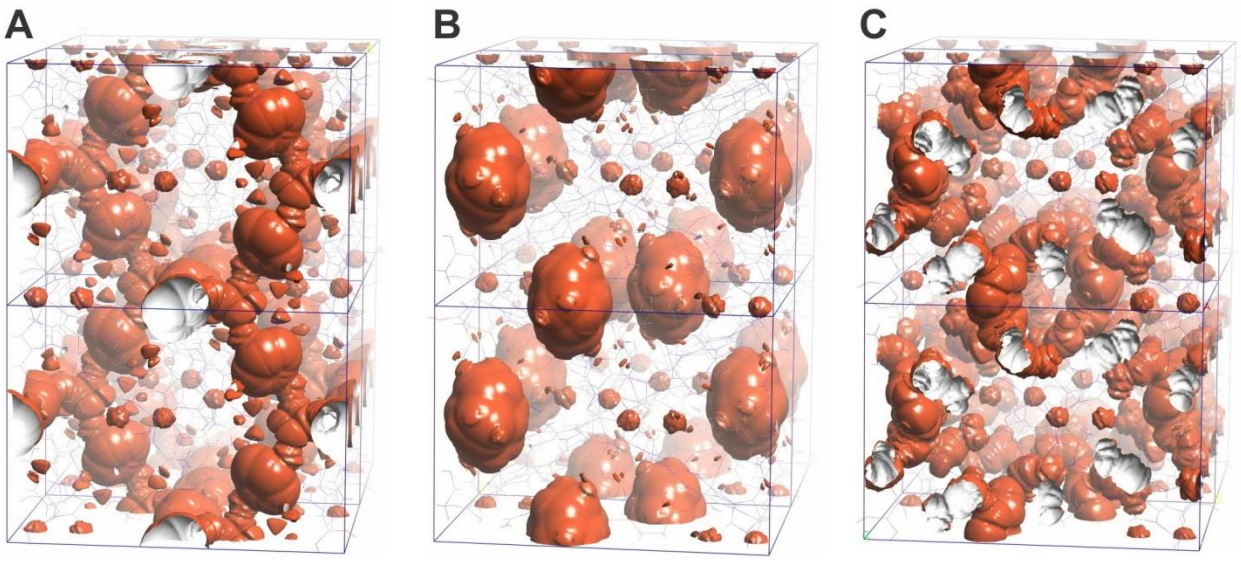

Figure 21. Connolly surface diagram of **bio-MOF-14** using N_2 as a probe molecule (probe radius 1.86 Å). The inner surfaces of the cavities have been shown in white, while the outer surfaces are represented in orange. A, B, and C represent configuration I, II, and III respectively.

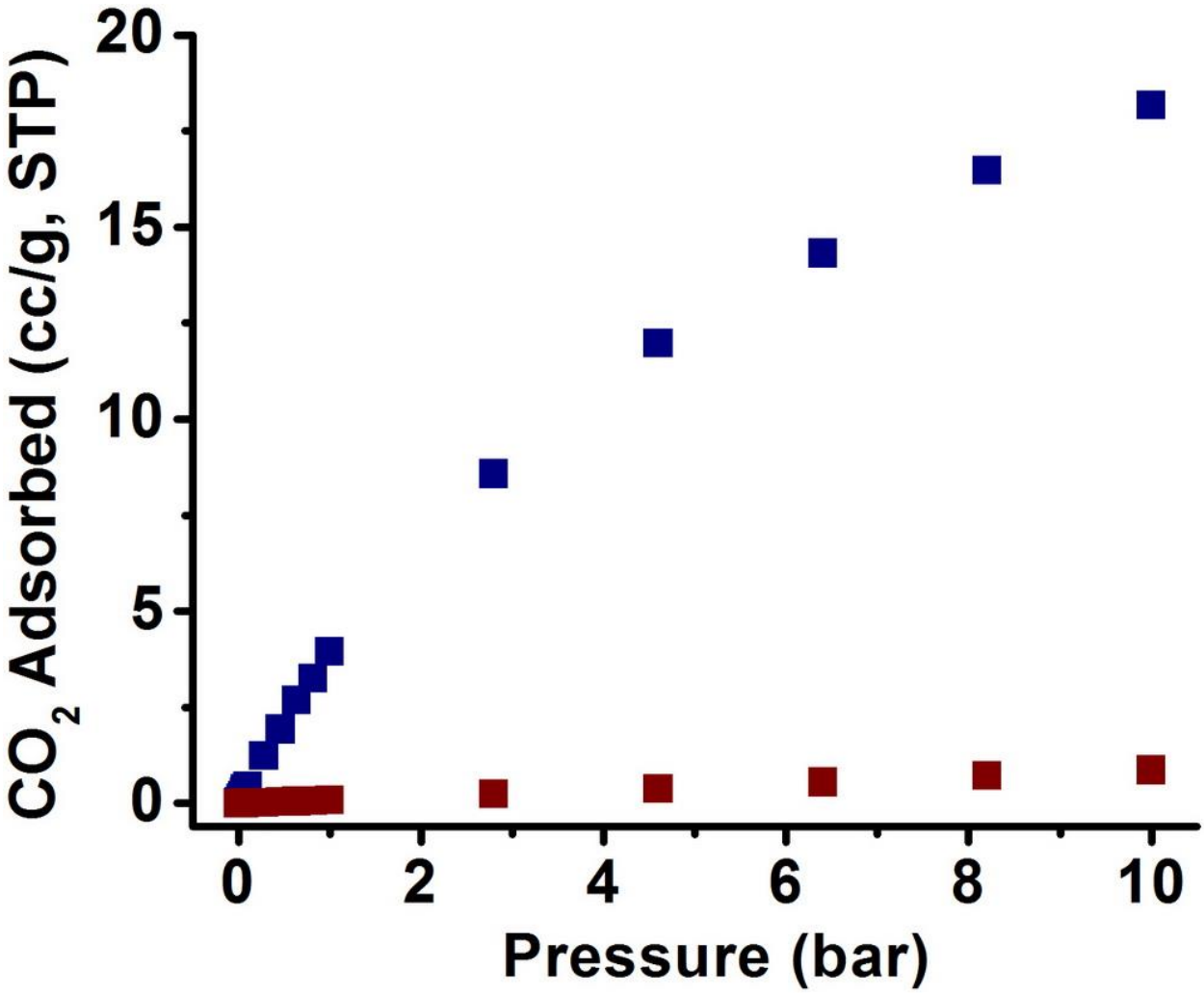

Figure 22. Adsorption isotherms at 298 K of CO_2 in **bio-MOF-14** from grand canonical Monte Carlo Simulations using two different conformations of the valerate chains.

We have explored many different adsorption configurations for CO_2 within **bio-MOF-12** using the van der Waals corrected DFT-D2 approach. We did not find any indication of chemical binding or significant charge transfer complexes. The strongest interaction sites for CO_2 were not the Lewis-base sites, but the Lewis-acid sites, as seen by the computed ground state structure shown in Figure 23. Previous calculations have demonstrated how CO_2 can act as both a Lewis acid and a Lewis base when interacting with CO_2-soluble polymers,[72] so it is not surprising that

similar interactions could be important in MOFs. Our calculations show that CO_2 is arranged so that it makes three Lewis-acid/Lewis-base interactions with slightly acidic protons on the framework, having O—H bond distances of 2.72, 2.75, and 2.85 Å. The binding energy of this configuration is 36 kJ/mol, which is in good agreement with the experimentally calculated isosteric heats for **bio-MOF-12**.

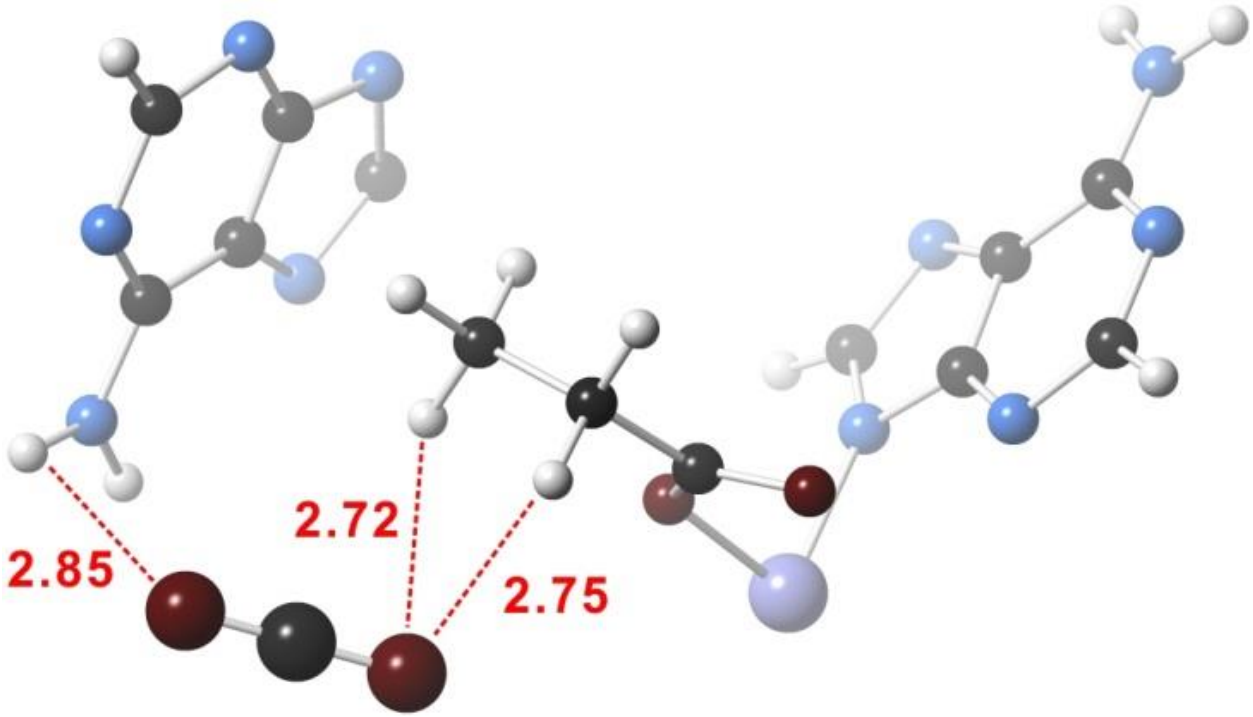

Figure 23. Ground state structure of CO_2 in **bio-MOF-12** as computed from DFT-D2. The dashed lines indicate Lewis acid/base interactions, with O—H bond lengths shown in angstroms (Co^{2+}, light purple spheres; C, dark gray spheres; O, dark red spheres; N, light blue spheres; H, white spheres).

2.2.6 Water Stability Studies.

Having shown that increasing the length of the aliphatic group can positively impact CO_2:N_2 selectivity, we next explored whether the identity of the aliphatic group could impact the water stability of the respective bio-MOFs. We first soaked a sample of each bio-MOF in water for 1 hour, and then we used PXRD and SEM imaging to initially evaluate the materials' stability. **Bio- MOF-11**, as mentioned previously, dissolved rapidly in water, as evidenced by PXRD (Figure 24); SEM images could not be obtained. **Bio-MOFs 12** and **13** dissolved partially in water. The intensity of their signature diffraction lines decreased substantially (Figure 24); however, it was clear from comparing PXRD patterns that **bio-MOF-13**, with butyrate, was noticeably more stable in water than **bio-MOF-12**, with propionate (Figure 24). SEM images of the soaked samples supported this conclusion: they revealed significant crystallite fragmentation and pitting of the crystal surfaces (Figure 25), consistent with degradation, for **bio-MOF-12** samples yet only a small amount of fragmentation and pitting for **bio-MOF-13** samples (Figure 26).

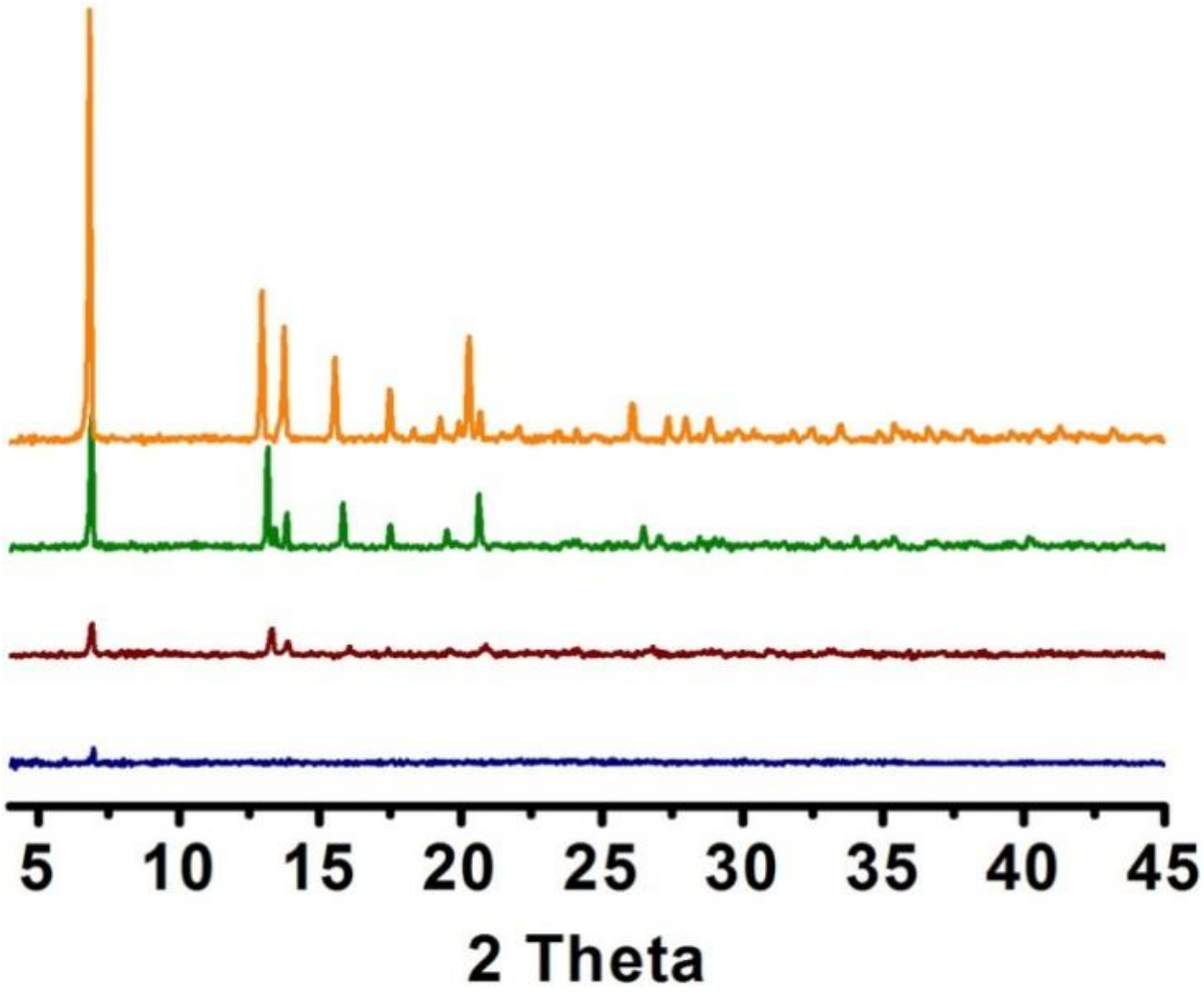

Figure 24. PXRD patterns of **bio-MOF-11** (navy), **bio-MOF-12** (dark red), **bio-MOF-13** (green), and **bio-MOF-14** (orange) after one hour soaking in water.

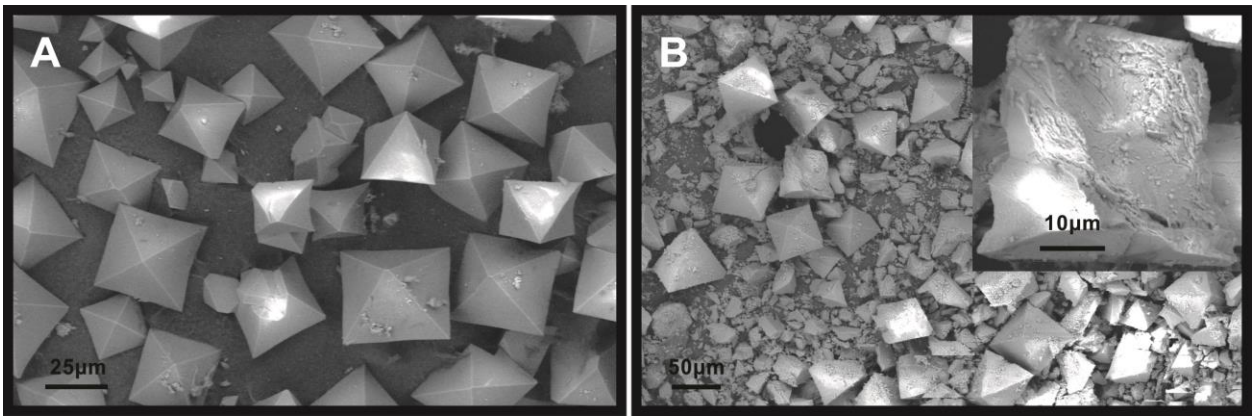

Figure 25. SEM images of **bio-MOF-12** before (A) and after (B) 1 hour soaking in water.

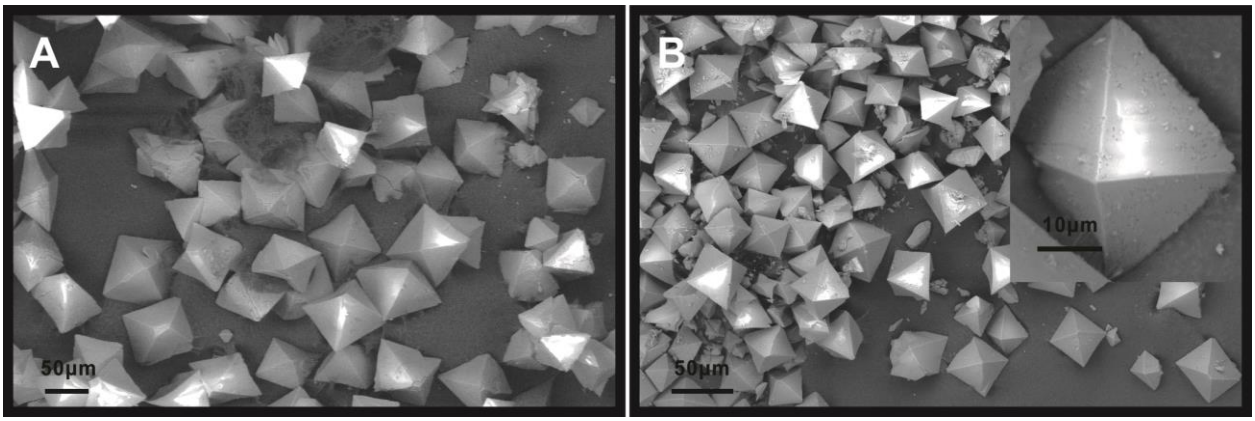

Figure 26. SEM images of **bio-MOF-13** before (A) and after (B) 1 hour soaking in water.

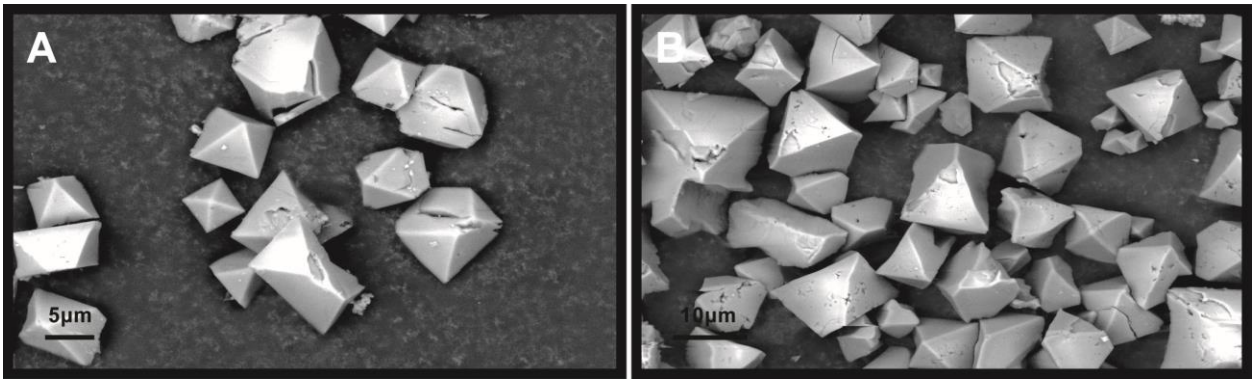

Figure 27. SEM images of **bio-MOF-14** after soaking in water for 7 days (A) and 30 days (B).

Bio-MOF-14, with the valerate groups, was the most stable of the series and showed no loss of crystallinity (Figure 24) and no significant crystal degradation after soaking in water for 1 hour (Figure 28). We therefore extended the water soaking period to 7 and 30 days; the PXRD pattern shows no loss in crystallinity (Figure 29), and SEM images show only minimal pitting on the crystal surface after 7 or 30 days soaking in water (Figure 27). To further prove that the material remains intact upon extended exposure to water, we collected CO_2 isotherms at 273 K for samples of **bio-MOF-14** which were soaked in water for either 7 or 30 day. The isotherms are nearly identical and they closely match the isotherm of the non-water-treated sample in both shape and capacity, indicating that water does not affect the porosity of the material (Figure 30).

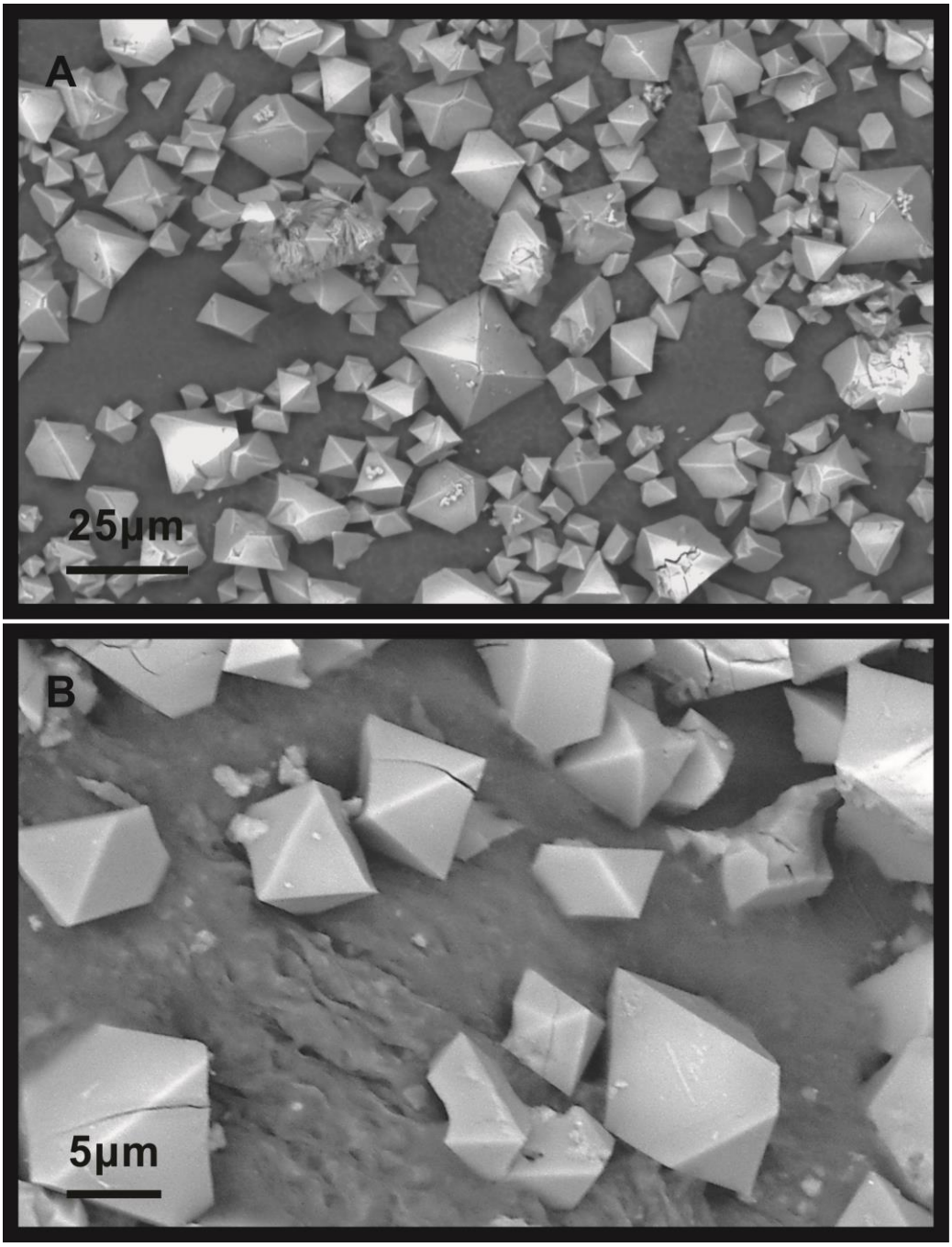

Figure 28. SEM images of **bio-MOF-14** before (A) and after (B) 1 hour soaking in water.

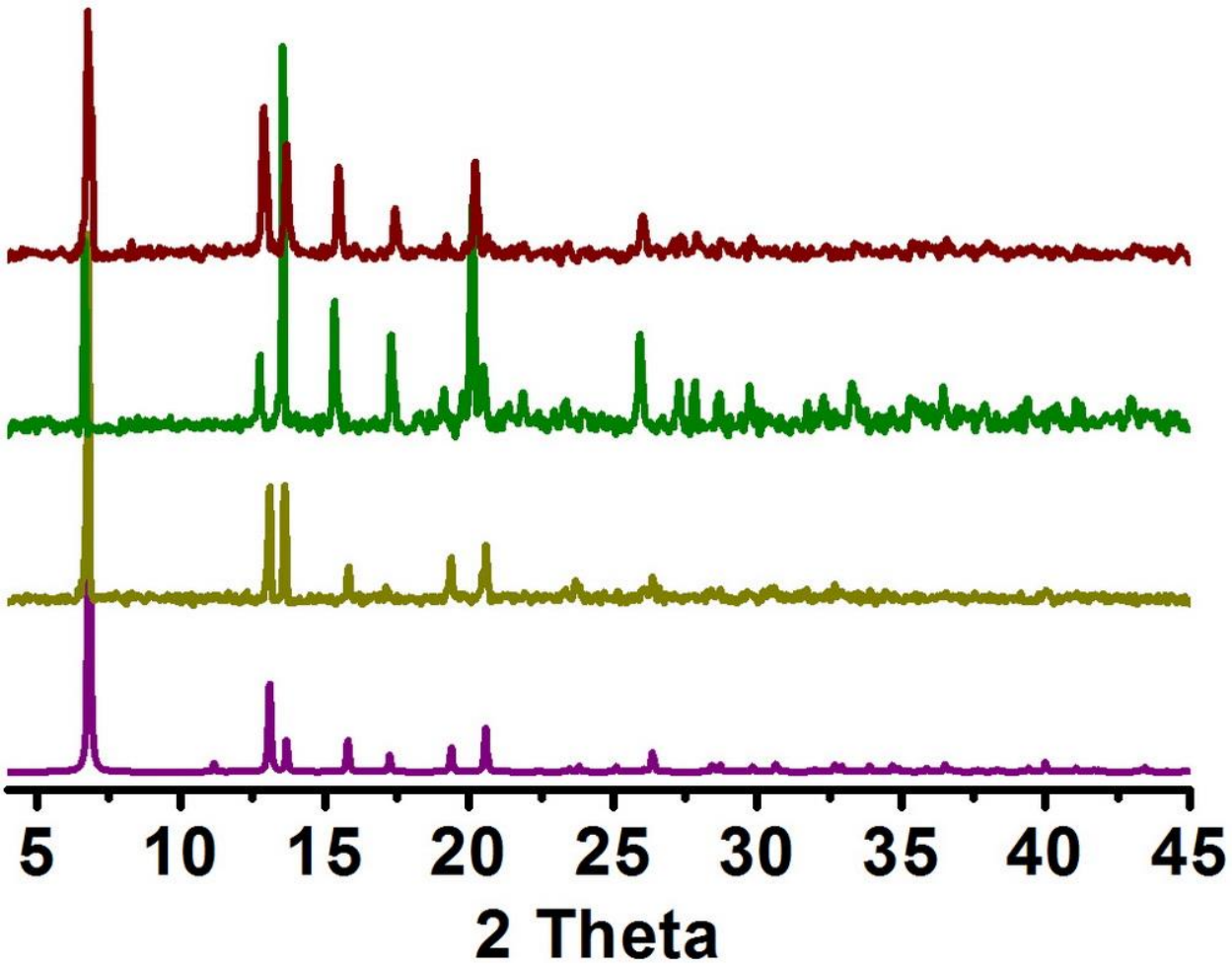

Figure 29. PXRD pattern of **bio-MOF-14** simulated from crystal structure (purple); PXRD patterns of **bio-MOF-14** before (dark yellow) and after soaking in water for 7 (green) or 30 (dark red) days.

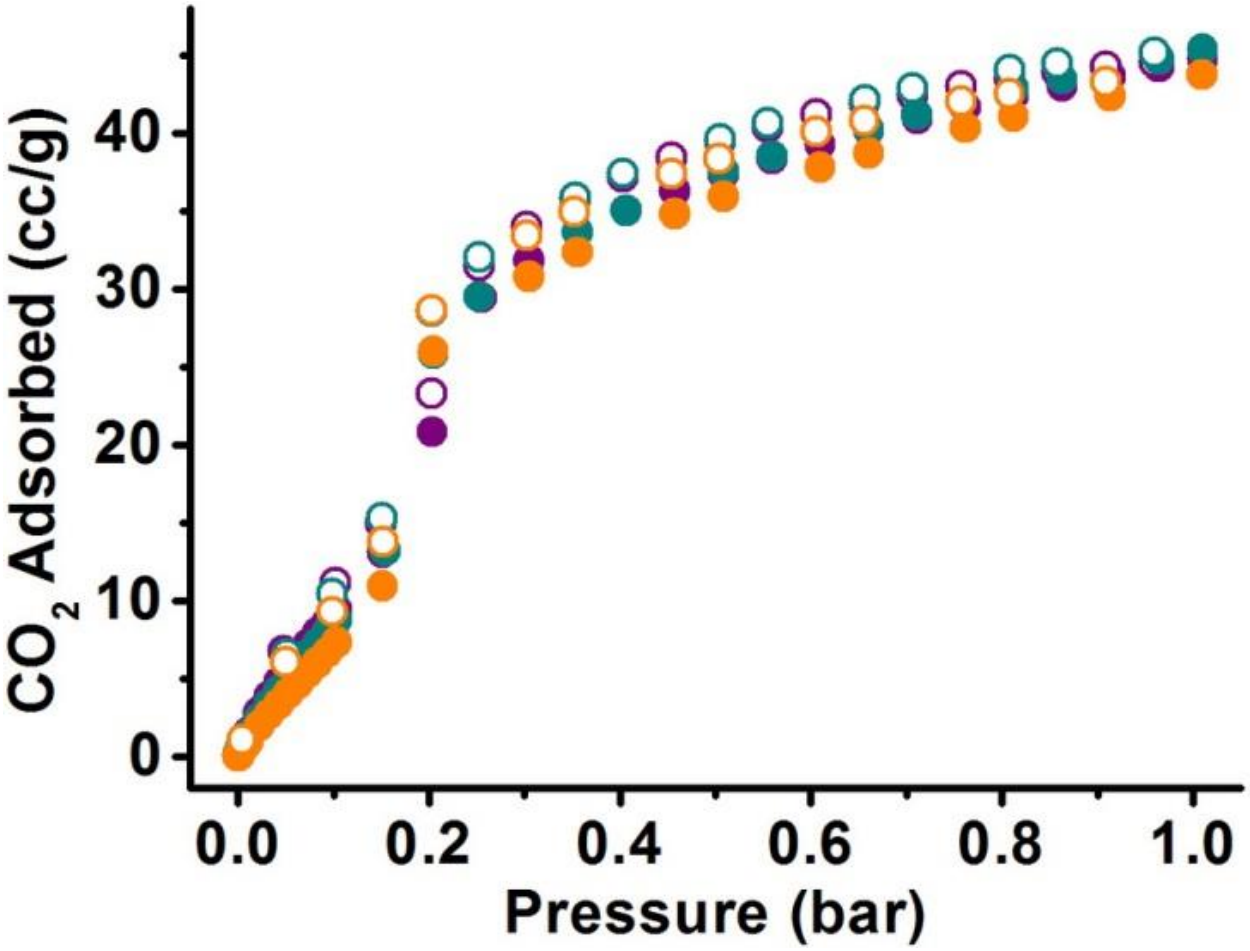

Figure 30. CO_2 isotherms of as synthesized **bio-MOF-14** (cyan), after soaking in water for 7 days (purple) and 30 days (orange).

2.3 CONCLUSIONS

Herein, we have shown that small, systematic modifications of the pore space in a series of isoreticular adenine-based bio-MOFs can lead to dramatic changes in the N_2 and CO_2 adsorption properties and the water stability of the materials. Specifically, we demonstrate that the decoration of the pore environment with aliphatic chains of increasing length leads to an increase in the CO_2:N_2 selectivity and an increase in the water stability of this series of bio-MOFs. Importantly, we used this systematic approach to produce **bio-MOF-14**, which is water stable and exhibits exceptional selectivitiy for CO_2 over N_2.

2.4 EXPERIMENTAL SECTION

2.4.1 Reagents and General Methods.

N,N'-dimethylformamide (DMF) was dried over 3 Å molecular sieves for 1 day prior to use. Other chemicals were obtained via commercial sources and used directly without further purification. Nanopure water (18.2 MΩ) was obtained using a Barnstead DiamondTM System.

Elemental microanalyses (EA) were performed by the University of Illinois, Department of Chemistry Microanalytical Laboratory using a Perkin-Elmer 240 Elemental Analyzer and an Exeter Analytical CE440.

Thermogravimetric analysis (TGA) was conducted on a TGA Q500 thermal analysis system. Prior to analysis, samples were dried under argon flow (UHP) until the powder could move around freely. Approximately 5 mg of sample was loaded into a platinum pan and heated under a constant N_2 (UHP) flow from room temperature to 600 ℃ at a rate of 5 ℃/min. Data were analyzed using the TA Universal Analysis software package.

Powder X-ray diffraction (PXRD) patterns were collected using a Bruker AXS D8 Discover powder diffractometer equipped with a Cu Kα X-ray source at 40 kV, 40 mA. Scan speed and step size were set at 0.2 sec/step and 0.02 °/step respectively. Generally, MOF samples were spread evenly on a glass slide and data were collected from 4 °< 2θ < 45 °. Simulated powder patterns from single-crystal X-ray diffraction data were generated using Mercury 3.0 software.

Scanning Electron Microscopy (SEM) images were taken using a Philips XL-30 field emission scanning electron microscope under BSE mode.

2.4.2 Preparation of Cobalt Salts.

Cobalt carbonate powder (1.19 g, 10 mmol) was suspended in nanopure water (50 ml). An aliphatic acid (~12 mmol, 1.2 equivalents) was added slowly to the suspension. Heat and stirring were required to fully dissolve the cobalt carbonate solid. Once the cobalt carbonate solid was dissolved, the reaction flask was heated in an oven (100 ℃ overnight) to remove water, yielding a purple solid. Yield: Co propionate, 1.93 g (94 %); products contained some water and CoO, as determined by EA. Anal. Calcd. for $Co(C_2H_5CO_2)_2$ (with 0.11 CoO and 0.33 H_2O impurity): C, 32.85; H, 4.90; N, 0.00. Found: C, 32.74; H, 4.74; N, 0.095; Co butyrate, 2.14 g (92 %). Anal. Calcd. for $Co(C_3H_7CO_2)_2$ (with 0.33 CoO and 0.53 H_2O impurity): C, 35.89; H, 5.67; N, 0.00. Found: C, 35.86; H, 5.615; N, 0.1; Co valerate, 2.22 g (85 %). Anal. Calcd. for $Co(C_4H_9CO_2)_2$ (with 0.05 CoO and 0.53 H_2O impurity): C, 43.74; H, 6.99; N, 0.00. Found: C, 43.64; H, 6.83; N, 0.12.

2.4.3 Synthesis of Bio-MOF-11.

Stock solutions of cobalt acetate (0.05 M) and adenine (0.05 M) in pre-dried DMF were prepared. To a Schlenk tube (40 mL) were added cobalt acetate solution (9.0 mL; 0.45 mmol), adenine solution (27.0 mL; 1.35 mmol), and nanopure water (120 μL). After the solution was frozen in liquid nitrogen and evacuated to 200 mTorr, it was heated in a 130 ℃ oven (24 h). Black, octahedral crystals were collected, washed (dry DMF, 3X), and dried under argon flow.

Yield: 102 mg, 90 % (based on cobalt acetate salt). Anal. Calcd. for $Co_2(ad)_2(CH_3CO_2)_2 \cdot 2.25$ DMF, 0.6 H_2O (ad = adeninate): C, 36.68; H, 4.59; N, 25.25. Found: C, 36.70; H, 4.06; N, 25.205.

2.4.4 Synthesis of Bio-MOF-12

Stock solutions of cobalt propionate (0.05 M) and adenine (0.05 M) in pre-dried DMF were prepared. To a Schlenk tube (40 mL) were added cobalt propionate solution (9.0 mL; 0.45 mmol), adenine solution (27.0 mL; 1.35 mmol), and nanopure water (120 µL). After the solution was frozen in liquid nitrogen and evacuated to 200 mTorr, it was heated in a 130 ℃ oven (24 h). Black, octahedral crystals were collected, washed (dry DMF, 3X), and dried under argon flow. Yield: 94 mg, 78 % (based on Co propionate). Anal. Calcd. for $Co_2(ad)_2(C_2H_5CO_2)_2 \cdot 2.25$ DMF, 0.3 H_2O: C, 38.92; H, 4.93; N, 24.44. Found: C, 38.99; H, 4.59; N, 24.36.

2.4.5 Synthesis of Bio-MOF-13.

Stock solutions of cobalt butyrate (0.05 M) and adenine (0.05 M) in pre-dried DMF were prepared. To a Schlenk tube (40 mL) were added cobalt valerate solution (9.0 mL; 0.45 mmol), adenine solution (27.0 mL; 1.35 mmol), and nanopure water (120 µL). After the solution was frozen in liquid nitrogen and evacuated to 200 mTorr, it was heated in a 130 ℃ oven (24 h). Black, octahedral crystals were collected, washed (dry DMF, 3X), and dried under argon flow. Yield: 90 mg, 71 % (based on Co butyrate). Anal. Calcd for $Co_2(ad)_2(C_3H_7CO_2)_2 \cdot 1.1$ DMF, 0.6 H_2O: C, 39.27; H, 4.78; N, 23.86. Found: C, 39.36; H, 4.185; N, 23.74.

2.4.6 Synthesis of Bio-MOF-14

Stock solutions of cobalt valerate (0.05 M) and adenine (0.05 M) in pre-dried DMF were prepared. To a Schlenk tube (40 mL) were added cobalt valerate solution (9.0 mL; 0.45 mmol), adenine solution (27.0 mL; 1.35 mmol), and nanopure water (120 μL). After the solution was frozen in liquid nitrogen and evacuated to 200 mTorr, it was heated in a 130 ℃ oven (24 h). Black, octahedral crystals were collected, washed (dry DMF, 3X), and dried under argon flow. Yield: 85 mg, 64 % (based on Co valerate). Anal. Calcd. for $Co_2(ad)_2(C_4H_9CO_2)_2 \cdot 0.6$ DMF, 0.6 H_2O: C, 40.72; H, 4.92; N, 23.09. Found: C, 40.8; H, 4.63; N, 22.93.

2.4.7 Gas Adsorption Measurements and Isosteric Heats of Adsorption

Gas adsorption isotherms were collected using a Quantachrome Autosorb-1 instrument. As synthesized crystals were thoroughly washed with anhydrous dichloromethane and dried under argon flow. Approximately 60 mg of each sample was added into a pre-weighed sample analysis tube. The samples were degassed at 100 ℃ under vacuum for 24-48 hours until the pressure change rate was no more than 3.5 mTorr/min. A liquid N_2 bath was used for the N_2 adsorption experiments at 77 K. A water/ethylene glycol bath was used for isotherms collected at 273 K, 298 K, 303 K, 308 K, and 313 K. BET surface areas were calculated using N_2 isotherms at 77 K. UHP grade N_2 and CO_2 gas adsorbates (99.999 %) were used in this study.

CO_2 adsorption isotherms of **bio-MOF-11** to **14** at different temperatures (273 K, 298 K, 303 K, 308 K and 313 K) were fit to the dual site Langmuir model.[73]

$$C = \frac{a \times P}{b + P} + \frac{c \times P}{d + P}$$

(*C*, moles adsorbed; *P*, pressure; *a*, *b*, *c*, and *d*, constants.)

Due to the unusual behavior of **bio-MOF-14**, we cannot fit the isotherms to the dual site Langmuir model.

Isosteric heats were computed by first plotting adsorption isosteres, plots of *ln(P)* versus *1/T* at constant loading of CO_2, by interpolating data within the experimental range from the dual site Langmuir model. Points on the adsorption isosteres were computed at 273, 298, 303, 308, and 313 K. The isostere data were then fitted to a line, with the slope of the line being proportional to the isosteric heat at that loading. The error bars for the isosteric heats were estimated by taking the difference between isosteric heats computed from using all five temperature data points with those computed from using only the first three temperatures. These two approaches give slightly different values because the points on the isosteres do not lie perfectly on straight lines. The absolute average errors in Q_{st} are 0.3, 1.7 and 1.7 kJ/mol for **bio-MOF-11**, **bio-MOF-12**, and **bio-MOF-13**, respectively.

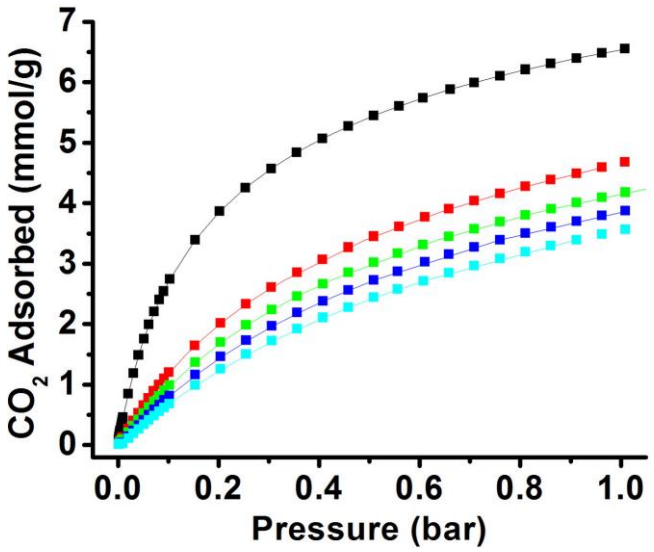

Figure 31. Dual site Langmuir fits of **bio-MOF-11** CO_2 adsorption isotherms at 273 K (black), 298 K (red), 303 K (green), 308 K (blue), and 313 K (cyan). (Square: experimental data; line: Langmuir fits)

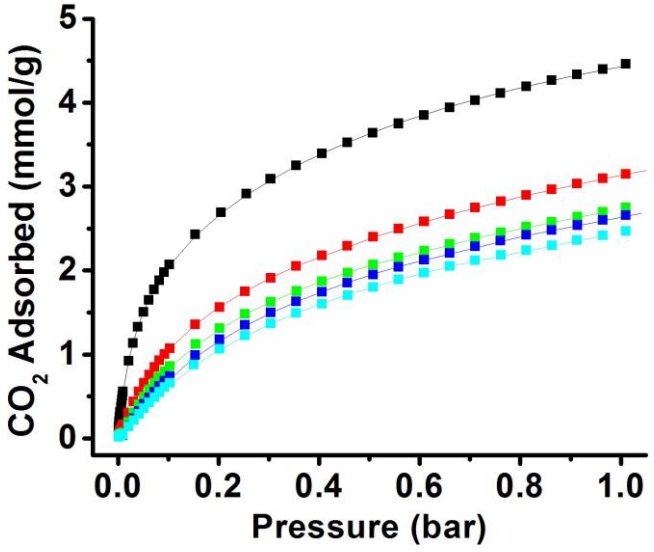

Figure 32. Dual site Langmuir fits of **bio-MOF-12** CO_2 adsorption isotherms at 273 K (black), 298 K (red), 303 K (green), 308 K (blue), and 313 K (cyan). (Squares: experimental data; lines: Langmuir fits)

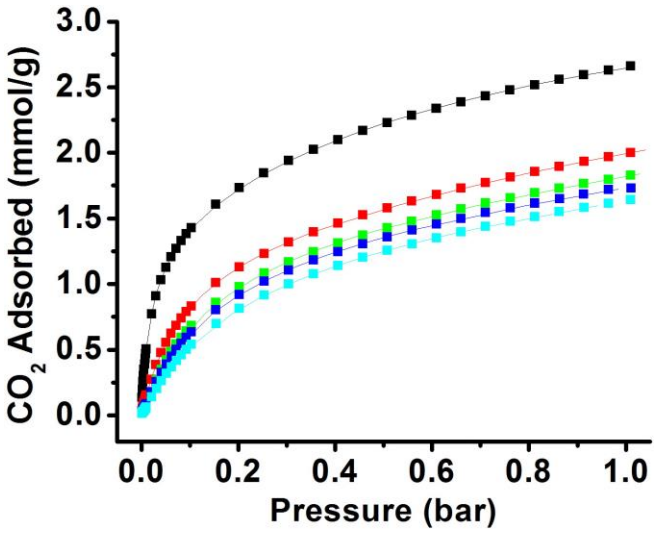

Figure 33. Dual site Langmuir fits of **bio-MOF-13** CO_2 adsorption isotherms at 273 K (black), 298 K (red), 303 K (green), 308 K (blue), and 313 K (cyan). (Squares: experimental data; lines: Langmuir fits)

2.4.8 Water Stability Experiments

Approximately 100 mg of **bio-MOF 11-14** samples were soaked in ~10 ml of water in a 20 ml glass vial and shaken vigorously. After 1 hour, PXRD patterns were collected for the wet samples. **Bio-MOF-14** was soaked in water for an extended period of time (7 or 30 days) and then dried under argon flow for SEM and gas adsorption studies.

2.4.9 Single X-ray Diffraction.

2.4.9.1 General Methods

The crystal structures of **bio-MOF-12**, **13**, and **14** were determined by single crystal X-ray diffraction experiments. A single crystal of either **bio-MOF-12**, **13**, or **14** was loaded into a glass capillary tube (Hampton research, glass 50) with Paratone oil. X-ray diffraction data were collected on a Bruker Smart Apex CCD diffractometer with graphite-monochromated MoKα (λ = 0.71073 Å) radiation at 273 K. SMART (V 5.628) was used for data collection and SAINT was used for cell refinement and data reduction. Absorption was corrected using Bruker program SADABS built into SAINT. Structures were solved by direct methods and refined by full-matrix least-squares analysis. All the non-hydrogen atoms were found from subsequent difference Fourier syntheses and refined anisothropically (except two terminal carbon atoms on the aliphatic chain in **bio-MOF-13** and water molecules were refined isotropically) with Bruker program SHELXTL[74] (V 6.10). Ideal positions for all hydrogen atoms were calculated and refined as a rigid model (except two hydrogen atoms on the amino group in **bio-MOF-13** were generated from Fourier syntheses and refined isotropically). Detailed single crystal data tables are given in the Supporting Information.

2.4.9.2 Modeling the Disordered Aliphatic Chains

The butyrate and valerate chains in **bio-MOF-13** and **14**, respectively, were found to be disordered. In the case of **bio-MOF-13**, the terminal ethyl group was treated with partial occupancy at two positions resulting in configuration I and configuration II with probability of 42.6 % and 57.4 %, respectively (Figure A2). Identical thermal parameters (U_{eq}) were applied to both configurations. The terminal carbon was considered to have 20 % higher thermal parameter

value than the β carbon. Except for the β, and γ carbons, the remaining non-hydrogen atoms were refined anisotropically. The aliphatic chain in **bio-MOF-14** was more severely disordered than that in **bio-MOF-13**. The disordered valerate chain was modeled as conformations I, II, and III with partial occupancies of 34.7 %, 47.6 %, and 17.7 %, respectively (Figure A3). Soft bond restraints were applied to the valerate carbon atoms. Except for the solvent oxygen atom, the remaining non-hydrogen atoms were refined anisotropically.

2.4.10 Modeling Details

Ideal adsorbed solution theory (IAST)[70] was employed to predict the adsorption isotherms of binary CO_2/N_2 mixtures with 10% CO_2, based on the pure component isotherms from experiments at 273 and 298 K. The adsorption isotherm data were fitted to a dual site Langmuir model to obtain the single component adsorption isotherms required for the IAST calculations, as described previously.[73] Plane wave periodic density functional theory (DFT) calculations were performed using the Vienna Ab initio Simulation Package (VASP).[75,76,77,78] DFT was used to compute the binding energies of CO_2 molecules in **bio-MOF-12**. The generalized gradient approximation functional of Perdew-Burke-Ernzerhof (PBE)[79] was used to describe the exchange-correlation functional; van der Waals interactions were included through use of the semi-empirical functional of Grimme (DFT-D2).[80] DFT molecular dynamics calculations at a temperature of 500 K were carried out to explore the conformational changes of the aliphatic chains in **bio-MOFs 12-14**. A cutoff energy of 400 eV and gamma point sampling of the Brillouin zone were used for all of the calculations. Classical grand canonical Monte Carlo (GCMC) simulations were carried out to model the adsorption of CO_2 in the bio-MOFs. The model of Garcia-Sanchez et al.[81] was used for CO_2-CO_2 interactions. The CO_2-framework

interactions were computed using the Universal Force Field[82] parameters for the framework atoms with Lorentz-Berthelot combining rules, along with point charges for the framework atoms computed from fitting the periodic DFT electrostatic potential.[83] The potential parameters and charges used are reported in Tables A16 and A17 of the Supporting Information.

3.0 DESIGN AND PREPARATION OF A CORE-SHELL METAL-ORGANIC FRAMEWORK FOR SELECTIVE CO_2 CAPTURE

This work, written in collaboration with Jeanne E. Sullivan, and Nathaniel L. Rosi*, was published in *J. Am. Chem. Soc.*, **2013**, 135, 9984-9987.[38] Copyright 2013, American Chemical Society.

Jeanne E. Sullivan helped with the synthesis and characterization of bio-MOFs.

3.1 INTRODUCTION

Chapter 2 describes an isoreticular series of cobalt-adeninate MOFs (**bio-MOFs-11-14**). Among them, **bio-MOF-11** is the most porous member which exhibits very high CO_2 capacity. Meanwhile, it is highly sensitive to water. In contrary, although **bio-MOF-14** is the least porous member, it exhibits not only excellent stability in water but also very high CO_2/N_2 selectivity due to molecular sieving effect. In this chapter, we demonstrate that through a core-shell strategy, these contradictory merits from **bio-MOF-11** and **14** can be possessed simultaneously by one material.

Hierarchical materials owe their properties to the organization of functional subunits on multiple levels from the molecular scale through the mesoscale.[84,85] Metal-organic frameworks (MOFs) can be viewed as a class of hierarchical materials in that they consist of organic and

inorganic molecular building blocks linked together into functional mesostructures.[1,86,87,88,89,90] MOF properties derive from the individual building blocks and their organization in the solid state (i.e. MOF topology); therefore, one approach toward controlling MOF properties involves judicious building block selection coupled with careful attention to topology design.[91] Efforts to increase the structural and functional complexity of MOFs beyond that which is achievable using this approach typically involve post-synthetic modification of either the ligands or the metal clusters.[7] More recently, the important concept of "heterogeneity within order" was forwarded and has led to increasing levels of MOF complexity, as exemplified by multivariate MOFs.[6,92,93,94]

Additional levels of MOF complexity have also been achieved through implementation of a core-shell strategy[95] where one MOF with one set of unique properties is encased (encapsulated) within a second MOF with a different set of unique yet complementary properties. Compared to traditional MOFs, core-shell MOFs add yet another level of structural complexity to the hierarchy: in addition to the organic and inorganic building blocks and their specific assembly, core-shell MOFs are stratified. The order of stratification within a core-shell MOF could, in principle, dramatically influence the properties of the material. For example, Hirai et al. have shown that a carefully designed core-shell MOF can be used to separate cetane and isocetane by size, a property which is not exhibited independently by either the core material or shell material.[96] However, despite a growing number of reports of core-shell MOF structures,[95,96,97,98,99,100,101,102,103,104] few have shown how a core-shell approach can affect MOF properties.[96,102,103]

In this work, we endeavored to design and prepare a core-shell MOF material whose collective gas adsorption properties were more than the sum of its parts. We used the isoreticular

series of **bio-MOFs 11-14** as the basis set of materials for this study.[36,42] Each MOF consists of cobalt-adeninate-monocarboxylate secondary building units (SBUs) linked together into an ***lvt*** net.[105] In terms of composition, these MOFs differ only in the identity of the monocarboxylate coordinated to the SBU: **bio-MOF-11** (acetate), **bio-MOF-12** (propionate), **bio-MOF-13** (butyrate), and **bio-MOF-14** (valerate). We have shown that the identity of the monocarboxylate significantly affects the gas adsorption properties (N_2 and CO_2) as well as the water stability of the material.[42] As the length of the aliphatic chain increases, the CO_2 capacity decreases, yet the CO_2:N_2 selectivity and the water stability significantly increase. Therefore, **bio-MOF-11** has a high capacity for CO_2 and low water stability, while **bio-MOF-14** has a low capacity for CO_2 but excludes N_2 at 273 and 298 K and is stable in water for a long period of time (at least 30 days).[42] An ideal material for selective CO_2 capture would combine the merits of **bio-MOF-11** (high CO_2 capacity) and **bio-MOF-14** (high CO_2:N_2 selectivity and water stability); therefore, we targeted a core-shell material comprising a **bio-MOF-11** core and a **bio-MOF-14** shell. The core would store CO_2 while the shell would act as a gas sieve and a protective shield against water.

3.2 RESULTS AND DISCUSSION

To implement this design strategy, we began by first preparing core **bio-MOF-11** crystals (Figure 34A) using our established methods.[42] These crystals were washed with dry dimethylformamide (DMF) and then placed in a shell growth solution containing cobalt valerate, adenine, and DMF. This mixture was heated to 130 ^{o}C, and the resulting crystals were washed and then imaged using a scanning electron microscope (SEM). SEM images showed no visible shell growth on the core surfaces (Figure 34B). This was likely due to the differences in the unit

cell parameters between **bio-MOF-11** (a = b = 15.44 Å, c = 22.78 Å) and **bio-MOF-14** (a = b = 15.85 Å, c = 22.35 Å).[42]

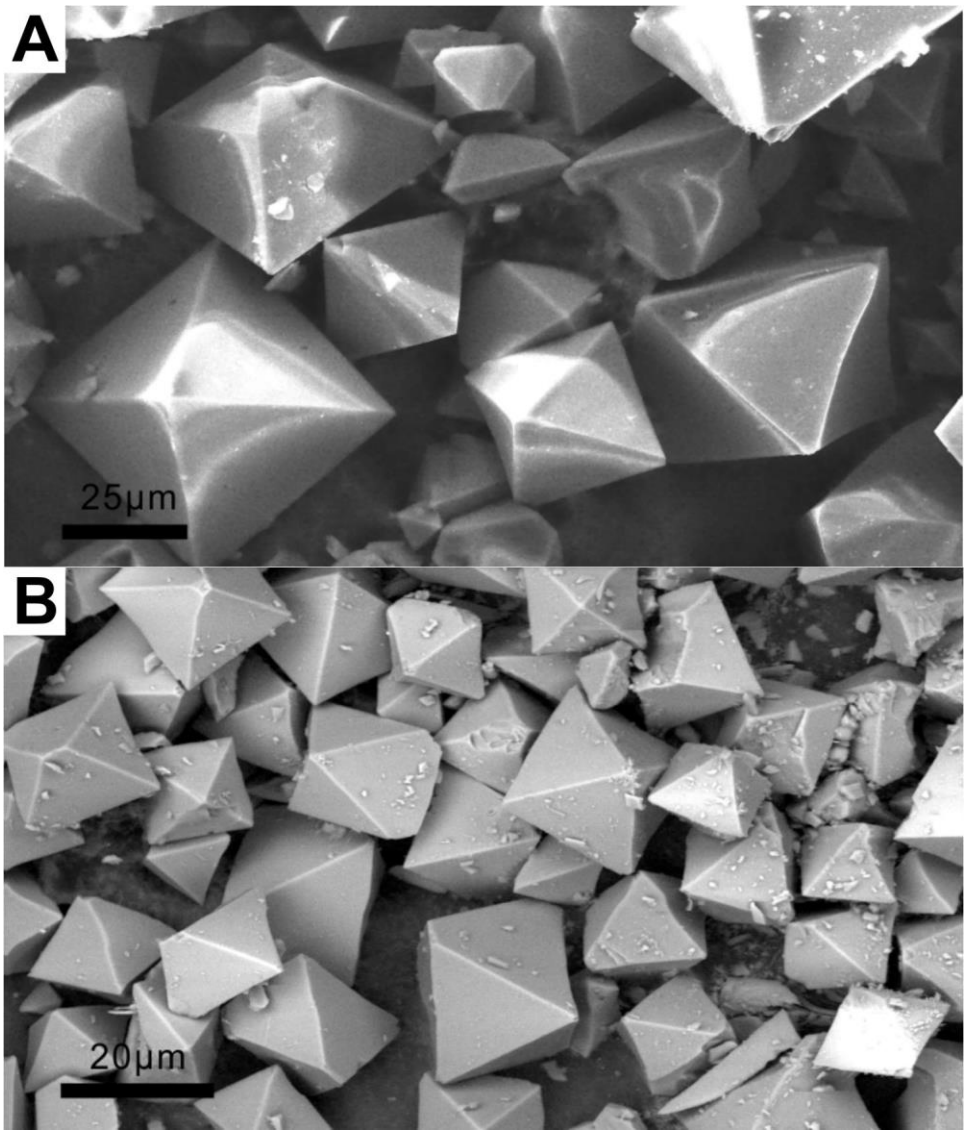

Figure 34. SEM images of **bio-MOF-11** before (A) and after (B) shell growth. No shelling was observed.

To allow for growth of a **bio-MOF-14** shell, we prepared cores of mixed composition (Figure 35) in which different amounts of valerate were doped into the **bio-MOF-11** lattice to achieve different acetate:valerate ratios ranging from 2.8:1 to 0.38:1, as determined by ^{1}H NMR (See experimental section 3.4.3) carried out on digested MOF samples. These cores are denoted as $C2_{0.74}C5_{0.26}$ (**I**), $C2_{0.60}C5_{0.40}$ (**II**), $C2_{0.43}C5_{0.57}$ (**III**), and $C2_{0.28}C5_{0.72}$ (**IV**), where C2 is acetate and C5 is valerate. Each of these mixed composition cores allowed for growth of the **bio-MOF-14** shell, as evidenced by SEM (Figure 36B and Figure 37 to 40). Close examination of the SEM images reveals that the triangular edges of the shell grow in alignment with those of the core, suggesting that the shell is not randomly deposited upon the core but rather grows as an extension of the core's crystal lattice. To our knowledge, this is the first example revealing how modulation of the MOF core composition can be utilized to carefully tailor core structure to enable effective MOF shell growth. **II** was selected for further study, because it allows for shell growth without sacrificing a major loss in porosity that would result from an increasing amount of C5. In order to fabricate a complete **bio-MOF-14** shell, the shelling process was repeated three times onto **II** to yield a core-shell material denoted as **II@bio-MOF-14** (Figure 35 and 36). A **II** core coated with multiple **bio-MOF-14** shells should have significantly more C5 than C2; ^{1}H NMR data collected for dissolved samples indeed confirms this hypothesis (See experimental section 3.4.3). Furthermore, the average size of **II@bio-MOF-14** is expected to be larger than **II**. Measurements of individual crystallite dimensions in SEM images confirm that **II@bio-MOF-14** crystallites have an average size of $84 \pm 12\,\mu m$, which is ~25% larger than **II** ($67 \pm 11\,\mu m$) (Figure 41 to 42).

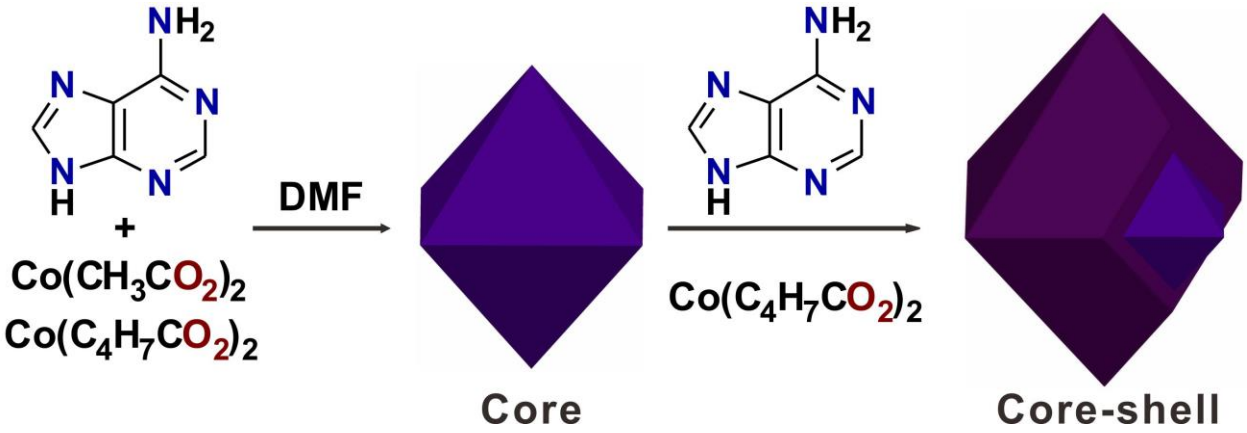

Figure 35. Synthetic scheme for the preparation of the core-shell crystal

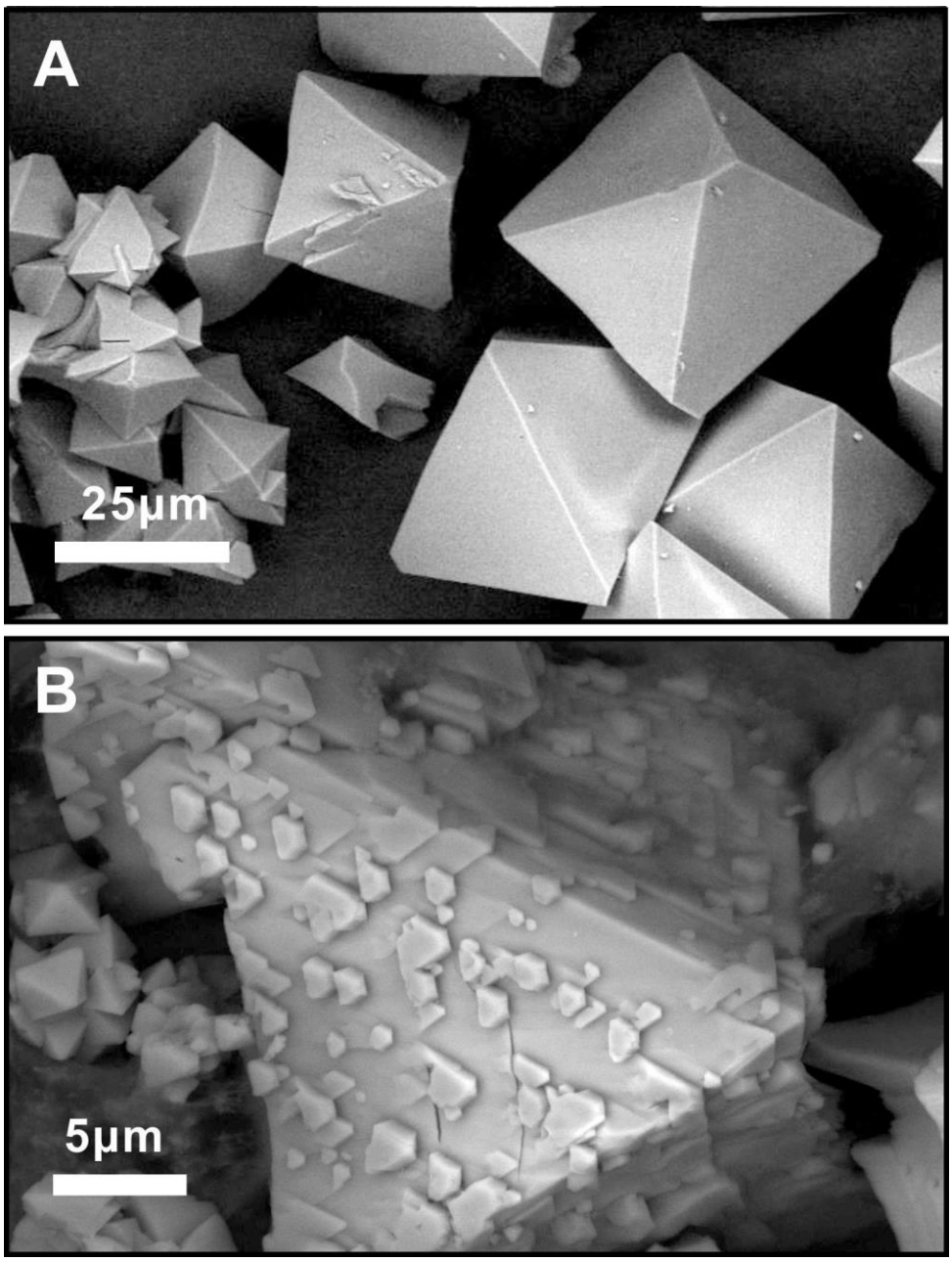

Figure 36. SEM images of the core crystal (A) and core-shell crystal (B)

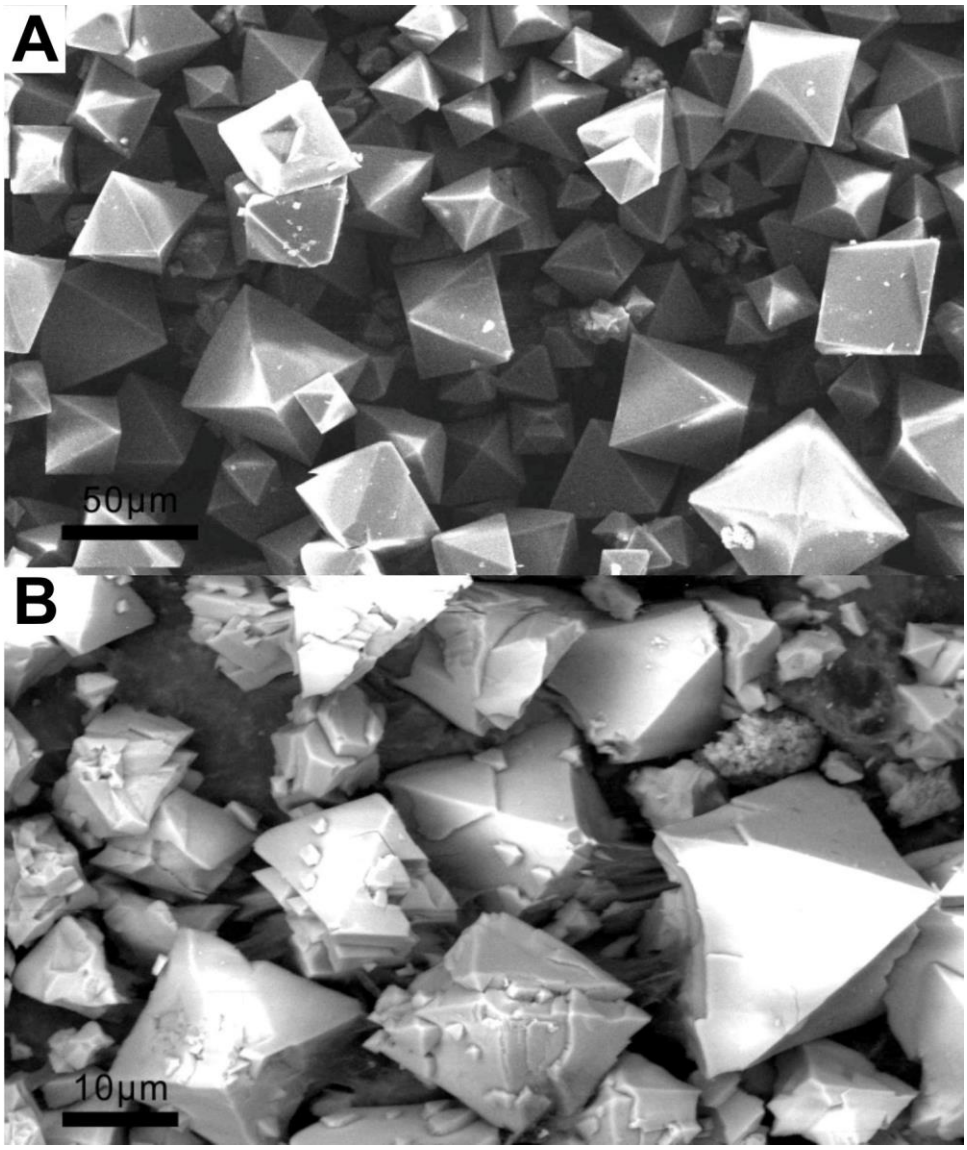

Figure 37. SEM images of **I** before (A) and after (B) shell growth. Shell growth is observed.

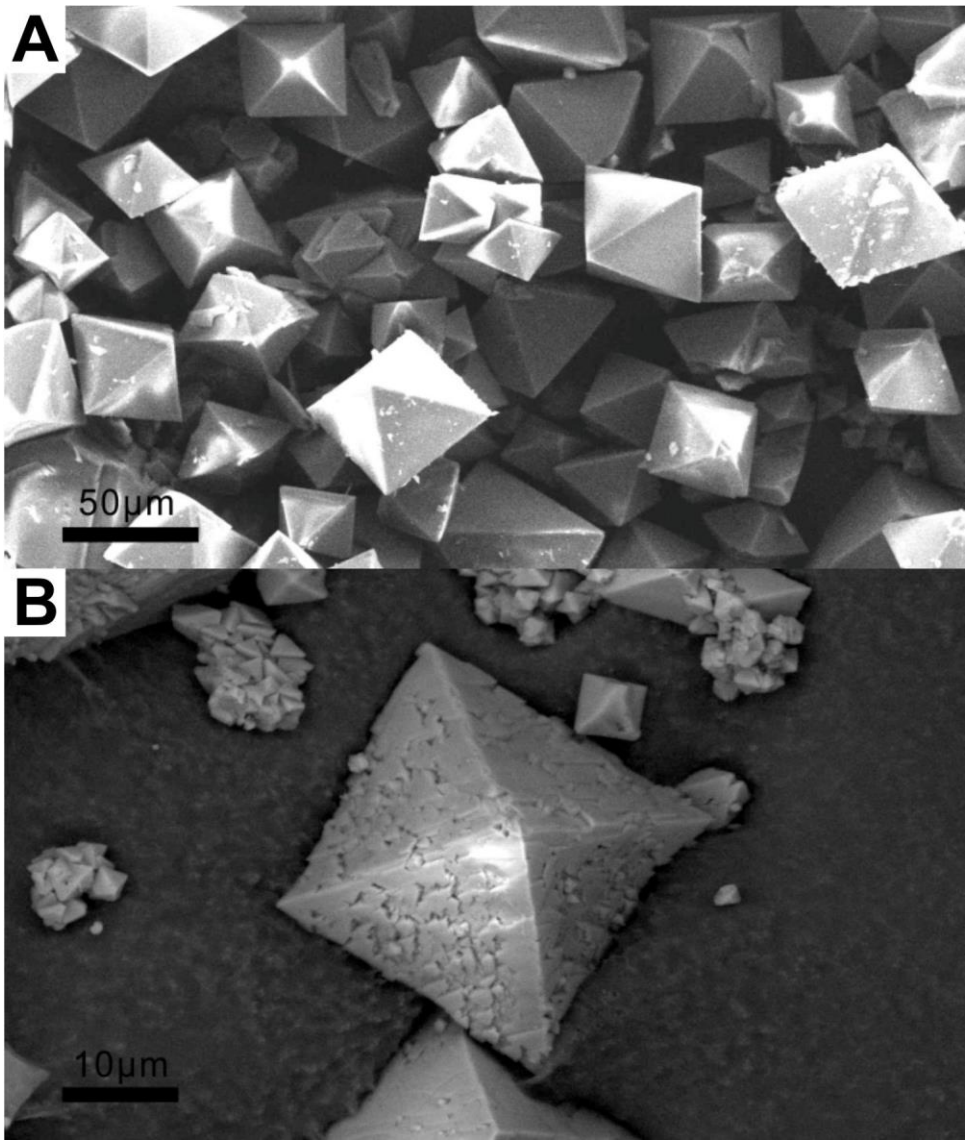

Figure 38. SEM images of **II** before (A) and after (B) shell growth. Shell growth is observed.

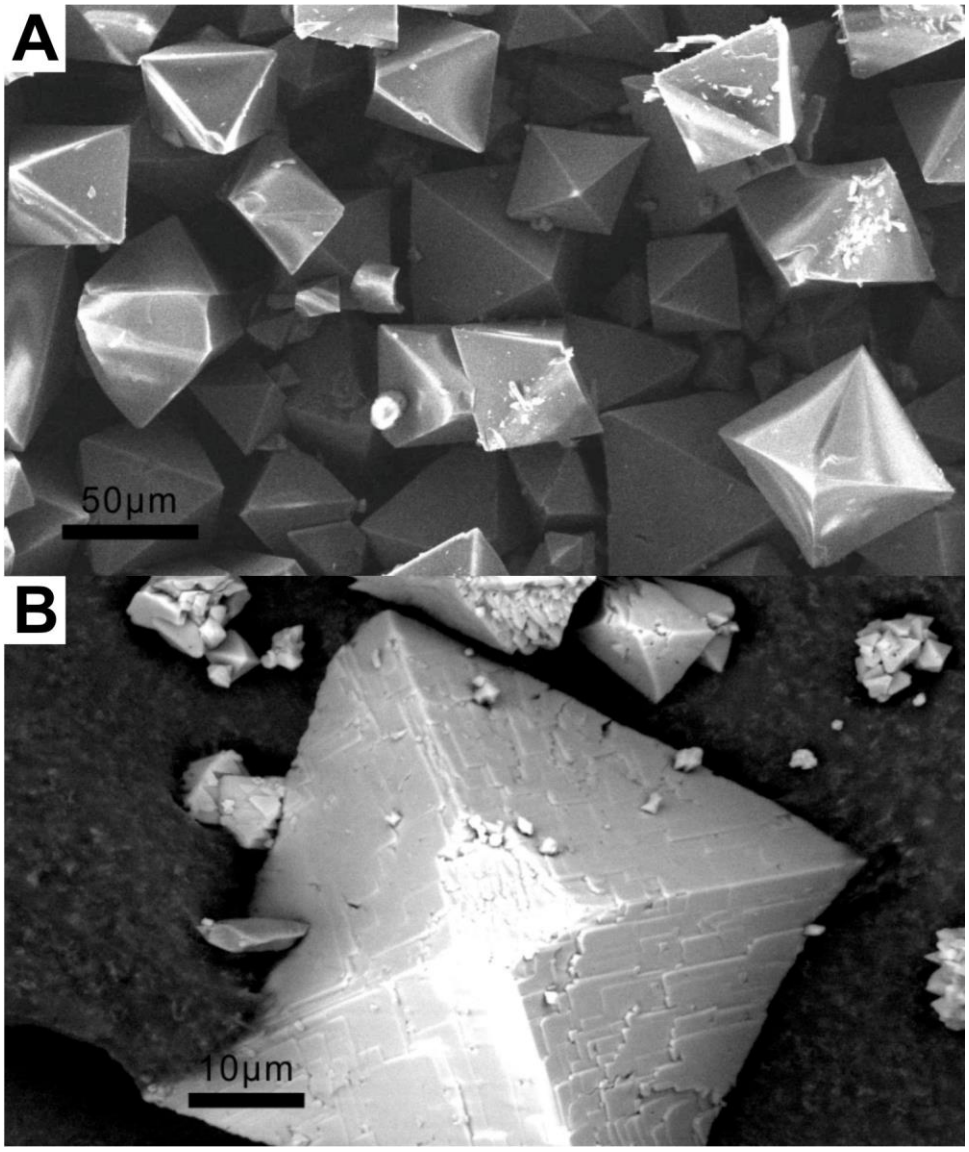

Figure 39. SEM images of **III** before (A) and after (B) shell growth. Shell growth is observed.

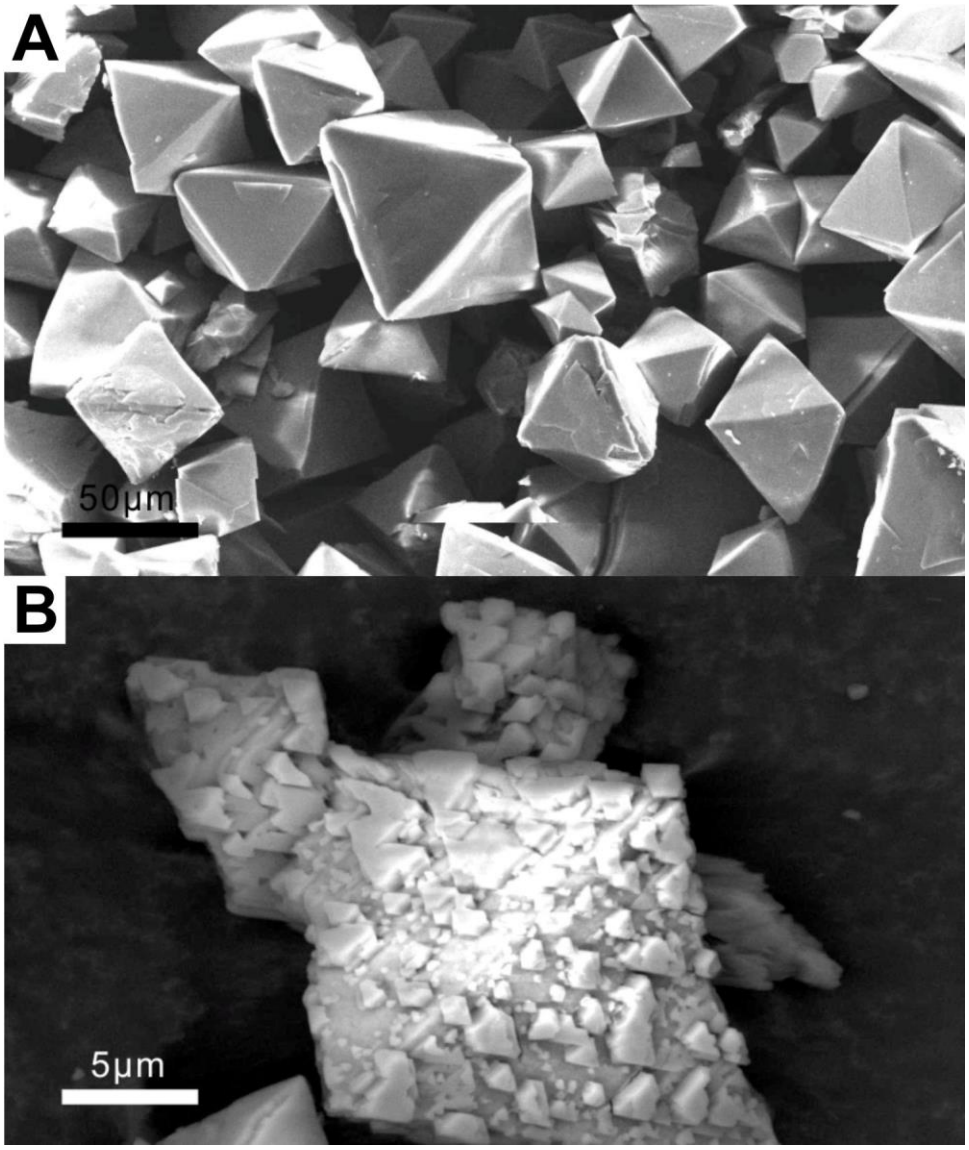

Figure 40. SEM images of **IV** before (A) and after (B) shell growth. Shell growth is observed.

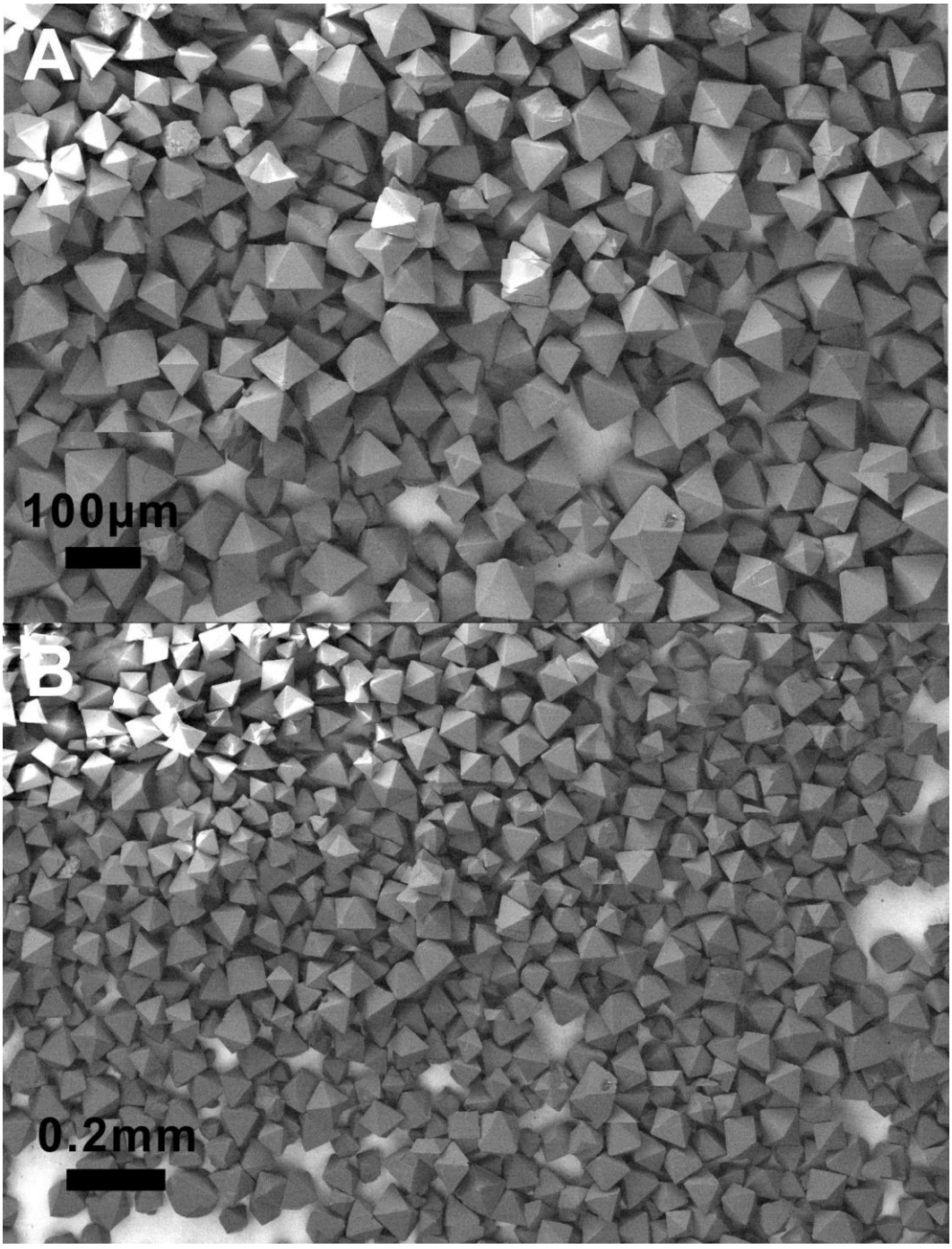
A
100μm
B
0.2mm

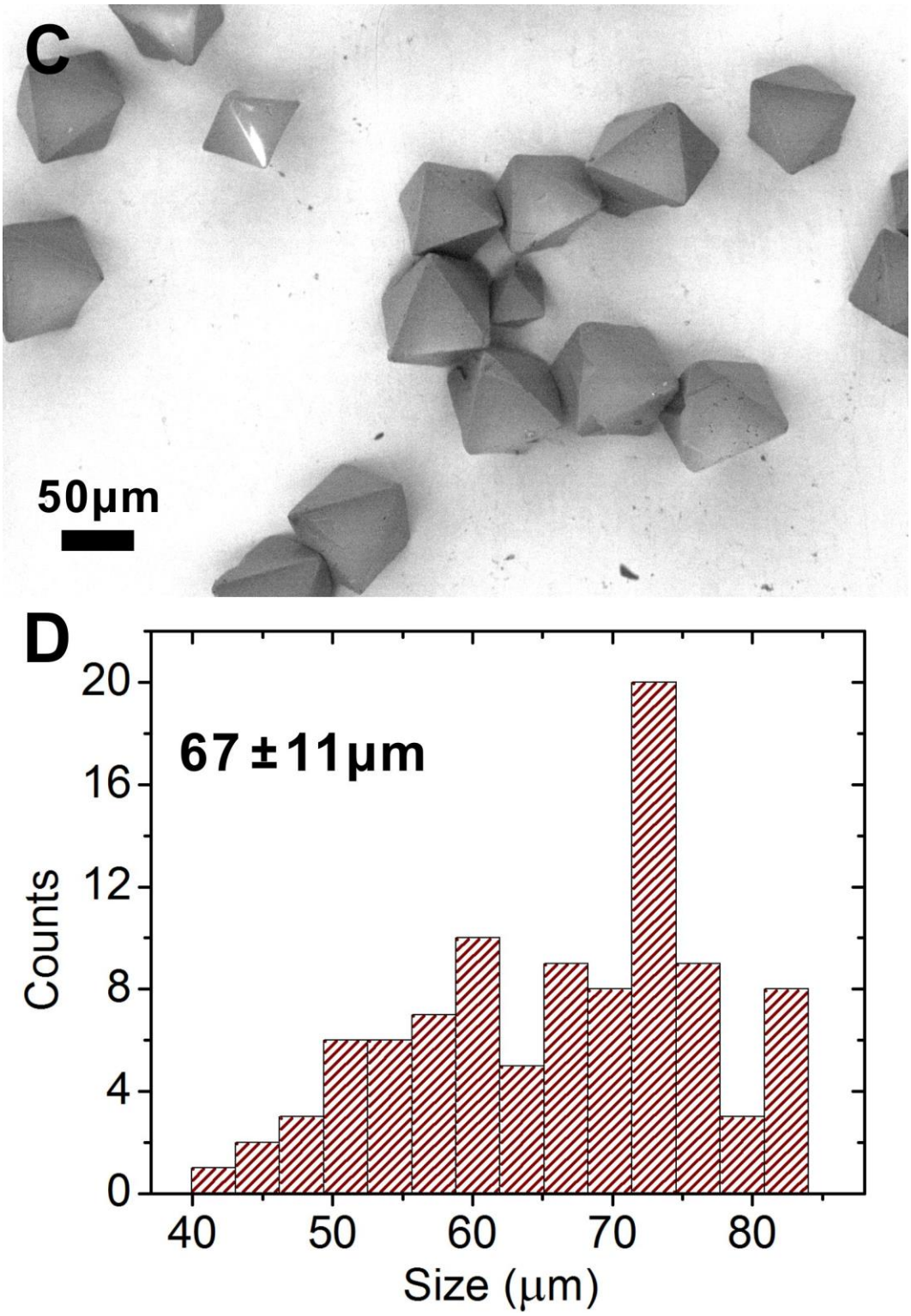

Figure 41. Additional SEM images of **II** (A, B, C) and size distribution based on 100 counts (D).

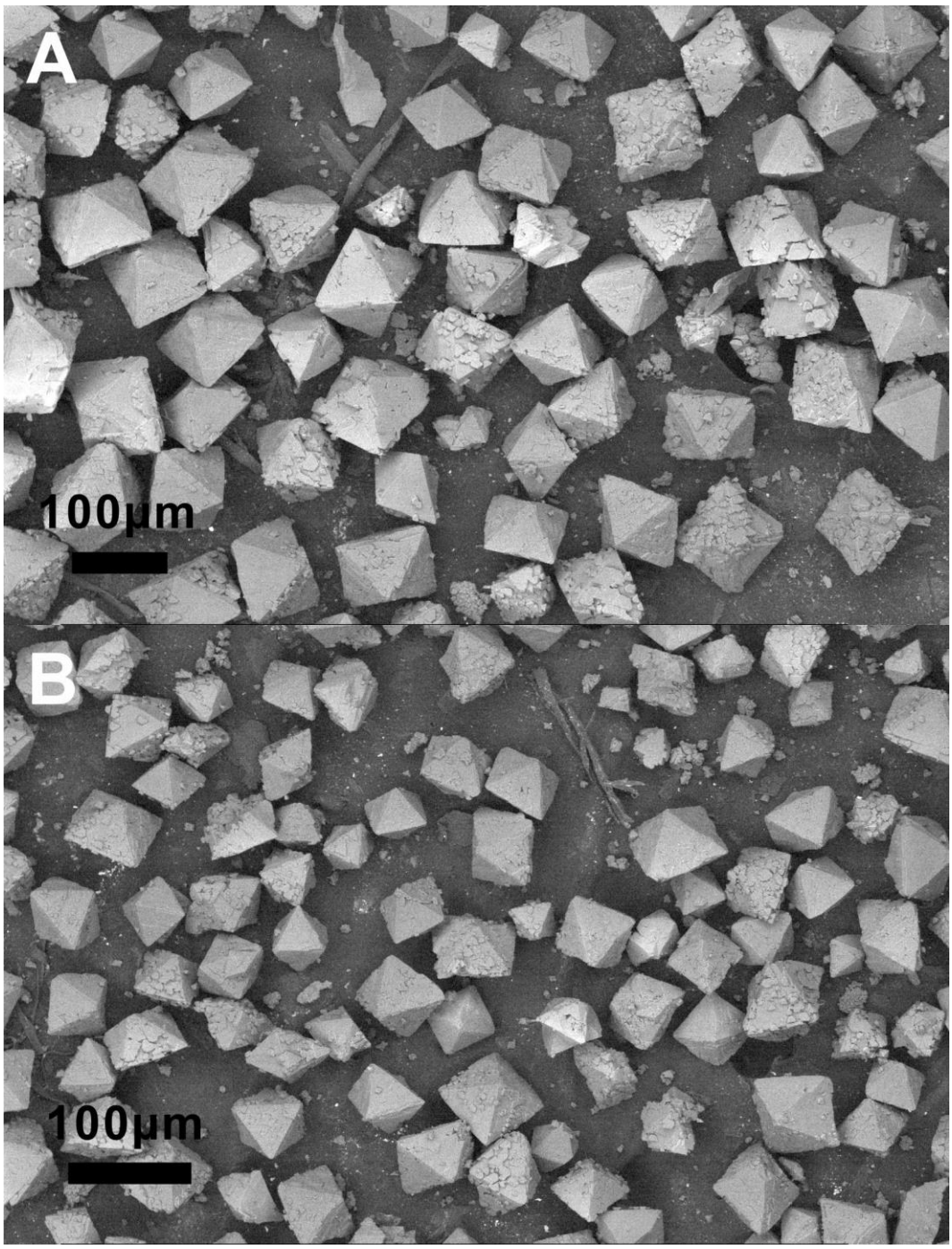
A
100µm
B
100µm

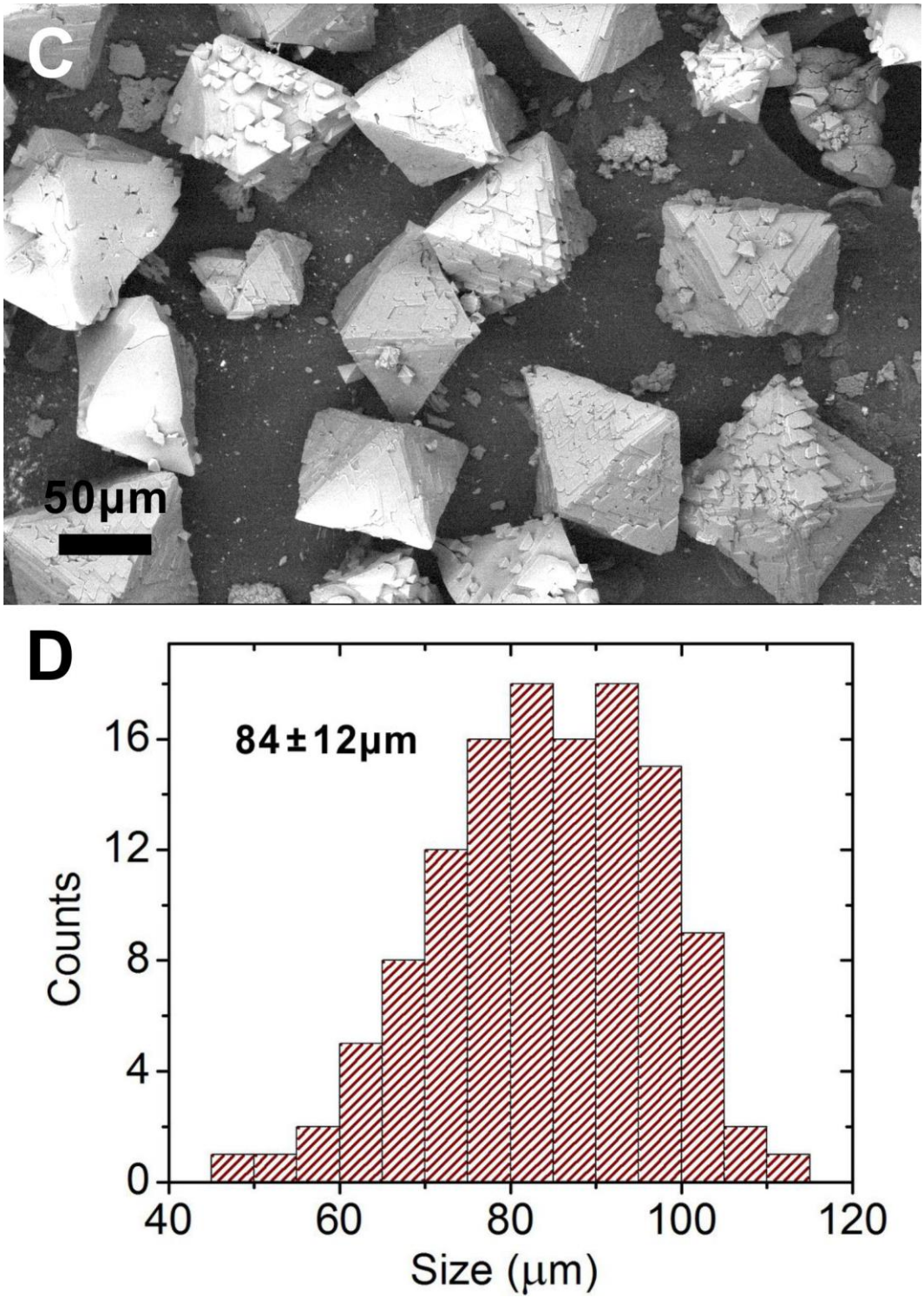

Figure 42. Additional SEM images of **II@bio-MOF-14** (A, B, C) and size distribution based on 124 counts (D).

A comparison and study of the powder X-ray diffraction (PXRD) patterns of the core and shell materials afforded a more complete understanding of the core-shell MOF materials (Figure 43). Because the unit cell parameters of **bio-MOF-11** differ from those of **bio-MOF-14**,[42] the diffraction lines corresponding to the $(2\bar{1}1)$ and (202) lattice planes for these materials appear at different 2 theta angles (Figure 43). Therefore, comparison of PXRD of these isoreticular materials could perhaps lead one to conclude that epitaxial shell growth would be difficult.[100,106] The diffraction lines corresponding to the $(2\bar{1}1)$ and (202) lattice planes for **II** appear at angles between those observed for **bio-MOF-11** and **bio-MOF-14** (Figure 43). In addition, the unit cell parameters of **II** obtained from single crystal X-ray experiments (a = b = 15.65 Å, c = 22.57 Å) are intermediate to those of **bio-MOF-11** and **bio-MOF-14**. We surmise, then, that the lattice of **II** is sufficiently similar to that of **bio-MOF-14** to allow for shell growth. After shelling, no shift was observed for the $(2\bar{1}1)$ and (202) diffraction lines of **II@bio-MOF-14** compared to those of **II,** which suggests that the shell may have adopted the unit cell of the core (Figure 43).

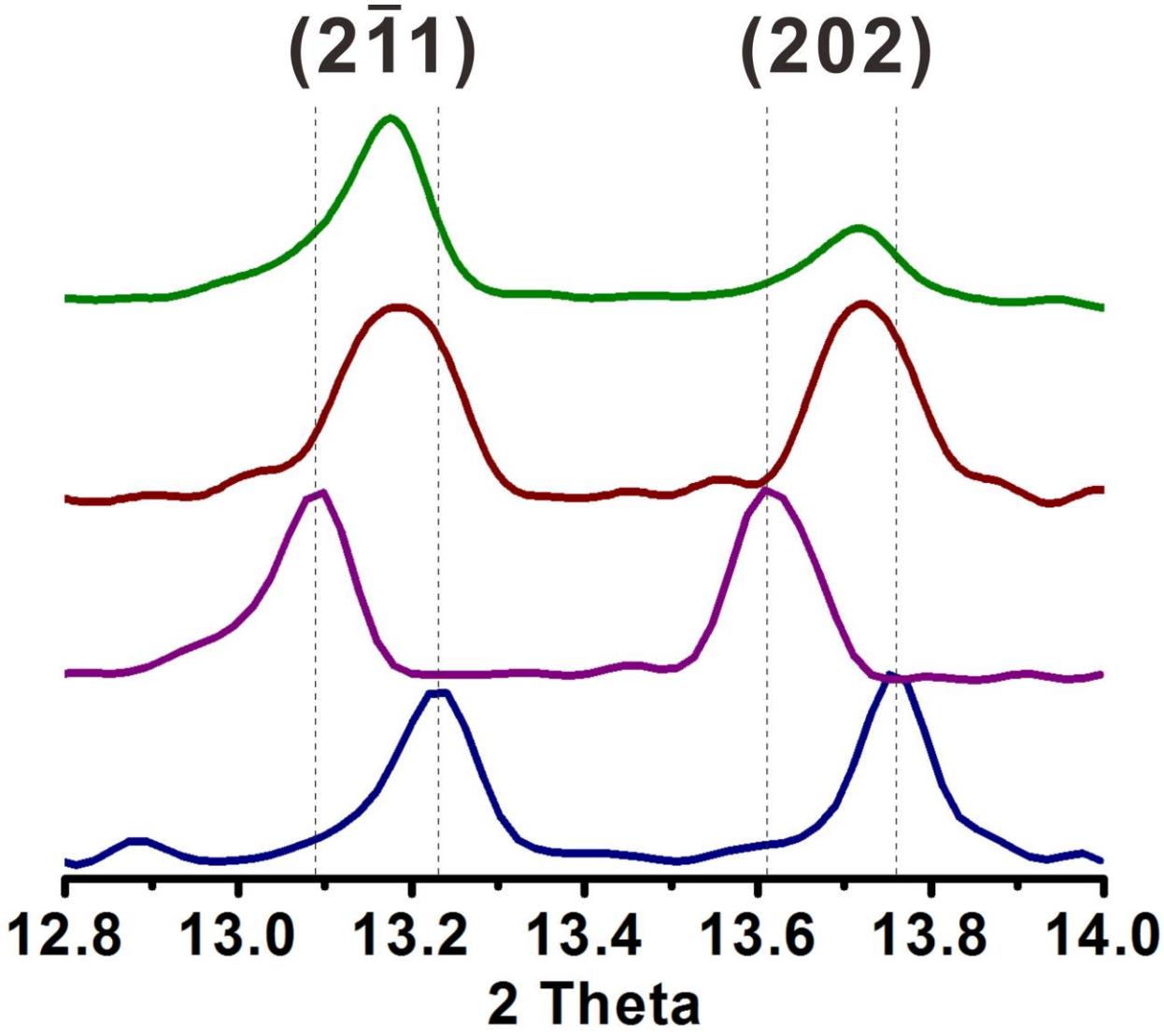

Figure 43. PXRD patterns of as-synthesized **bio-MOF-11** (navy), **bio-MOF-14** (purple), **II** (dark red), and **II@bio-MOF-14** (green) (the intensities of the diffraction lines are normalized for ease of comparison).

We next explored the porosity of this material to further confirm the existence of the core-shell structure and to understand how the core-shell architecture affects the gas adsorption behavior. Thermogravimetric analysis (TGA) data provided the first indication that the porosity of **II@bio-MOF-14** was intermediate between **II** and **bio-MOF-14** (Figure 44); specifically, the observed solvent loss for **II@bio-MOF-14** was between that observed for **II** and **bio-MOF-14**. Gas adsorption studies reveal that the core adsorbs 92 cc/g CO_2 at 1 bar and 273 K, while the core-shell material adsorbs 58.3 cc/g under these conditions (Figure 45A). We note that because of its more porous core the core-shell material adsorbs 30 % more CO_2 than **bio-MOF-14** (44.8 cc/g) (Figure 45A). Interestingly, the characteristic stepwise adsorption behavior of **bio-MOF-14** was not observed for **II@bio-MOF-14**. We have previously reported that the stepwise CO_2 adsorption of **bio-MOF-14** results from conformation changes to the valerate chains during CO_2 uptake.[42] However, the **bio-MOF-14** shell is not structurally identical to pure-phase **bio-MOF-14**, as described above, which could account for the observed change in CO_2 adsorption behavior. We next examined the N_2 adsorption behavior to determine whether the **bio-MOF-14** shell would prevent N_2 adsorption to the core. The core-shell structure shows a much lower N_2 uptake at 77 K than the core crystal and only slightly higher than **bio-MOF-14** (Figure 45B). These data suggest that the **bio-MOF-14** shell efficiently prevents any significant N_2 uptake by the core. To explore this further, we ground the same core-shell sample in an agate mortar to fracture the crystallites and then collected N_2 and CO_2 adsorption isotherms for the ground material. SEM images reveal that most of the crystals were crushed to fragments (Figure 46) which should expose the interior of the core-shell crystal directly to the adsorbate molecules. No change was observed for the CO_2 adsorption isotherm (Figure 47B). However, after grinding, a significantly higher amount of N_2 was adsorbed at 77 K (108 cc/g compared to 54 cc/g adsorbed

before grinding) (Figure 47A). At 273 K, the amount of N_2 adsorbed differs by nearly a factor of four (3.3 cc/g before grinding and 12.2 cc/g after grinding) (Figure 48). We reason that, before grinding, N_2 molecules must pass through the **bio-MOF-14** shell to enter the porous core. After grinding the core-shell material, the cores are directly exposed to N_2; therefore, the N_2 adsorption is no longer limited by diffusion through the **bio-MOF-14** shell.

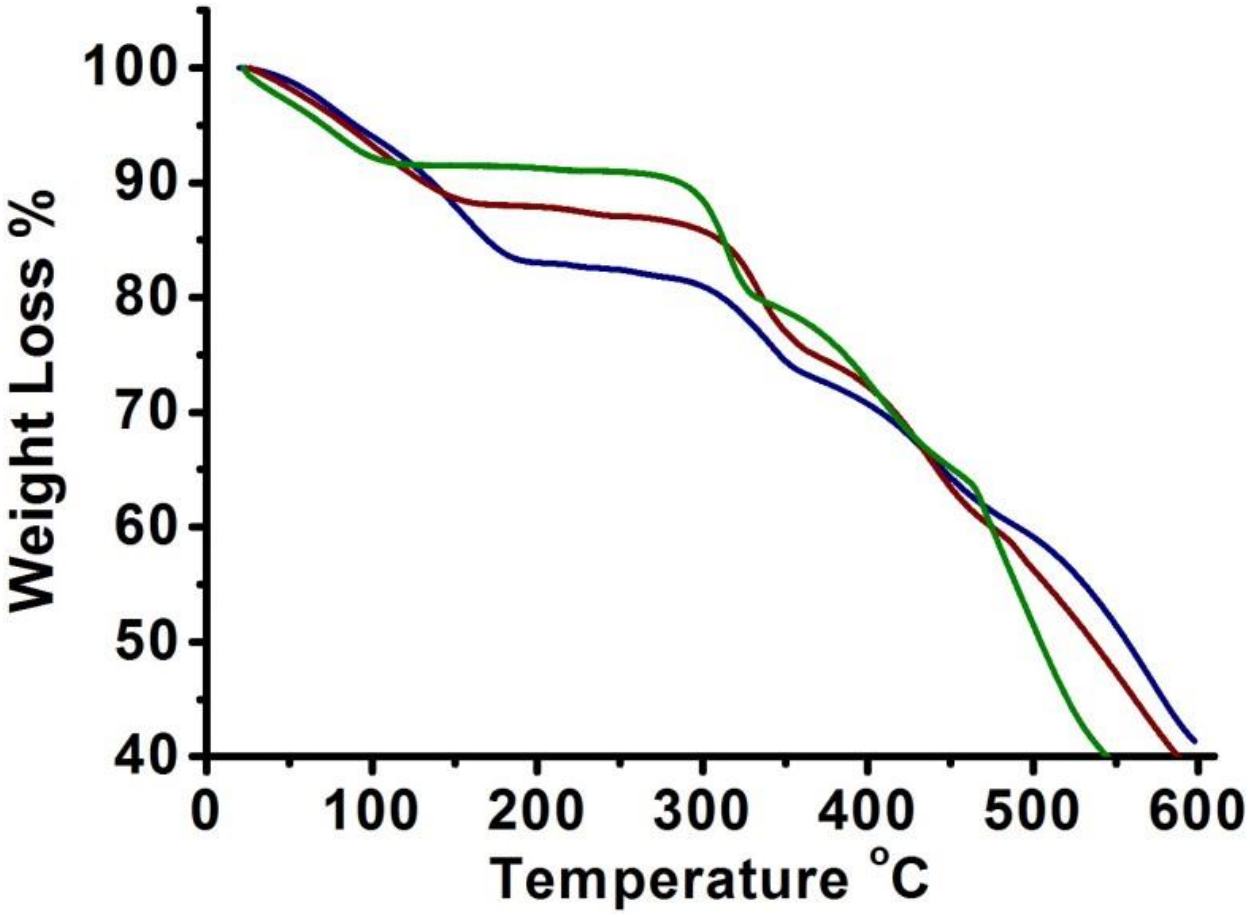

Figure 44. TGA of **bio-MOF-14** (green), **II@bio-MOF-14** (red), and **II** (navy). Solvent loss occurs between room temperature and 200 ℃.

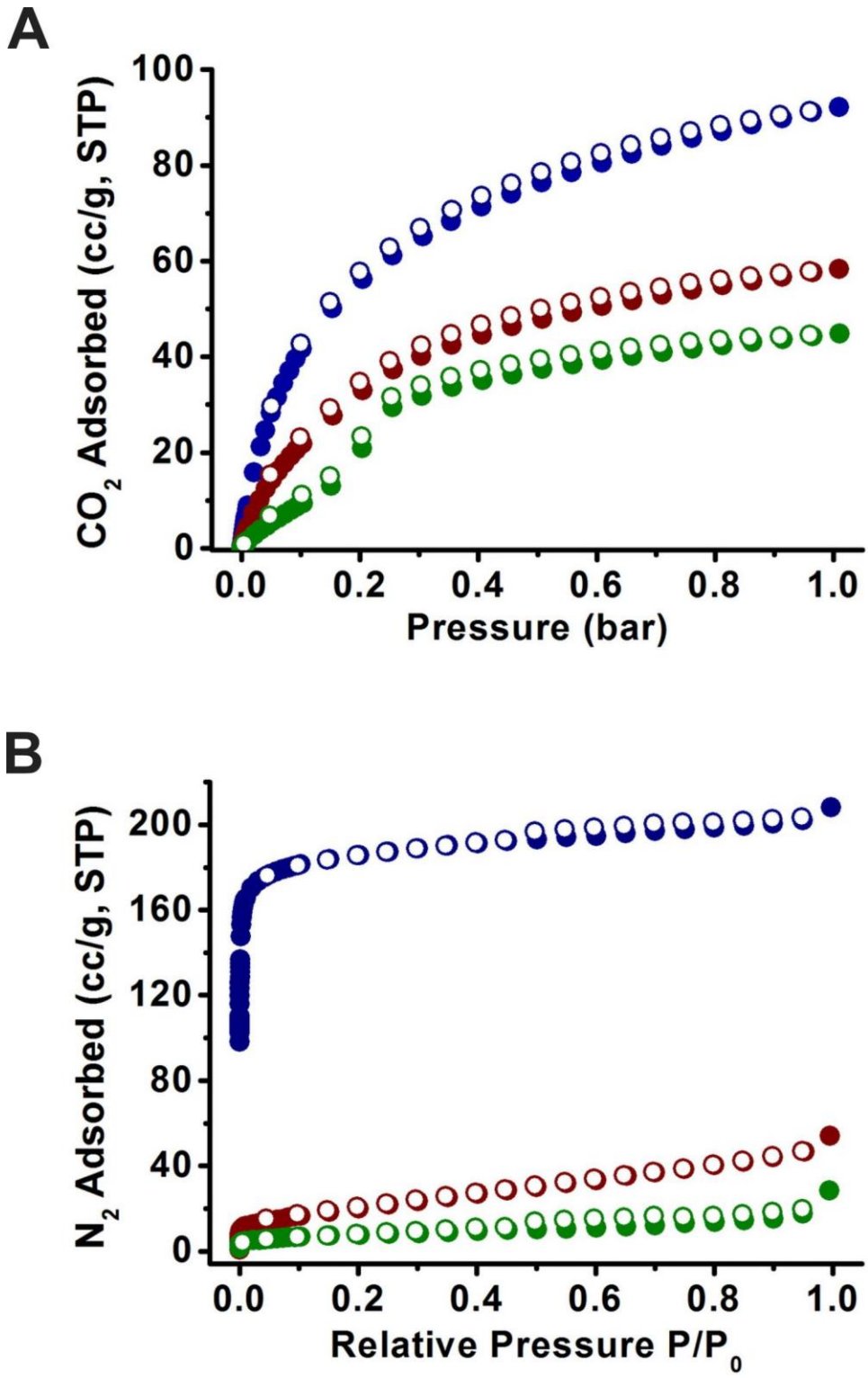

Figure 45. CO_2 (A) and N_2 (B) adsorption isotherms at 273 K and 77 K, respectively (core, navy; core-shell, dark red; **bio-MOF-14**, green).

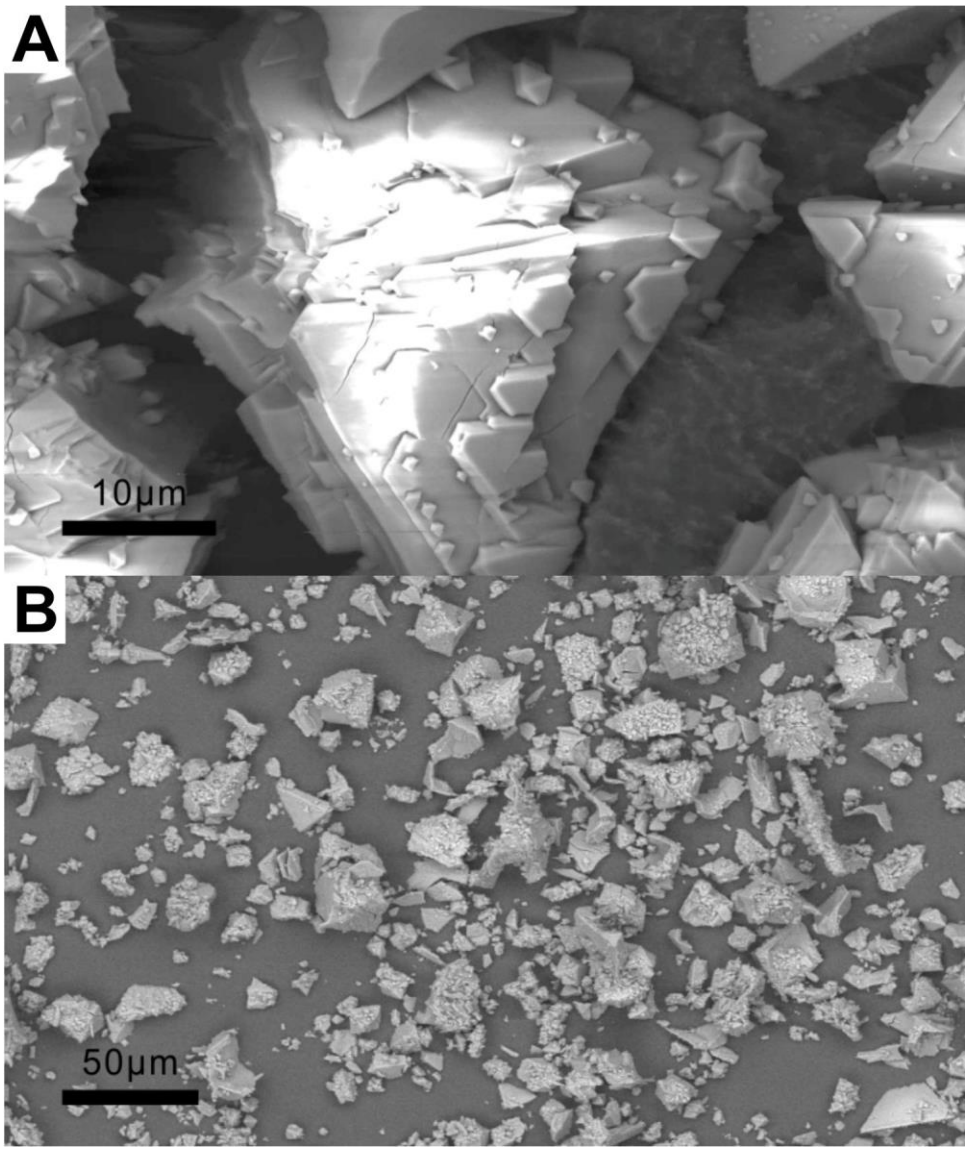

Figure 46. SEM images of **II@bio-MOF-14** before (A) and after (B) grinding.

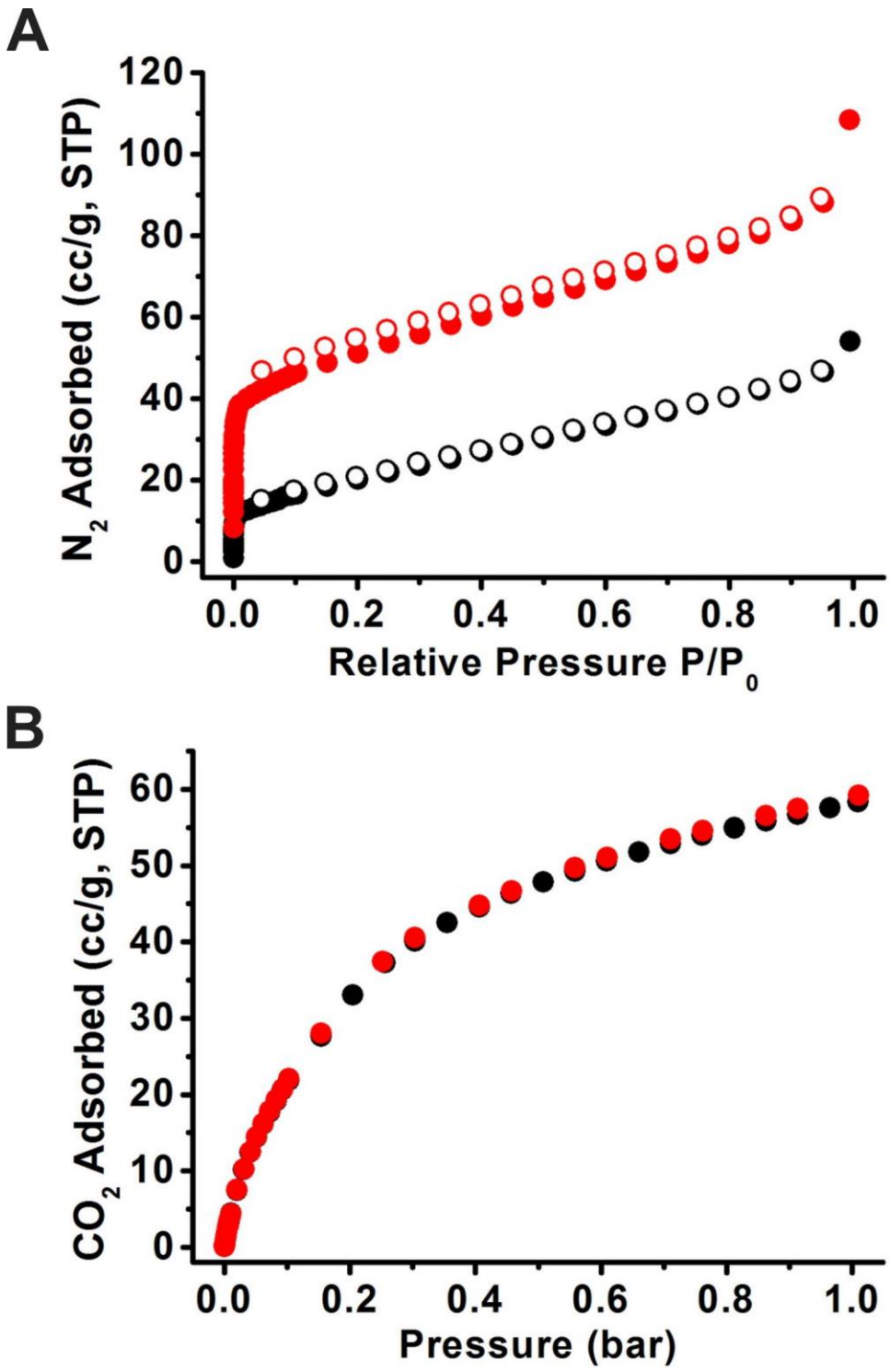

Figure 47. N_2 (C) and CO_2 (D) adsorption isotherms at 273 K and 77 K before (black) and after (red) grinding.

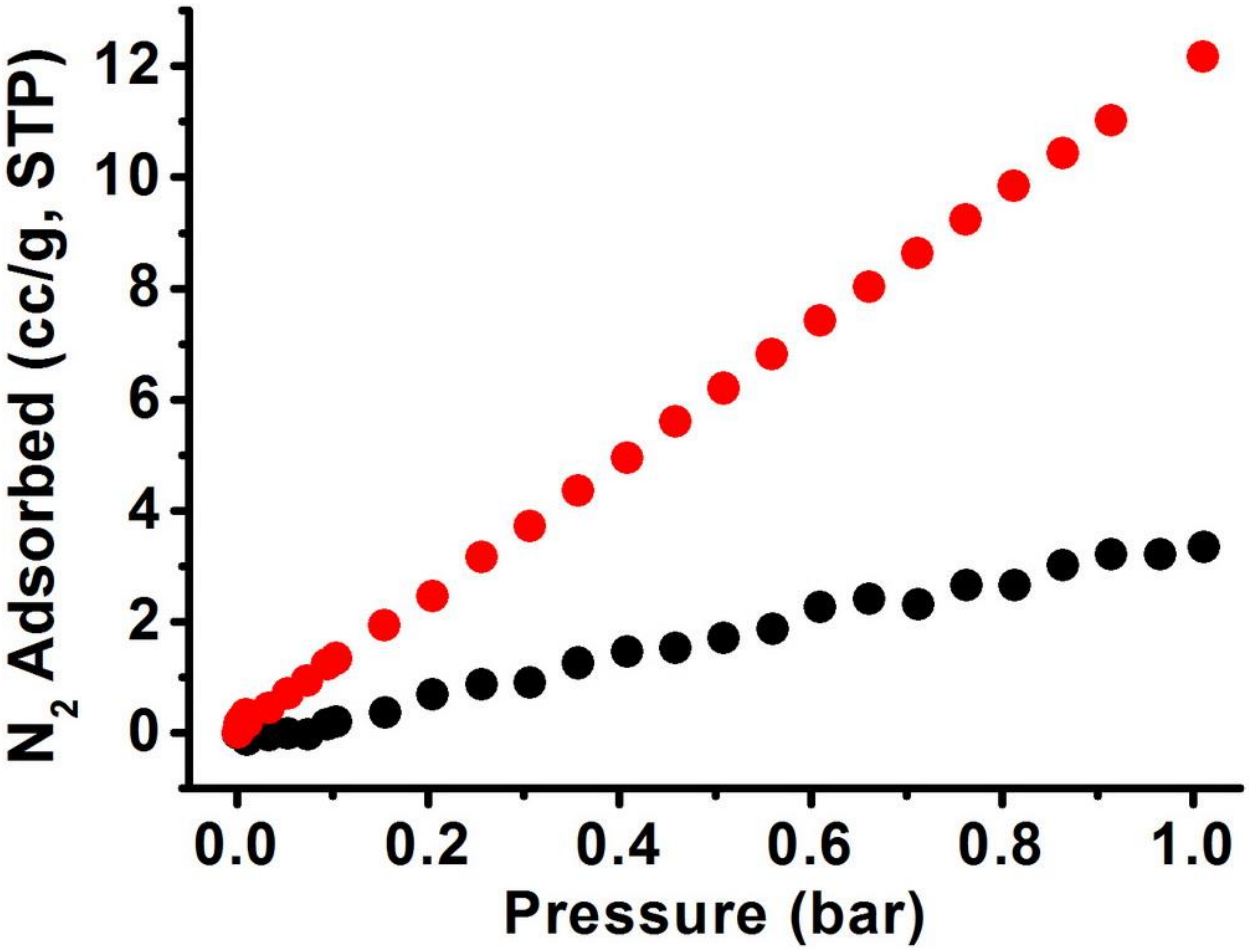

Figure 48. N_2 isotherms of **II@bio-MOF-14** at 273 K before (black) and after (red) grinding.

We also prepared the **bio-MOF-14@II** core-shell material (Figure 49B) so that we could compare its gas adsorption properties with those of **II@bio-MOF-14**. The N_2 and CO_2 adsorption isotherms for **bio-MOF-14@II** before and after grinding the material were essentially the same (Figure 50-52), indicating that controlling the order of stratification is critical for achieving a new material with unique collective properties.

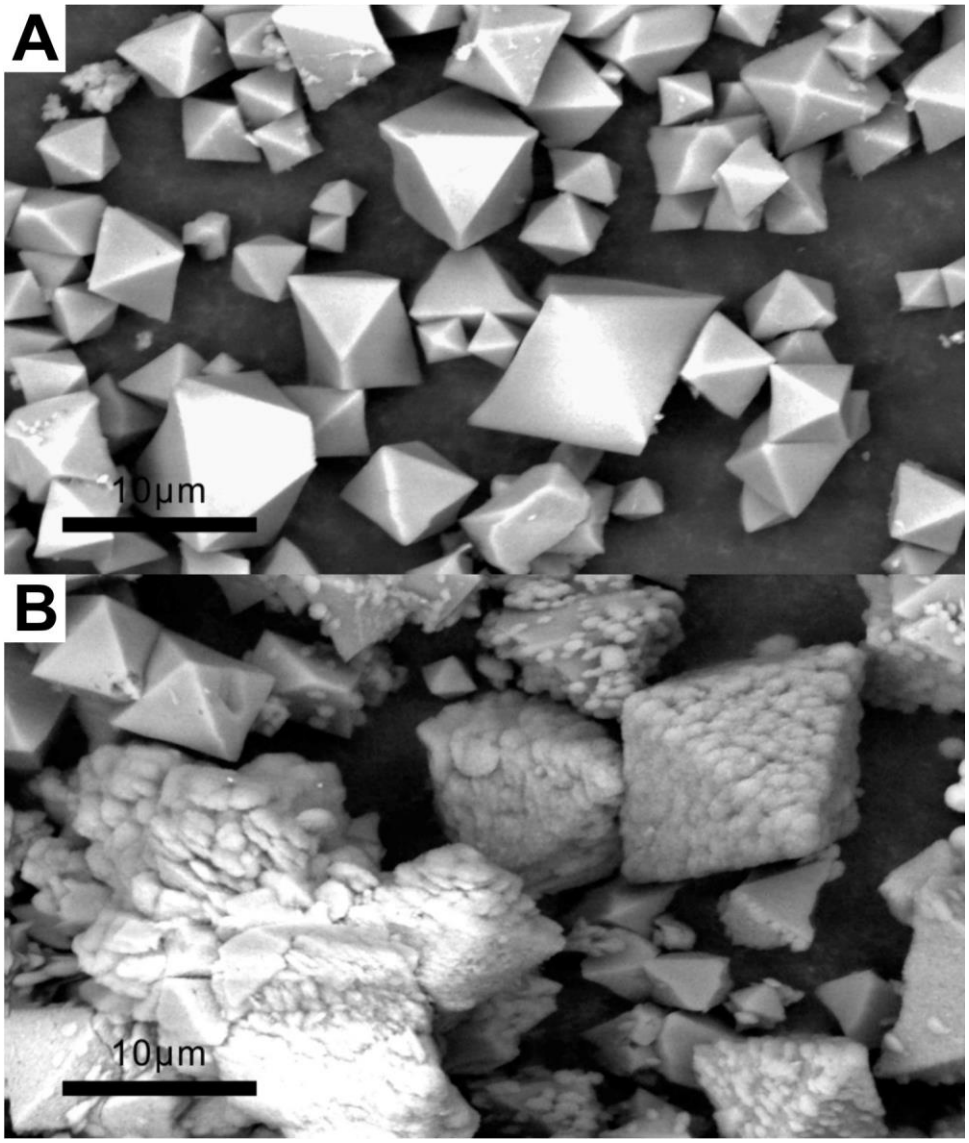

Figure 49. SEM images of **bio-MOF-14** (A) and **bio-MOF-14@II** (B).

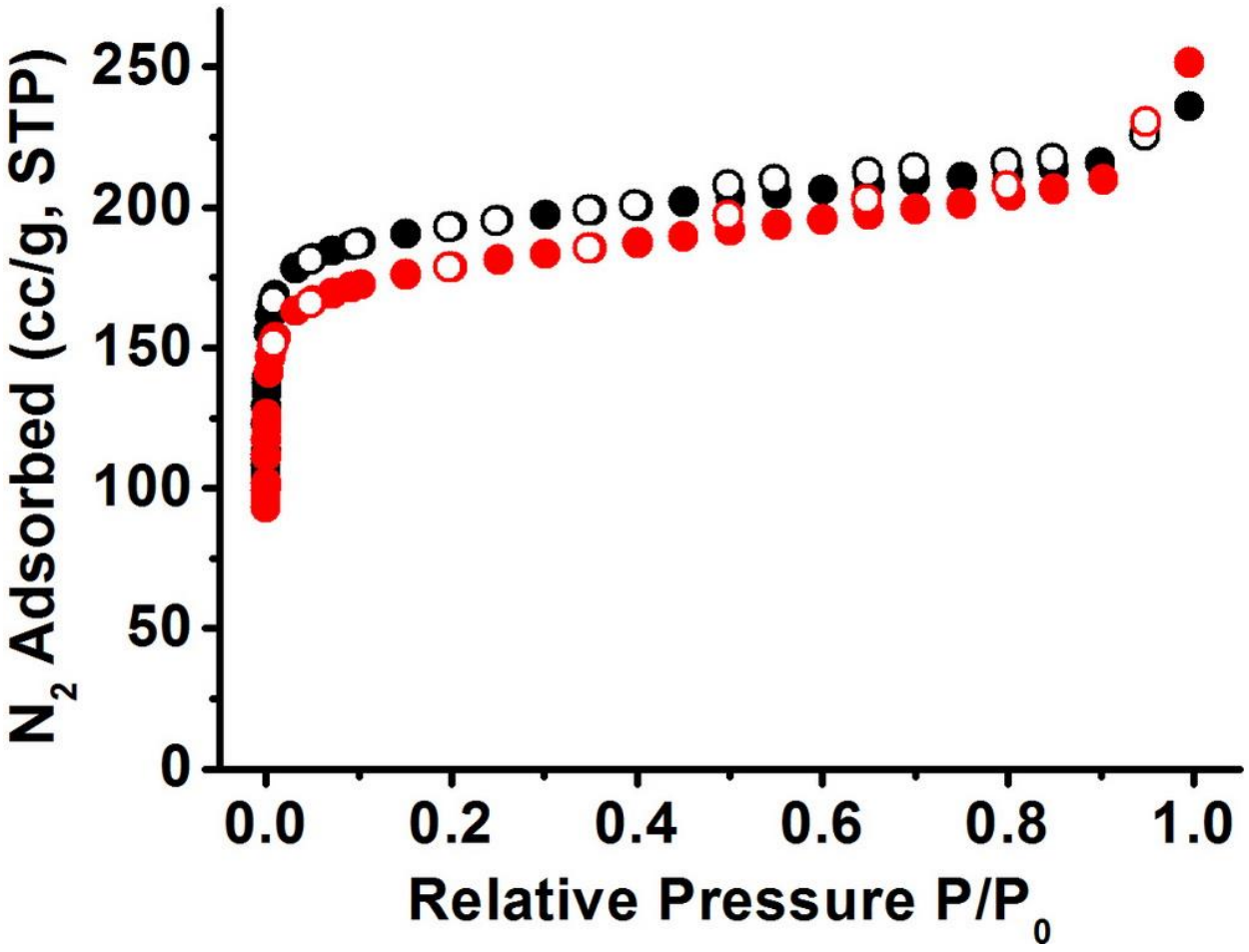

Figure 50. N_2 isotherms of **bio-MOF-14@II** at 77 K before (black) and after (red) grinding. Filled and hollow circles indicate adsorption and desorption respectively.

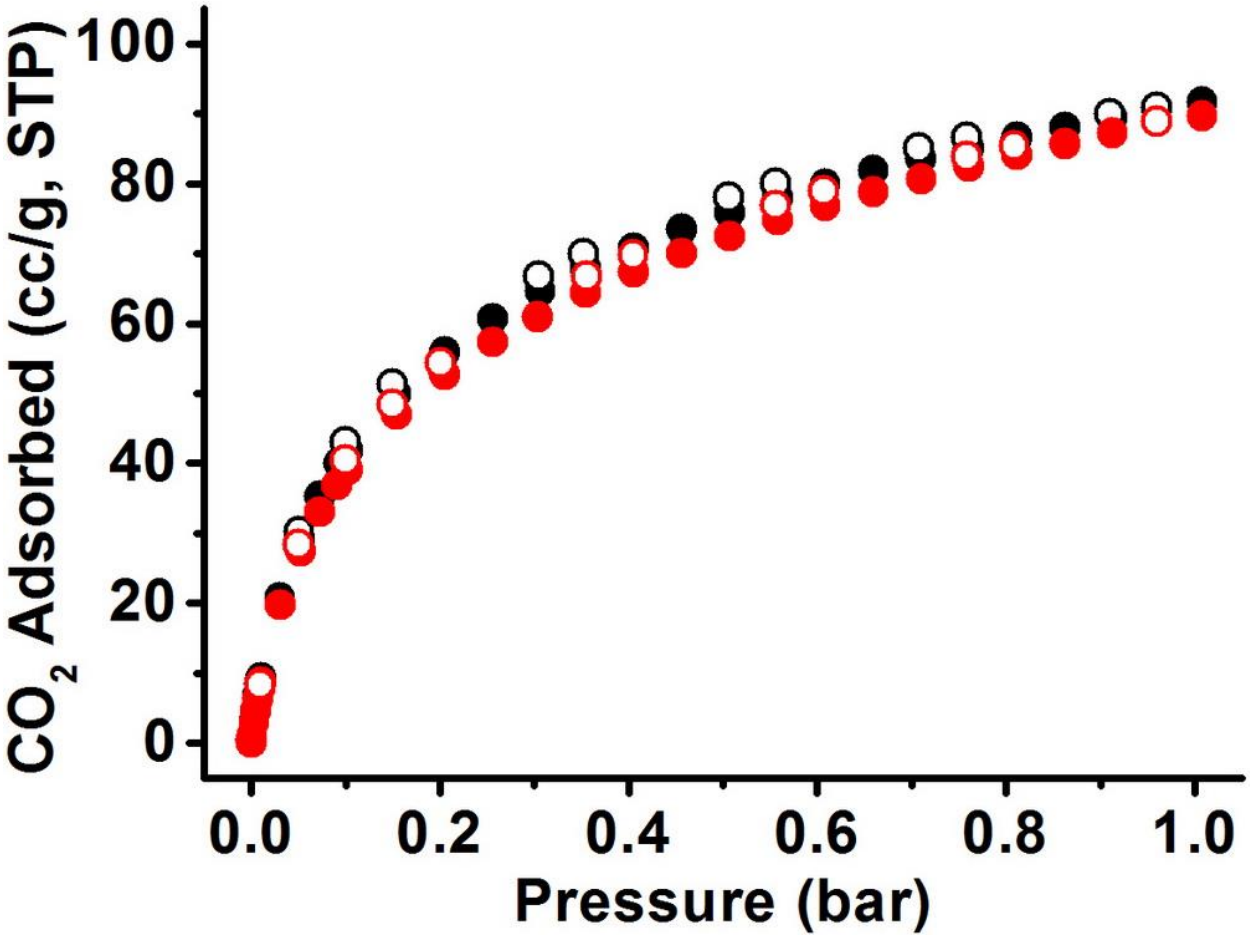

Figure 51. CO_2 isotherms of **bio-MOF-14@II** at 273 K before (black) and after (red) grinding. Filled and hollow circles indicate adsorption and desorption respectively.

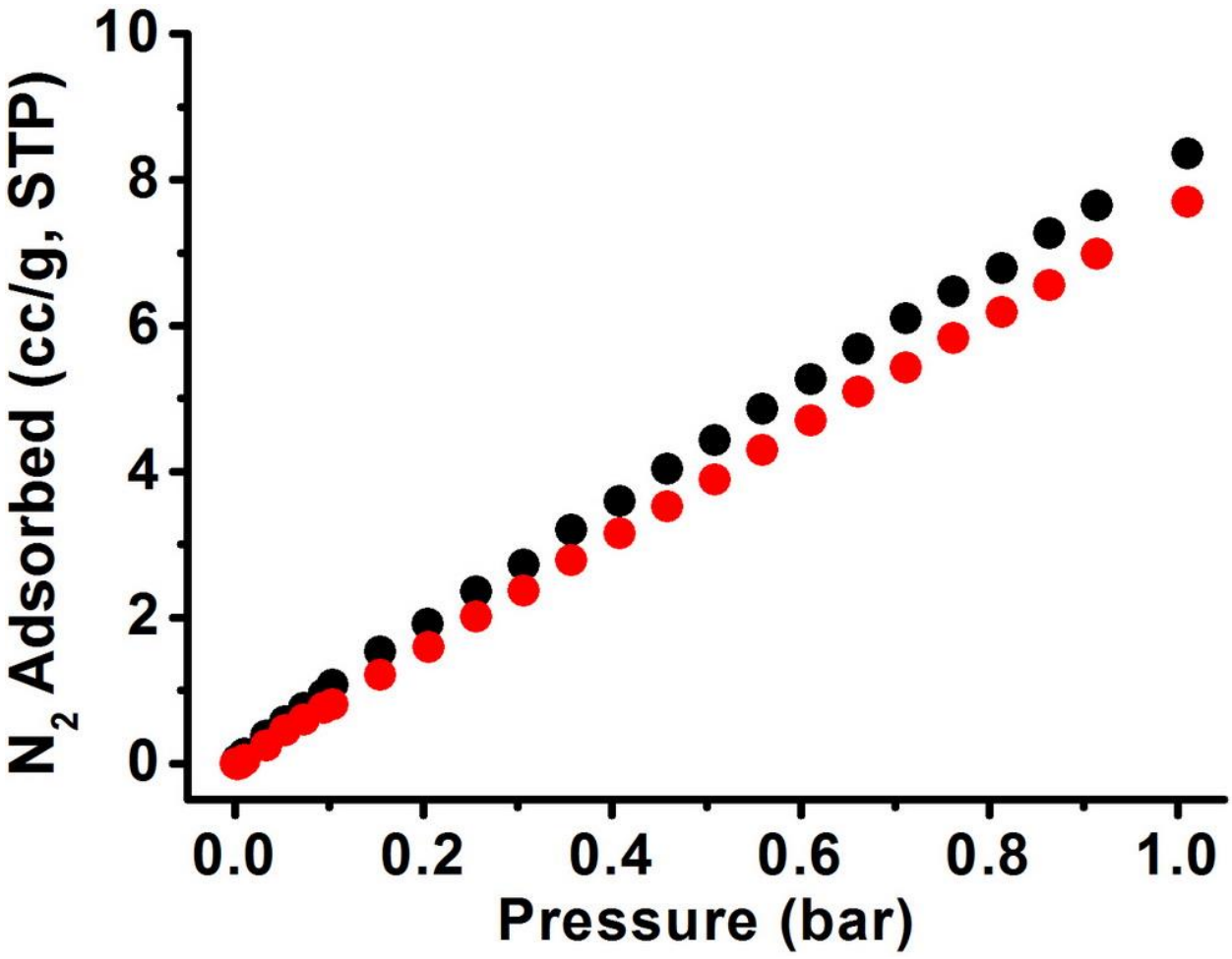

Figure 52. N_2 isotherms of **bio-MOF-14@II** at 273 K before (black) and after (red) grinding.

To investigate whether the hydrophobic and water resistant **bio-MOF-14** shell could protect the water sensitive core, we conducted a water stability test. After soaking in water for 1 day, the core crystals were significantly degraded (Figure 53A) and their PXRD patterns indicated partial loss of crystallinity (Figure 54). On the other hand, no significant crystallite degradation was observed for **II@bio-MOF-14** (Figure 53B). PXRD patterns also indicate that its crystallinity was retained (Figure 54).

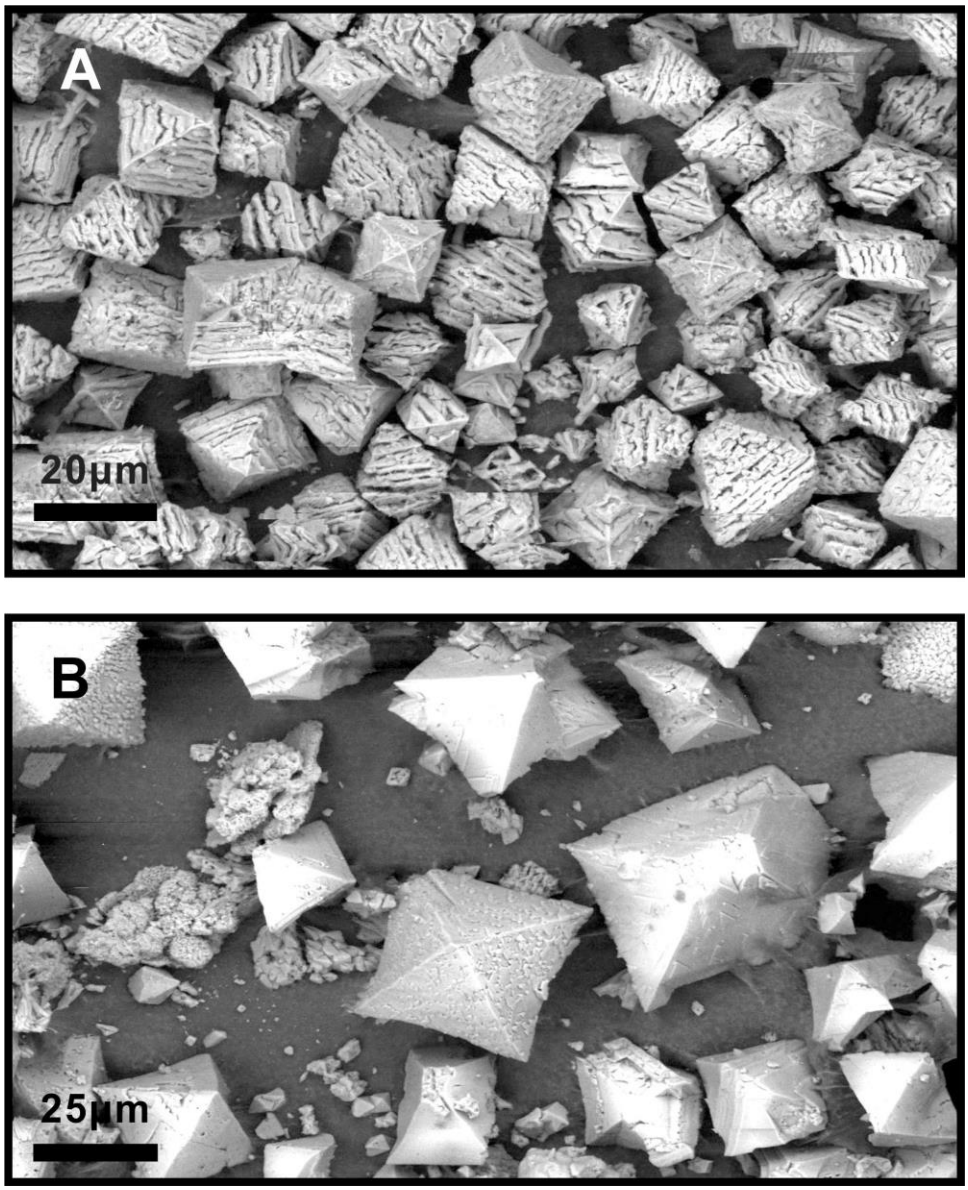

Figure 53. SEM images of core (A) and core-shell (B) after soaking in water for 1 day.

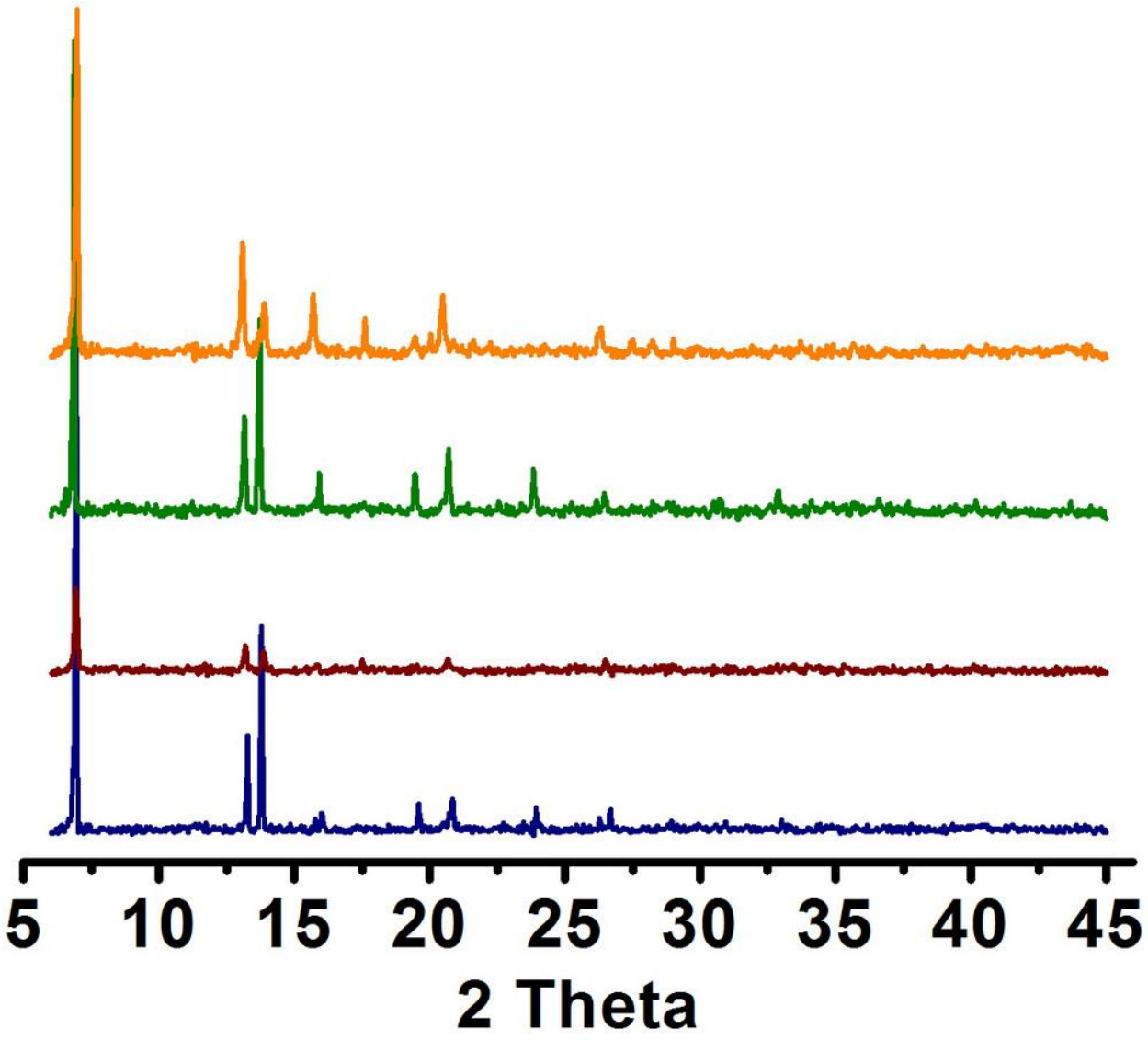

Figure 54. PXRD patterns of as synthesized **II** (blue), **II@bio-MOF-14** (green) and **II** (dark red), **II@bio-MOF-14** (orange) after soaking in water for 1 day.

3.3 CONCLUSION

To summarize, we successfully designed and synthesized a cobalt-adeninate core-shell structure with a porous mixed ligand core and a water resistant **bio-MOF-14** shell. Collectively, all of our acquired data, including PXRD, SEM, gas adsorption, and water stability studies, support the existence of the reported core-shell architecture. We demonstrated how the shell can affect the N_2 and CO_2 adsorption behavior, creating a new material that has an internal capacity for CO_2 yet excludes N_2. Further, we demonstrated that the water resistant shell protects the water sensitive core. To our knowledge, there exists no demonstration prior to this work that details how MOF stratification can lead to new materials with both selective gas storage properties and enhanced water stability.

3.4 EXPERIMENTAL SECTION

3.4.1 General procedures and instrumentation

Cobalt carbonate was purchased from Fisher Scientific, while all the other chemicals were purchased from Aldrich Chemical Co. N, N'-dimethylformamide (DMF) was pre-dried with 3 Å molecular sieves overnight before use. Other chemicals were used directly without further purification. Nanopure water (18.2 MΩ) was obtained using a Barnstead DiamondTM System.

Powder X-ray diffraction (PXRD) patterns were collected using a Bruker AXS D8 Discover powder diffractometer equipped with a Cu Kα X-ray source at 40 kV, 40 mA. Scan speed and step size were set at 0.2 sec/step and 0.02 °/step respectively. Generally, MOF samples were first spread evenly onto a glass slide. Sample height was aligned with laser and data were collected for desired range. Thermogravimetric analysis (TGA) was conducted on a TGA Q500 thermal analysis system. Prior to analysis, samples were dried under argon flow (UHP) to remove excess solvent. Approximately 5 mg of sample were loaded into a platinum pan and heated under a constant N_2 (UHP) flow from room temperature to 600 °C at a rate of 5 °C/min. Scanning electron microscopy (SEM) images were obtained using a Philips XL-30 field emission scanning electron microscope under BSE mode. Gas adsorption isotherms were collected using a Quantachrome Autosorb-1 instrument. As synthesized crystals were thoroughly washed with anhydrous dichloromethane and dried under argon flow. Approximately 60 mg of each sample was added into a pre-weighed sample analysis tube. The samples were degassed at 100 °C under vacuum for 24-48 hours until the pressure change rate was no more than 3.5 mTorr/min. A liquid N_2 bath was used for the N_2 adsorption experiments at 77 K. A water/ethylene glycol bath was used for isotherms collected at 273 K. UHP grade N_2 and CO_2 gas adsorbates (99.999 %) were used in this study. Proton nuclear magnetic resonance spectra (^{1}H-NMR) were collected on Bruker Avance 300 MHz spectrometers. Chemical shifts are in parts per million using the residual solvent peak as the reference value. The value used for proton spectra is 2.5 ppm for d_6-DMSO.

3.4.2 Synthesis and preparation of materials

3.4.2.1 Preparation of bio-MOF-11 and bio-MOF-14

Bio-MOF-11 and **bio-MOF-14** were synthesized using reported methods.[1] To synthesize **bio-MOF-11**, cobalt acetate and adenine were dissolved in pre-dried DMF to make 0.05 M stock solutions. Cobalt acetate solution (9.0 ml; 0.45 mmol), adenine solution (27.0 mL; 1.35 mmol), and nanopure water (120 μL) were mixed into a 40 ml Schlenk tube. After freezing in liquid nitrogen, the Schlenk tube was vacuumed to 200 mTorr. Then, it was heated in a 130 ^{o}C oven for 24 h. Black, octahedral crystals were collected, washed (dry DMF, 3X), and dried under argon flow. Yield: 102 mg, 90 % (based on cobalt acetate salt). The synthesis of **bio-MOF-14** followed the same procedure as **bio-MOF-11**. However, cobalt valerate[1] was used instead of cobalt acetate. Final yield: 85 mg, 64 % (based on Co valerate).

3.4.2.2 Preparation of I, II, III, and IV

I, II, III, and **IV** were synthesized using similar procedures as **bio-MOF-11** or **bio-MOF-14**, but different volumes of the cobalt solutions (0.05 M) were used, as listed below:

I: 6 ml cobalt acetate solution + 3 ml cobalt valerate solution

II: 4.5 ml cobalt acetate solution + 4.5 ml cobalt valerate solution

III: 3 ml cobalt acetate solution + 6 ml cobalt valerate solution

IV: 1.5 ml cobalt acetate solution + 7.5 ml cobalt valerate solution

3.4.2.3 Preparation of II@bio-MOF-14

II obtained from one Schlenk tube (~100 mg) was thoroughly washed with dry DMF and added into a 40 ml Schlenk tube along with some solvent (~1 ml). Cobalt valerate (9 ml) and

adenine (27 ml) stock solutions (0.05 M) were added. The Schlenk tube was vacuum sealed as described above and heated in a 130 ^{o}C oven for 24 h. The crystals were washed with dry DMF and re-coated using the same procedure two more times. The final product was washed with dry DMF and dry DCM and then dried under argon flow to yield **II@bio-MOF-14**.

3.4.2.4 Preparation of bio-MOF-14@II

Bio-MOF-14 (~100mg) was thoroughly washed with dry DMF and added into a 40 ml Schlenk tube along with some solvent (~1 ml). Cobalt valerate (4.5 ml), cobalt acetate (4.5 ml) and adenine (27 ml) stock solutions (0.05 M) were added. The Schlenk tube was vacuum sealed and heated in a 130 ^{o}C oven for 24 h. The crystals were washed with dry DMF and re-coated using the same procedure two more times. The final product was washed with dry DMF and dry DCM and then dried under argon flow to yield **bio-MOF-14@II**.

3.4.3 ^{1}H-NMR analysis

Approximately 5 mg of each MOF sample was first dried under argon flow (**bio-MOF-14@II** was washed with DCM before drying) and dissolved in 0.65 ml d_6-DMSO and 3 µl concentrate DCl mixture. ^{1}H-NMR of **I**, **II**, **III**, **IV**, **II@bio-MOF-14**, and **bio-MOF-14@II** were collected at room temperature. The integration for the methyl hydrogen in valerate was set as 1. The ratios between C2 (acetate) and C5 (valerate) were calculated by comparing the integration of their methyl hydrogens.

I: $^{-}$OOCC***H*$_{3}$, δ 1.91 (singlet, 2.8 H); $^{-}$OOCCH$_2$CH$_2$CH$_2$C***H*$_{3}$, δ 0.85 (triplet, 1 H)

II: $^{-}$OOCC***H*$_{3}$, δ 1.91 (singlet, 1.5 H); $^{-}$OOCCH$_2$CH$_2$CH$_2$C***H*$_{3}$, δ 0.85 (triplet, 1 H)

III: $^{-}$OOCC***H*$_{3}$, δ 1.91 (singlet, 0.76 H); $^{-}$OOCCH$_2$CH$_2$CH$_2$C***H*$_{3}$, δ 0.85 (triplet, 1 H)

IV: $^{-}$OOCC***H*$_{3}$**, δ 1.91 (singlet, 0.38 H); $^{-}$OOCCH$_2$CH$_2$CH$_2$C***H*$_{3}$**, δ 0.85 (triplet, 1 H)

II@bio-MOF-14: $^{-}$OOCC***H*$_{3}$**, δ 1.91 (singlet, 0.18 H); $^{-}$OOCCH$_2$CH$_2$CH$_2$C***H*$_{3}$**, δ 0.85 (triplet, 1 H)

bio-MOF-14@II: $^{-}$OOCC***H*$_{3}$**, δ 1.91 (singlet, 1.3 H); $^{-}$OOCCH$_2$CH$_2$CH$_2$C***H*$_{3}$**, δ 0.85 (triplet, 1 H)

4.0 STEPWISE LIGAND EXCHANGE FOR THE PREPARATION OF A FAMILY OF MESOPOROUS MOFS

This work, written in collaboration with Mark T. Kozlowski, Evan A. Doud, Maike N. Blakely, and Nathaniel L. Rosi, was published in *J. Am. Chem. Soc.*, **2013**, 135, 11688-11691.[10] Copyright 2013, American Chemical Society.

Mark T. Kozlowski, Evan A. Doud, and Maike N. Blakely helped with the synthesis and characterization of bio-MOFs.

4.1 INTRODUCTION

The realization of mesoporosity in metal-organic frameworks (MOFs) has opened the door to new potential applications for this class of periodic porous materials.[107,108,109] Several mesoporous MOFs have been reported.[109] However, the overwhelming majority has a distribution of micropores (< 2 nm) and mesopores (2-50 nm); micropores can gate entry to the mesopores and therefore limit the size of species that are allowed to freely diffuse and migrate throughout the structure. Only a few mesoporous MOFs exhibit continuous uninterupted mesoporous channels.[11,12,26,110,111] Cubic **Bio-MOF-100**[11] has continuous and interconnected mesoporous channels running throughout its structure. It is one of only two reported MOF

materials having a pore volume exceeding 4 cc/g,[9,11] and we have shown that it can be used as a scaffold for organizing large molecules, including short peptides.

In this communication, we report three new isoreticular analogues of **bio-MOF-100**: **bio-MOF-101**, **102**, and **103**. We utilize a stepwise ligand exchange strategy to prepare these materials in which shorter ligands are replaced by longer ligands in what appears to be a crystal to crystal transformation. **Bio-MOF-102** and **bio-MOF-103** each have pore volumes that exceed 4 cc/g; together with **bio-MOF-100**, they represent three of only four reported MOFs that exceed this threshold.[3] To our knowledge, this report documents the first demonstration that ligand exchange can be utilized to systematically increase the pore dimensions of MOF materials.[7,112,113,114,115,116,117,118,119,120] This strategy is very promising because 1) it represents a potentially universal method for increasing MOF porosity; 2) the nature of the ligand exchange process avoids the possibility of interpenetration, provided that a non-interpenetrated MOF is used as the starting material; and 3) it allows access to products that may be thermodynamically unfavorable.

4.2 RESULTS AND DISCUSSION

We began this study by first attempting to synthesize isoreticular analogues of **bio-MOF-100** using various linear dicarboxylate linkers. **Bio-MOF-100** adopts the highly open ***lcs*** net[41] and consists of zinc-adeninate clusters ($Zn_8Ad_4O_2^{8+}$; Ad = adeninate) periodically linked with 4,4'-biphenyldicarboxylate (BPDC).[11] Although we succeeded in preparing **bio-MOF-101**, the isoreticular analogue of **bio-MOF-100** having 2,6-naphthalenedicarboxylate (NDC) linkers, at this stage we were unable to prepare analogues with linkers longer than BPDC. This prompted

us to explore ligand exchange as a strategy for accessing more porous analogues of **bio-MOF-100**.

To realize this design strategy, we first studied the conversion between **bio-MOF-101** and **bio-MOF-100** (Figure 55 and 56). **Bio-MOF-101** was thoroughly washed with N,N'-dimethylformamide (DMF) and subsequently soaked in a 0.05 M H_2-BPDC/DMF/NMP (DMF:NMP=1:1 ; NMP = N-methylpyrolidinone) solution for 24 h in a 75 ^{o}C oven; the solution was removed, replaced with a fresh H_2-BPDC solution, and the mixture was again heated at 75 ^{o}C for 24 h. Upon inspection using an optical microscope, the product crystals were mostly transparent and slightly cracked (Figure 56). ^{1}H-NMR spectra of the dissolved crystalline product revealed only the presence of adenine and BPDC linkers; no NDC was detected, indicating that it was completely replaced by BPDC (Figure 57).

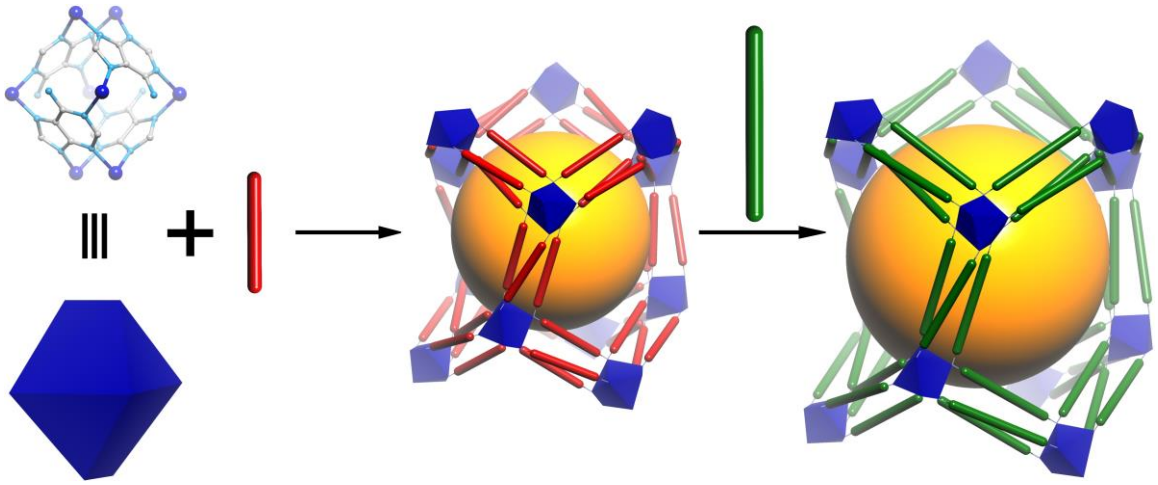

Figure 55. Scheme depicting pore expansion strategy.

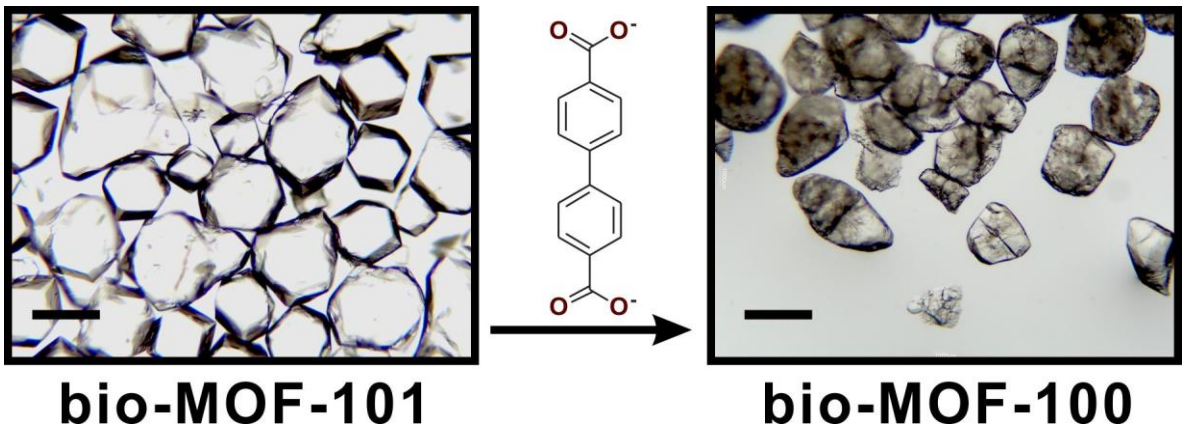

Figure 56. As-synthesized **bio-MOF-101** was converted to **bio-MOF-100** via ligand exchange with BPDC. Light microscope images of the crystalline MOFs have scale bars representing 0.2 mm.

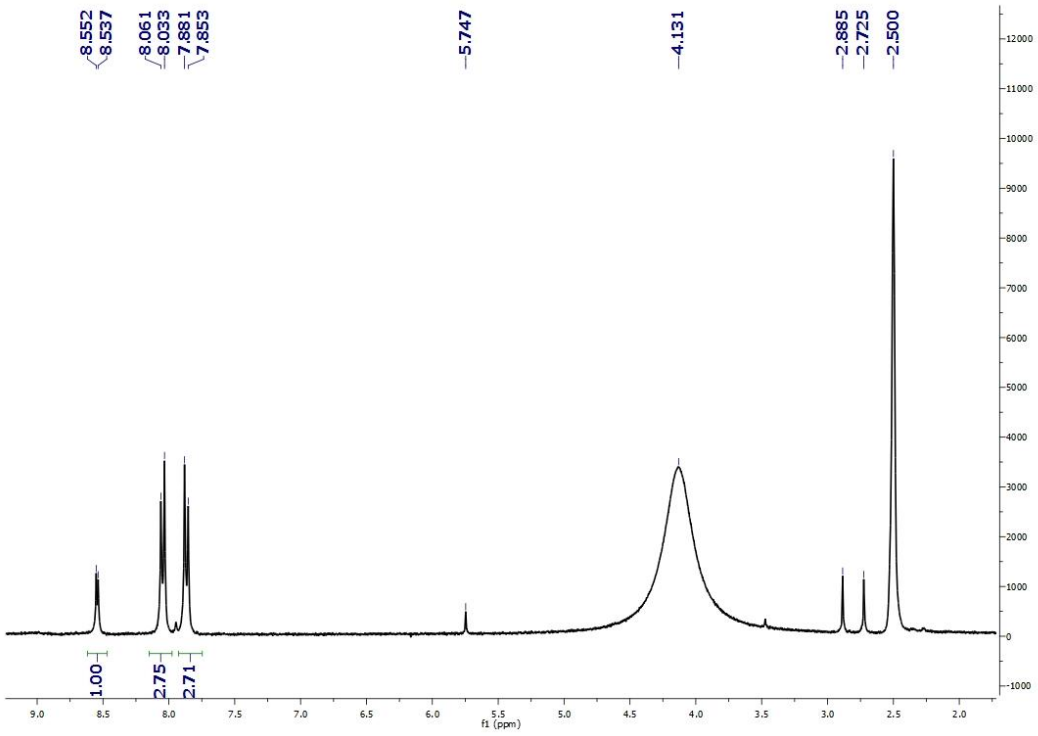

Figure 57. ^{1}H-NMR spectrum of digested **bio-MOF-100** from ligand exchange (peak at $\delta = 7.9$ corresponds to the aldehyde proton in DMF).

Having successfully converted **bio-MOF-101** to **bio-MOF-100** through ligand exchange, we endeavored to expand the pores of **bio-MOF-100** by using a similar process to replace BPDC with the slightly longer azobenzene-4,4'-dicarboxylate (ABDC) and the much longer 2'-amino-1,1':4,1''- terphenyl-4,4''-dicarboxylate (NH_2-TPDC). Due to their characteristic dark orange (ABDC) and light orange color (NH_2-TPDC), we expected to observe a crystal color change after successful ligand exchange. When soaked in an H_2-ABDC solution, the colorless **bio-MOF-100** crystals did indeed transform into a dark orange crystals without noticeable cracks (Figure 58). We monitored this process by imaging a single crystal of **bio-MOF-100** at different time points during reaction (Figure 59). It is clear from these images that the crystal remains intact and progresses from colorless to pale orange to dark orange throughout the course of the ligand exchange reaction. The resulting new crystalline material, named **bio-MOF-102**, was then soaked in an H_2-NH_2-TPDC solution to yield light orange crystals, named **bio-MOF-103** (Figure 58). ^{1}H-NMR spectra of dissolved samples of **bio-MOF-102** revealed the presence of adenine and ABDC and a trace amount of residual BPDC (Figure 60). Complete ligand exchange was not observed for the entirety of the product crystals in the transformation of **bio-MOF-102** to **bio-MOF-103**: integration of appropriate peaks in the ^{1}H-NMR spectrum of the dissolved products indicate ~85% NH_2-TPDC and ~15% residual ABDC (Figure 61).

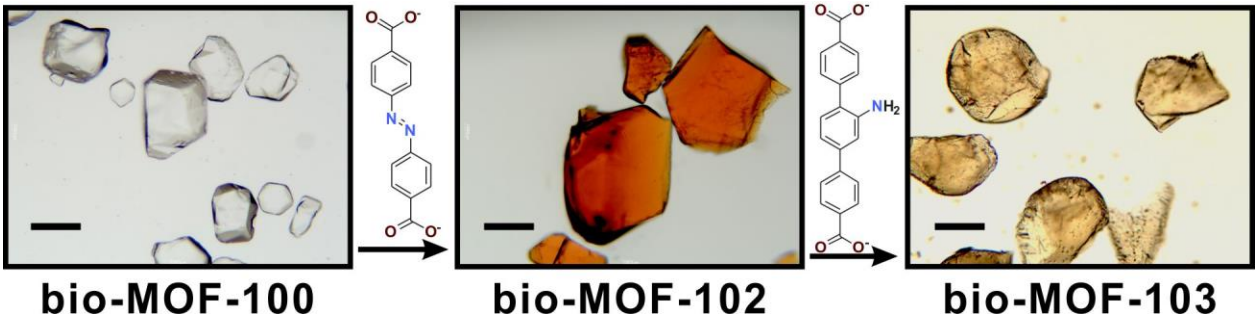

Figure 58. BPDC in **bio-MOF-100** was replaced with ABDC to yield **bio-MOF-102**; thereafter ABDC in **bio-MOF-102** was replaced with NH_2-TPDC to yield **bio-MOF-103**. Light microscope images of the crystalline MOFs have scale bars representing 0.2 mm.

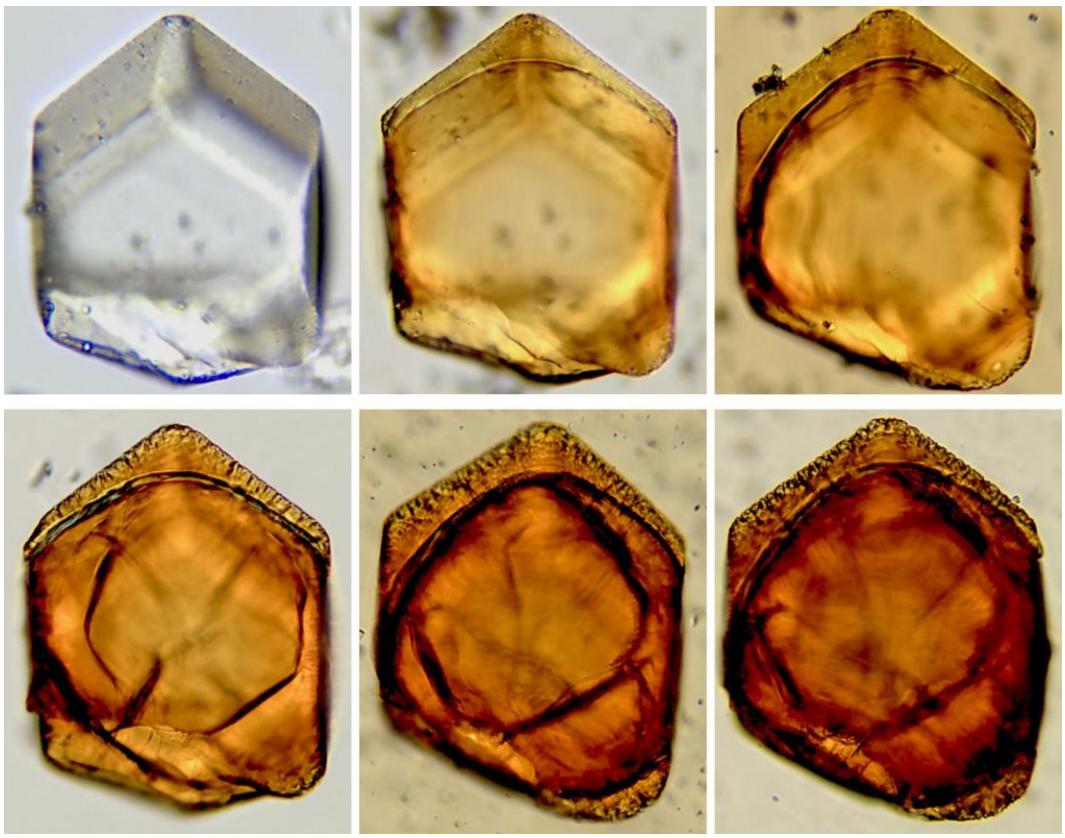

Figure 59. Transformation process from a single crystal of **bio-MOF-100** (top left) to **bio-MOF-102** (bottom right) monitored by an optical microscope.

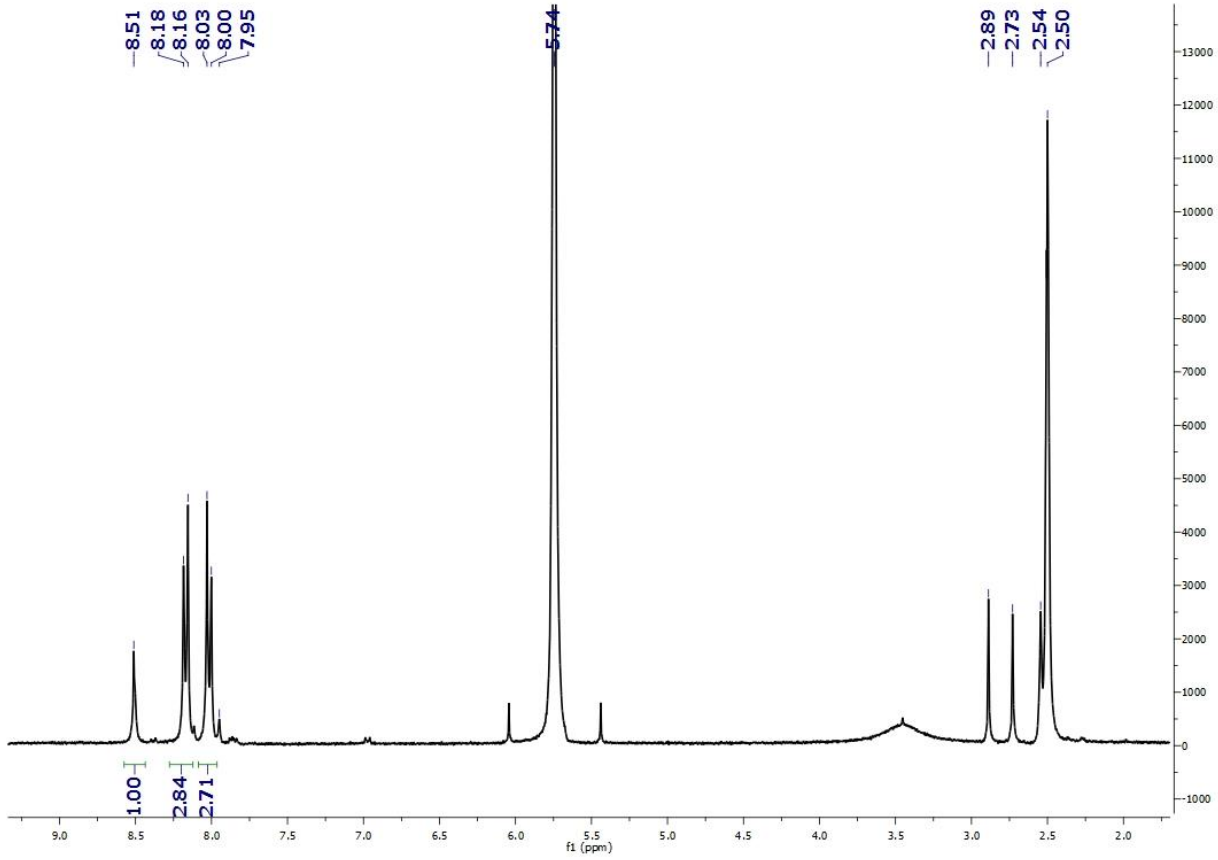

Figure 60. ^{1}H-NMR spectrum of digested **bio-MOF-102** (peak at δ = 7.9 corresponds to the aldehyde proton in DMF; peaks at δ = 7.87 correspond to residual BPDC ligand).

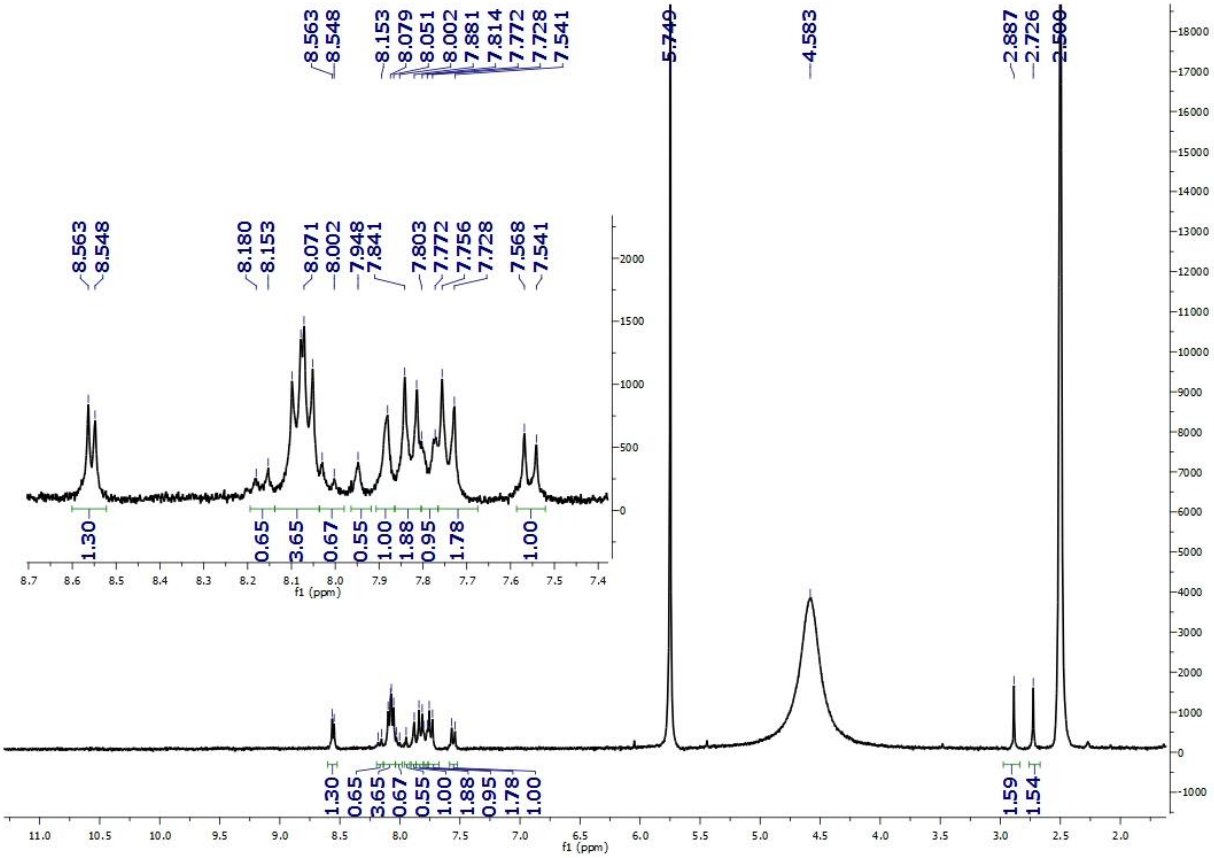

Figure 61. ^{1}H-NMR spectrum of digested **bio-MOF-103**. Residual ABDC peaks were observed at δ 8.18 (d, *J* = 8.3 Hz), 8.02 (d, *J* = 8.2 Hz). The NH_2-TPDC/ABDC ratio was calculated by comparing the integrations of peaks at δ = 8.08 and 8.18 ppm (3.65:0.65). The NH_2-TPDC peaks are slightly shifted compared to the pure ligand, which is likely due to protonation of the amino group in the acidic solvent.

After characterizing the chemical composition following the ligand exchange reactions, we studied the structures of the product crystals. We loaded single crystals of each product onto an X-ray diffractometer and collected diffraction data for unit cell analysis. The unit cell

parameters (Table 6) of a product crystal from the reaction of **bio-MOF-101** with BPDC closely matched the reported values,[11] indicating successful conversion of **bio-MOF-101** to **bio-MOF-100**. A product crystal of the **bio-MOF-100**/ABDC exchange reaction had a cubic unit cell with *a*=*b*=*c*=75.24 Å, which is ~6 Å longer than the unit cell parameter of **bio-MOF-100**. We were able to collect and solve a complete data set for the single crystal, which verified that it was indeed an isoreticular analogue of **bio-MOF-100** and that BPDC was completely replaced by ABDC. Finally, a product crystal of the **bio-MOF-102**/NH_2-TPDC exchange reaction had a cubic unit cell with *a*=*b*=*c*=82.254 Å, which is ~7 Å longer than that observed for **bio-MOF-102**. However, these crystals were extremely weakly diffracting, so at this stage we resorted to constructing a model of the **bio-MOF-103** structure using the single crystal unit cell parameters (Table 7).

Table 6. Unit cell parameters obtained from single crystal X-ray experiments.

Unit cell parameters	a = b = c =(Å)	Literature value of a(Å)	α = β = γ =
Bio-MOF-101	62.04	N/A	90 ^{o}
Bio-MOF-100	68.90	69.12[2a]	90 ^{o}
Bio-MOF-102	75.24	N/A	90 ^{o}
Bio-MOF-103	82.25	N/A	90 ^{o}

Powder X-ray diffraction (PXRD) patterns were collected to examine the phase purity of the bulk product (Figure 62). These data confirm that 1) **bio-MOF-100** was produced from **bio-MOF-101** (Figure 62A); 2) **bio-MOF-102** was produced from **bio-MOF-100** (Figure 62B); and 3) **bio-MOF-103** was produced from **bio-MOF-102** (Figure 62C). In all cases, the principal diffraction lines shifted toward lower angles after longer linkers replaced shorter linkers. The product MOF powder patterns are in very good agreement with those simulated from single-crystal diffraction data or from the structural model, in the case of **bio-MOF-103**. In each case, no reactant diffraction lines were observed in the product MOF, even for **bio-MOF-103** in which complete ligand exchange was not observed. Since three linkers connect neighboring $Zn_8Ad_4O_2^{8+}$ building blocks together within the structure, the longest linker should determine the distance between two building blocks. These data support the conclusion that ligand exchange reactions result in complete structural transformation for the entire sample.

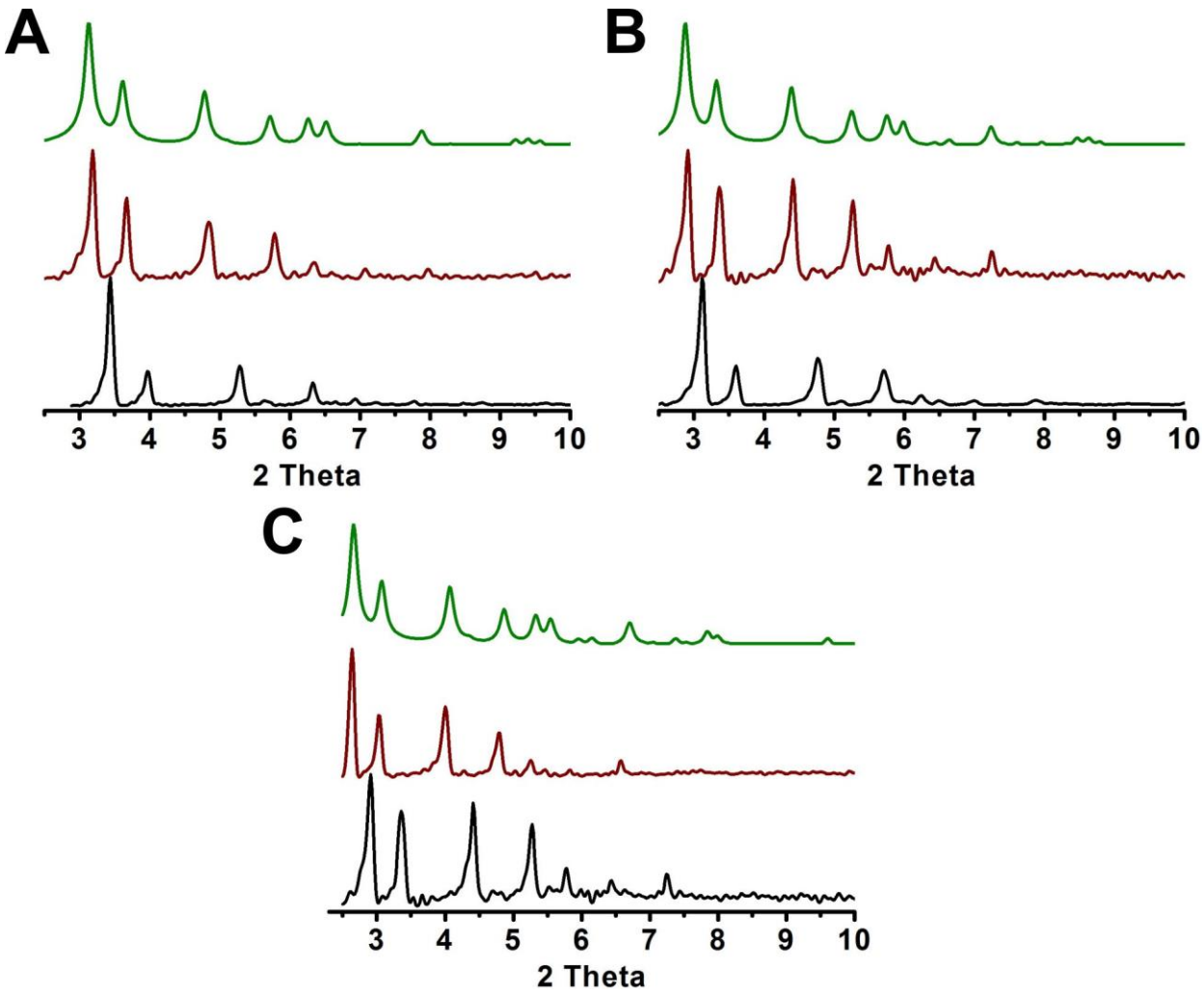

Figure 62. (A) PXRD patterns of as-synthesized **bio-MOF-101** (black), **bio-MOF-100** obtained from ligand exchange (red) and **bio-MOF-100** simulated from crystal structure (green); (B) PXRD patterns of as-synthesized **bio-MOF-100** (black), **bio-MOF-102** (red) and **bio-MOF-102** simulated from single crystal data (green); (C) PXRD patterns of **bio-MOF-102** (black), **bio-MOF-103** (red) and **bio-MOF-103** simulated from single crystal model (green).

We expected to observe a volume change for the solid materials after replacing short linkers with long linkers. A certain amount of **bio-MOF-101** crystal was loaded into an NMR tube (1.2 mm of tube length, Figure 63). Stepwise ligand exchange reactions were performed within the NMR tube (Supporting Information). After ligand exchange by BPDC and allowing the product to settle completely, the height of the sample increased to 1.5 mm. The **bio-MOF-100** product (Figure 63B) was reacted with H_2-ABDC to yield orange **bio-MOF-102** (Figure 63C), which has an expanded sample height of 2.3 mm. Finally, the **bio-MOF-102** product (Figure 63C) was reacted with H_2-NH_2-TPDC. The light orange product crystals of **bio-MOF-103** (Figure 63D) have a height of 3.1 mm. This continuous change in sample height offers qualitative visual proof of the volume change of the crystals after ligand exchange.

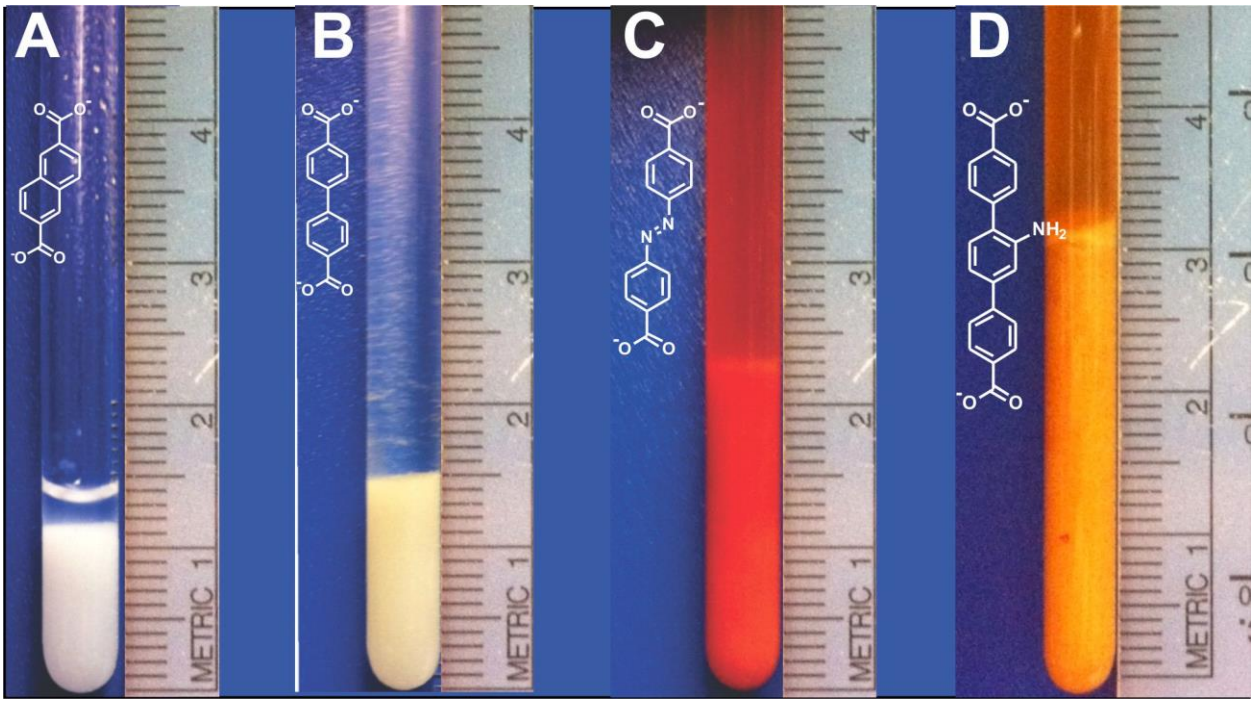

Figure 63. Volume expansion experiment showing as-synthesized **bio-MOF-101** (A), **bio-MOF-100** (B), **bio-MOF-102** (C), and **bio-MOF-103** (D).

The porosities of **bio-MOF-101** and the products of ligand exchange, **bio-MOF-100**, **102**, and **103**, were investigated by N_2 gas adsorption at 77 K. Crystalline samples were completely exchanged with ethanol and activated using established methods.[121] Each material exhibits a Type IV adsorption isotherm characteristic of mesoporous materials (Figure 64A). The analogue with the shortest linker, **bio-MOF-101**, adsorbs the least amount of N_2 and has a calculated pore volume of 2.83 cc/g. The **bio-MOF-100** sample prepared herein adsorbed 2444 cc/g N_2 which is slightly lower than the previously reported value.[11] We surmise that this may be due to defects created during the ligand exchange process. As expected, **bio-MOF-102** and **103** show the highest N_2 uptakes and exhibit calculated pore volumes of 4.36 cc/g and 4.13 cc/g, respectively. The pore volume of **bio-MOF-102** exceeded the reported pore volume of **bio-MOF-100**, making it the second most porous MOF reported in terms of the pore volume metric. We note that only the isotherm for **bio-MOF-103** shows hysteresis upon desorption; we hypothesize that this may be due to the incomplete exchange of ABDC by NH_2-TPDC (*vide supra*). We calculated the pore size distribution for each material using the QSDFT method (Figure 64B).[122] These data definitively demonstrate that the ligand exchange method can be used to systematically increase the pore size of this class of mesoporous bio-MOFs from ~2.00 nm to 2.84 nm, which agrees well with the pore sizes predicted from the crystal structures (2.1 nm to 2.9 nm).

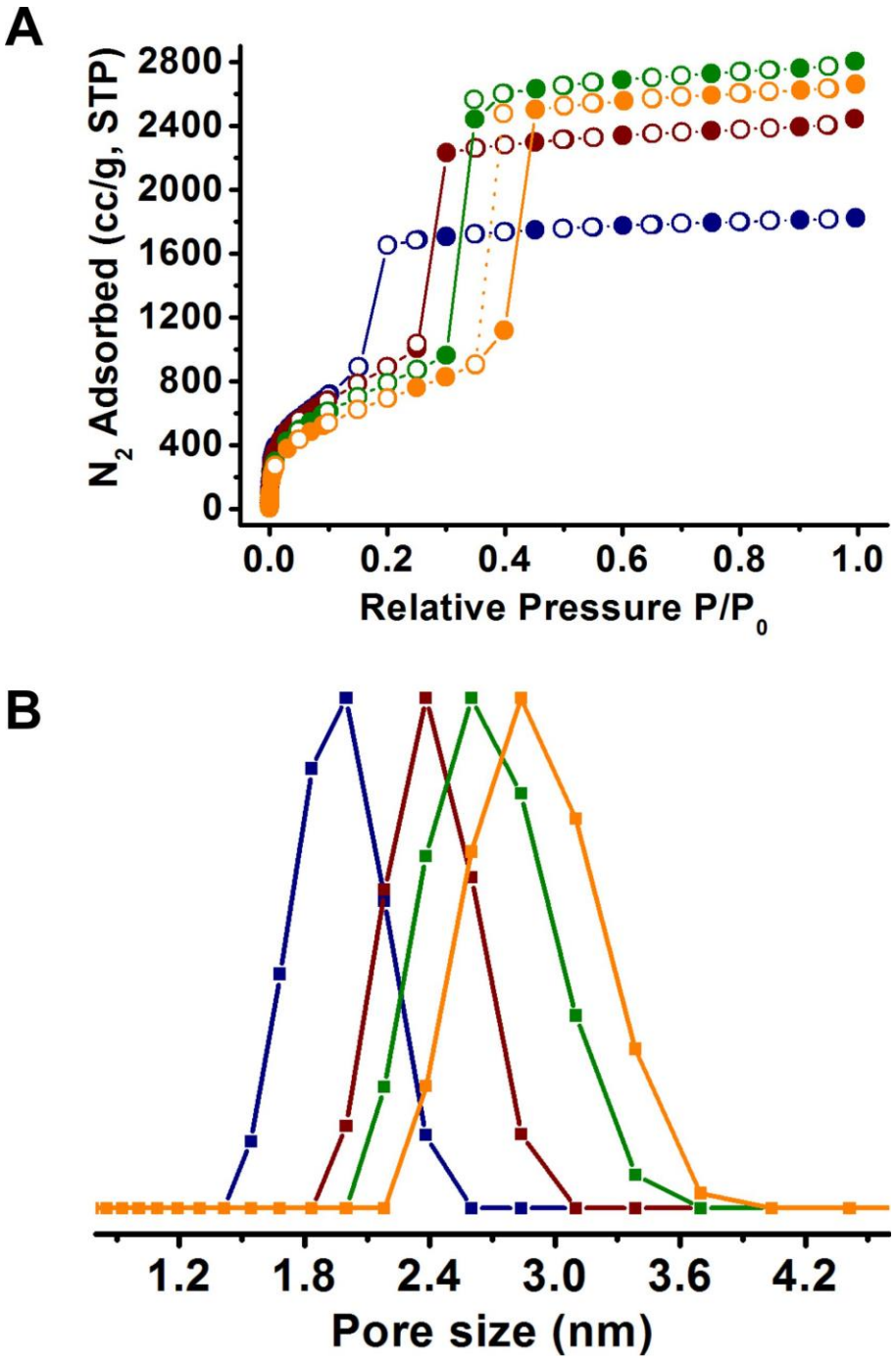

Figure 64. (A) N_2 adsorption isotherms of **bio-MOF-101** (navy), **bio-MOF-100** (red), **bio-MOF-102** (green), **bio-MOF-103** (orange) at 77 K. (B) normalized pore size distribution (PSD) of **bio-MOF-101** (navy), **bio-MOF-100** (red), **bio-MOF-102** (green), **bio-MOF-103** (orange) calculated by quenched solid state functional theory (QSDFT) method.[122]

4.3 CONCLUSION

In summary, we have demonstrated that using ligand exchange, a short linker molecule in a MOF can be replaced with a longer one to produce a more porous isoreticular analogue without sacrificing loss of crystallinity. This process can be applied sequentially to yield product MOFs with increasingly larger pore sizes. We predict that this method can also be used to isolate new MOFs that cannot be prepared using traditional synthetic methods. We have established herein that, collectively, **bio-MOFs 100-103** are one of the most porous families of MOF materials based on the important metric of total pore volume.

4.4 EXPERIMENTAL SECTION

4.4.1 General procedures and instrumentation

2,6-naphthalenedicarboxylic acid (NDC) and 4,4'-azobenzenedicarboxylic acid (ABDC) were purchased from TCI; all other chemicals were purchased from Aldrich Chemical Co. All chemicals were used directly without further purification. Nanopure water (18.2 MΩ) was obtained using a Barnstead DiamondTM System. Powder X-ray diffraction (PXRD) patterns were collected using a Bruker AXS D8 Discover powder diffractometer equipped with a Cu Kα X-ray source at 40 kV, 40 mA. Scan speed and step size were set at 0.1 sec/step and 0.02 °/step, respectively. Generally, MOF samples were first spread evenly onto a glass slide. Sample height was aligned with a laser and data were collected for the desired range. Optical

microscopy images were collected using an Olympus BH-2 microscope. Elemental microanalyses (EA) were performed by the University of Illinois Department of Chemistry Microanalytical Laboratory using a Perkin-Elmer 240 Elemental Analyzer and an Exeter Analytical CE440.

Supercritical CO_2 activation experiments were performed on a Tousimis SAMDRI-PVT-3B. Prior to activation, **bio-MOF-101**, **bio-MOF-100**, **bio-MOF-102**, and **bio-MOF-103** were thoroughly washed with dry ethanol. The samples were than soaked in dry ethanol for one day, and the dry ethanol was refreshed after 10 minutes and 20 minutes of soaking. MOF sample was then added into a sample cell and placed into the chamber of the supercritical drier. Dry liquid CO_2 (99.8%) was charged into the chamber. The sample cell was allowed to purge for 5 min every 30 min. The chamber temperature was kept at ~0-10 ^{o}C during the process. After 4 hours, the chamber temperature was raised to ~38 ^{o}C and held for 1 hour followed by slow venting overnight.

Gas adsorption isotherms were collected on a Quantachrome Autosorb-1 instrument. Approximately 45-50 mg of each sample was added into a pre-weighed sample analysis tube. The samples were degassed at room temperature under vacuum for ~24 hours until the pressure change rate was no more than 3.5 mTorr/min. A liquid N_2 bath was used for the N_2 adsorption experiments at 77 K. UHP grade N_2 gas adsorbates (99.999 %) were used in this study.

Proton nuclear magnetic resonance spectra (^{1}H-NMR) were collected on Bruker Avance 300 MHz spectrometers. Chemical shifts are in parts per million using the residual solvent peak as the reference value. The value used for proton spectra is 2.5 ppm for d_6-DMSO.

^{1}H-NMR spectra of bio-MOF-101, bio-MOF-100, bio-MOF-102, and bio-MOF-103

Approximately 5 mg of each MOF sample was first thoroughly washed with DMF, dichloromethane (DCM) and then dried under argon flow. d_6-DMSO (0.65 ml) and concentrate DCl (3 μl) were added to dissolve the MOF. ^{1}H-NMR of **bio-MOF-100**, **bio-MOF-102**, and **bio-MOF-103** were collected at room temperature. The integration for the two hydrogen atoms in adenine was set as 1. The ratios between ABDC and NH_2-TPDC were calculated by comparing the integration of their aromatic hydrogens.

4.4.2 Synthesis and preparation of materials and ^{1}H NMR Characterization

4.4.2.1 Synthesis of dimethyl 2'-amino-1,1':4,1''-terphenyl-4,4''-dicarboxylate

A solution of 4-(methoxycarbonyl)-phenylboronic acid (1.44 g, 8 mmol), and 2,5-dibromoaniline (374 mg, 4/3 mmol) in 4 ml of N,N'-dimethylformidamide (DMF) was combined with a solution of sodium carbonate (566 mg, 16/3 mmol) and palladium acetate (2.4 mg, 0.8 mol%) in 4.66 ml of water. The mixture was stirred at 60 ^{o}C overnight. After cooling to room temperature, 100 ml of water was added to the reaction mixture. The aqueous phase was then extracted by ethyl acetate (3X). The combined organic phases were dried with anhydrous sodium sulfate and transferred to a silica gel column. Elution with pure ethyl acetate gave dimethyl 2'-amino-1,1':4,1''-terphenyl-4,4''-dicarboxylate as a light yellowish powder (yield: 520 mg, 96% based on 2,5-dibromoaniline. A small amount of ethyl acetate was present in the product. ^{1}H-NMR (300MHz, $CDCl_3$): 8.11 and 8.08 (2AA' parts of 2AA'XX' spin systems, 2H each), 7.65 and 7.58 (2XX' parts of 2AA'XX' spin systems, 2H each), δ 7.23 (d, J = 7.9 Hz, 1H), 7.12 (dd, J = 7.9, 1.5 Hz, 1H), 7.06 (d, J = 1.1 Hz, 1H), 3.93 (s, 3H), 3.92 (s, 3H). The spectrum matches those reported previously.[123]

4.4.2.2 Synthesis of 2'-amino-1,1':4,1''-terphenyl-4,4''-dicarboxylic acid (H_2-NH_2-TPDC)

2'-amino-1,1':4,1''-terphenyl-4,4''-dicarboxylic acid (g, mmol) was suspended in 180 ml ethanol and 20 ml of water. After adding KOH (1.0 g, 17.8 mmol), the reaction mixture was refluxed overnight. After removal of most of the solvent *in vacuo*, water was added to fully dissolve the precipitate. The aqueous solution was acidified with concentrated HCl to pH ~2 and centrifuged to isolate light yellow solid. The solid was washed with water (3X) and dried in 100 ^{o}C oven to give 2'-amino-1,1':4,1''-terphenyl-4,4''-dicarboxylic acid (yield: 480 mg, 98%). ^{1}H NMR (300 MHz, d_6-DMSO) δ 12.98 (s, 2H), 8.02 (2AA' parts of 2AA'XX' spin systems, 4H), 7.74 and 7.61 (2XX' parts of 2AA'XX' spin systems, 2H each), 7.61 (d, J = 8.2 Hz, 1H), 7.16 (d, J = 7.7 Hz, 1H), 7.15 (d, J = 1.6 Hz, 1H), 7.01 (dd, J = 8.0, 1.4 Hz, 1H).

4.4.2.3 Solvothermal synthesis of bio-MOF-101

Stock solutions of $Zn(OAc)_2 \cdot 6H_2O$ (0.05 M), adenine (0.05 M), and 2,6-naphthalene dicarboxylic acid (H_2-NDC) (0.1 M) in DMF were prepared prior to the MOF synthesis. To a 20 ml glass vial was added 9 ml of the $Zn(OAc)_2 \cdot 6H_2O$, 3 ml of the adenine stock solution, and 3 ml of the NDC stock solution along with 1.5 ml of nanopure water. The reaction mixture was heated in an 85 ^{o}C oven for 24 hours to yield colorless polyhedral crystals. Yield: 181 mg (95 % based on adenine). Anal. Calcd. for $Zn_8(ad)_4(NDC)_6(OH)_2 \cdot 2\ (Me_2NH_2)$, 34 DMF, 13.4 H_2O (ad = adeninate; NDC = 2,6-naphthalene dicarboxylate): C, 45.76; H, 6.49; N, 15.09. Found: C, 45.79; H, 6.53; N, 15.04.

4.4.2.4 Solvothermal synthesis of Bio-MOF-100

Bio-MOF-100 was prepared according to the reported procedure.[11]

4.4.2.5 Ligand exchange from as-synthesized bio-MOF-101 to bio-MOF-100

To ~200 mg of **bio-MOF-101** was added H_2-BPDC/DMF/NMP (DMF:NMP=1:1; NMP = N-methylpyrolidinone) solution (0.05 M, 4 ml). The vial was heated at 75 ^oC for 24 h. The solution was removed, replaced with 4 ml fresh H_2-BPDC solution and the mixture was again heated at 75 ^oC for 24 h. The product (**bio-MOF-100**) was thoroughly washed with hot DMF. The product composition was analyzed via ^1H NMR (Figure 57). The ratio of the adenine hydrogen peak to each BPDC aromatic hydrogen peak is ~1:3, which is consistent with the expected ratio for **bio-MOF-100**.

4.4.2.6 Ligand exchange from as-synthesized bio-MOF-100 to bio-MOF-102

To ~200 mg of **bio-MOF-100** was added H_2-ABDC/DMF solution (0.05 M, 4 ml). The mixture was heated at 75 ^oC for 24 h. The solution was removed, replaced with fresh H_2-ABDC solution (4 ml) and the mixture was again heated at 75 ^oC for 24 h. The product (**bio-MOF-102**) was thoroughly washed with hot DMF until the solution was colorless. The product composition was analyzed via ^1H NMR (Figure 60). The ratio of the adenine hydrogen peak to each BPDC aromatic hydrogen peak is ~1:3, which is consistent with the expected ratio for **bio-MOF-102**.

4.4.2.7 Ligand exchange from as-synthesized bio-MOF-102 to bio-MOF-103

Bio-MOF-102 obtained from the previous step was soaked in H_2-NH_2TPDC/DMF solution (2 ml, 0.05 M) and heated at 75 ^oC for 24 h. The solution was removed, replaced with 2 ml fresh H_2-NH_2TPDC solution and the mixture was again heated at 75 ^oC for 24 h. The product (**bio-MOF-103**) was thoroughly washed with hot DMF until the solution showed no or very weak fluorescence when placed under a UV lamp. The product composition was analyzed via ^1H NMR (Figure 61). See figure caption for integration details.

4.4.2.8 Continuous ligand exchange experiment in NMR tube

To an NMR tube loaded with **bio-MOF-101** (1.2 mm of tube height) was added H_2-BPDC/DMF/NMP solution (DMF : NMP = 1 : 1, 0.05 M, 1 ml). The NMR tube was heated at 75 ^{o}C for 24 h (the tube was tilted at a ~70 ^{o} angle to ensure maximum contact between MOF and solution). The solution was removed, replaced with 1 ml fresh H_2-BPDC solution and heated for another 24 h at 75 ^{o}C. The sample was further exchanged by H_2-ABDC and H_2-NH_2TPDC using similar procedures. 0.05 M H_2-ABDC/DMF solution and 0.05 M H_2-NH_2TPDC/DMF solution were used. Prior to the subsequent ligand exchange, MOF crystals were thoroughly washed with DMF to completely remove the residual ligand in the solution.

4.4.3 Single crystal X-ray diffraction experiments

4.4.3.1 Total structure of Bio-MOF-101

A single crystal of **bio-MOF-101** with dimensions 0.40×0.40×0.30 mm was loaded into a glass capillary tube (Hampton research, glass 50) along with mother liquor. X-ray diffraction data were collected on a Bruker X8 Prospector Ultra equipped with an Apex II CCD detector and an IμS micro-focus CuK\α X-ray source (λ = 1.54178 nm) at room temperature.

A body-centered cubic unit cell with a = b = c = 62.0387 (51) was derived from the least-square refinement of 9983 reflections in the range of 2.664 < θ < 33.183. Centrosymmetric space group Ia-3d was chosen based on systematic absences.

After integration of the data by Bruker program SAINT, empirical absorption correction was applied using SADABS. Because of weak diffraction, the initial attempt to solve the structure by direct methods using SHELXTL[124] was not successful. We calculated the theoretical coordinates for the Zn-adeninate SBU based on the crystal structure of previously

reported **bio-MOF-100**. For example, in **bio-MOF-100**, Zn1 is located at (x=0.489 y=0.230 z=0.190) and the center of the Zn-adeninate SBU is at (x=0.5 y=0.25 z=0.125).[2] So the equivalent Zn in **bio-MOF-101** will be at x=(0.489-0.5) ×69.12/62.04+0.5, y=(0.230-0.25) ×69.12/62.04+0.25, z=(0.190-0.125) ×69.12/62.04+0.125. Due to the flexibility of the structure, adenine was constrained as a rigid model adapted from Cambridge Structural Database. All the atoms were stable after first least-square refinement. However, the carbon and oxygen atoms from NDC still could not be generated via Fourier syntheses. Therefore, Materials Studio (v5.0) was used to build a model of NDC first and then distance restraints were applied using standard values. Naphthalene rings were restrained to be planar and ideal positions of the hydrogen atoms were calculated. All of the non-hydrogen atoms were refined anisotropically with rigid-bond restraints applied to anisotropic displacement parameters. Platon was used to remove solvent electron density.[125] Finally, R-factors converged to wR2 = 0.1757 and R1 = 0.0536.

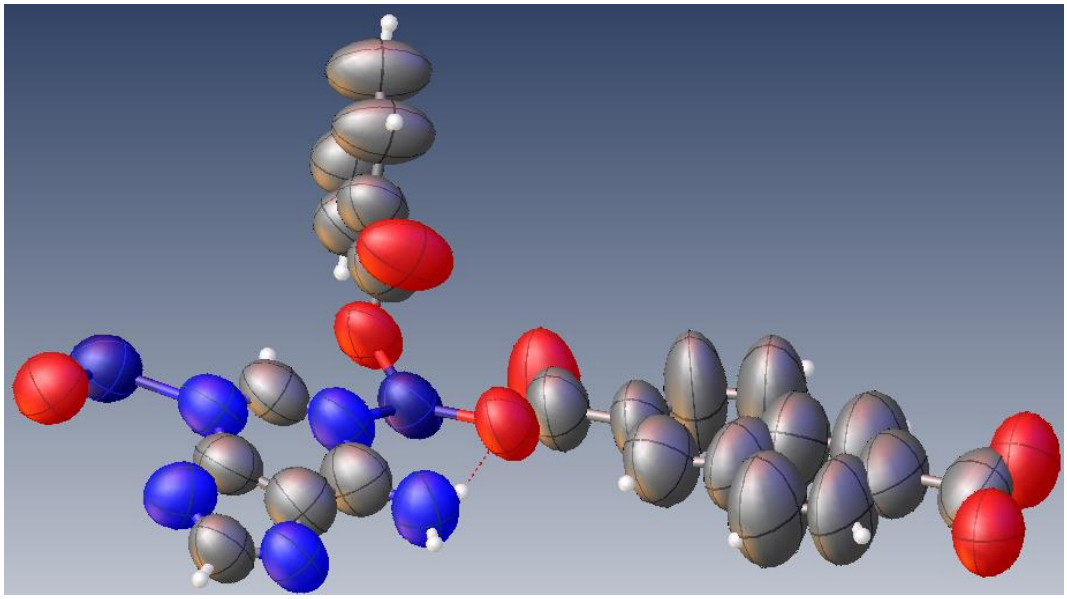

Figure 65. Anisotropic displacement ellipsoids of the content of the asymmetric unit are shown at 50% level. The figure was produced with Olex 2.[126]

4.4.3.2 Total structure of bio-MOF-102

A single crystal of **bio-MOF-102** with dimensions 0.24×0.15×0.15 mm was loaded into a glass capillary tube (Hampton research, glass 50) along with mother liquor. X-ray diffraction data were collected on a Bruker X8 Prospector Ultra equipped with an Apex II CCD detector and an IμS micro-focus CuK\α X-ray source (λ = 1.54178 nm) at room temperature.

A body-centered cubic unit cell with a = b = c = 75.2379 (13) was derived from the least-square refinement of 9722 reflections in the range of $2.697 < \theta < 21.132$. Centrosymmetric space group Ia-3d was chosen based on systematic absences.

After integration of the data by Bruker program SAINT, empirical absorption correction was applied using SADABS. The structure was solved by direct methods using SHELXTL[124] which located all the Zn atoms. However, due to the weak diffraction, only part of the carbon and nitrogen atoms on adenine and carboxylate were found. Materials Studio (v5.0) was used to construct a model of **bio-MOF-102** with possible locations of adenine and ABDC. Adenine was constrained as a rigid model adapted from the Cambridge structural database while distance restraints were applied to the phenyl rings in ABDC. Due to the fact that diffraction was extremely weak, only zinc atoms and a bridging oxygen atom were refined anisotropically. Finally, R-factors were converged to wR2 = 0.5803 and R1 = 0.2380.

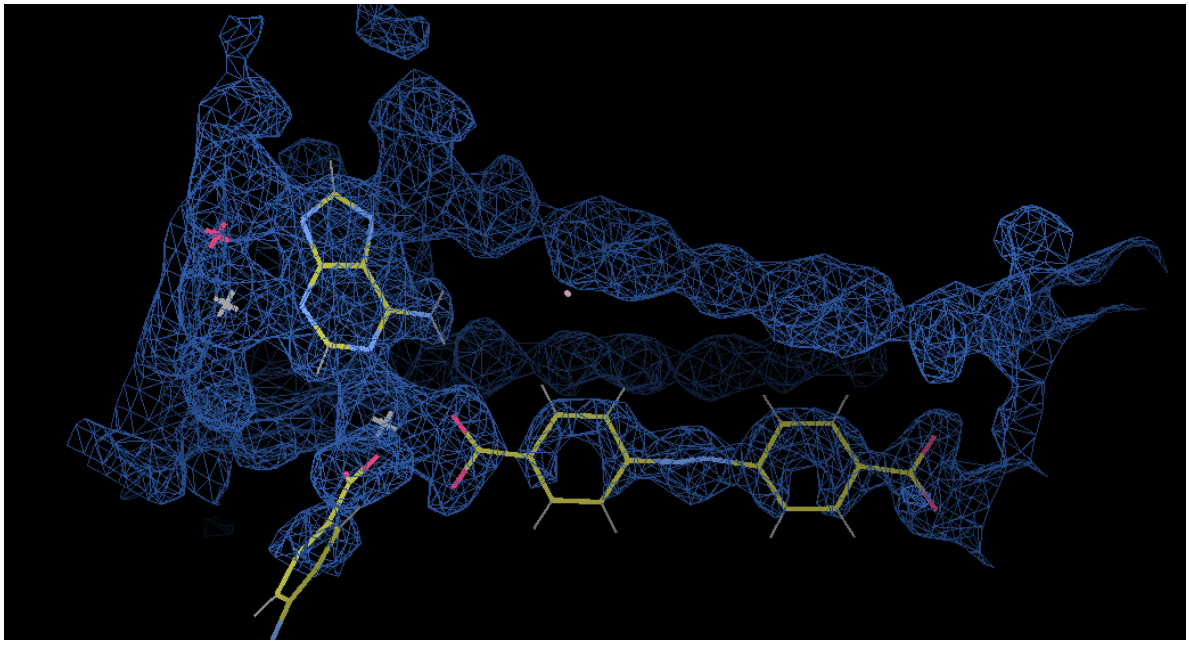

Figure 66. Electron density map of a fragment of **bio-MOF-102** at 0.7 e/Å^3. The figure was produced with Coot 0.6.2.[127]

4.4.3.3 Unit cell determination of bio-MOF-100 and bio-MOF-103

A single crystal of **bio-MOF-100** and **bio-MOF-103** were mounted onto MiTeGen micromount with fluorolube. X-ray diffraction data were collected on a Bruker X8 Prospector Ultra equipped with an Apex II CCD detector and an IμS micro-focus CuK\α X-ray source (λ = 1.54178 nm) at room temperature. A total of 90 frames of data were collected for unit cell analysis. After spots harvesting, 6227 and 372 reflections were obtained for **bio-MOF-100** and **bio-MOF-103** respectively. Body-centered cubic unit cells with dimensions of 68.903(11) Å (**bio-MOF-100**) and 82.25(12) Å (**bio-MOF-103**) were derived from the least-square refinement. Due to the extremely weak diffraction of **bio-MOF-103**, we did not proceed with complete data collection.

4.4.3.4 Bio-MOF-103 model

The crystal structure model of **bio-MOF-103** was constructed based on Ia-3d space group with unit cell parameter of 82.25 Å. Due to the fact that the Zn-adeninate building block is rigid, ideal positions of each of its atoms were calculated using the method described above. NH_2TPDC ligands were then constructed in Materials Studio 5.0. All the fractional coordinates and occupancy values are listed in the following table.

Table 7. Fractional coordinates and occupancy of atoms in **bio-MOF-103** model.

Atom name	Fractional coordinates x	y	z	0ccupancy
ZN1	0.44706	0.22806	0.12436	1
ZN2	0.4913	0.23298	0.17937	1
C3	0.46065	0.26109	0.1359	1
C4	0.47961	0.26072	0.15768	1
C5	0.48843	0.28456	0.15501	1
C6	0.46588	0.23784	0.15243	1
C7	0.47168	0.26884	0.14386	1
N8	0.47681	0.24517	0.16266	1
N9	0.45206	0.26783	0.12369	1
N10	0.45791	0.24396	0.14004	1
N11	0.49013	0.27125	0.16427	1
N12	0.47759	0.28485	0.14268	1
C13	0.48889	0.38478	0.67304	1
C14	0.47672	0.3831	0.68458	1
C15	0.46986	0.3966	0.69231	1
C16	0.47558	0.41202	0.68837	1
C17	0.48779	0.41386	0.67681	1
C18	0.49457	0.40052	0.66916	1
C19	0.51705	0.33236	0.64089	1
O20	0.50729	0.3207	0.63663	1
O21	0.53234	0.3331	0.63707	1
C22	0.51017	0.3457	0.64927	1
C23	0.49404	0.34419	0.65442	1
C24	0.48699	0.35753	0.66231	1
C25	0.49647	0.37112	0.666	1
C26	0.51272	0.3726	0.66135	1
C27	0.51934	0.35953	0.65287	1
C28	0.44978	0.46389	0.72228	1
O29	0.43547	0.46184	0.72847	1
O30	0.45899	0.47653	0.72393	1
C31	0.45634	0.45043	0.71383	1
C32	0.44645	0.43693	0.71095	1
C33	0.45287	0.42404	0.70203	1
C34	0.46883	0.42551	0.69653	1
C35	0.47896	0.4386	0.70003	1
C36	0.47248	0.45172	0.70857	1
C37	0.39854	0.37875	0.67235	1
C38	0.40673	0.39102	0.66408	1
C39	0.41845	0.38713	0.65251	1
C40	0.39151	0.45423	0.68076	1
O41	0.37984	0.45602	0.69114	1
O42	0.40022	0.46566	0.67437	1

C43	0.39582	0.43802	0.67698	1
C44	0.38614	0.42537	0.68285	1
C45	0.39015	0.4095	0.67847	1
C46	0.40363	0.40731	0.66844	1
C47	0.41374	0.41983	0.6632	1
C48	0.40956	0.43575	0.66717	1
N49	0.42307	0.32122	0.74317	1
H50	0.43703	0.37729	0.72314	1
H51	0.44992	0.35493	0.71175	1
H52	0.41369	0.36818	0.76876	1
H53	0.40209	0.41502	0.738	1
H54	0.39979	0.38946	0.78013	1
H55	0.41543	0.39338	0.72622	1
H56	0.45	0.33488	0.69617	1
H57	0.46069	0.28928	0.72903	1
H58	0.46447	0.31393	0.68571	1
H59	0.4465	0.31056	0.7397	1
H60	0.50221	0.40161	0.66088	1
H61	0.43025	0.3687	0.64065	1
H62	0.40672	0.33162	0.67281	1
H63	0.43934	0.32316	0.62707	1
H64	0.41336	0.30596	0.66611	1
H65	0.43225	0.34884	0.63362	1
N66	0.42671	0.39886	0.64463	0.5
H67	0.34291	0.5056	0.79403	1
H68	0.34442	0.53601	0.72707	1
H69	0.37923	0.54572	0.77888	1
H70	0.38218	0.55587	0.76158	1
H71	0.4896	0.43902	0.67743	1
H72	0.50153	0.43136	0.66533	1
H73	0.39632	0.33976	0.67501	1
H74	0.38652	0.35317	0.68482	1
O75	0.5	0.25	0.1929	0.5

4.4.4 Crystal structures of bio-MOF-101, bio-MOF-100, bio-MOF-102, and bio-MOF-103

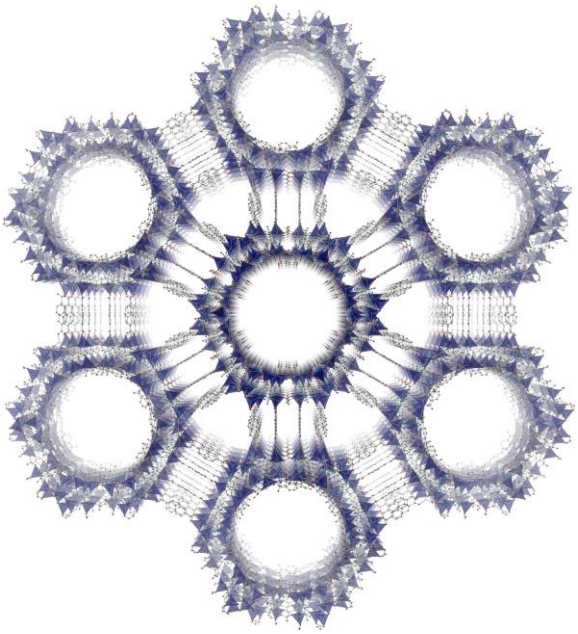

Figure 67. Perspective view of the (111) facet of the crystal structure of **bio-MOF-101**.

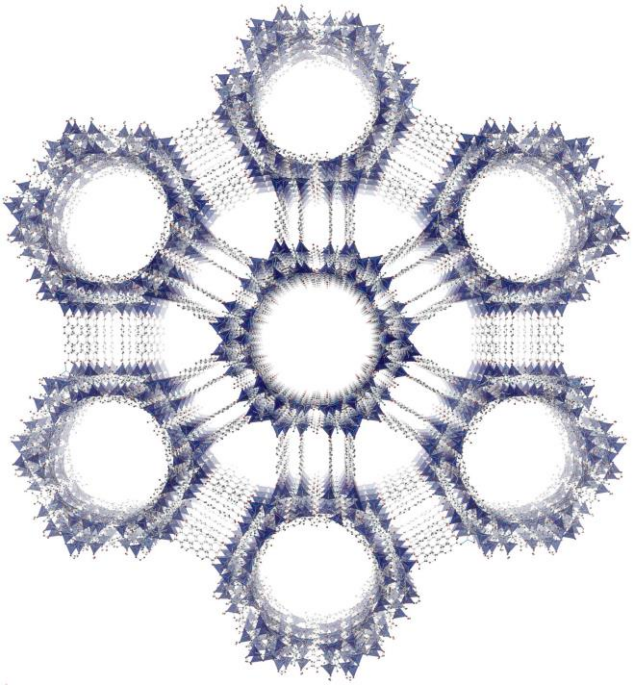

Figure 68. Perspective view of the (111) facet of the crystal structure of **bio-MOF-100**.

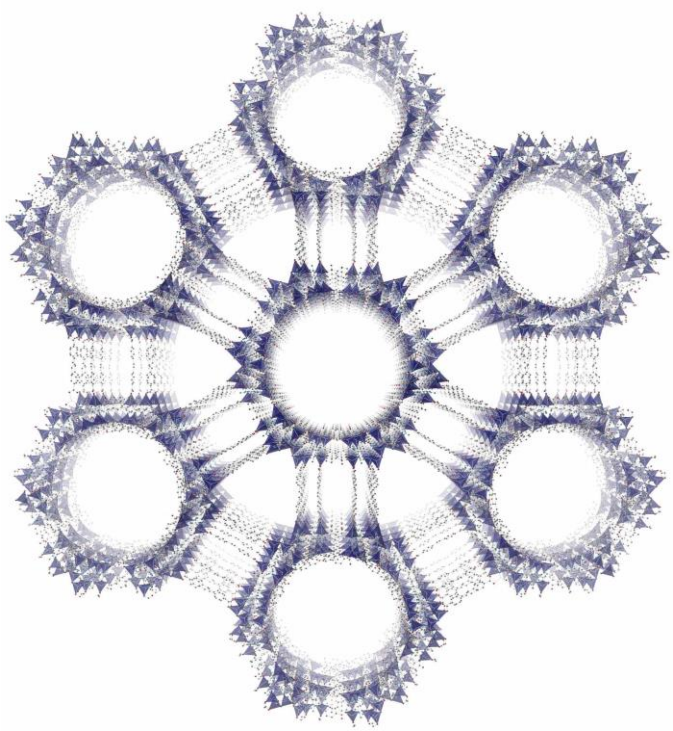

Figure 69. Perspective view of the (111) facet of the crystal structure of **bio-MOF-102**.

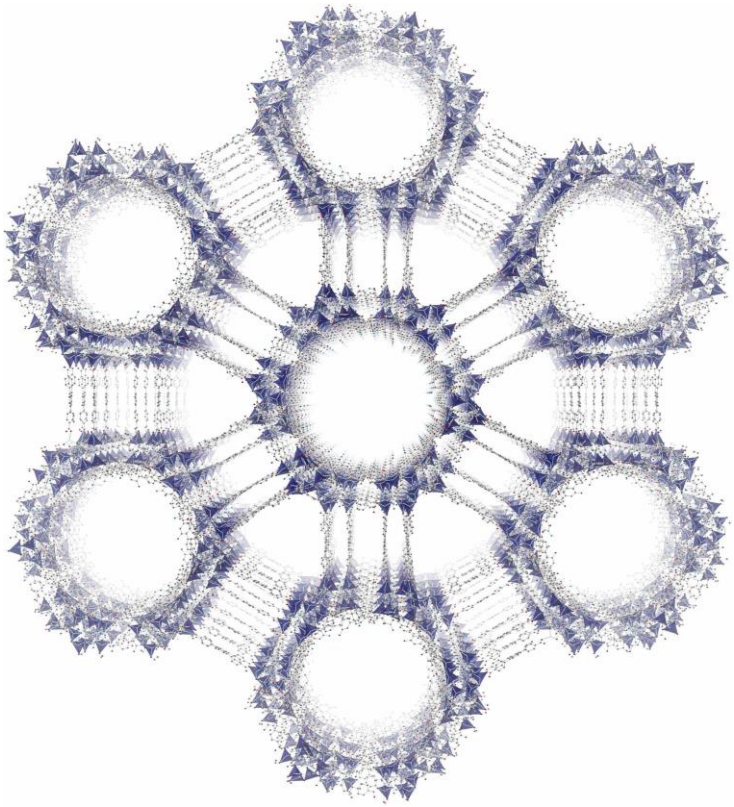

Figure 70. Perspective view of the (111) facet of the crystal structure model of **bio-MOF-103**.

4.4.5 Brunauer-Emmett-Teller (BET) Surface area, pore volume, and pore size distribution calculations

Pore size distribution for **bio-MOF-101**, **bio-MOF-100**, **bio-MOF-102**, and **bio-MOF-103** were calculated using Quantachrome software. Selection of adsorption points for BET surface area calculation was guided by criteria described by Snurr.[9,128]

Pore volume values were calculated using the amount of N_2 adsorbed at P/P_o=0.995. Pore size distributions were calculated with a quenched solid state functional theory (QSDFT) slit-cylinder pore geometry on carbon kernel using AS1-Win version 2.0 software Quantachrome).

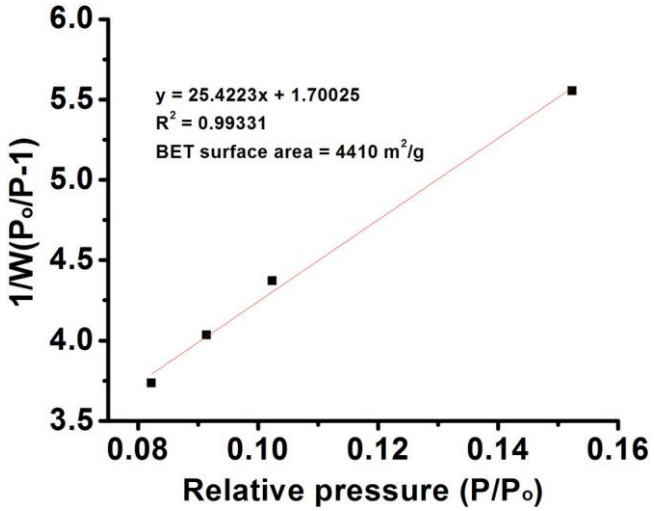

Figure 71. Plot of linear region for **bio-MOF-101** BET surface area calculation.

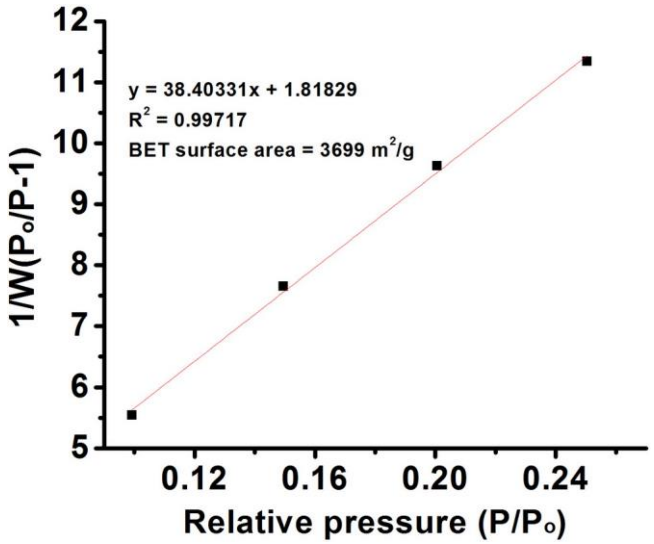

Figure 72. Plot of linear region for **bio-MOF-100** BET surface area calculation.

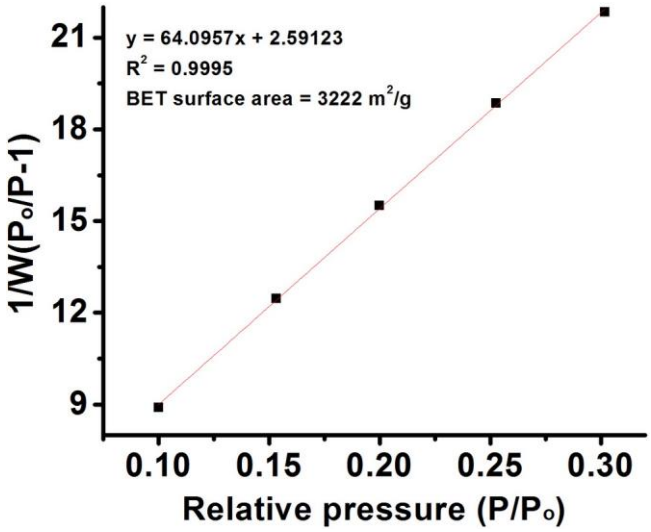

Figure 73. Plot of linear region for **bio-MOF-102** BET surface area calculation.

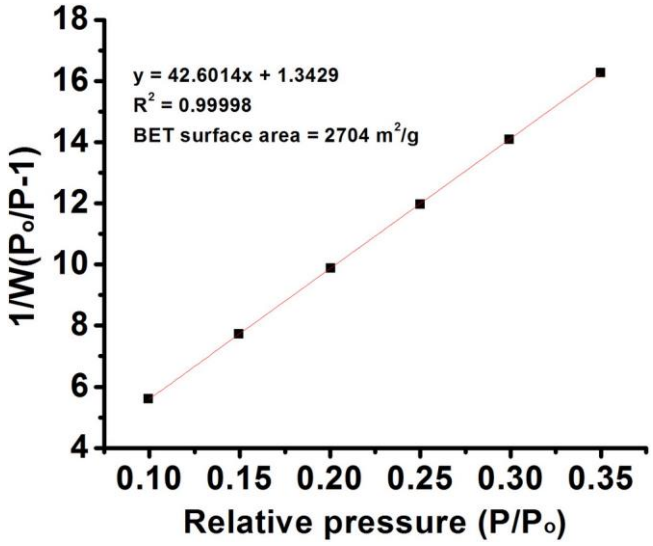

Figure 74. Plot of linear region for **bio-MOF-103** BET surface area calculation.

5.0 DESIGN OF A SERIES OF BIO-MOF-100 STRUCTURAL ANALOGUES FOR AU NANOCLUSTER SEPARATION

5.1 INTRODUCTION

Despite the great potential of highly tunable MOFs for a variety of separations, the separation of large species such as nanoparticles, proteins, and quantum dots using MOFs has not been extensively explored.[16] This is mainly because it is challenging to synthesize a MOF that meets all of the criteria required for a successful separation, among these being 1) a continuous mesoporous channel (a MOF without micropores that gate entry into the mesopores); 2) 3-dimensional interconnected channels that allow for more efficient and rapid diffusion of species; and 3) a strong driving force to help the diffusion process. Of the reported mesoporous MOFs, only a few of them meet even the first criterion.[11,12,26]

Size-selective separation of nanoparticles is an important challenge. Consider thiolated gold nanoclusters as an example. These nanoparticle species having only a few hundred gold atoms exhibit distinct molecular features.[129,130,131,132,133,134,135,136] In contrast to larger plasmonic nanoparticles, it is extremely challenging to synthesize monodispersed gold nanoclusters of well-defined size.[137] Traditional synthetic methods often times lead to a polydisperse mixture of clusters with various sizes.[138,139] Each specific cluster size will exhibit slightly different optical and potentially catalytic properties. The size-focusing method developed by Jin's group usually

produces highly monodisperse clusters.[137] However, the polydispersity and yield of the products are highly dependent on various reaction conditions.

A variety of separation methods have thus been employed. These include fractionated precipitation,[139,140] size exclusive column chromatography (SEC),[141] HPLC,[142] and gel electrophoresis.[143] Although these methods help isolation cluster samples with narrower size distribution, they have obvious limitations as well. For example, fractionated precipitation can only yield rough fractions; HPLC has limited analytical quantities; gel electrophoresis is restricted to a water environment; and SEC is limited by the availability of the equipment and separation capacity, etc.[144]

In this communication, we demonstrate a proof-of-concept study of the separation of thiolate-protected gold nanoclusters using MOFs. More specifically, we selected $Au_{25}(SR)_{18}^-$ (**Au25**$^-$), $Au_{38}(SR)_{24}$ (**Au38**), and $Au_{144}(SR)_{60}$ (**Au144**)(SR=C_8H_9S, 2-phenylethanethiol) as a target separation mixture based on the following reasoning: 1) Their properties have been widely studied over the past decade; 2) They have either well defined crystal structures (**Au25**$^-$[135] and **Au38**[134]) or proposed structure (**Au144**[133]) which allow us to measure or estimate their exact sizes; 3) They can be easily prepared in pure phase.

5.2 RESULTS AND DISCUSSION

5.2.1 Choosing MOF candidates

For a successful separation, a good MOF candidate must first be identified according to the criteria described above. Previously, An *et al* discovered an exceptionally porous MOF

named **bio-MOF-100** (Figure 75A).[11] The inherent octahedral-shaped Zn-adeninate secondary building units (SBUs) are linked by 4, 4'-biphenyldicarboxylic acid (BPDC) via four triangular facets into a cubic ***lcs*** network topology.[105] Exclusively mesoporous channels with 2.5 nm inner diameter are interconnected and run along diagonals of the cube. The formula of the framework of **bio-MOF-100**, $Zn_8(OH)_2(adenine)_4(BPDC)_6^{2-}$, reveals its negatively charged nature which suggests that electrostatics could be used as a potential driving force to promote nanoparticle separation.[11] Its pore uniformity and accessibility together with its anionic nature make **bio-MOF-100** an ideal candidate for nanoparticle separation.

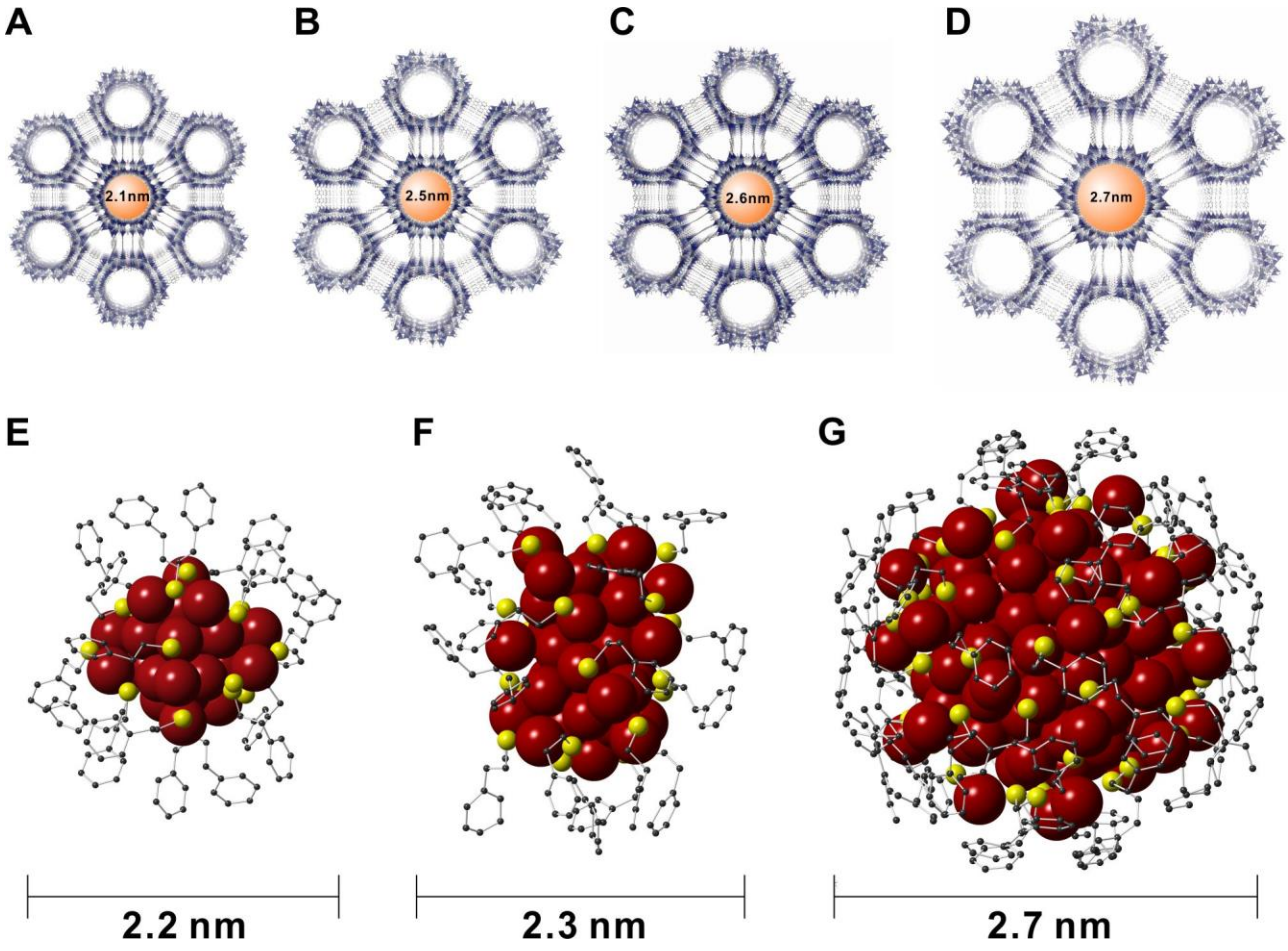

Figure 75. Crystal structures of **bio-MOF-101** (A), **bio-MOF-100** (B), **bio-MOF-104** (C), **bio-MOF-105** (D), **Au25**$^{-}$ (E), **Au38** (F), and predicted structural model of **Au144** (G).

Second, in order to separate nanoparticles having a variety of diameters, a series of isoreticular MOFs having pore diameters similar to the particle diameters are required. A recent work has shown that the pore size of **bio-MOF-100** can be tailored not only by direct synthesis using new ligands, but also by stepwise ligand exchange strategy.[10] Spherically-shaped **Au25**$^{-}$, as shown in the crystal structure (Figure 75E), has a diameter of ~2.2 nm while cylindrically-shaped **Au38** has dimensions of ~2.3 × 2.3 × 2.9 nm. Although the structure of **Au144** has not yet been crystallographically resolved, its size is estimated to be ~ 2.7 nm based on a predicted structural model.[133] Given the size range of gold nanoclusters (2.2 to 2.7 nm), we selected two members of **bio-MOF-100** structural analogues, **bio-MOF-100** (2.5 nm pore diameter) and **bio-MOF-101** (2.1 nm pore diameter).[10] Meanwhile, two new members of **bio-MOF-100** structural analogues, **bio-MOF-104** (ligand: 1,4-phenyldiacrylic acid (PDAC)) and **bio-MOF-105** (4,4'-stilbenedicarboxylic acid (SBDC)) were also obtained via solvothermal synthesis.

5.2.2 Structural Characterization of bio-MOF-104 and bio-MOF-105

Single crystal X-ray diffraction studies show that both **bio-MOF-104** and **bio-MOF-105** share the same underlying topology (Figure 75C and D). By increasing the linker lengths, their unit cell parameters grow correspondingly from 62.04 Å (**bio-MOF-101**) to 69.12 (**bio-MOF-100**), 69.61 (**bio-MOF-104**) and to 76.62 Å (**bio-MOF-105**) (Table 8). The measured channel diameters range from 2.1 nm to 2.7 nm (Fugire 75) which is comparable to the diameter range of the chosen Au clusters. Platon[125] calculation reveals their void spaces range from 80.2% for the least porous analogue (**bio-MOF-101**) to 87.7% for the most porous one (**bio-MOF-105**).

Table 8. Unit cell parameters and calculated void spaces.

	a = b = c =	α = β = γ =	Calculated voids (%)
Bio-MOF-101	62.04 Å	90 °	80.2
Bio-MOF-100	69.12 Å	90 °	84.8
Bio-MOF-104	69.61 Å	90 °	85.7
Bio-MOF-105	76.62 Å	90 °	87.7

Powder X-ray diffraction patterns of **bio-MOF-101** to **105** resemble each other in terms of relative peak positions and intensity. The peak positions are shifted, following the same trend as the unit cell parameters and therefore indicating their isostructural nature (Figure 76).

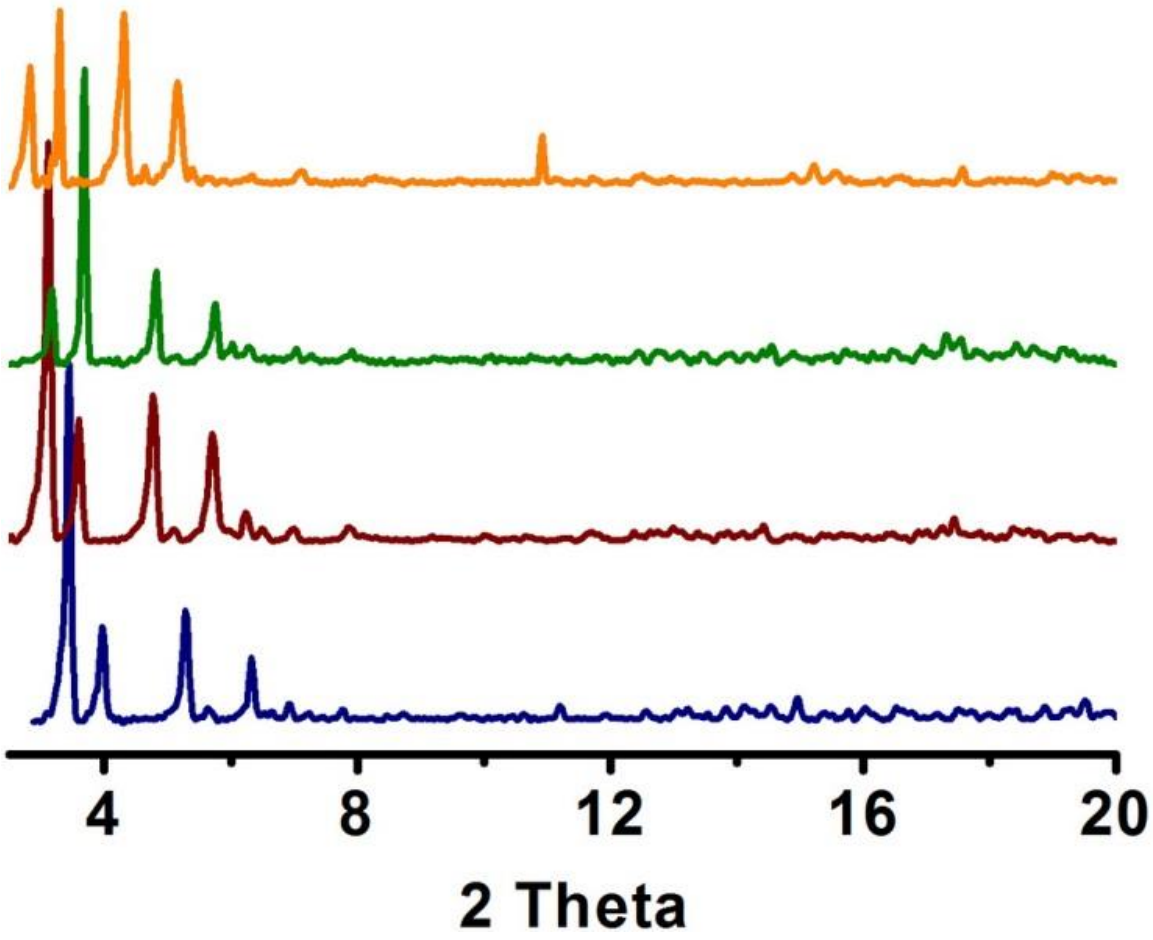

Figure 76. PXRD patterns of **bio-MOF-101** (navy), **bio-MOF-100** (dark red), **bio-MOF-104** (green), and **bio-MOF-105** (orange).

5.2.3 Porosity Characterization

The porosities of **bio-MOF-101**, **100**, **104**, and **105** were initially investigated by thermogravimetric analysis (TGA) (Figure 77). After gradually heating this series of materials to 600 ^{o}C under N_2 flow, all four samples exhibited large weight loss below 200 ^{o}C corresponding to the evaporation of solvent. From the most to the less porous, **bio-MOF-105** exhibits a solvent

weight loss of 69.0% at 200 ^{o}C followed by **bio-MOF-104** (68.9%), **bio-MOF-100** (64.6%) and **bio-MOF-101** (58.5%) at the same temperature (Figure 77).

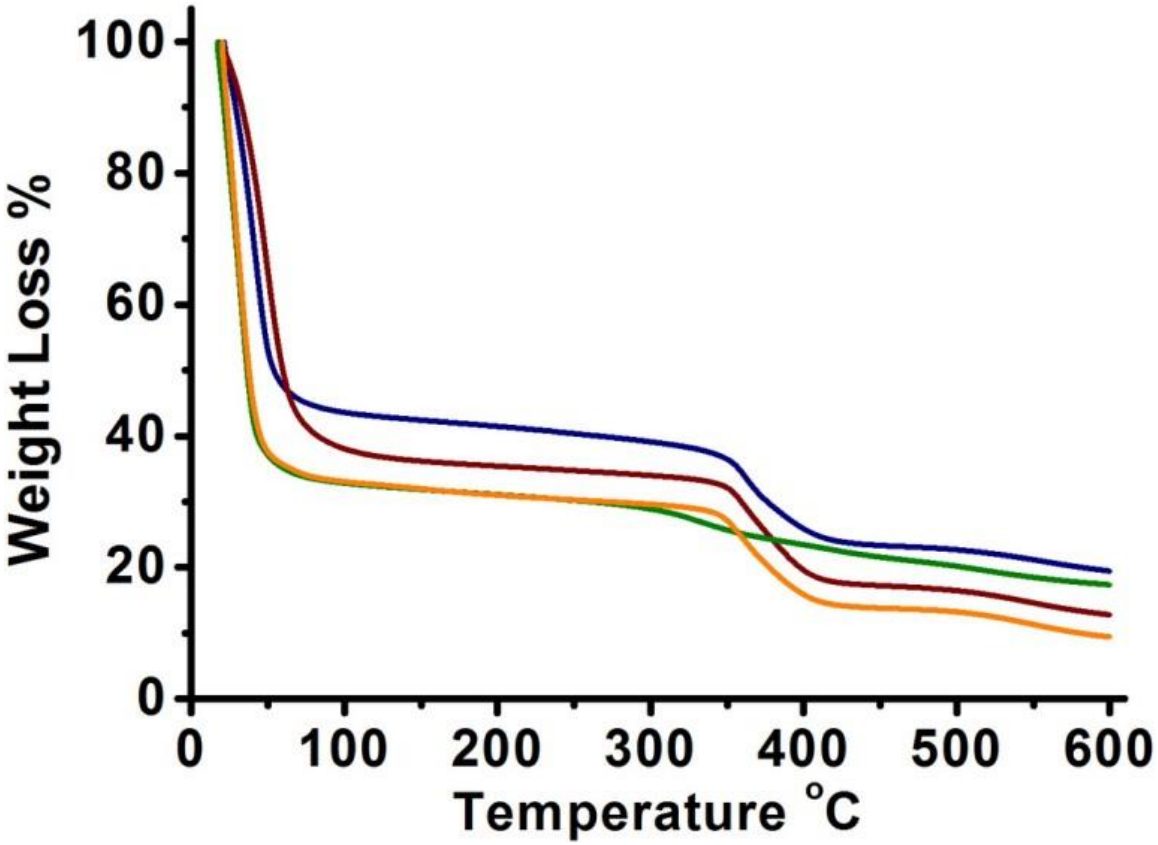

Figure 77. TGA of **bio-MOF-101** (navy), **bio-MOF-100** (dark red), **bio-MOF-104** (green), and **bio-MOF-105** (orange).

Next, we investigated their porosity by N_2 adsorption isotherms. After solvent exchange by ethanol, **bio-MOF-101** to **105** were activated via supercritical CO_2 using an established method.[121] The resulting N_2 isotherms, however, did not follow the same trend as the TGA data. **Bio-MOF-104** and **bio-MOF-105** adsorb much less N_2 than **bio-MOF-100** and **101** (Figure 78). At this stage we cannot fully explain this observation, but we propose that the presence of the C-C double bond may increase the flexibility of the frameworks which could cause structure collapse and thus decreased adsorption capacity. Pore size distributions calculated by QSDFT show that **bio-MOF-101** and **100** have pore sized of 2.0 and 2.5 nm which correspond well with their crystal structures (Figure 79). **Bio-MOF-105**, however, exhibits a larger pore (2.9 nm) and a smaller pore (1.7 nm) which is likely due to partial collapse of the framework upon activation (Figure 79). **Bio-MOF-104**, on the other hand, exhibits similar pore size (~2.4 nm) compared to **bio-MOF-100** (Figure 79).

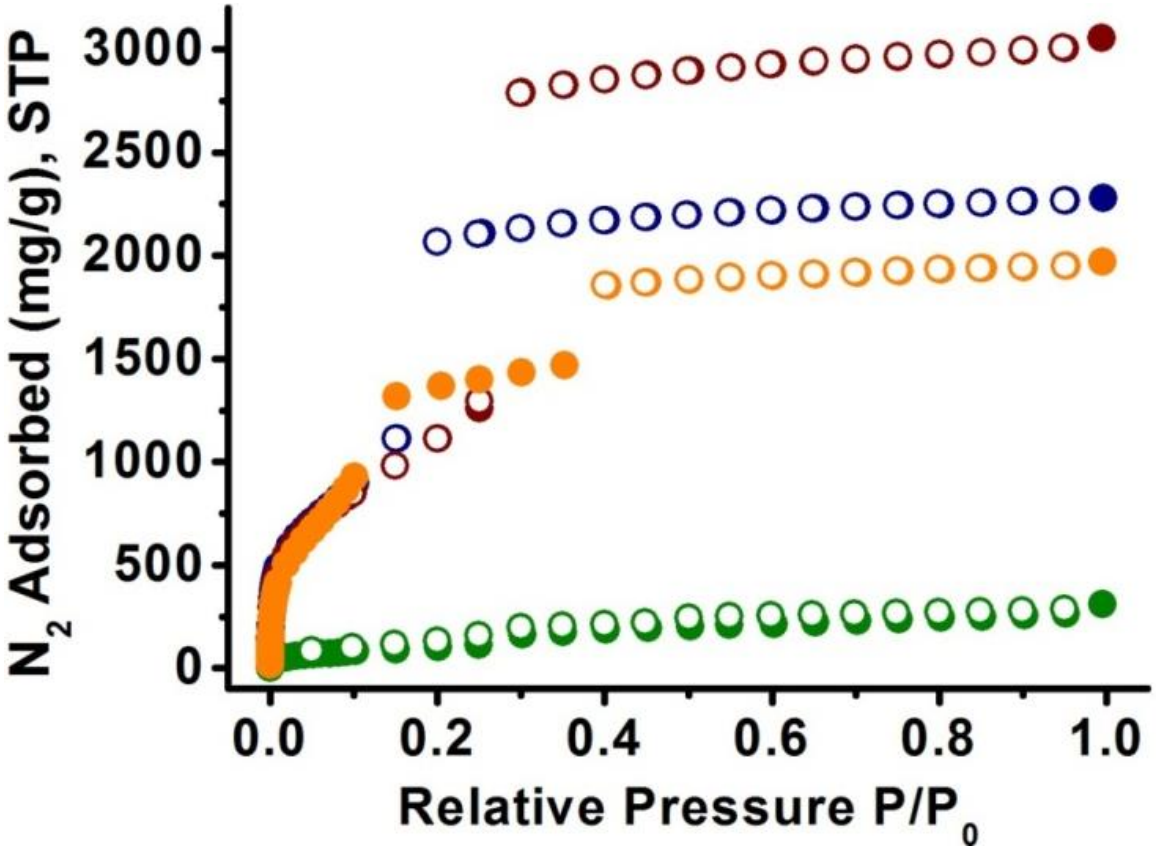

Figure 78. N_2 adsorption isotherms of **bio-MOF-101** (navy), **bio-MOF-100** (dark red), **bio-MOF-104** (green), and **bio-MOF-105** (orange) at 77 K.

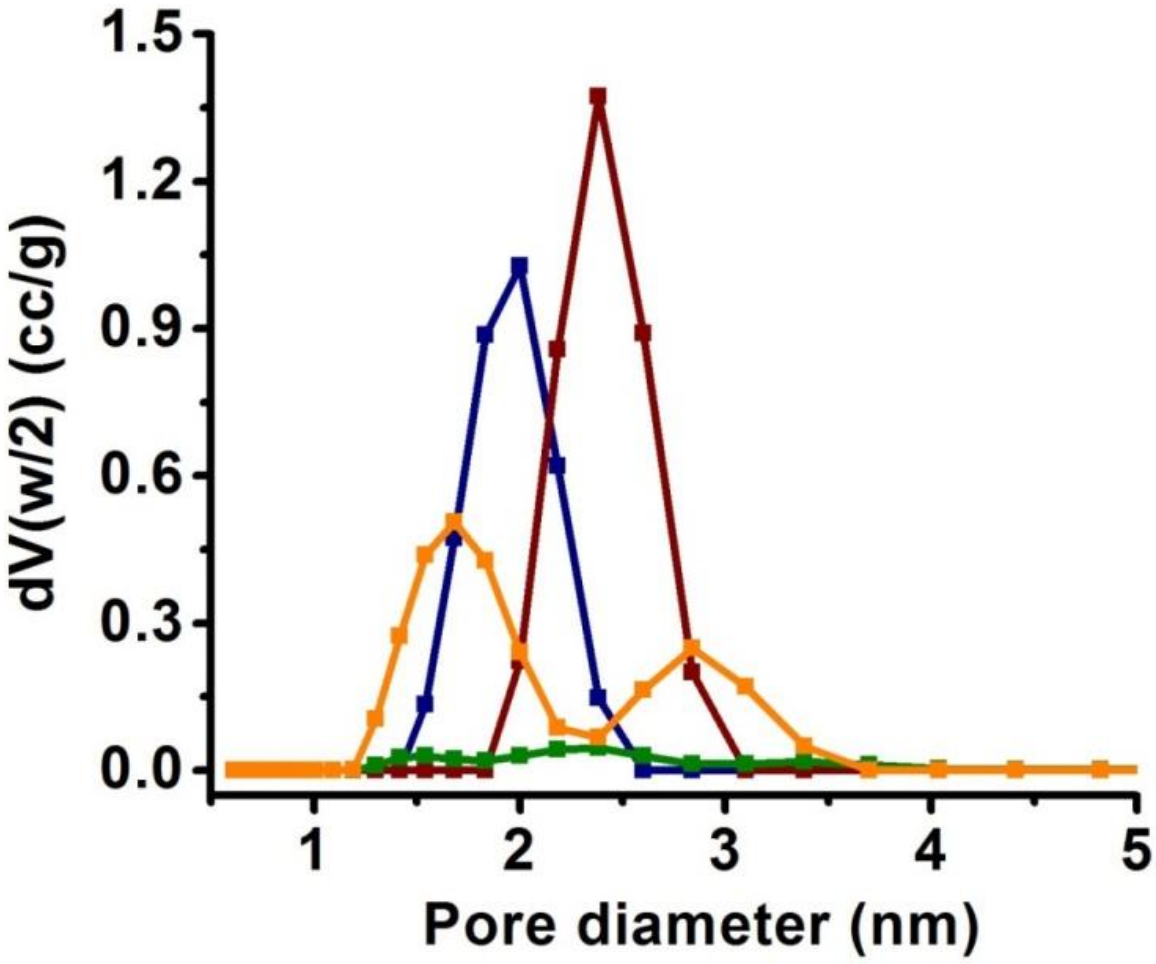

Figure 79. Pore size distributions of **bio-MOF-101** (navy), **bio-MOF-100** (dark red), **bio-MOF-104** (green), and **bio-MOF-105** (orange) calculated by QSDFT method.

5.2.4 Encapsulation of thiolated Au clusters

With this series of bio-MOFs designed, synthesized, and characterized, we were keen to explore their separation performance. **Au25**$^{-}$, **Au38**, and **Au144** were synthesized based on previously reported procedures.[135,145,146] 2 mL of each Au cluster solution in dichloromethane (0.4 mg/mL for **Au25**$^{-}$, 0.4 mg/mL for **Au38** and 0.2 mg/ml for **Au144**) was prepared in separate

glass vials (Figure 80A, B, and C). To each vial was added ~10 mg of each MOF. After soaking for 7 days, all four vials containing **Au25**$^{-}$ solution underwent significant decolorization (Figure 80D). Meanwhile, the corresponding bio-MOFs turned dark brown suggesting that **Au25**$^{-}$ was successfully encapsulated by these bio-MOFs. Significant color change, however, was not observed for all four vials of the **Au38** solutions (Figure 80E). In this case, only **bio-MOF-105** turned slightly brown. The rest of the bio-MOFs white in color (Figure 80Eiv). After soaking bio-MOFs in **Au144** solution for 7 days, only **bio-MOF-105** was able to significantly decolorize the solution. Meanwhile, **bio-MOF-105** crystals turned to dark brown (Figure 80Fiv). **Bio-MOF-101**, **100**, and **104**, however, do not show significant uptake of **Au144** (Figure 80Fi, ii, and iii). After soaking in these Au cluster solutions, all the bio-MOFs remain intact and crystalline as evidenced by PXRD patterns (Figure 81).

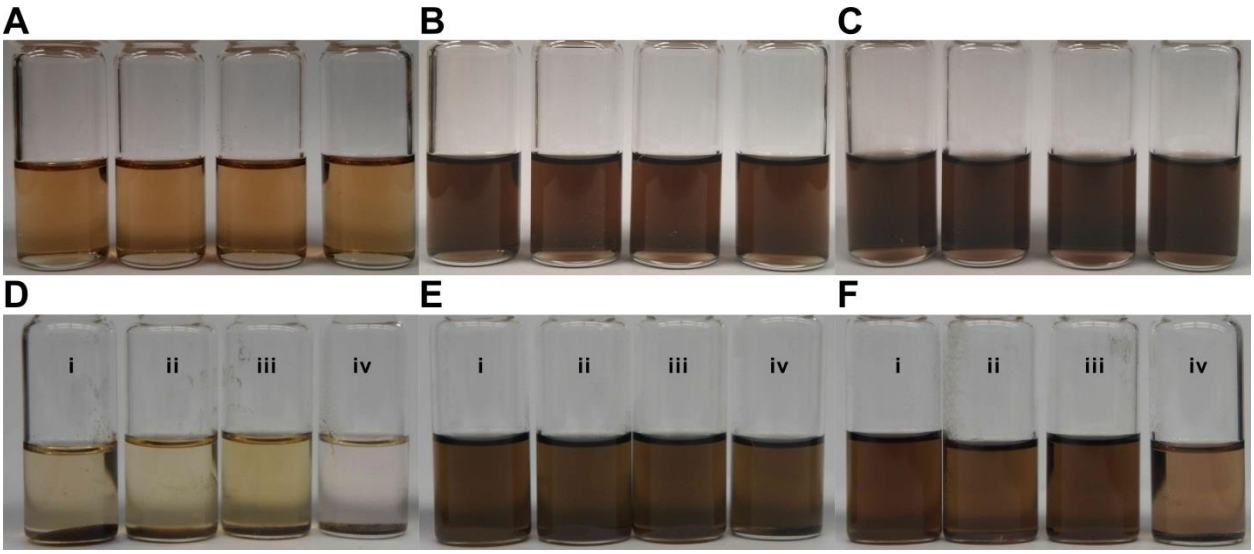

Figure 80. (A) 0.4 mg/ml **Au25**$^{-}$ in DCM; (B) 0.4 mg/ml **Au38** in DCM; (C) 0.2 mg/ml **Au144** in DCM. **Bio-MOF-101**(i), **102**(ii), **104**(iii), and **105**(iv) were soaked in **Au25**$^{-}$ (D), **Au38**, and **Au144** (F) solutions for 7 days.

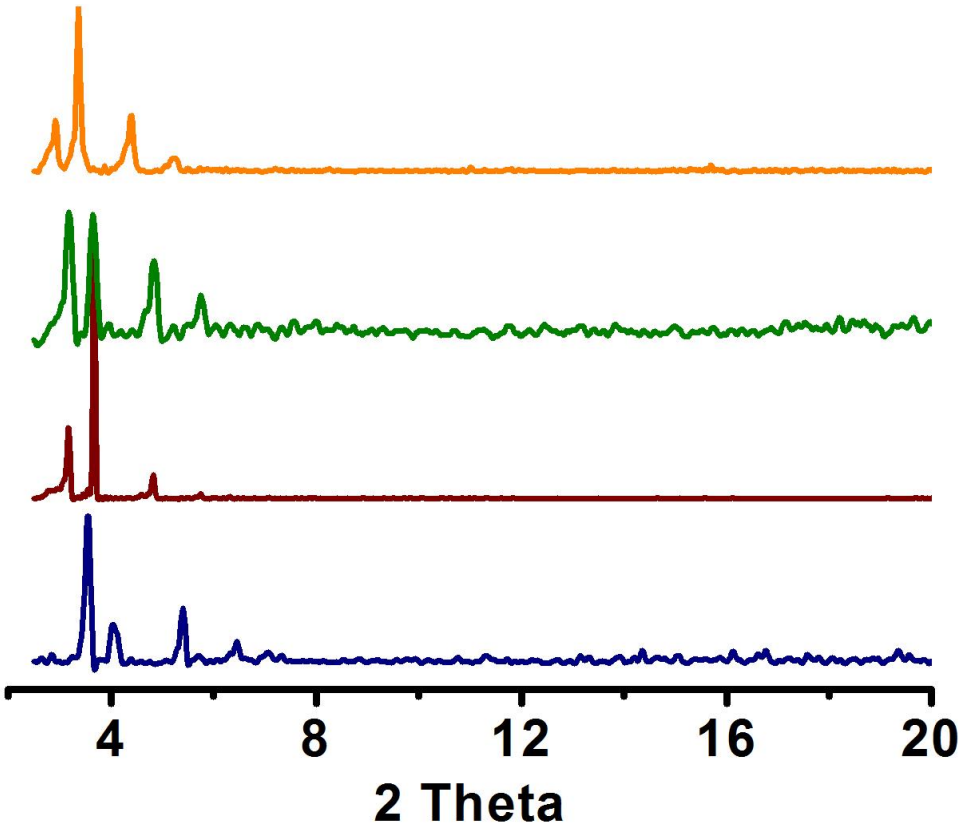

Figure 81. PXRD patterns of **bio-MOF-101** (navy), **bio-MOF-100** (dark red), **bio-MOF-104** (green), and **bio-MOF-105** (orange) after soaking in **Au25**$^{-}$ for 7 days.

These distinctive color changes of the solutions and of the bio-MOFs provide visual proof that the smallest cluster **Au25**$^{-}$ can be absorbed by the whole series of bio-MOFs while the largest cluster **Au144** can only be efficiently captured by the largest analogue **bio-MOF-105**. Surprisingly, **Au38**, having similar size as **Au25**$^{-}$, cannot be efficiently adsorbed by any of the MOFs. This led us to explore the mechanism of this nanoparticle adsorption process.

5.2.5 Mechanism Study

Since **Au25**$^{-}$, **Au38**, and **Au144** have the same surface capping molecule, they are expected to exhibit similar van der Waals interactions with the MOF frameworks. Therefore, we expect that van der Waals forces are not responsible for the discriminative adsorption between **Au25**$^{-}$ and **Au38**. This prompted us to investigate electrostatic interactions.

We first digested **Au25**$^{-}$**@bio-MOF-101** (**Au25**$^{-}$ encapsulated in **bio-MOF-101**) in a mixture of DCM and acetic acid (to decompose the framework). After the decomposition of the framework, **Au25**$^{-}$ was fully released into DCM leaving white MOF residual components (Figure 82). UV spectra of as-synthesized **Au25**$^{-}$ and **Au25**$^{-}$ released from the MOF were collected and compared. The UV spectrum of the released **Au25**$^{-}$ exhibits several major changes compared to the as-synthesized clusters, including a new peak at 360 nm, red-shifting of the 450 nm peak and blue shifting of the 685 nm peak (Figure 83). By comparison with literature, we found that the released cluster is actually $Au_{25}(SR)_{18}^{+}$ (**Au25**$^{+}$) as opposed to the negatively charged $Au_{25}(SR)_{18}^{-}$.[147] Clearly, **Au25**$^{-}$ was slowly oxidized to **Au25**$^{+}$ in air and was then captured by **bio-MOF-101** through a cation exchange process.

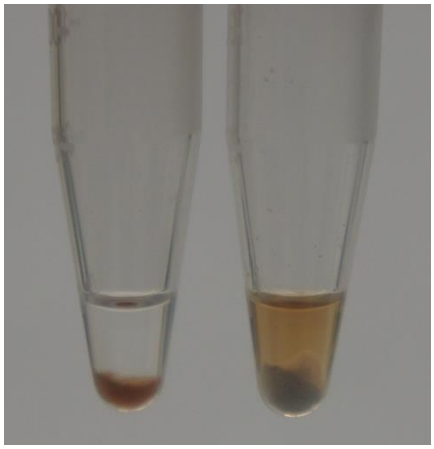

Figure 82. Au25@bio-MOF-101 in DCM (left). After the addition of acetic acid, **$Au25^{+}$** was released into DCM layer (right)

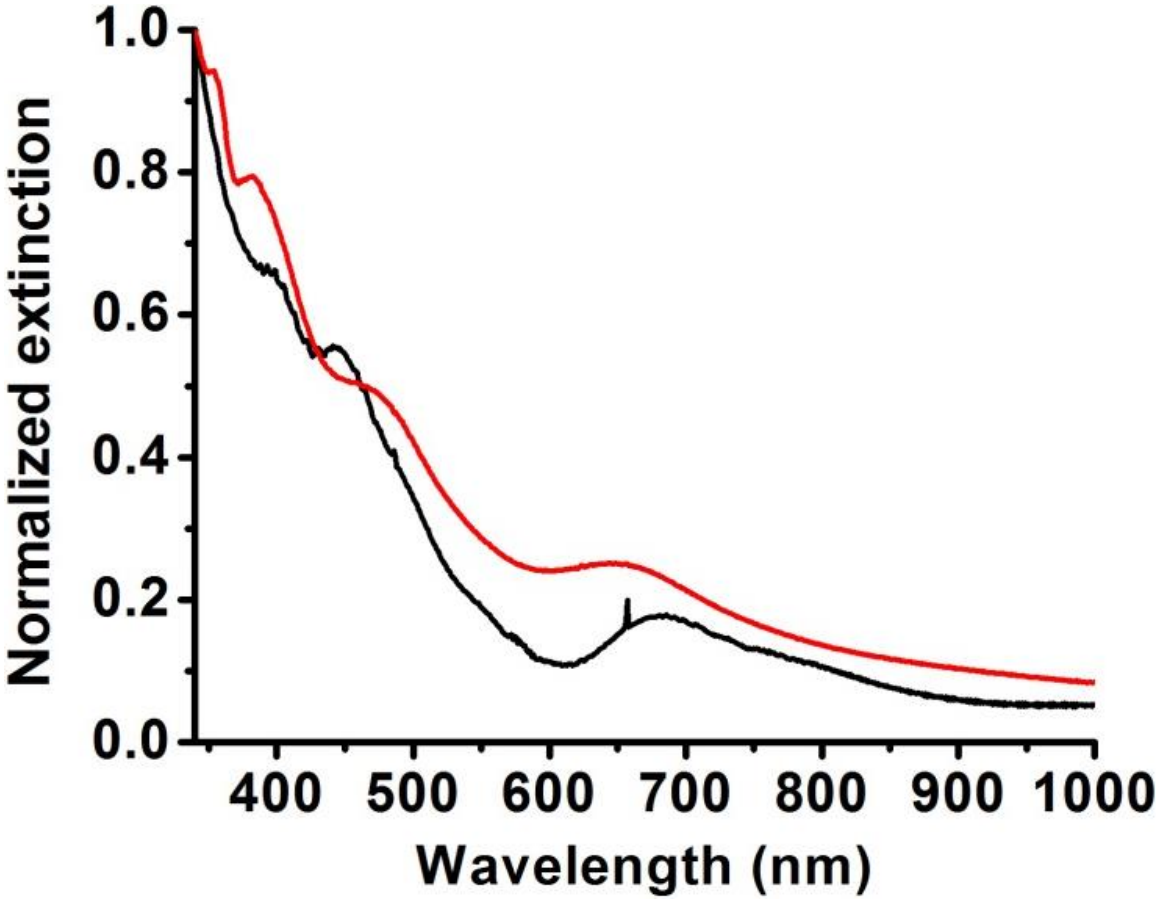

Figure 83. UV-vis spectra of as-synthesized **$Au25^{-}$** (black) and **Au25** released from **bio-MOF-101** (red).

To further verify this conclusion, we designed a control experiment to compare the encapsulation speed of **Au25** at different oxidation states and environments. We first oxidized **Au25**$^{-}$ to **Au25**$^{+}$ by hydrogen peroxide and monitored the whole process using UV-Vis spectroscopy. Then **bio-MOF-101** was soaked in three separate vials of solutions. Vial #1 contains 1ml of **Au25**$^{+}$/DCM solution (1mg/ml). Vial #2 contains 1ml **Au25**$^{-}$/DCM solution (1mg/ml) in air. And vial #3 contains 1ml of **Au25**$^{-}$/DCM solution (1mg/ml) under argon atmosphere. After 5 hours, **bio-MOF-101** crystals in vial #1 turned black. indicating a fast uptake process (Figure 84). Meanwhile, **bio-MOF-101** samples in vial #2 and 3 were still colorless. After 1 day, the solution in vial #1 underwent significant decolorization while solutions in vial #2 and 3 changed color from orange to brown indicating an oxidation process of **Au25**$^{-}$ to **Au25**$^{+}$. After 4 and 7 days, vial #1 was approaching colorless while MOF crystals in vial #2 just started tuning black. Under argon protection, MOF crystals did not turn to black even after 7 days soaking. By monitoring the UV absorbance at 450 nm, we found the same trend. This provides a semi-quantitative evidence that positive charge is the dominant force that drives **Au25** into the **bio-MOF-101** framework.

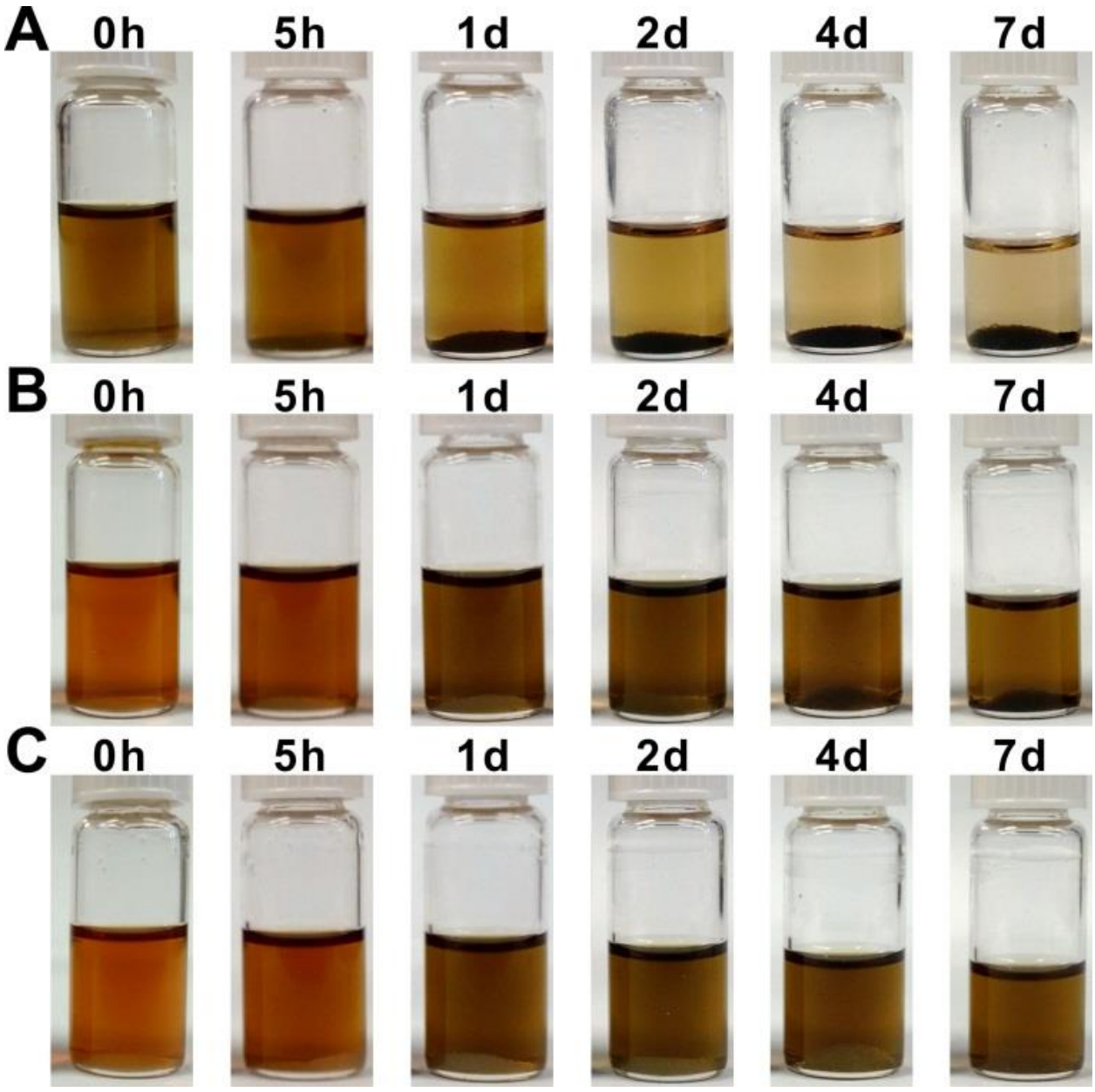

Figure 84. Color changes of **bio-MOF-101** soaked in **Au25**$^{+}$ (A), **Au25**$^{-}$ (B), and **Au25**$^{-}$ under argon atmosphere (C).

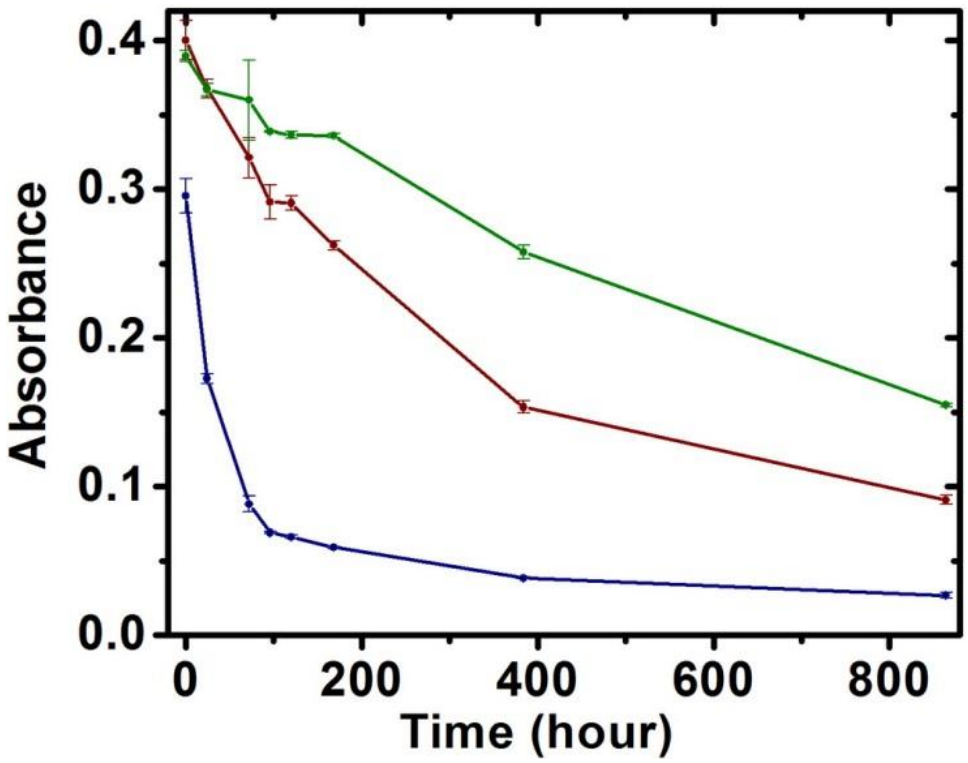

Figure 85. Dependence of UV intensity (450 nm) on time (**Bio-MOF-101** soaked in **Au25**$^{+}$ (blue), **Au25**$^{-}$ (dark red), and **Au25**$^{-}$ under argon atmosphere (green)). Error bars were derived from three measurements.

Au144, on the other hand, is generally considered charge neutral.[145] As-synthesized **Au144** can only be ionized by electrospray ionization (ESI) with the addition of cesium salt. As this stage, we do not fully understand the uptake mechanism. However, we did observe that after encapsulation in **bio-MOF-105**, **Au144** can be direct ionized by ESI without Cs^{+}. This may suggest that **Au144** has been oxidized to positively charged species before entering the MOF pore.

5.2.6 Separation of Cluster Mixture

Thus far, we understand that the encapsulation process of Au clusters by bio-MOFs is driven by electrostatic interactions. Due to the positive charges on **Au25** and **Au144** upon oxidation by air, they can be absorbed into bio-MOFs much faster compared to **Au38**. Meanwhile, the small pore size of **bio-MOF-101** can also selectively adsorb **Au25** over **Au144**. Inspired by these results, we performed a mixed component separation experiment.

An **Au25-38-144** mixture solution was first prepared by mixing **Au25**$^{-}$, **Au38**, and **Au144** in DCM (1 mg/ml for each cluster). Approximately 20 mg of **bio-MOF-101** were soaked in 1 ml of this mixture. The solution and digested MOF were monitored by Matrix-assisted laser desorption ionization time-of-flight (MALDI-TOF) mass spectra. After one day, the solution still contained all three Au clusters as revealed by Maldi spectra (Figure 86). The **Au25** peak decreased after four days soaking and eventually disappeared after 60 days (Figure 86). Digested **bio-MOF-101** only shows **Au25** signal, indicated that it excludes **Au38** and **Au144** throughout the separation process (Figure 87). Following the successful separation of **Au25** from the mixture, **Bio-MOF-105** was then added to the remaining **Au38-144** mixture. After one day soaking, both **Au38** and **Au144** still co-existed in the solution (Figure 88). However, only **Au38** was detected in the solution after 4 days (Figure 88). **Bio-MOF-105**, on the other hand, only absorbed **Au144** but not **Au38** (Figure 89). If **Bio-MOF-105** is directed soaked in **Au25-38-144** mixture, both **Au25** and **Au144** were observed in the MOF (Figure 90) after 4 days of soaking. Meanwhile, only **Au38** was left in the solution (Figure 90).

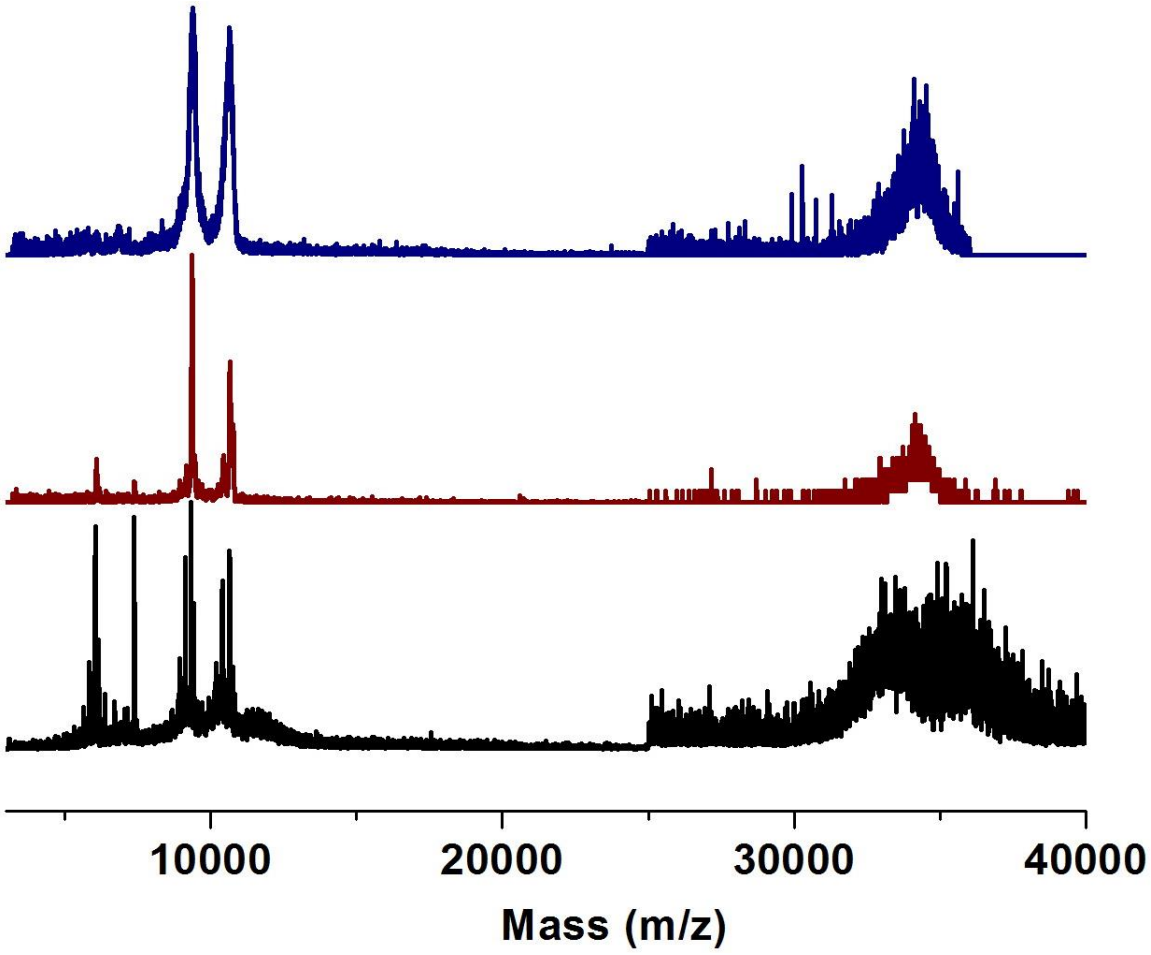

Figure 86. Maldi-TOF spectra of Au cluster **Au25-38-144** mixture after soaking by **bio-MOF-101** for 1 (black), 4 (dark red), and 60 (navy) days. Region above 25000 Da was magnified 10 times for easy visualization. Peak at ~7385 Da corresponds to $Au_{25}(SR)_{18}^{+}$ (calc. 7394 Da). Peaks within 5000-7300 Da correspond to $Au_{25}(SR)_{18}^{+}$ fragments. Peak at ~10762 Da corresponds to $Au_{38}(SR)_{24}^{+}$ (calc. 10778 Da). Peaks within 8500-10500 Da correspond to $Au_{38}(SR)_{24}^{+}$ fragments. The broad peak at ~35000 Da correspond to $Au_{144}(SR)_{60}^{+}$ and its fragments.

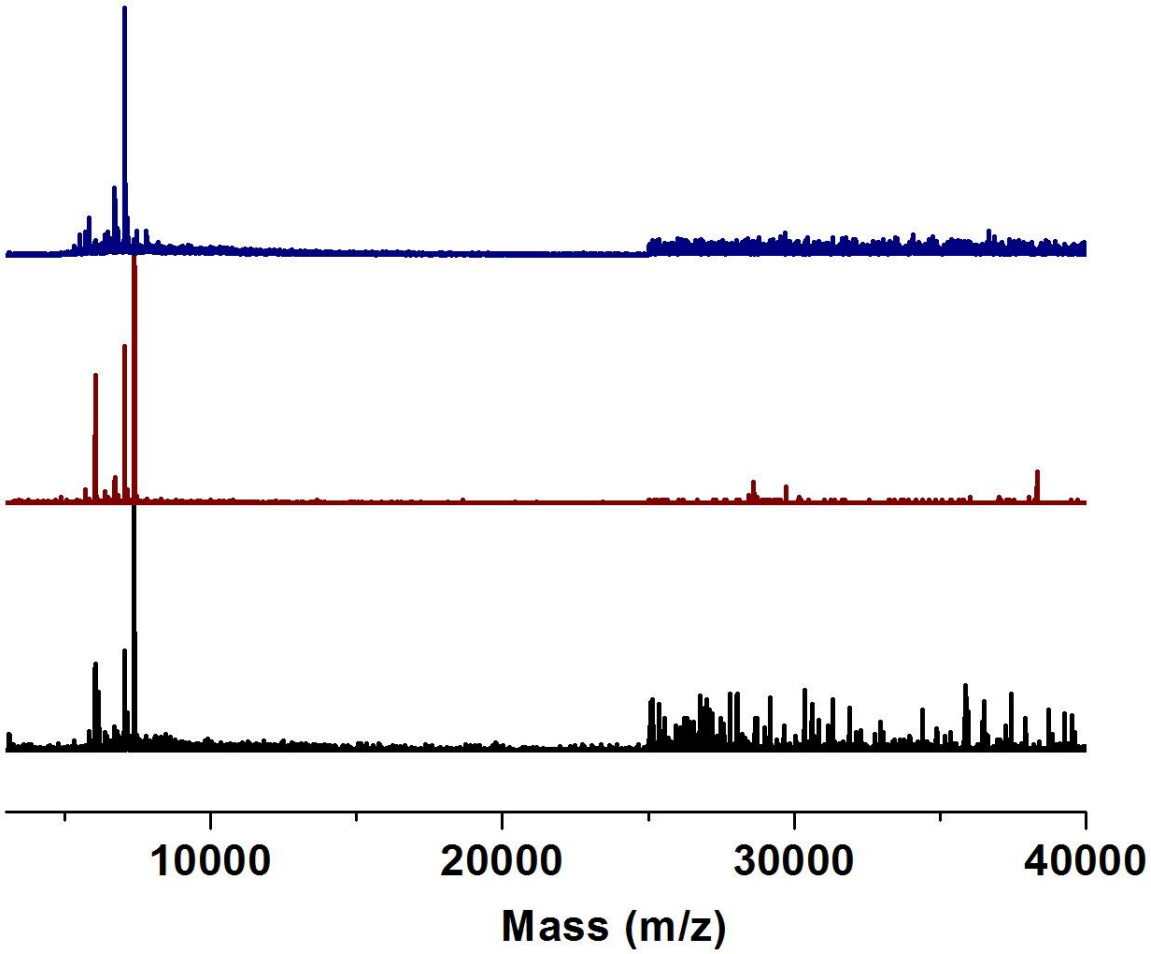

Figure 87. Maldi-TOF spectra of digested **bio-MOF-101** after soaking in **Au25-38-144** mixture for 1 (black), 4 (dark red), and 60 (navy) days. Region above 25000 Da was magnified 10 times for easy visualization. Peak at ~7385 Da corresponds to $Au_{25}(SR)_{18}^{+}$ (calc. 7394 Da). Peaks within 5000-7300 Da correspond to $Au_{25}(SR)_{18}^{+}$ fragments.

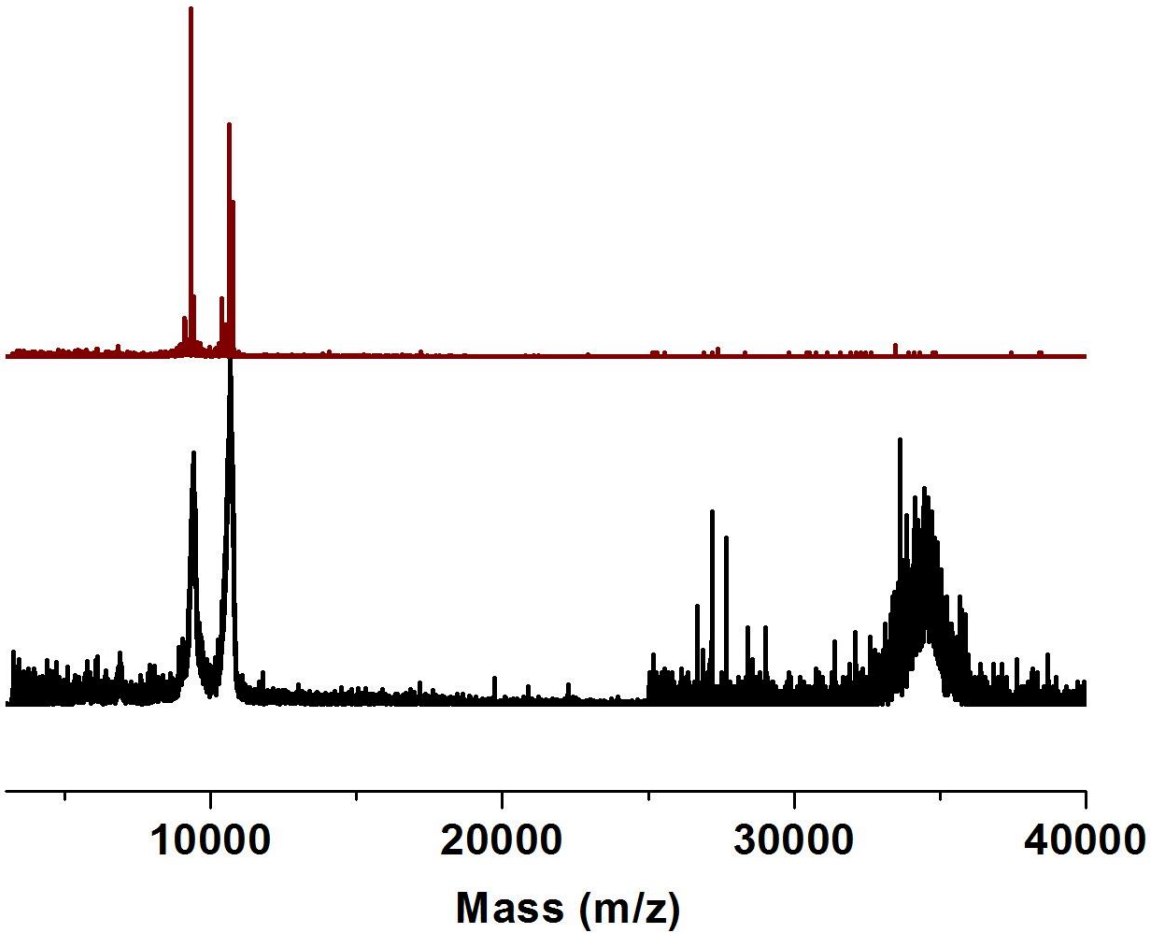

Figure 88. Maldi-TOF spectra of **Au38-144** mixture solution after soaking by **bio-MOF-105** for 1 (black) and 4 (dark red) days. Region above 25000 Da was intensified 10 times for easy visualization. Peak at ~7385 Da corresponds to $Au_{25}(SR)_{18}^{+}$ (calc. 7394 Da). Peaks within 5000-7300 Da correspond to $Au_{25}(SR)_{18}^{+}$ fragments. The broad peak at ~35000 Da correspond to $Au_{144}(SR)_{60}^{+}$ and its fragments.

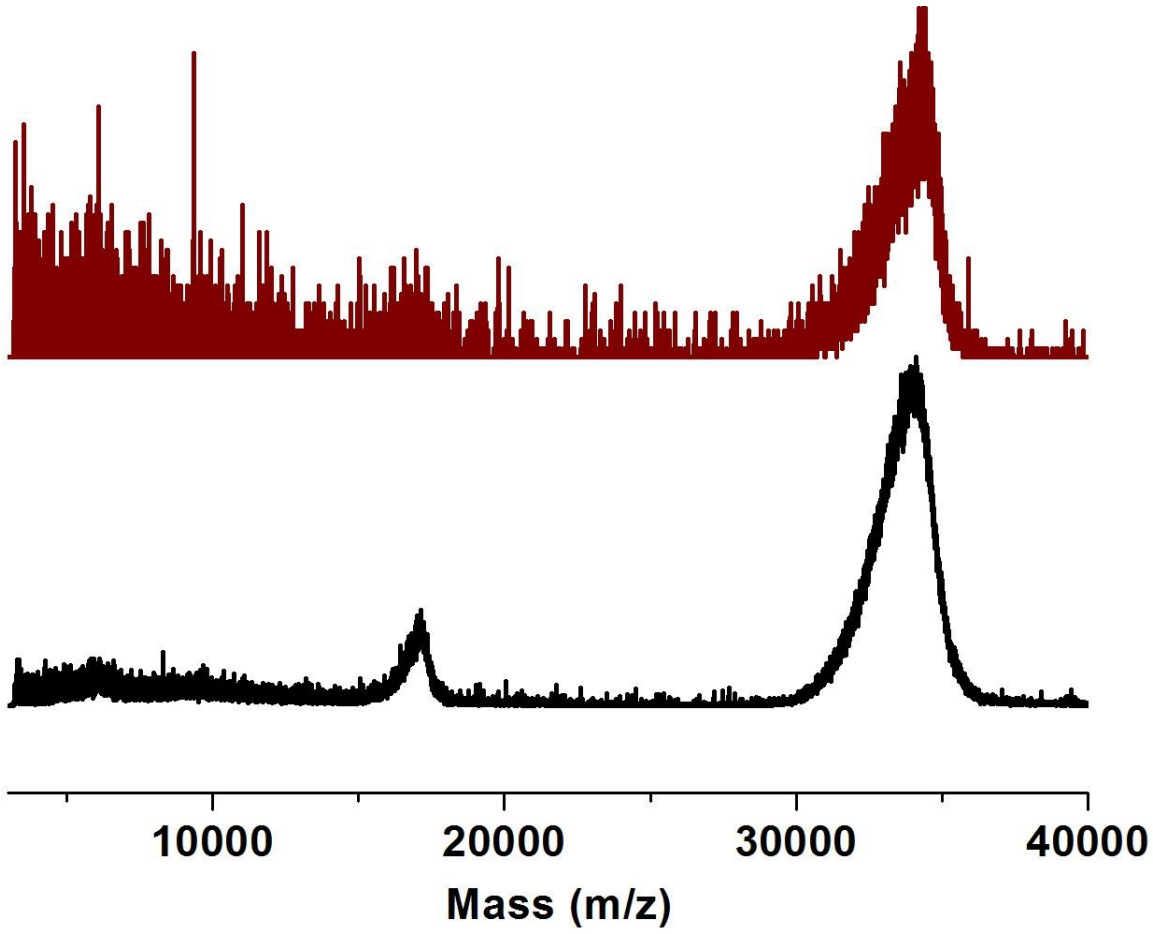

Figure 89. Maldi-TOF spectra of digested **bio-MOF-105** after soaking in **Au38-144** mixture for 1 (black) and 4 (dark red) days. The broad peaks at ~35000 Da and ~17000 Da correspond to $Au_{144}(SR)_{60}^{+}$, $Au_{144}(SR)_{60}^{2+}$ and their fragments.

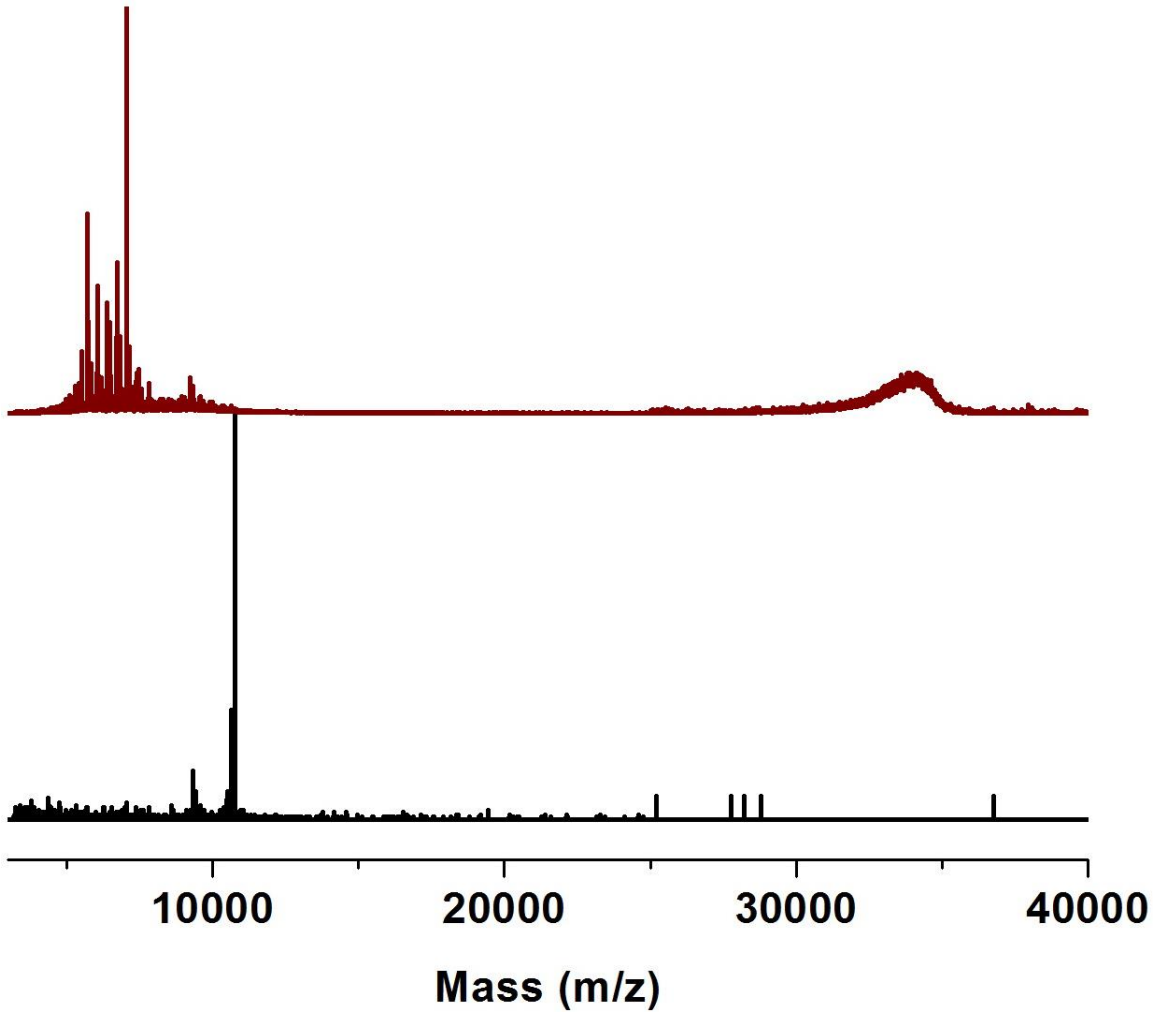

Figure 90. Maldi-TOF spectra of solution (black) and digested **bio-MOF-105** (dark red) after soaking in **Au25-38-144** mixture 4 days. Peak at ~7385 Da corresponds to $Au_{25}(SR)_{18}^{+}$ (calc. 7394 Da). Peaks within 5000-7300 Da correspond to $Au_{25}(SR)_{18}^{+}$ fragments. Peak at ~10762 Da corresponds to $Au_{38}(SR)_{24}^{+}$ (calc. 10778 Da). Peaks within 8500-10500 Da correspond to $Au_{38}(SR)_{24}^{+}$ fragments. The broad peak at ~35000 Da correspond to $Au_{144}(SR)_{60}^{+}$ and its fragments.

5.3 CONCLUSION

To summarize, we have designed and synthesized a series of new **bio-MOF-100** structural analogues with finely tailored pore sizes. We demonstrated that these exclusively mesoporous bio-MOFs are able to efficiently separate **$Au25^-$**, **Au38**, and **Au144** clusters via charge difference as well as size difference. The experimental procedures are simply stationary soaking which requires no special instrumentation and minimal care. This demonstration opens the door to using carefully designed MOFs for the separation of large species.

5.4 EXPERIMENTAL SECTION

5.4.1 General procedures and instrumentations

4,4'-stilbenedicarboxylic acid was purchased from TCI America. All other chemicals were purchased from SigmaAldrich and used without further purification. Nanopure water (18.2 MΩ) was obtained using a Barnstead DiamondTM System.

Elemental microanalyses (EA) were performed by the University of Illinois, Department of Chemistry Microanalytical Laboratory using a Perkin-Elmer 240 Elemental Analyzer and an Exeter Analytical CE440.

Thermogravimetric analysis (TGA) was conducted on a TGA Q500 thermal analysis system. Prior to analysis, samples were dried under argon flow (UHP) until the powder could move around freely. Approximately 5 mg of sample was loaded into a platinum pan and heated under a constant N_2 (UHP) flow from room temperature to 600 ℃ at a rate of 5 ℃/min.

Powder X-ray diffraction (PXRD) patterns were collected using a Bruker AXS D8 Discover powder diffractometer equipped with a Cu Kα X-ray source at 40 kV, 40 mA. Scan speed and step size were set at 0.1 sec/step and 0.02 °/step respectively. Generally, MOF samples were spread evenly on a glass slide and data were collected from 2.5 °< 2θ < 20 °.

Supercritical CO_2 activation experiments were performed on a Tousimis SAMDRI-PVT-3B. Prior to activation, **bio-MOF-101**, **bio-MOF-100**, **bio-MOF-104**, and **bio-MOF-105** were thoroughly washed with dry ethanol. The samples were than soaked in dry ethanol for one day, and the dry ethanol was refreshed after 10 minutes and 20 minutes of soaking. MOF sample was then added into a sample cell and placed into the chamber of the supercritical drier. Dry liquid CO_2 (99.8%) was charged into the chamber. The sample cell was allowed to purge for 5 min every 30 min. The chamber temperature was kept at ~0-10 ^oC during the process. After 4 hours, the chamber temperature was raised to ~38 ^oC and held for 1 hour followed by slow venting overnight.

Gas adsorption isotherms were collected on a Quantachrome Autosorb-1 instrument. Approximately 45-50 mg of each sample was added into a pre-weighed sample analysis tube. The samples were degassed at room temperature under vacuum for ~24 hours until the pressure change rate was no more than 3.5 mTorr/min. A liquid N_2 bath was used for the N_2 adsorption experiments at 77 K. UHP grade N_2 gas adsorbates (99.999 %) were used in this study.

MALDI-TOF mass spectra were obtained on an Applied Biosystem Voyager System 6174 MALDI-TOF mass spectrometer using *trans*-2-[3-(4-*tert*-butylphenyl)-2-methyl-2-propenylidene]malononitrile (DCTB) as the matrix.

5.4.2 Materials synthesis and preparation

5.4.2.1 Solvothermal synthesis of bio-MOF-101

Stock solutions of $Zn(OAc)_2 \cdot 6H_2O$ (0.05 M), adenine (0.05 M), and 2,6-naphthalene dicarboxylic acid (H_2-NDC) (0.1 M) in DMF were prepared prior to the MOF synthesis. To a 20 ml glass vial was added 9 ml of the $Zn(OAc)_2 \cdot 6H_2O$, 3 ml of the adenine stock solution, and 3 ml of the NDC stock solution along with 1.5 ml of nanopure water. The reaction mixture was heated in an 85 ^oC oven for 24 hours to yield colorless polyhedral crystals.

5.4.2.2 Solvothermal synthesis of Bio-MOF-100

Bio-MOF-100 was prepared according to the reported procedure.[11]

5.4.2.3 Solvothermal synthesis of bio-MOF-104

Stock solutions of $Zn(OAc)_2 \cdot 6H_2O$ (0.05 M), adenine (0.05 M), and 1,4-phenyldiacrylic acid (H_2-PDAC) (0.1 M) in DMF were prepared prior to the MOF synthesis. To a 20 ml glass vial was added 3 ml of the $Zn(OAc)_2 \cdot 6H_2O$, 1.5 ml of the adenine stock solution, 1.5 ml of the H_2-PDAC stock solution and 7 ml of N-Methyl-2-pyrrolidone (NMP) along with 1.5 ml of nanopure water. The reaction mixture was heated in a 100 ^oC oven for 24 hours to yield colorless polyhedral crystals.

5.4.2.4 Solvothermal synthesis of bio-MOF-105

Stock solutions of $Zn(OAc)_2 \cdot 6H_2O$ (0.05 M), adenine (0.05 M), HNO_3 (1 M) and 4,4'-stilbenedicarboxylic acid (H_2-SBDC) (0.1 M) in DMF were prepared prior to the MOF synthesis. To a 20 ml glass vial was added 4.5 ml of the $Zn(OAc)_2 \cdot 6H_2O$, 1.5 ml of the adenine stock

solution, 1.7 ml of HNO_3 stock solution, 3 ml of the H_2-SBDC stock solution and 1.5 ml nanopure water. The reaction mixture was heated in a 130 ^oC oven for 24 hours to yield colorless polyhedral crystals.

5.4.2.5 Synthesis of $Au25^-$, Au38, Au144

All the Au clusters were synthesized according to literature procedures.[135,145,146]

5.4.2.6 Oxidation of $Au25^-$ to $Au25^+$

As-synthesized **$Au25^-$** (~5 mg) was dissolved in 1ml THF. 10 μl of H_2O_2 (50%) was then added and mixed thoroughly. Small amount of solution was diluted and monitored by UV-vis (Figure A5). After 20 h, THF was removed under argon flow. Sample was then washed by nanopure water several times and dried under argon flow to give **$Au25^+$**.

5.4.2.7 Bio-MOFs preparation for Au clusters separation

As-synthesized bio-MOFs were washed with DMF (3X) and DCM (3X). The samples were than soaked in DCM for one day, and the DCM was refreshed after 10 minutes and 20 minutes of soaking. Then these bio-MOFs are ready for Au cluster separation

5.4.3 Single crystal X-ray data collection of bio-MOF-104 and bio-MOF-105

Crystallographic data were collected through the SCrALS (Service Crystallography at Advanced Light Source) program at the Small-Crystal Crystallography Beamline 11.3.1 at the Advanced Light Source (ALS), Lawrence Berkeley National Laboratory. Specifically, intensity data were collected at 298K on a D8 goniostat equipped with a Bruker APEXII CCD detector

using synchrotron radiation tuned to λ=0.77490Å. For data collection frames were measured for a duration of 2-s at 0.3^{o} intervals of ω with a maximum 2θ value of ~60^{o}. The data frames were collected using the program APEX2 and processed using the program SAINT routine within APEX2. The data were corrected for absorption and beam corrections based on the multi-scan technique as implemented in SADABS.

The structure was solved by direct methods using SHELXTL[124] which located all the Zn atoms. However, due to the weak diffraction, only part of the carbon and nitrogen atoms on adenine and carboxylate were found. Materials Studio (v5.0) was used to construct models of **bio-MOF-104** and **bio-MOF-105** with possible locations of adenine and carboxylates. The reliability of the models was confirmed by electron density maps of the crystal structures (Figure 91 and 92). Restraints and constraints were applied to optimize adenine and carboxylates. Zinc and apex oxygen atoms were refined anisotropically. All other atoms were refined isotropically.

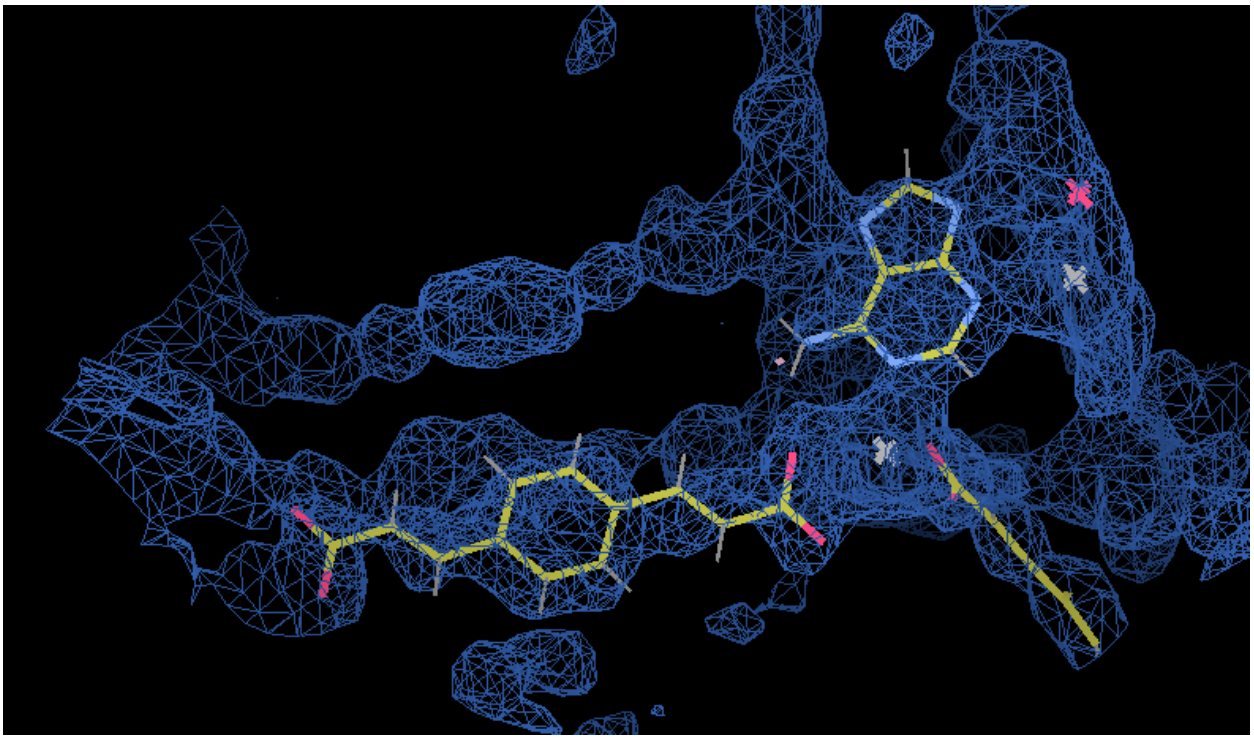

Figure 91. Electron density map of a fragment of **bio-MOF-104** at 0.35 e/Å^3. The figure was produced with Coot 0.6.2.

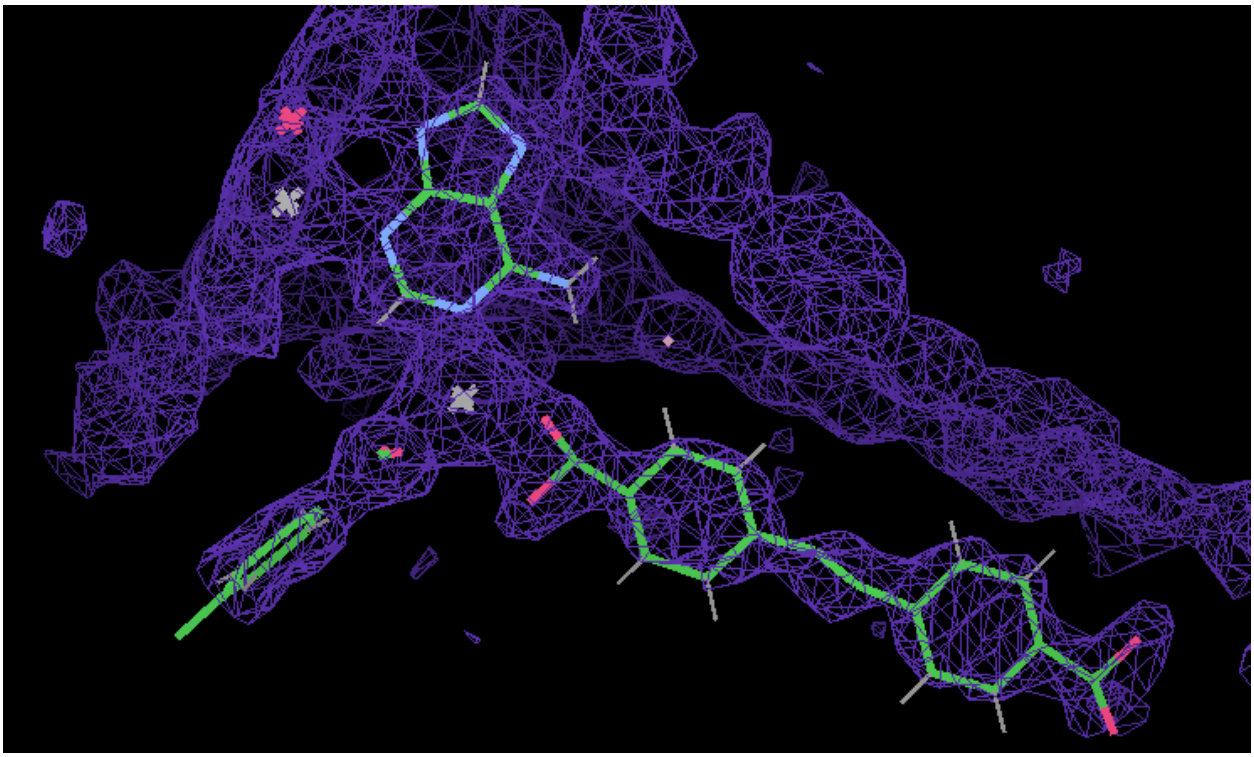

Figure 92. Electron density map of a fragment of **bio-MOF-105** at 0.48 e/Å^3. The figure was produced with Coot 0.6.2.

5.4.4 Elemental analysis

As-synthesized **bio-MOF-104**:

Formula: $Zn_8(ad)_4(PDAC)_6(OH)_2$ • 2DMA, 46DMF, $27H_2O$, 0.25NMP

Calcd. C, 44.47; H, 7.27; N, 15.04. Found: C, 44.48; H, 7.50; N, 15.04.

As-synthesized **bio-MOF-105**:

Formula: $Zn_8(ad)_4(SBDC)_6(OH)_2$ • 2DMA, 36DMF, $67H_2O$

Calcd. C, 41.37; H, 7.28; N, 12.27. Found: C, 41.36; H, 7.26; N, 12.34.

APPENDIX

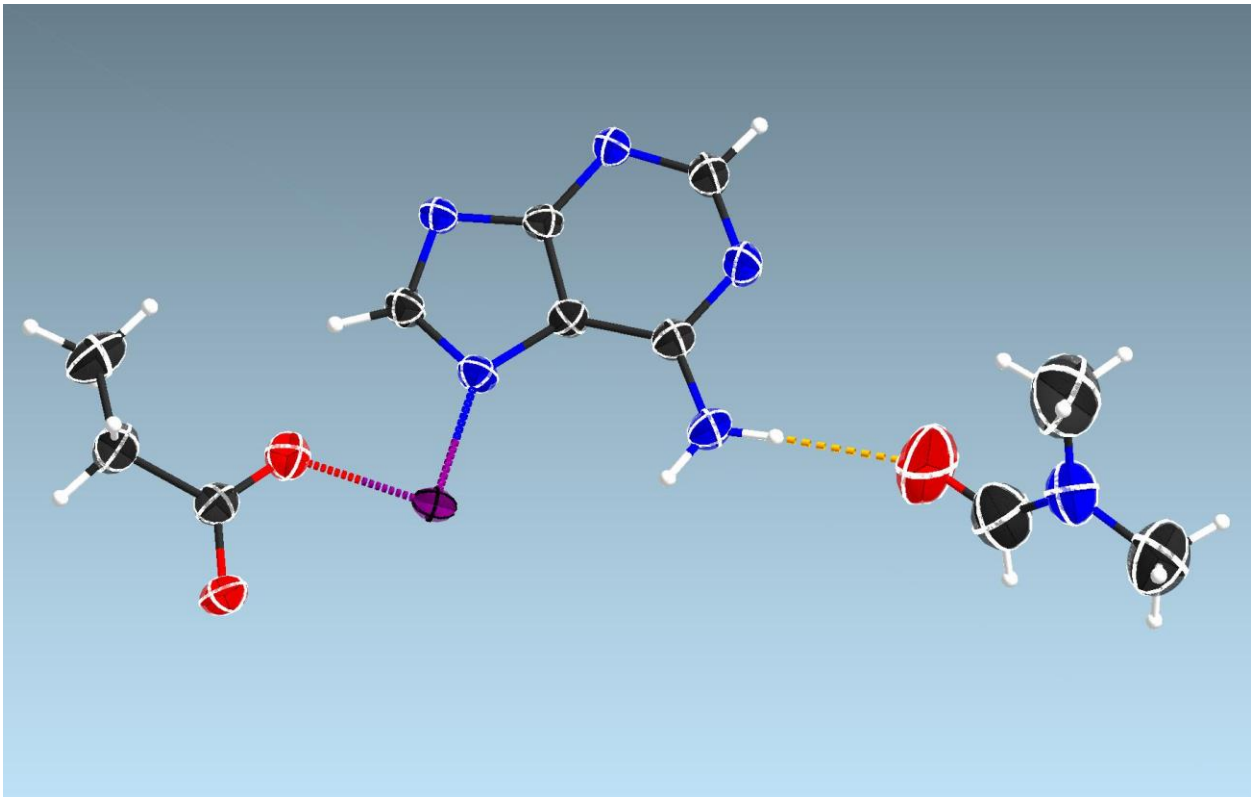

Figure A1. The asymmetric unit present in **bio-MOF-12** with all atoms represented by thermal ellipsoids drawn at the 50% probability level. The image was generated using Shelxle program.[148]

Table A1. Crystal data and structure refinement for **Bio-MOF-12**.

Identification code	bio-MOF-12	
Empirical formula	C11 H16 Co N6 O3	
Formula weight	339.23	
Temperature	273(2) K	
Wavelength	0.71073 Å	
Crystal system	Tetragonal	
Space group	$I\,4_1/a$	
Unit cell dimensions	a = 17.243(3) Å	= 90°.
	b = 17.243(3) Å	= 90°.
	c = 20.157(6) Å	= 90°.
Volume	5993(2) $Å^3$	
Z	16	
Density (calculated)	1.504 Mg/m^3	
Absorption coefficient	1.164 mm^{-1}	
F(000)	2800	
Crystal size	0.20 × 0.20 × 0.20 mm^3	
Theta range for data collection	2.36 to 28.39 °.	
Index ranges	-22<=h<=22, -23<=k<=22, -26<=l<=26	
Reflections collected	30135	
Independent reflections	3750 [R(int) = 0.0962]	
Completeness to theta = 28.39 °	99.7 %	
Absorption correction	multi-scan (Bruker SADABS)	
Max. and min. transmission	0.8005 and 0.8005	
Refinement method	Full-matrix least-squares on F^2	
Data / restraints / parameters	3750 / 0 / 190	
Goodness-of-fit on F^2	1.032	
Final R indices [I>2sigma(I)]	R1 = 0.0474, wR2 = 0.0855	
R indices (all data)	R1 = 0.0899, wR2 = 0.0985	
Largest diff. peak and hole	0.360 and -0.237 e.$Å^{-3}$	

Table A2. Atomic coordinates ($\times 10^4$) and equivalent isotropic displacement parameters ($Å^2 \times 10^3$) for **bio-MOF-12**. U(eq) is defined as one third of the trace of the orthogonalized U^{ij} tensor.

	x	y	z	U(eq)
Co(1)	376(1)	4692(1)	604(1)	28(1)
C(1)	1162(2)	3444(2)	1344(1)	32(1)
C(2)	1268(2)	4415(2)	1988(1)	29(1)
C(3)	1274(2)	5117(2)	2340(2)	36(1)
C(4)	550(2)	3866(2)	-701(2)	36(1)
C(5)	895(2)	3222(2)	-1103(2)	53(1)
C(6)	1182(2)	2534(2)	-712(2)	71(1)
C(7)	1698(2)	3806(2)	2242(1)	27(1)
C(8)	2100(2)	4529(2)	3091(2)	43(1)
N(1)	920(1)	4176(1)	1399(1)	29(1)
N(2)	883(2)	5754(1)	2159(1)	50(1)
N(3)	1708(2)	5151(1)	2900(1)	44(1)
N(4)	1628(1)	3182(1)	1832(1)	30(1)
N(5)	2128(1)	3834(1)	2806(1)	32(1)
O(1)	727(1)	3910(1)	-101(1)	43(1)
O(2)	110(1)	4338(1)	-997(1)	44(1)
O(3)	1056(2)	7295(2)	2787(2)	109(1)
N(6)	1342(2)	8549(2)	2990(2)	71(1)
C(11)	876(3)	7957(3)	2914(2)	84(1)
C(10)	2160(3)	8433(3)	2936(3)	129(2)
C(9)	1078(4)	9314(3)	3149(3)	131(2)

Table A3. Bond lengths [Å] and angles [ᵊ] for **Bio-MOF-12**.

Co(1)-O(2)#1	2.031(2)
Co(1)-O(1)	2.051(2)
Co(1)-N(1)	2.058(2)
Co(1)-N(4)#2	2.072(2)
Co(1)-N(5)#3	2.112(2)
Co(1)-Co(1)#1	2.9560(9)
C(1)-N(1)	1.334(3)
C(1)-N(4)	1.348(3)
C(1)-H(1)	0.9300
C(2)-C(7)	1.383(4)
C(2)-N(1)	1.393(3)
C(2)-C(3)	1.404(4)
C(3)-N(2)	1.338(4)
C(3)-N(3)	1.356(4)
C(4)-O(1)	1.249(3)
C(4)-O(2)	1.263(3)
C(4)-C(5)	1.497(4)
C(5)-C(6)	1.508(5)
C(5)-H(5A)	0.9700
C(5)-H(5B)	0.9700
C(6)-H(3)	0.9600
C(6)-H(4)	0.9600
C(6)-H(5)	0.9600
C(7)-N(5)	1.360(3)
C(7)-N(4)	1.361(3)
C(8)-N(3)	1.325(4)
C(8)-N(5)	1.329(4)
C(8)-H(6)	0.9300
N(2)-H(7)	0.8600
N(2)-H(8)	0.8600
N(4)-Co(1)#4	2.072(2)
N(5)-Co(1)#5	2.112(2)
O(2)-Co(1)#1	2.031(2)
O(3)-C(11)	1.210(5)

N(6)-C(11)	1.307(5)
N(6)-C(10)	1.429(6)
N(6)-C(9)	1.432(5)
C(11)-H(11A)	0.9300
C(10)-H(10A)	0.9600
C(10)-H(10B)	0.9600
C(10)-H(10C)	0.9600
C(9)-H(9A)	0.9600
C(9)-H(9B)	0.9600
C(9)-H(9C)	0.9600
O(2)#1-Co(1)-O(1)	159.01(9)
O(2)#1-Co(1)-N(1)	103.93(9)
O(1)-Co(1)-N(1)	96.87(9)
O(2)#1-Co(1)-N(4)#2	89.98(9)
O(1)-Co(1)-N(4)#2	89.63(9)
N(1)-Co(1)-N(4)#2	98.59(9)
O(2)#1-Co(1)-N(5)#3	88.65(9)
O(1)-Co(1)-N(5)#3	86.42(9)
N(1)-Co(1)-N(5)#3	96.04(9)
N(4)#2-Co(1)-N(5)#3	165.20(9)
O(2)#1-Co(1)-Co(1)#1	81.07(6)
O(1)-Co(1)-Co(1)#1	78.17(6)
N(1)-Co(1)-Co(1)#1	174.92(7)
N(4)#2-Co(1)-Co(1)#1	80.40(6)
N(5)#3-Co(1)-Co(1)#1	84.83(6)
N(1)-C(1)-N(4)	116.3(3)
N(1)-C(1)-H(1)	121.8
N(4)-C(1)-H(1)	121.8
C(7)-C(2)-N(1)	108.7(2)
C(7)-C(2)-C(3)	117.6(3)
N(1)-C(2)-C(3)	133.6(3)
N(2)-C(3)-N(3)	118.1(3)
N(2)-C(3)-C(2)	124.4(3)
N(3)-C(3)-C(2)	117.5(3)
O(1)-C(4)-O(2)	124.5(3)
O(1)-C(4)-C(5)	118.1(3)

O(2)-C(4)-C(5)	117.4(3)
C(4)-C(5)-C(6)	115.5(3)
C(4)-C(5)-H(5A)	108.4
C(6)-C(5)-H(5A)	108.4
C(4)-C(5)-H(5B)	108.4
C(6)-C(5)-H(5B)	108.4
H(5A)-C(5)-H(5B)	107.5
C(5)-C(6)-H(3)	109.5
C(5)-C(6)-H(4)	109.5
H(3)-C(6)-H(4)	109.5
C(5)-C(6)-H(5)	109.5
H(3)-C(6)-H(5)	109.5
H(4)-C(6)-H(5)	109.5
N(5)-C(7)-N(4)	125.7(2)
N(5)-C(7)-C(2)	125.1(3)
N(4)-C(7)-C(2)	109.2(2)
N(3)-C(8)-N(5)	128.5(3)
N(3)-C(8)-H(6)	115.7
N(5)-C(8)-H(6)	115.7
C(1)-N(1)-C(2)	102.4(2)
C(1)-N(1)-Co(1)	119.22(19)
C(2)-N(1)-Co(1)	136.98(18)
C(3)-N(2)-H(7)	120.0
C(3)-N(2)-H(8)	120.0
H(7)-N(2)-H(8)	120.0
C(8)-N(3)-C(3)	119.3(3)
C(1)-N(4)-C(7)	103.3(2)
C(1)-N(4)-Co(1)#4	128.33(19)
C(7)-N(4)-Co(1)#4	128.12(18)
C(8)-N(5)-C(7)	111.9(2)
C(8)-N(5)-Co(1)#5	127.0(2)
C(7)-N(5)-Co(1)#5	120.87(18)
C(4)-O(1)-Co(1)	129.6(2)
C(4)-O(2)-Co(1)#1	126.4(2)
C(11)-N(6)-C(10)	119.2(4)
C(11)-N(6)-C(9)	123.4(5)

C(10)-N(6)-C(9)	117.4(4)
O(3)-C(11)-N(6)	127.1(5)
O(3)-C(11)-H(11A)	116.4
N(6)-C(11)-H(11A)	116.4
N(6)-C(10)-H(10A)	109.5
N(6)-C(10)-H(10B)	109.5
H(10A)-C(10)-H(10B)	109.5
N(6)-C(10)-H(10C)	109.5
H(10A)-C(10)-H(10C)	109.5
H(10B)-C(10)-H(10C)	109.5
N(6)-C(9)-H(9A)	109.5
N(6)-C(9)-H(9B)	109.5
H(9A)-C(9)-H(9B)	109.5
N(6)-C(9)-H(9C)	109.5
H(9A)-C(9)-H(9C)	109.5
H(9B)-C(9)-H(9C)	109.5

Symmetry transformations used to generate equivalent atoms:

#1 -x,-y+1,-z #2 -y+1/4,x+1/4,-z+1/4 #3 y-1/4,-x+3/4,z-1/4

#4 y-1/4,-x+1/4,-z+1/4 #5 -y+3/4,x+1/4,z+1/4

Table A4. Anisotropic displacement parameters (Å2 × 103) for Bio-MOF-12. The anisotropic displacement factor exponent takes the form: -22[h2 a*2U11 + ... + 2 h k a* b* U12].

	U^{11}	U^{22}	U^{33}	U^{23}	U^{13}	U^{12}
Co(1)	25(1)	29(1)	29(1)	8(1)	-3(1)	-1(1)
C(1)	37(2)	30(2)	30(2)	2(1)	-8(1)	1(1)
C(2)	31(2)	27(1)	29(2)	3(1)	-1(1)	-1(1)
C(3)	39(2)	31(2)	36(2)	0(1)	-3(1)	3(1)
C(4)	31(2)	32(2)	44(2)	0(1)	4(1)	-1(1)
C(5)	63(2)	49(2)	46(2)	-8(2)	1(2)	17(2)
C(6)	80(3)	47(2)	86(3)	-3(2)	-7(2)	27(2)
C(7)	27(1)	25(1)	30(2)	4(1)	-2(1)	1(1)
C(8)	55(2)	36(2)	38(2)	-7(1)	-14(2)	8(2)
N(1)	31(1)	29(1)	28(1)	4(1)	-6(1)	0(1)
N(2)	66(2)	30(1)	53(2)	-5(1)	-21(2)	19(1)
N(3)	61(2)	32(1)	41(2)	-8(1)	-17(1)	11(1)
N(4)	34(1)	27(1)	30(1)	0(1)	-9(1)	4(1)
N(5)	36(1)	27(1)	34(1)	-3(1)	-8(1)	3(1)
O(1)	45(1)	44(1)	39(1)	-4(1)	1(1)	4(1)
O(2)	40(1)	33(1)	57(2)	1(1)	-7(1)	11(1)
O(3)	123(3)	57(2)	146(3)	-27(2)	-7(2)	-2(2)
N(6)	73(2)	61(2)	77(2)	-11(2)	-9(2)	-8(2)
C(11)	78(3)	77(3)	97(4)	-11(3)	-7(3)	-11(3)
C(10)	79(4)	123(5)	186(7)	-57(5)	11(4)	-24(3)
C(9)	168(6)	63(3)	162(6)	-30(4)	-58(5)	23(4)

Table A5. Hydrogen coordinates (×104) and isotropic displacement parameters (Å2×10 3) for Bio-MOF-12.

	x	y	z	U(eq)
H(1)	1017	3131	989	39
H(5A)	1325	3430	-1357	63
H(5B)	508	3043	-1417	63
H(3)	1393	2155	-1010	107
H(4)	758	2309	-470	107
H(5)	1576	2699	-407	107
H(6)	2395	4586	3474	51
H(7)	911	6167	2396	60
H(8)	603	5749	1806	60
H(11A)	349	8056	2964	101
H(10A)	2262	7903	2819	194
H(10B)	2402	8550	3352	194
H(10C)	2364	8768	2598	194
H(9A)	522	9319	3167	196
H(9B)	1252	9671	2815	196
H(9C)	1284	9466	3572	196

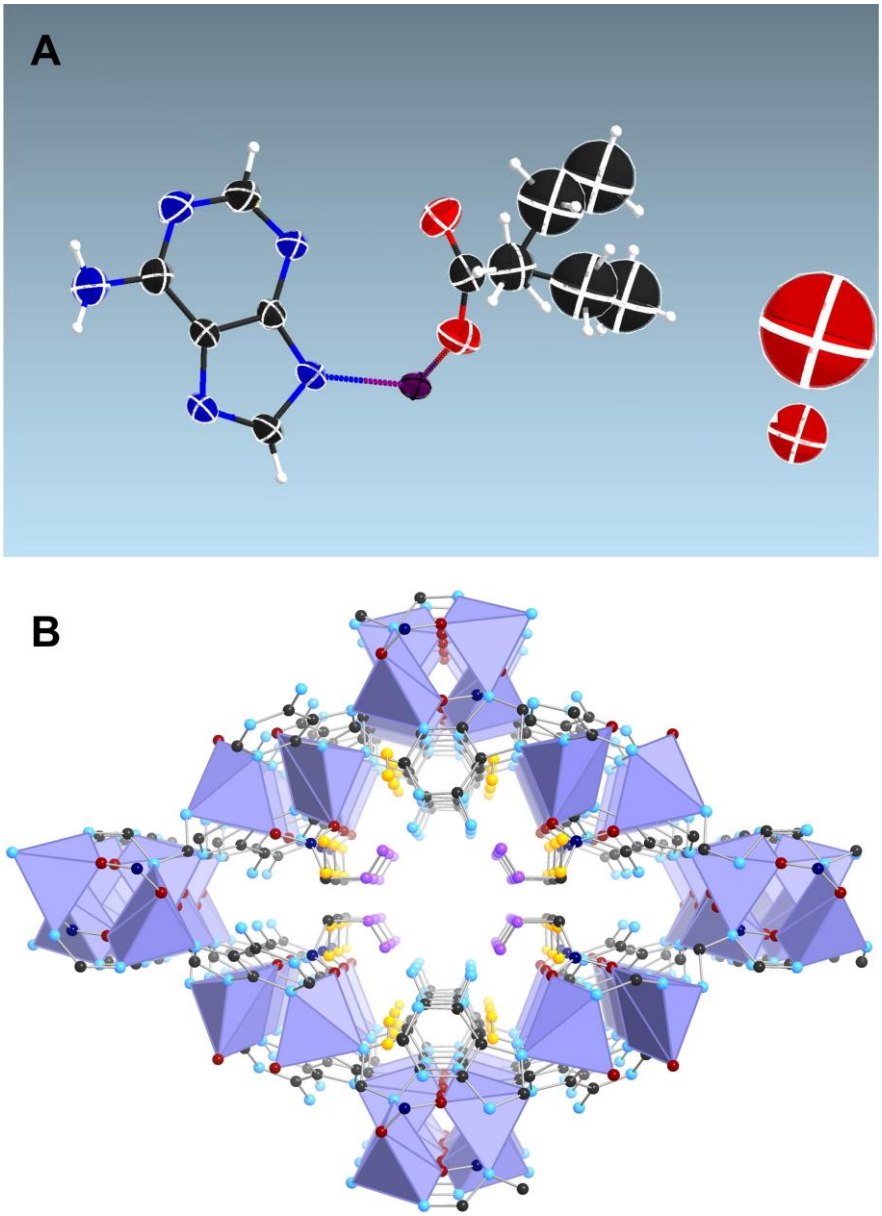

Figure A2. (A) The asymmetric unit present in **bio-MOF-13** with all atoms represented by thermal ellipsoids drawn at the 50% probability level. The image was generated using Shelxle program;[148] (B) Perspective view of the crystal structure of **bio-MOF-13**. (Co^{2+}, light purple tetrahedra; C, dark gray spheres; O, dark red spheres; N, light blue spheres. H atoms have been omitted for clarity. Disordered butyrate chains were illustrate as orange (configuration I), and purple (configuration II)).

Table A6. Crystal data and structure refinement for **bio-MOF-13.**

Identification code	bio-MOF-13
Empirical formula	C9 H15 Co N5 O3
Formula weight	300.19
Temperature	273(2) K
Wavelength	0.71073 Å
Crystal system	Tetragonal
Space group	I 4_1/a
Unit cell dimensions	a = 15.7869(10) Å = 90°.
	b = 15.7869(10) Å = 90°.
	c = 22.328(3) Å = 90°.
Volume	5564.7(8) $Å^3$
Z	16
Density (calculated)	1.433 Mg/m^3
Absorption coefficient	1.242 mm^{-1}
F(000)	2480
Crystal size	0.25 × 0.25 × 0.25 mm^3
Theta range for data collection	2.58 to 28.25 °.
Index ranges	-20<=h<=20, -21<=k<=20, -29<=l<=29
Reflections collected	28249
Independent reflections	3450 [R(int) = 0.0320]
Completeness to theta = 28.25 °	100.0 %
Absorption correction	Multi scan (Bruker SADABS)
Max. and min. transmission	0.7466 and 0.7466
Refinement method	Full-matrix least-squares on F^2
Data / restraints / parameters	3450 / 5 / 165
Goodness-of-fit on F^2	1.040
Final R indices [I>2sigma(I)]	R1 = 0.0541, wR2 = 0.1677
R indices (all data)	R1 = 0.0687, wR2 = 0.1836
Largest diff. peak and hole	0.760 and -0.395 e.$Å^{-3}$

Table A7. Atomic coordinates ($\times 10^4$) and equivalent isotropic displacement parameters ($Å^2 \times 10^3$) for **bio-MOF-13**. U(eq) is defined as one third of the trace of the orthogonalized U^{ij} tensor.

	x	y	z	U(eq)
O(1)	5765(2)	6094(2)	9997(1)	65(1)
Co(1)	5407(1)	5170(1)	10590(1)	39(1)
O(2)	5149(2)	5924(2)	9122(1)	60(1)
N(1)	1556(3)	6911(4)	10443(2)	95(2)
N(2)	2201(2)	6181(3)	9676(2)	90(2)
N(3)	3581(2)	5559(2)	9747(1)	49(1)
N(4)	4250(2)	5783(2)	10706(1)	41(1)
N(5)	3188(2)	6506(2)	11166(1)	41(1)
C(1)	3964(2)	6177(2)	11203(1)	46(1)
C(2)	2950(2)	6309(2)	10587(1)	41(1)
C(3)	2227(2)	6482(3)	10243(2)	67(1)
C(4)	2867(3)	5745(4)	9465(2)	78(2)
C(5)	3602(2)	5868(2)	10315(1)	38(1)
C(6)	5651(2)	6299(2)	9467(2)	49(1)
C(7)	6147(3)	7046(3)	9235(3)	79(1)
C(8B)	6364(12)	7028(11)	8627(8)	167(4)
C(9B)	6773(14)	6457(12)	8368(10)	200(5)
C(8A)	7003(12)	6922(15)	9219(12)	167(4)
C(9A)	7462(14)	6275(16)	9261(15)	200(5)
O(1W)	9886(9)	7084(7)	9838(6)	133(6)
O(2W)	9740(30)	6740(20)	9010(20)	500(30)

Table A8. Bond lengths [Å] and angles [°] for **bio-MOF-13**.

O(1)-C(6)	1.239(4)
O(1)-Co(1)	2.050(3)
Co(1)-O(2)#1	2.041(3)
Co(1)-N(5)#2	2.071(2)
Co(1)-N(4)	2.083(3)
Co(1)-N(3)#1	2.107(3)
Co(1)-Co(1)#1	2.9798(8)
O(2)-C(6)	1.254(4)
O(2)-Co(1)#1	2.041(3)
N(1)-C(3)	1.334(5)
N(1)-H(1N1)	0.85(2)
N(1)-H(2N1)	0.87(2)
N(2)-C(4)	1.341(5)
N(2)-C(3)	1.354(5)
N(3)-C(4)	1.326(5)
N(3)-C(5)	1.359(4)
N(3)-Co(1)#1	2.107(3)
N(4)-C(1)	1.350(4)
N(4)-C(5)	1.352(4)
N(5)-C(1)	1.333(4)
N(5)-C(2)	1.381(4)
N(5)-Co(1)#3	2.071(2)
C(1)-H(1A)	0.9300
C(2)-C(5)	1.382(4)
C(2)-C(3)	1.403(5)
C(4)-H(4A)	0.9300
C(6)-C(7)	1.508(5)
C(7)-C(8A)	1.366(18)
C(7)-C(8B)	1.400(17)
C(7)-H(7A)	0.9700
C(7)-H(7B)	0.9700

C(7)-H(7C)	0.9700
C(7)-H(7D)	0.9701
C(8B)-C(9B)	1.25(2)
C(8B)-H(7C)	0.9207
C(8B)-H(8B1)	0.9700
C(8B)-H(8B2)	0.9700
C(9B)-H(9B1)	0.9600
C(9B)-H(9B2)	0.9600
C(9B)-H(9B3)	0.9600
C(8A)-C(9A)	1.26(2)
C(8A)-H(8A1)	0.9700
C(8A)-H(8A2)	0.9700
C(9A)-H(9A1)	0.9600
C(9A)-H(9A2)	0.9600
C(9A)-H(9A3)	0.9600
O(1W)-O(1W)#4	1.36(2)

C(6)-O(1)-Co(1)	139.7(3)
O(2)#1-Co(1)-O(1)	157.56(11)
O(2)#1-Co(1)-N(5)#2	105.85(11)
O(1)-Co(1)-N(5)#2	96.58(11)
O(2)#1-Co(1)-N(4)	88.71(11)
O(1)-Co(1)-N(4)	89.50(12)
N(5)#2-Co(1)-N(4)	96.29(10)
O(2)#1-Co(1)-N(3)#1	88.63(12)
O(1)-Co(1)-N(3)#1	87.07(13)
N(5)#2-Co(1)-N(3)#1	99.36(10)
N(4)-Co(1)-N(3)#1	164.26(10)
O(2)#1-Co(1)-Co(1)#1	86.61(8)
O(1)-Co(1)-Co(1)#1	71.08(8)
N(5)#2-Co(1)-Co(1)#1	166.81(8)
N(4)-Co(1)-Co(1)#1	79.38(7)
N(3)#1-Co(1)-Co(1)#1	84.98(7)
C(6)-O(2)-Co(1)#1	118.5(2)
C(3)-N(1)-H(1N1)	121(4)
C(3)-N(1)-H(2N1)	111(4)

H(1N1)-N(1)-H(2N1)	123(6)
C(4)-N(2)-C(3)	119.0(3)
C(4)-N(3)-C(5)	112.5(3)
C(4)-N(3)-Co(1)#1	126.7(2)
C(5)-N(3)-Co(1)#1	120.8(2)
C(1)-N(4)-C(5)	103.4(2)
C(1)-N(4)-Co(1)	127.6(2)
C(5)-N(4)-Co(1)	129.03(19)
C(1)-N(5)-C(2)	102.7(2)
C(1)-N(5)-Co(1)#3	119.2(2)
C(2)-N(5)-Co(1)#3	138.1(2)
N(5)-C(1)-N(4)	115.9(3)
N(5)-C(1)-H(1A)	122.1
N(4)-C(1)-H(1A)	122.1
N(5)-C(2)-C(5)	108.8(3)
N(5)-C(2)-C(3)	133.6(3)
C(5)-C(2)-C(3)	117.6(3)
N(1)-C(3)-N(2)	117.8(4)
N(1)-C(3)-C(2)	124.2(4)
N(2)-C(3)-C(2)	118.0(3)
N(3)-C(4)-N(2)	127.9(3)
N(3)-C(4)-H(4A)	116.0
N(2)-C(4)-H(4A)	116.0
N(4)-C(5)-N(3)	125.7(3)
N(4)-C(5)-C(2)	109.2(2)
N(3)-C(5)-C(2)	125.0(3)
O(1)-C(6)-O(2)	123.7(3)
O(1)-C(6)-C(7)	117.2(4)
O(2)-C(6)-C(7)	119.1(4)
C(8A)-C(7)-C(8B)	74.3(13)
C(8A)-C(7)-C(6)	114.2(11)
C(8B)-C(7)-C(6)	116.4(8)
C(8A)-C(7)-H(7A)	130.7
C(8B)-C(7)-H(7A)	108.2
C(6)-C(7)-H(7A)	108.2
C(8A)-C(7)-H(7B)	36.0

C(8B)-C(7)-H(7B)	108.2
C(6)-C(7)-H(7B)	108.2
H(7A)-C(7)-H(7B)	107.4
C(8A)-C(7)-H(7C)	113.2
C(8B)-C(7)-H(7C)	40.9
C(6)-C(7)-H(7C)	108.6
H(7A)-C(7)-H(7C)	73.6
H(7B)-C(7)-H(7C)	140.6
C(8A)-C(7)-H(7D)	104.4
C(8B)-C(7)-H(7D)	131.2
C(6)-C(7)-H(7D)	108.5
H(7A)-C(7)-H(7D)	36.3
H(7B)-C(7)-H(7D)	73.1
H(7C)-C(7)-H(7D)	107.5
C(9B)-C(8B)-C(7)	126.2(18)
C(9B)-C(8B)-H(7C)	152.0
C(7)-C(8B)-H(7C)	43.6
C(9B)-C(8B)-H(8B1)	105.8
C(7)-C(8B)-H(8B1)	105.8
H(7C)-C(8B)-H(8B1)	65.0
C(9B)-C(8B)-H(8B2)	105.8
C(7)-C(8B)-H(8B2)	105.8
H(7C)-C(8B)-H(8B2)	102.2
H(8B1)-C(8B)-H(8B2)	106.2
C(8B)-C(9B)-H(9B1)	109.5
C(8B)-C(9B)-H(9B2)	109.5
H(9B1)-C(9B)-H(9B2)	109.5
C(8B)-C(9B)-H(9B3)	109.5
H(9B1)-C(9B)-H(9B3)	109.5
H(9B2)-C(9B)-H(9B3)	109.5
C(9A)-C(8A)-C(7)	133(2)
C(9A)-C(8A)-H(8A1)	103.9
C(7)-C(8A)-H(8A1)	103.9
C(9A)-C(8A)-H(8A2)	103.9
C(7)-C(8A)-H(8A2)	103.9
H(8A1)-C(8A)-H(8A2)	105.4

C(8A)-C(9A)-H(9A1)	109.5
C(8A)-C(9A)-H(9A2)	109.5
H(9A1)-C(9A)-H(9A2)	109.5
C(8A)-C(9A)-H(9A3)	109.5
H(9A1)-C(9A)-H(9A3)	109.5
H(9A2)-C(9A)-H(9A3)	109.5

Symmetry transformations used to generate equivalent atoms:

#1 -x+1,-y+1,-z+2 #2 -y+5/4,x+1/4,-z+9/4 #3 y-1/4,-x+5/4,-z+9/4

#4 -x+2,-y+3/2,z+0

Table A9. Anisotropic displacement parameters ($Å^2 \times 10^3$) for **Bio-MOF-13**. The anisotropic displacement factor exponent takes the form: $-2^2[h^2 a^{*2} U^{11} + ... + 2 h k a^* b^* U^{12}]$

	U^{11}	U^{22}	U^{33}	U^{23}	U^{13}	U^{12}
O(1)	78(2)	68(2)	48(1)	1(1)	6(1)	-8(1)
Co(1)	37(1)	47(1)	34(1)	-14(1)	-3(1)	1(1)
O(2)	57(1)	52(1)	71(2)	-6(1)	-12(1)	-8(1)
N(1)	58(2)	161(4)	64(2)	-39(3)	-11(2)	50(3)
N(2)	53(2)	156(4)	60(2)	-43(2)	-18(2)	41(2)
N(3)	39(1)	70(2)	39(1)	-19(1)	-4(1)	8(1)
N(4)	41(1)	47(1)	34(1)	-12(1)	1(1)	6(1)
N(5)	43(1)	48(1)	34(1)	-7(1)	7(1)	2(1)
C(1)	48(2)	55(2)	35(2)	-12(1)	3(1)	8(1)
C(2)	39(2)	50(2)	36(1)	-8(1)	4(1)	3(1)
C(3)	46(2)	101(3)	54(2)	-20(2)	-4(2)	20(2)
C(4)	55(2)	126(4)	51(2)	-38(2)	-12(2)	26(2)
C(5)	36(1)	42(1)	37(1)	-9(1)	5(1)	-1(1)
C(6)	52(2)	41(2)	54(2)	-1(1)	4(1)	-3(1)
C(7)	83(3)	69(3)	84(3)	12(2)	1(3)	-27(2)

Table A10. Hydrogen coordinates ($\times 10^4$) and isotropic displacement parameters ($Å^2 \times 10^3$) for **Bio-MOF-13**.

	x	y	z	U(eq)
H(1N1)	1560(40)	7150(40)	10784(16)	113
H(2N1)	1250(30)	7090(40)	10140(20)	113
H(1A)	4288	6217	11549	55
H(4A)	2821	5551	9073	93
H(7A)	5818	7555	9308	94
H(7B)	6664	7093	9467	94
H(7C)	5912	7215	8851	94
H(7D)	6071	7516	9510	94
H(8B1)	5835	7077	8410	200
H(8B2)	6673	7549	8553	200
H(9B1)	6818	6588	7950	300
H(9B2)	6486	5926	8417	300
H(9B3)	7330	6419	8539	300
H(8A1)	7175	7177	8843	200
H(8A2)	7218	7296	9528	200
H(9A1)	8045	6444	9293	300
H(9A2)	7390	5930	8911	300
H(9A3)	7303	5958	9610	300

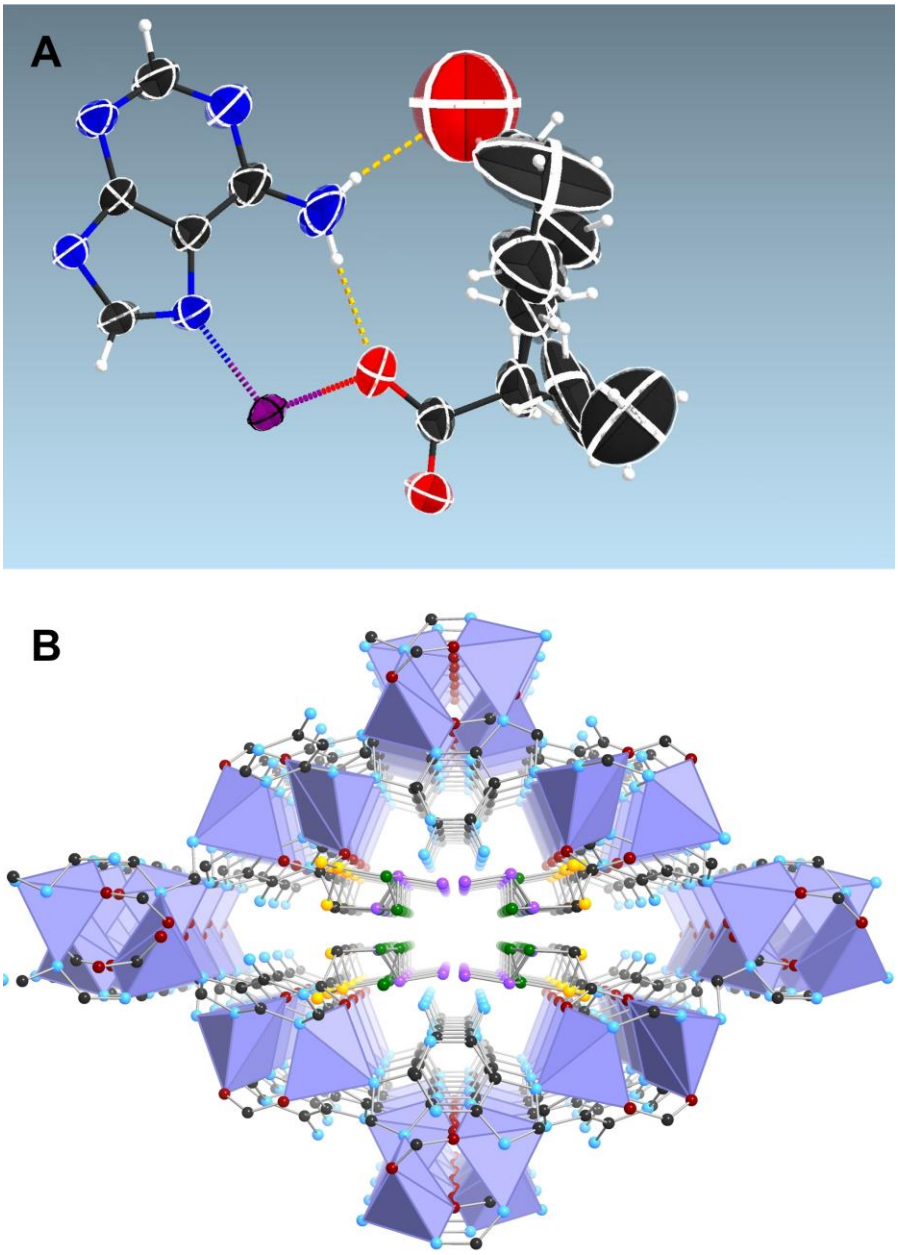

Figure A3. (A) The asymmetric unit present in **bio-MOF-14** with all atoms represented by thermal ellipsoids drawn at the 50% probability level. The image was generated using Shelxle program.[148] (B) Perspective view of the crystal structure of **bio-MOF-14**. (Co^{2+}, light purple tetrahedra; C, dark gray spheres; O, dark red spheres; N, light blue spheres. H atoms have been omitted for clarity. Disordered valerate chains were illustrate as orange (configuration I), purple (configuration II), and green (configuration III)).

Table A11. Crystal data and structure refinement for **bio-MOF-14**.

Identification code	bio-MOF-14	
Empirical formula	C10 H14 Co N5 O2.50	
Formula weight	303.19	
Temperature	273(2) K	
Wavelength	0.71073 Å	
Crystal system	Tetragonal	
Space group	$I\,4_1/a$	
Unit cell dimensions	a = 15.852(3) Å	= 90°.
	b = 15.852(3) Å	= 90°.
	c = 22.346(8) Å	= 90°.
Volume	5616(2) $Å^3$	
Z	16	
Density (calculated)	1.434 Mg/m^3	
Absorption coefficient	1.229 mm^{-1}	
F(000)	2496	
Crystal size	0.08 × 0.08 × 0.08 mm^3	
Theta range for data collection	2.57 to 28.30 °.	
Index ranges	-21<=h<=21, -21<=k<=16, -29<=l<=29	
Reflections collected	21045	
Independent reflections	3426 [R(int) = 0.1036]	
Completeness to theta = 28.30 °	98.1 %	
Absorption correction	Multi scan (Bruker SADABS)	
Max. and min. transmission	0.9081 and 0.9081	
Refinement method	Full-matrix least-squares on F^2	
Data / restraints / parameters	3426 / 145 / 222	
Goodness-of-fit on F^2	1.029	
Final R indices [I>2sigma(I)]	R1 = 0.0658, wR2 = 0.1834	
R indices (all data)	R1 = 0.1442, wR2 = 0.2298	
Largest diff. peak and hole	0.660 and -0.514 $e.Å^{-3}$	

Table A12. Atomic coordinates ($\times 10^4$) and equivalent isotropic displacement parameters ($Å^2 \times 10^3$) for **bio-MOF-14**. U(eq) is defined as one third of the trace of the orthogonalized U^{ij} tensor.

	x	y	z	U(eq)
N(4)	1328(5)	9725(4)	2827(3)	92(2)
Co(1)	400(1)	10164(1)	595(1)	45(1)
N(1)	1729(3)	11749(3)	1782(2)	46(1)
O(1)	-142(3)	9071(3)	888(2)	66(1)
N(2)	996(3)	10688(3)	1329(2)	47(1)
C(2)	1197(4)	10466(3)	1909(2)	47(1)
C(1)	1331(4)	11453(4)	1296(2)	53(2)
O(2)	-743(3)	8925(3)	4(2)	69(1)
N(5)	1940(3)	11096(3)	2749(2)	54(1)
C(3)	1637(3)	11107(3)	2176(2)	43(1)
C(6)	-636(4)	8697(4)	531(3)	56(2)
C(4)	1026(5)	9735(4)	2257(3)	69(2)
C(5)	1748(5)	10388(4)	3030(3)	77(2)
N(3)	601(5)	9075(4)	2062(3)	97(2)
C(7)	-1128(6)	7958(5)	761(4)	92(2)
C(8)	-2038(10)	8022(14)	660(17)	146(10)
C(9)	-2530(13)	8789(14)	807(17)	166(12)
C(10)	-3430(20)	8870(20)	610(20)	220(20)
C(8A)	-1360(20)	7947(13)	1396(8)	124(7)
C(9A)	-1840(20)	8631(17)	1693(11)	194(10)
C(10A)	-1990(30)	8580(30)	2354(12)	370(30)
C(8B)	-1470(50)	8230(40)	1348(14)	144(10)
C(9B)	-1540(40)	7690(40)	1878(13)	169(12)
C(10B)	-1010(50)	7800(30)	2420(20)	161(17)
O(1S)	0	7500	2814(14)	363(13)

Table A13. Bond lengths [Å] and angles [°] for **bio-MOF-14**.

N(4)-C(5)	1.324(8)
N(4)-C(4)	1.363(8)
Co(1)-O(2)#1	2.041(4)
Co(1)-O(1)	2.042(5)
Co(1)-N(2)	2.069(4)
Co(1)-N(1)#2	2.081(4)
Co(1)-N(5)#3	2.109(5)
Co(1)-Co(1)#1	2.9903(16)
N(1)-C(1)	1.341(7)
N(1)-C(3)	1.354(7)
N(1)-Co(1)#4	2.081(4)
O(1)-C(6)	1.265(7)
N(2)-C(1)	1.325(7)
N(2)-C(2)	1.379(7)
C(2)-C(3)	1.369(7)
C(2)-C(4)	1.421(8)
C(1)-H(1A)	0.9300
O(2)-C(6)	1.245(7)
O(2)-Co(1)#1	2.041(4)
N(5)-C(5)	1.321(8)
N(5)-C(3)	1.368(7)
N(5)-Co(1)#5	2.109(5)
C(6)-C(7)	1.498(9)
C(4)-N(3)	1.318(8)
C(5)-H(5A)	0.9300
N(3)-H(3A)	0.8600
N(3)-H(3B)	0.8600
C(7)-C(8)	1.464(15)
C(7)-C(8A)	1.465(14)
C(7)-C(8B)	1.485(18)
C(7)-H(7A)	0.9700

C(7)-H(7B)	0.9700
C(7)-H(7C)	0.9700
C(7)-H(7D)	0.9700
C(7)-H(7E)	0.9700
C(7)-H(7F)	0.9700
C(8)-C(9)	1.481(17)
C(8)-H(7C)	0.6663
C(8)-H(7E)	0.6301
C(8)-H(8A)	0.9700
C(8)-H(8B)	0.9700
C(9)-C(10)	1.495(18)
C(9)-H(9A)	0.9700
C(9)-H(9B)	0.9700
C(10)-H(10A)	0.9600
C(10)-H(10B)	0.9600
C(10)-H(10C)	0.9600
C(8A)-C(9A)	1.483(17)
C(8A)-H(8A1)	0.9700
C(8A)-H(8A2)	0.9700
C(9A)-C(10A)	1.500(18)
C(9A)-H(9A1)	0.9700
C(9A)-H(9A2)	0.9700
C(10A)-H(10D)	0.9600
C(10A)-H(10E)	0.9600
C(10A)-H(10F)	0.9600
C(8B)-C(9B)	1.468(18)
C(8B)-H(8B1)	0.9700
C(8B)-H(8B2)	0.9700
C(9B)-C(10B)	1.497(19)
C(9B)-H(9B1)	0.9700
C(9B)-H(9B2)	0.9700
C(10B)-O(1S)	1.88(6)
C(10B)-H(10G)	0.9600
C(10B)-H(10H)	0.9600
C(10B)-H(10I)	0.9600
O(1S)-C(10B)#6	1.88(6)

C(5)-N(4)-C(4)	119.1(6)
O(2)#1-Co(1)-O(1)	157.28(18)
O(2)#1-Co(1)-N(2)	96.56(19)
O(1)-Co(1)-N(2)	106.14(18)
O(2)#1-Co(1)-N(1)#2	89.67(19)
O(1)-Co(1)-N(1)#2	88.84(18)
N(2)-Co(1)-N(1)#2	96.28(18)
O(2)#1-Co(1)-N(5)#3	86.80(19)
O(1)-Co(1)-N(5)#3	88.48(19)
N(2)-Co(1)-N(5)#3	99.48(18)
N(1)#2-Co(1)-N(5)#3	164.14(17)
O(2)#1-Co(1)-Co(1)#1	69.77(13)
O(1)-Co(1)-Co(1)#1	87.66(13)
N(2)-Co(1)-Co(1)#1	165.72(14)
N(1)#2-Co(1)-Co(1)#1	80.02(12)
N(5)#3-Co(1)-Co(1)#1	84.26(12)
C(1)-N(1)-C(3)	102.3(5)
C(1)-N(1)-Co(1)#4	129.2(4)
C(3)-N(1)-Co(1)#4	128.5(3)
C(6)-O(1)-Co(1)	117.1(4)
C(1)-N(2)-C(2)	101.2(4)
C(1)-N(2)-Co(1)	120.3(4)
C(2)-N(2)-Co(1)	138.4(4)
C(3)-C(2)-N(2)	109.7(5)
C(3)-C(2)-C(4)	117.6(5)
N(2)-C(2)-C(4)	132.7(5)
N(2)-C(1)-N(1)	117.5(5)
N(2)-C(1)-H(1A)	121.2
N(1)-C(1)-H(1A)	121.2
C(6)-O(2)-Co(1)#1	142.1(4)
C(5)-N(5)-C(3)	112.0(5)
C(5)-N(5)-Co(1)#5	126.3(4)
C(3)-N(5)-Co(1)#5	121.6(4)
N(1)-C(3)-N(5)	125.5(5)
N(1)-C(3)-C(2)	109.2(5)

N(5)-C(3)-C(2)	125.3(5)
O(2)-C(6)-O(1)	123.0(6)
O(2)-C(6)-C(7)	118.7(6)
O(1)-C(6)-C(7)	118.2(6)
N(3)-C(4)-N(4)	118.5(6)
N(3)-C(4)-C(2)	124.4(6)
N(4)-C(4)-C(2)	117.1(6)
N(5)-C(5)-N(4)	128.9(6)
N(5)-C(5)-H(5A)	115.6
N(4)-C(5)-H(5A)	115.6
C(4)-N(3)-H(3A)	120.0
C(4)-N(3)-H(3B)	120.0
H(3A)-N(3)-H(3B)	120.0
C(8)-C(7)-C(8A)	85(2)
C(8)-C(7)-C(8B)	76(4)
C(8A)-C(7)-C(8B)	19(2)
C(8)-C(7)-C(6)	114.0(12)
C(8A)-C(7)-C(6)	118.0(13)
C(8B)-C(7)-C(6)	106(3)
C(8)-C(7)-H(7A)	108.8
C(8A)-C(7)-H(7A)	120.3
C(8B)-C(7)-H(7A)	139.3
C(6)-C(7)-H(7A)	108.8
C(8)-C(7)-H(7B)	108.8
C(8A)-C(7)-H(7B)	24.4
C(8B)-C(7)-H(7B)	38.9
C(6)-C(7)-H(7B)	108.8
H(7A)-C(7)-H(7B)	107.7
C(8)-C(7)-H(7C)	21.6
C(8A)-C(7)-H(7C)	105.4
C(8B)-C(7)-H(7C)	97.2
C(6)-C(7)-H(7C)	107.4
H(7A)-C(7)-H(7C)	93.0
H(7B)-C(7)-H(7C)	129.1
C(8)-C(7)-H(7D)	120.9
C(8A)-C(7)-H(7D)	110.6

C(8B)-C(7)-H(7D)	129.9
C(6)-C(7)-H(7D)	107.8
H(7A)-C(7)-H(7D)	14.8
H(7B)-C(7)-H(7D)	94.6
H(7C)-C(7)-H(7D)	107.0
C(8)-C(7)-H(7E)	18.9
C(8A)-C(7)-H(7E)	102.6
C(8B)-C(7)-H(7E)	94.5
C(6)-C(7)-H(7E)	109.1
H(7A)-C(7)-H(7E)	94.6
H(7B)-C(7)-H(7E)	126.3
H(7C)-C(7)-H(7E)	2.8
H(7D)-C(7)-H(7E)	108.4
C(8)-C(7)-H(7F)	120.0
C(8A)-C(7)-H(7F)	109.3
C(8B)-C(7)-H(7F)	128.6
C(6)-C(7)-H(7F)	109.4
H(7A)-C(7)-H(7F)	15.1
H(7B)-C(7)-H(7F)	93.7
H(7C)-C(7)-H(7F)	106.6
H(7D)-C(7)-H(7F)	1.7
H(7E)-C(7)-H(7F)	107.9
C(7)-C(8)-C(9)	123(2)
C(7)-C(8)-H(7C)	32.4
C(9)-C(8)-H(7C)	135.5
C(7)-C(8)-H(7E)	29.8
C(9)-C(8)-H(7E)	136.1
H(7C)-C(8)-H(7E)	2.8
C(7)-C(8)-H(8A)	106.6
C(9)-C(8)-H(8A)	106.6
H(7C)-C(8)-H(8A)	115.8
H(7E)-C(8)-H(8A)	114.2
C(7)-C(8)-H(8B)	106.6
C(9)-C(8)-H(8B)	106.6
H(7C)-C(8)-H(8B)	74.2
H(7E)-C(8)-H(8B)	76.9

H(8A)-C(8)-H(8B)	106.6
C(8)-C(9)-C(10)	121(2)
C(8)-C(9)-H(9A)	107.2
C(10)-C(9)-H(9A)	107.2
C(8)-C(9)-H(9B)	107.2
C(10)-C(9)-H(9B)	107.2
H(9A)-C(9)-H(9B)	106.8
C(9)-C(10)-H(10A)	109.5
C(9)-C(10)-H(10B)	109.5
H(10A)-C(10)-H(10B)	109.5
C(9)-C(10)-H(10C)	109.5
H(10A)-C(10)-H(10C)	109.5
H(10B)-C(10)-H(10C)	109.5
C(7)-C(8A)-C(9A)	123.5(18)
C(7)-C(8A)-H(8A1)	106.4
C(9A)-C(8A)-H(8A1)	106.4
C(7)-C(8A)-H(8A2)	106.4
C(9A)-C(8A)-H(8A2)	106.4
H(8A1)-C(8A)-H(8A2)	106.5
C(8A)-C(9A)-C(10A)	119(2)
C(8A)-C(9A)-H(9A1)	107.5
C(10A)-C(9A)-H(9A1)	107.5
C(8A)-C(9A)-H(9A2)	107.5
C(10A)-C(9A)-H(9A2)	107.5
H(9A1)-C(9A)-H(9A2)	107.0
C(9A)-C(10A)-H(10D)	109.5
C(9A)-C(10A)-H(10E)	109.5
H(10D)-C(10A)-H(10E)	109.5
C(9A)-C(10A)-H(10F)	109.5
H(10D)-C(10A)-H(10F)	109.5
H(10E)-C(10A)-H(10F)	109.5
C(9B)-C(8B)-C(7)	125(3)
C(9B)-C(8B)-H(8B1)	106.1
C(7)-C(8B)-H(8B1)	106.1
C(9B)-C(8B)-H(8B2)	106.1
C(7)-C(8B)-H(8B2)	106.1

H(8B1)-C(8B)-H(8B2)	106.3
C(8B)-C(9B)-C(10B)	123(2)
C(8B)-C(9B)-H(9B1)	106.6
C(10B)-C(9B)-H(9B1)	106.6
C(8B)-C(9B)-H(9B2)	106.6
C(10B)-C(9B)-H(9B2)	106.6
H(9B1)-C(9B)-H(9B2)	106.5
C(9B)-C(10B)-O(1S)	146(6)
C(9B)-C(10B)-H(10G)	109.5
O(1S)-C(10B)-H(10G)	38.4
C(9B)-C(10B)-H(10H)	109.5
O(1S)-C(10B)-H(10H)	80.9
H(10G)-C(10B)-H(10H)	109.5
C(9B)-C(10B)-H(10I)	109.5
O(1S)-C(10B)-H(10I)	96.7
H(10G)-C(10B)-H(10I)	109.5
H(10H)-C(10B)-H(10I)	109.5
C(10B)-O(1S)-C(10B)#6	125(4)

Symmetry transformations used to generate equivalent atoms:

#1 -x,-y+2,-z #2 y-5/4,-x+5/4,-z+1/4 #3 -y+5/4,x+3/4,z-1/4

#4 -y+5/4,x+5/4,-z+1/4 #5 y-3/4,-x+5/4,z+1/4

#6 -x+0,-y+3/2,z+0

Table A14. Anisotropic displacement parameters ($Å^2 \times 10^3$) for **Bio-MOF-14**. The anisotropic displacement factor exponent takes the form: $-2\pi^2[h^2 a^{*2} U^{11} + ... + 2 h k a^* b^* U^{12}]$

	U^{11}	U^{22}	U^{33}	U^{23}	U^{13}	U^{12}
N(4)	146(6)	63(4)	67(4)	24(3)	-44(4)	-42(4)
Co(1)	44(1)	52(1)	38(1)	-14(1)	-3(1)	1(1)
N(1)	55(3)	42(3)	41(2)	0(2)	-11(2)	-5(2)
O(1)	62(3)	58(3)	79(3)	-6(2)	-11(2)	-9(2)
N(2)	55(3)	47(3)	40(2)	-7(2)	-5(2)	-1(2)
C(2)	53(3)	41(3)	46(3)	-3(2)	-7(2)	0(3)
C(1)	67(4)	56(4)	37(3)	-5(2)	-10(3)	-7(3)
O(2)	81(3)	74(3)	53(2)	3(2)	13(2)	-2(2)
N(5)	68(3)	47(3)	45(2)	7(2)	-18(2)	-6(2)
C(3)	43(3)	41(3)	45(3)	-5(2)	-5(2)	1(2)
C(6)	59(4)	44(3)	65(4)	-4(3)	9(3)	-6(3)
C(4)	95(5)	51(4)	62(4)	3(3)	-22(4)	-18(4)
C(5)	115(6)	62(4)	55(4)	9(3)	-31(4)	-23(4)
N(3)	149(6)	55(4)	87(4)	11(3)	-47(4)	-42(4)
C(7)	93(6)	77(5)	106(6)	23(5)	-1(5)	-27(4)
C(8)	78(9)	119(18)	240(30)	9(19)	58(16)	-29(11)
C(9)	115(15)	111(19)	270(30)	10(20)	120(20)	-15(12)
C(10)	210(30)	160(40)	290(50)	-80(30)	-20(40)	90(30)
C(8A)	158(16)	101(15)	114(10)	35(10)	41(11)	-53(12)
C(9A)	220(20)	190(20)	172(17)	-16(16)	76(17)	-18(18)
C(10A)	400(50)	520(60)	200(20)	10(30)	170(40)	120(50)
C(8B)	170(20)	120(20)	143(15)	7(15)	72(17)	-70(20)
C(9B)	230(30)	150(20)	132(14)	11(19)	60(20)	-40(20)
C(10B)	260(40)	90(30)	120(20)	-20(30)	70(30)	-70(30)

Table A15. Hydrogen coordinates ($\times 10^4$) and isotropic displacement parameters ($Å^2 \times 10^3$) for **Bio-MOF-14**.

	x	y	z	U(eq)
H(1A)	1290	11773	948	64
H(5A)	1933	10351	3424	93
H(3A)	520	8650	2295	116
H(3B)	405	9069	1704	116
H(7A)	-921	7450	568	110
H(7B)	-1025	7901	1187	110
H(7C)	-1658	7944	545	110
H(7D)	-821	7450	655	110
H(7E)	-1673	7944	564	110
H(7F)	-832	7440	662	110
H(8A)	-2296	7560	878	175
H(8B)	-2131	7909	239	175
H(9A)	-2225	9267	643	199
H(9B)	-2521	8851	1239	199
H(10A)	-3664	9379	779	329
H(10B)	-3744	8395	750	329
H(10C)	-3453	8900	184	329
H(8A1)	-835	7886	1617	149
H(8A2)	-1675	7432	1460	149
H(9A1)	-2382	8670	1497	233
H(9A2)	-1544	9157	1615	233
H(10D)	-2342	9047	2476	562
H(10E)	-1466	8605	2563	562
H(10F)	-2275	8061	2446	562
H(8B1)	-1143	8715	1469	173
H(8B2)	-2039	8436	1269	173
H(9B1)	-1446	7113	1742	203

H(9B2)	-2123	7716	2009	203
H(10G)	-444	7613	2344	241
H(10H)	-1240	7483	2749	241
H(10I)	-996	8390	2532	241

Table A16. Lennard-Jones parameters for the bio-MOF atoms and the CO_2 molecule. ε is the well depth and σ is the diameter of the molecule. The charges on the CO_2 atoms are 0.6512 for C and -0.3256 for each O.

	ε (K)	σ (Å)
C	52.84	3.431
Co	7.045	2.557
H	22.14	2.571
N	34.72	3.261
O	30.19	3.118
C (CO_2)	29.933	2.745
O (CO_2)	85.671	3.017

Table A17. Atomic charges in the frameworks of **bio-MOF-12**, **bio-MOF-13**, and **bio-MOF-14**. The labels of each atomic type are given in Figure A4.

Atom type	**bio-MOF-12**	**bio-MOF-13**	**bio-MOF-14**
Co	0.620	0.456	0.581
O1	-0.737	-0.505	-0.650
O2	-0.573	-0.614	-0.613
N1	-0.070	0.089	-0.074
N2	-0.263	-0.193	-0.237
N3	-0.446	-0.464	-0.412
N4	-0.697	-0.691	-0.535
N5	-0.871	-0.820	-0.882
C1	-0.299	-0.498	-0.242
C2	0.488	0.563	0.494
C3	0.782	0.831	0.650
C4	-0.082	-0.143	-0.170
C5	0.368	0.406	0.281
C6	0.817	0.720	0.817
C7	-0.200	-0.231	-0.520
C8	-0.124	-0.064	0.033
H1	0.135	0.149	0.205
H2	0.068	0.048	0.074
H3	0.365	0.335	0.371
H4	0.424	0.360	0.434
H5	0.069	0.095	0.161
H6	0.072	0.067	0.135
H7	0.037	0.058	0.078
H8	0.053	0.061	0.026
H9	0.063	0.038	0.019
H10		0.035	-0.011
H11		0.060	0.095
C9		-0.147	0.132
C10			-0.400
H12			0.083
H13			0.076

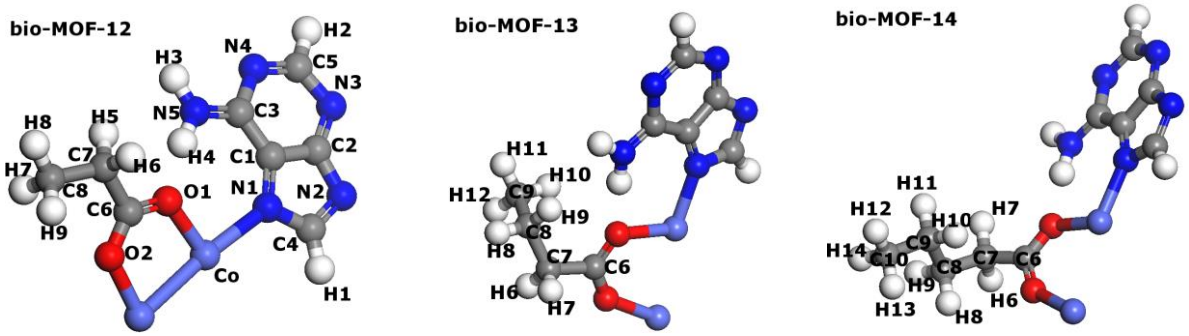

Figure A4. Labels for atom types in **bio-MOF-12**, **bio-MOF-13**, and **bio-MOF-14**. Note that the unlabeled atoms in **bio-MOF-13** and **bio-MOF-14** are the same to those in **bio-MOF-12** at the same sites.

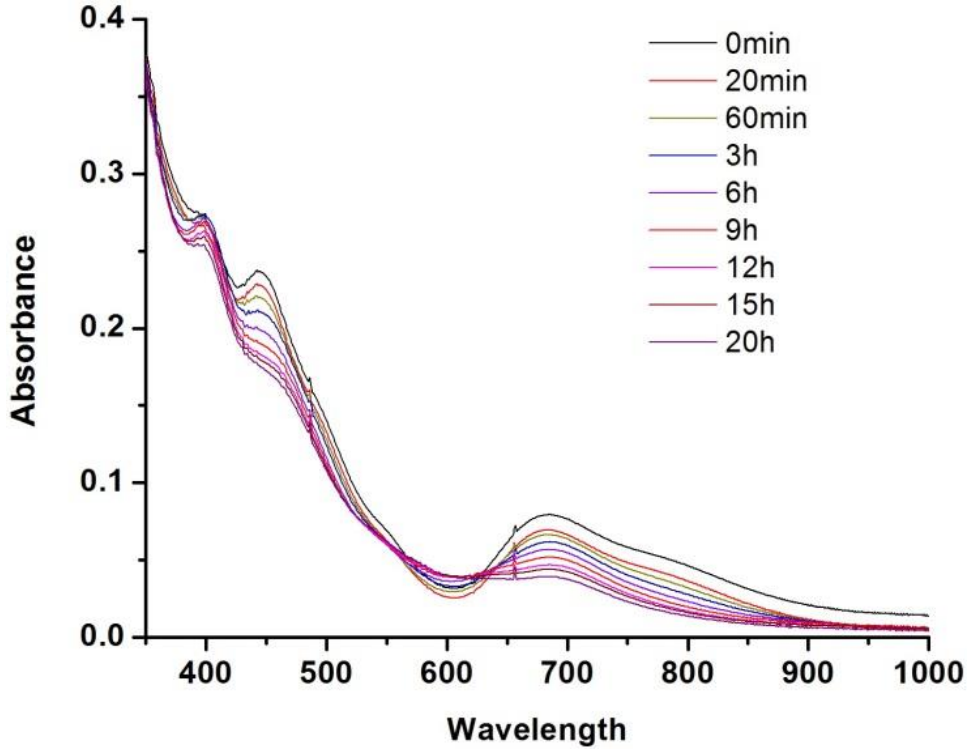

Figure A5. Oxidation of $Au25(SR)18^{-}$ to $Au25(SR)18^{+}$ monitored by UV-vis.

Table A18. CO_2 adsorption data of **bio-MOF-11** at various temperatures.

CO_2 adsorption of **bio-MOF-11** at various temperature									
273K		298K		303K		308K		313K	
Pressure (bar)	CO_2 adsorbed (cc/g)	Pressure (bar)	CO_2 adsorbed (cc/g)	Pressure (bar)	CO_2 adsorbed (cc/g)	Pressure (bar)	CO_2 adsorbed (cc/g)	Pressure (bar)	CO_2 adsorbed (cc/g)
2.07E-03	2.150316	2.05E-03	0.572088	2.09E-03	0.432483	2.13E-03	0.28638	2.14E-03	0.210191
3.12E-03	3.241832	3.10E-03	0.900596	3.13E-03	0.686371	3.19E-03	0.481782	3.08E-03	0.357191
4.11E-03	4.266571	4.18E-03	1.235827	4.21E-03	0.946757	4.12E-03	0.661274	4.13E-03	0.52391
5.19E-03	5.343746	5.35E-03	1.482992	5.19E-03	1.071349	5.33E-03	0.680097	5.38E-03	0.50307
6.26E-03	6.384843	6.17E-03	1.727468	6.23E-03	1.222382	6.39E-03	0.701385	6.45E-03	0.478421
7.15E-03	7.24981	7.16E-03	2.029983	7.22E-03	1.460808	7.44E-03	0.735222	7.50E-03	0.46632
8.19E-03	8.256398	8.20E-03	2.34527	8.33E-03	1.643212	8.48E-03	0.783176	8.55E-03	0.478645
9.27E-03	9.272845	9.28E-03	2.664142	9.32E-03	1.877157	9.53E-03	0.851746	9.60E-03	0.501501
1.04E-02	10.26151	1.04E-02	2.923632	1.05E-02	2.064716	1.06E-02	0.934209	1.07E-02	0.531305
2.05E-02	18.89414	2.03E-02	5.952584	2.08E-02	4.606283	2.12E-02	3.148837	2.15E-02	2.455295
3.10E-02	26.60355	3.05E-02	8.989154	3.10E-02	7.085107	3.14E-02	5.257697	3.17E-02	4.205396
4.14E-02	33.34424	4.07E-02	11.91861	4.12E-02	9.461749	4.16E-02	7.299332	4.18E-02	5.914713
5.18E-02	39.29705	5.10E-02	14.70219	5.15E-02	11.75369	5.18E-02	9.27038	5.20E-02	7.578766
6.23E-02	44.67732	6.11E-02	17.36118	6.17E-02	13.95599	6.19E-02	11.18899	6.22E-02	9.201587
7.26E-02	49.45413	7.14E-02	19.93591	7.19E-02	16.07247	7.21E-02	13.04643	7.24E-02	10.78945
8.29E-02	53.82602	8.16E-02	22.36118	8.21E-02	18.13181	8.23E-02	14.86107	8.24E-02	12.3614
9.08E-02	56.93026	9.19E-02	24.69076	9.23E-02	20.12302	9.25E-02	16.60377	9.27E-02	13.86322
1.03E-01	61.37028	1.02E-01	26.93385	1.02E-01	22.04589	1.03E-01	18.32698	1.03E-01	15.30005
1.54E-01	76.04648	1.53E-01	36.84377	1.54E-01	30.68682	1.54E-01	26.08681	1.54E-01	22.15032
2.02E-01	86.53498	2.04E-01	45.06498	2.04E-01	38.00161	2.05E-01	32.77977	2.05E-01	28.16139
2.54E-01	95.31193	2.55E-01	52.20679	2.55E-01	44.39564	2.55E-01	38.78636	2.55E-01	33.62838
3.05E-01	102.4136	3.06E-01	58.39399	3.06E-01	50.06498	3.06E-01	44.10232	3.06E-01	38.54636
3.56E-01	108.4247	3.57E-01	63.8789	3.57E-01	55.13087	3.57E-01	48.97549	3.57E-01	43.07601
4.07E-01	113.5681	4.07E-01	68.78143	4.08E-01	59.74701	4.08E-01	53.34312	4.08E-01	47.20544
4.58E-01	118.0563	4.58E-01	73.23601	4.58E-01	63.93582	4.58E-01	57.38112	4.58E-01	51.08031
5.09E-01	121.9935	5.09E-01	77.28858	5.09E-01	67.69753	5.09E-01	61.08815	5.09E-01	54.66634
5.60E-01	125.5472	5.60E-01	80.97096	5.57E-01	70.94586	5.57E-01	64.27665	5.57E-01	57.73114
6.07E-01	128.5515	6.10E-01	84.4362	6.07E-01	74.20069	6.10E-01	67.74033	6.07E-01	60.81007
6.61E-01	131.6932	6.58E-01	87.4302	6.58E-01	77.24376	6.58E-01	70.57254	6.58E-01	63.74109
7.09E-01	134.2502	7.09E-01	90.37825	7.09E-01	80.02958	7.09E-01	73.30614	7.09E-01	66.4505
7.60E-01	136.7438	7.60E-01	93.12038	7.60E-01	82.68498	7.60E-01	75.87595	7.60E-01	69.06109
8.11E-01	139.0703	8.11E-01	95.72715	8.11E-01	85.11787	8.11E-01	78.35925	8.11E-01	71.48165
8.61E-01	141.2172	8.61E-01	98.19634	8.61E-01	87.49899	8.62E-01	80.64783	8.61E-01	73.82064
9.12E-01	143.279	9.12E-01	100.5481	9.12E-01	89.69838	9.12E-01	82.80912	9.12E-01	75.94721
9.63E-01	145.1799	9.63E-01	102.8179	9.63E-01	91.818	9.63E-01	84.90857	9.63E-01	78.03792
1.01E+00	146.8563	1.01E+00	104.7811	1.01E+00	93.57482	1.01E+00	86.71626	1.01E+00	79.85121

Table A19. CO_2 adsorption data of **bio-MOF-12** at various temperatures.

CO_2 adsorption of **bio-MOF-12** at various temperature									
273K		298K		303K		308K		313K	
Pressure (bar)	CO_2 adsorbed (cc/g)	Pressure (bar)	CO_2 adsorbed (cc/g)	Pressure (bar)	CO_2 adsorbed (cc/g)	Pressure (bar)	CO_2 adsorbed (cc/g)	Pressure (bar)	CO_2 adsorbed (cc/g)
2.04E-03	2.959261	2.06E-03	0.770179	2.11E-03	0.458477	2.13E-03	0.240891	2.05E-03	0.265764
3.10E-03	4.400574	3.12E-03	1.164792	3.17E-03	0.734773	3.18E-03	0.451306	3.05E-03	0.447721
4.07E-03	5.641106	4.20E-03	1.56299	4.08E-03	0.984852	4.09E-03	0.648277	4.13E-03	0.643795
5.14E-03	6.952673	5.10E-03	1.870658	5.29E-03	1.04894	5.33E-03	0.663066	5.28E-03	0.717071
6.24E-03	8.21046	6.13E-03	2.231435	6.34E-03	1.100255	6.41E-03	0.664411	6.35E-03	0.776677
7.15E-03	9.195984	7.20E-03	2.602071	7.40E-03	1.172411	7.46E-03	0.685027	7.41E-03	0.845023
8.18E-03	10.27652	8.26E-03	2.968449	8.45E-03	1.264509	8.51E-03	0.722225	8.51E-03	0.905302
9.26E-03	11.35325	9.29E-03	3.298526	9.50E-03	1.371174	9.56E-03	0.762112	9.53E-03	0.984628
1.04E-02	12.38829	1.03E-02	3.63891	1.06E-02	1.484336	1.06E-02	0.828441	1.06E-02	1.050509
2.16E-02	20.67315	2.10E-02	6.820912	2.13E-02	4.288531	2.15E-02	3.188948	2.18E-02	3.040604
3.00E-02	25.28795	3.14E-02	9.809752	3.16E-02	6.771613	3.19E-02	5.306324	3.21E-02	4.790481
4.02E-02	29.76516	4.18E-02	12.42303	4.19E-02	9.016717	4.22E-02	7.256532	4.23E-02	6.451172
5.08E-02	33.64518	5.21E-02	14.79631	5.22E-02	11.08323	5.24E-02	9.060413	5.25E-02	8.007664
6.15E-02	36.84892	6.24E-02	16.95828	6.24E-02	12.98234	6.26E-02	10.73858	6.27E-02	9.487967
7.19E-02	39.63766	7.26E-02	18.92439	7.27E-02	14.7134	7.28E-02	12.31883	7.29E-02	10.89522
8.23E-02	42.08197	8.29E-02	20.70631	8.29E-02	16.29095	8.30E-02	13.81078	8.30E-02	12.26527
9.26E-02	44.28853	9.32E-02	22.37216	9.32E-02	17.80733	9.32E-02	15.20257	9.32E-02	13.52754
1.03E-01	46.29902	1.03E-01	23.93761	1.03E-01	19.20316	1.03E-01	16.52646	1.03E-01	14.74275
1.54E-01	54.35128	1.55E-01	30.31887	1.55E-01	25.0661	1.55E-01	22.17967	1.51E-01	19.59553
2.05E-01	60.3312	2.02E-01	34.96258	2.02E-01	29.3199	2.02E-01	26.37633	2.02E-01	23.81526
2.56E-01	65.30476	2.53E-01	39.16909	2.53E-01	33.13338	2.53E-01	30.2335	2.53E-01	27.45328
3.04E-01	69.17671	3.04E-01	42.7242	3.05E-01	36.37767	3.04E-01	33.47376	3.04E-01	30.57724
3.55E-01	72.83893	3.55E-01	45.93645	3.55E-01	39.23139	3.55E-01	36.41868	3.55E-01	33.39936
4.06E-01	76.03818	4.06E-01	48.76933	4.06E-01	41.80993	4.06E-01	39.0035	4.06E-01	35.85511
4.57E-01	78.92708	4.57E-01	51.3649	4.57E-01	44.17851	4.57E-01	41.42899	4.57E-01	38.14592
5.07E-01	81.55739	5.08E-01	53.67902	5.08E-01	46.28288	5.08E-01	43.61561	5.08E-01	40.29265
5.58E-01	83.97324	5.58E-01	55.92502	5.59E-01	48.208	5.59E-01	45.66195	5.59E-01	42.31143
6.09E-01	86.20356	6.09E-01	57.8759	6.09E-01	50.08605	6.09E-01	47.59871	6.09E-01	44.16484
6.60E-01	88.27903	6.60E-01	59.73334	6.60E-01	51.80791	6.60E-01	49.42679	6.60E-01	45.89746
7.11E-01	90.22095	7.11E-01	61.55963	7.11E-01	53.41572	7.11E-01	51.1128	7.11E-01	47.50751
7.61E-01	92.05575	7.62E-01	63.208	7.62E-01	54.92157	7.62E-01	52.68588	7.62E-01	48.89683
8.12E-01	93.86143	8.12E-01	64.83418	8.12E-01	56.39112	8.12E-01	54.23161	8.13E-01	50.16627
8.63E-01	95.5201	8.63E-01	66.40165	8.63E-01	57.76229	8.63E-01	55.56761	8.63E-01	51.40389
9.13E-01	97.08914	9.14E-01	67.91713	9.14E-01	59.06624	9.14E-01	56.86013	9.14E-01	52.8145
9.64E-01	98.56182	9.64E-01	69.33559	9.65E-01	60.34643	9.64E-01	58.208	9.64E-01	54.14176
1.01E+00	99.87451	1.01E+00	70.51853	1.01E+00	61.52714	1.01E+00	59.44517	1.01E+00	55.22364

Table A20. CO_2 adsorption data of **bio-MOF-13** at various temperatures.

CO_2 adsorption of **bio-MOF-13** at various temperature									
273K		298K		303K		308K		313K	
Pressure (bar)	CO_2 adsorbed (cc/g)	Pressure (bar)	CO_2 adsorbed (cc/g)	Pressure (bar)	CO_2 adsorbed (cc/g)	Pressure (bar)	CO_2 adsorbed (cc/g)	Pressure (bar)	CO_2 adsorbed (cc/g)
2.05E-03	3.045982	2.03E-03	0.758526	2.07E-03	0.407386	2.09E-03	0.403576	2.12E-03	0.299601
3.06E-03	4.356429	3.08E-03	1.126249	3.13E-03	0.670013	3.16E-03	0.612647	3.18E-03	0.468785
4.16E-03	5.66329	4.15E-03	1.478286	4.21E-03	0.938915	4.06E-03	0.807377	4.12E-03	0.60951
5.14E-03	6.737552	5.24E-03	1.826962	5.24E-03	1.01824	5.19E-03	0.953928	5.24E-03	0.699368
6.22E-03	7.827724	6.10E-03	2.099449	6.31E-03	1.124233	6.20E-03	1.152243	6.28E-03	0.793484
7.15E-03	8.688881	7.38E-03	2.500336	7.37E-03	1.237171	7.28E-03	1.358625	7.31E-03	0.951463
8.20E-03	9.597544	8.24E-03	2.758706	8.29E-03	1.443553	8.31E-03	1.562318	8.43E-03	1.050733
9.28E-03	10.47708	9.26E-03	3.065926	9.42E-03	1.585175	9.45E-03	1.725003	9.44E-03	1.210729
1.04E-02	11.29319	1.03E-02	3.386143	1.05E-02	1.719177	1.05E-02	1.921077	1.05E-02	1.369381
2.15E-02	17.26057	2.03E-02	6.095102	2.08E-02	3.979743	2.11E-02	3.954421	2.15E-02	3.060324
3.01E-02	20.32672	3.07E-02	8.579079	3.12E-02	6.02698	3.15E-02	5.716623	3.19E-02	4.51284
4.06E-02	23.07892	4.14E-02	10.61982	4.16E-02	7.832878	4.18E-02	7.301349	4.21E-02	5.858692
5.13E-02	25.24044	5.17E-02	12.40846	5.19E-02	9.420069	5.21E-02	8.71734	5.24E-02	7.093847
6.19E-02	27.0004	6.22E-02	13.94568	6.23E-02	10.85466	6.24E-02	10.00381	6.26E-02	8.234437
7.24E-02	28.47645	7.25E-02	15.3182	7.25E-02	12.13441	7.26E-02	11.19684	7.28E-02	9.290772
8.27E-02	29.7851	8.27E-02	16.5305	8.28E-02	13.27724	8.29E-02	12.26662	8.30E-02	10.28795
9.30E-02	30.93398	9.30E-02	17.62829	9.31E-02	14.33178	9.31E-02	13.26446	9.32E-02	11.20065
1.03E-01	31.97172	1.03E-01	18.63645	1.03E-01	15.29646	1.03E-01	14.18344	1.03E-01	12.03671
1.55E-01	36.02586	1.55E-01	22.59109	1.55E-01	19.19733	1.55E-01	17.95657	1.55E-01	15.61332
2.02E-01	38.84148	2.03E-01	25.26778	2.03E-01	21.872	2.03E-01	20.55976	2.03E-01	18.20934
2.53E-01	41.37073	2.54E-01	27.60655	2.54E-01	24.23139	2.54E-01	22.88374	2.54E-01	20.50352
3.05E-01	43.49012	3.05E-01	29.53861	3.05E-01	26.15628	3.05E-01	24.77502	3.05E-01	22.40398
3.55E-01	45.37019	3.56E-01	31.25241	3.56E-01	27.86559	3.56E-01	26.46193	3.56E-01	24.08932
4.06E-01	47.02035	4.07E-01	32.74526	4.06E-01	29.34769	4.07E-01	27.90571	4.07E-01	25.55259
4.57E-01	48.55129	4.57E-01	34.14646	4.57E-01	30.71304	4.57E-01	29.23632	4.57E-01	26.91122
5.08E-01	49.90006	5.08E-01	35.38498	5.08E-01	31.96208	5.08E-01	30.41993	5.08E-01	28.09842
5.59E-01	51.14149	5.59E-01	36.56546	5.59E-01	33.1094	5.59E-01	31.54215	5.59E-01	29.18859
6.09E-01	52.35603	6.10E-01	37.66728	6.09E-01	34.21996	6.10E-01	32.61305	6.10E-01	30.28817
6.60E-01	53.46569	6.60E-01	38.72025	6.60E-01	35.23731	6.60E-01	33.59477	6.60E-01	31.30776
7.11E-01	54.49783	7.11E-01	39.68942	7.11E-01	36.18048	7.11E-01	34.54197	7.11E-01	32.21777
7.62E-01	55.46206	7.62E-01	40.65612	7.62E-01	37.10057	7.62E-01	35.39058	7.62E-01	33.09573
8.12E-01	56.40008	8.12E-01	41.56366	8.12E-01	37.93887	8.12E-01	36.1937	8.13E-01	33.88316
8.63E-01	57.29754	8.63E-01	42.45193	8.63E-01	38.74445	8.63E-01	36.94304	8.63E-01	34.7069
9.14E-01	58.13091	9.14E-01	43.28217	9.14E-01	39.5543	9.14E-01	37.74168	9.14E-01	35.43338
9.64E-01	58.89997	9.65E-01	44.10187	9.65E-01	40.27137	9.65E-01	38.47466	9.65E-01	36.15941
1.01E+00	59.61816	1.01E+00	44.83082	1.01E+00	40.94519	1.01E+00	38.74289	1.01E+00	36.74853

Table A21. CO_2 adsorption data of **bio-MOF-14** at various temperatures.

CO_2 adsorption of **bio-MOF-14** at various temperature									
273K		298K		303K		308K		313K	
Pressure (bar)	CO_2 adsorbed (cc/g)	Pressure (bar)	CO_2 adsorbed (cc/g)	Pressure (bar)	CO_2 adsorbed (cc/g)	Pressure (bar)	CO_2 adsorbed (cc/g)	Pressure (bar)	CO_2 adsorbed (cc/g)
2.03E-03	0.323802	2.28E-02	0.385874	3.31E-02	0.262851	3.31E-02	0.044369	4.34E-02	0.097701
3.04E-03	0.488056	3.30E-02	0.817237	4.33E-02	0.605925	4.33E-02	0.351589	5.36E-02	0.358087
4.10E-03	0.65119	4.32E-02	1.218348	5.34E-02	0.945637	5.34E-02	0.645588	6.36E-02	0.621163
5.17E-03	0.803343	5.33E-02	1.607583	6.36E-02	1.284677	6.36E-02	0.93152	7.38E-02	0.863622
6.25E-03	0.953032	6.35E-02	1.966791	7.37E-02	1.610944	7.37E-02	1.21409	8.40E-02	1.089723
7.32E-03	1.098015	7.36E-02	2.328463	8.38E-02	1.91189	8.38E-02	1.482096	9.41E-02	1.336217
8.38E-03	1.233362	8.38E-02	2.653386	9.40E-02	2.21799	9.40E-02	1.740017	1.04E-01	1.580245
9.46E-03	1.371846	9.39E-02	2.984807	1.04E-01	2.517142	1.04E-01	2.009815	1.54E-01	2.576525
1.05E-02	1.500695	1.04E-01	3.295612	1.54E-01	3.80406	1.54E-01	3.139874	2.05E-01	3.452696
2.21E-02	2.792767	1.54E-01	4.686282	2.04E-01	4.973334	2.05E-01	4.167526	2.55E-01	4.364944
3.25E-02	3.830951	2.04E-01	5.991574	2.55E-01	6.156277	2.55E-01	5.23753	3.06E-01	5.152602
4.27E-02	4.742975	2.55E-01	7.338323	3.06E-01	7.272666	3.06E-01	6.199525	3.57E-01	6.066195
5.29E-02	5.60458	3.06E-01	8.636445	3.56E-01	8.418635	3.57E-01	7.173845	4.07E-01	6.940797
6.31E-02	6.391565	3.56E-01	9.99507	4.07E-01	9.576256	4.07E-01	8.133599	4.58E-01	7.868955
7.32E-02	7.189755	4.07E-01	11.40008	4.58E-01	10.77869	4.58E-01	9.133465	5.09E-01	8.778515
8.34E-02	7.944696	4.57E-01	12.89965	5.08E-01	12.00242	5.09E-01	10.11137	5.59E-01	9.692556
9.35E-02	8.687985	5.08E-01	14.54466	5.59E-01	13.30592	5.59E-01	11.14597	6.10E-01	10.55752
1.04E-01	9.436427	5.58E-01	16.36423	6.09E-01	14.65312	6.10E-01	12.19917	6.61E-01	11.46619
1.51E-01	13.09685	6.09E-01	18.396	6.60E-01	16.1137	6.60E-01	13.31063	7.11E-01	12.3688
2.03E-01	20.85219	6.59E-01	20.60032	7.11E-01	17.61776	7.11E-01	14.41021	7.62E-01	13.262
2.55E-01	29.45435	7.10E-01	22.72285	7.61E-01	19.26993	7.62E-01	15.57007	8.12E-01	14.20741
3.05E-01	31.8487	7.61E-01	24.55609	8.12E-01	20.936	8.12E-01	16.78349	8.63E-01	15.15955
3.56E-01	33.64317	8.12E-01	26.04804	8.63E-01	22.47434	8.63E-01	18.0303	9.14E-01	16.13902
4.07E-01	35.08672	8.63E-01	27.35625	9.13E-01	23.93806	9.13E-01	19.28584	9.64E-01	17.09362
4.58E-01	36.31246	9.14E-01	28.57908	9.64E-01	25.22431	9.64E-01	20.54027	1.01E+00	18.15713
5.08E-01	37.39255	9.65E-01	29.69524	1.01E+00	26.23605	1.01E+00	21.66585		
5.59E-01	38.38121	1.01E+00	30.6727						
6.10E-01	39.29324								
6.61E-01	40.1526								
7.11E-01	40.93174								
7.62E-01	41.67615								
8.13E-01	42.39658								
8.63E-01	43.05427								
9.14E-01	43.66289								
9.65E-01	44.26612								
1.01E+00	44.79474								

Table A22. Crystal data and structure refinement for **bio-MOF-101**.

Identification code	bio-MOF-101	
Empirical formula	C46 H26 N10 O13 Zn4	
Formula weight	1188.25	
Temperature	296(2) K	
Wavelength	1.54178 Å	
Crystal system	Cubic	
Space group	Ia-3d	
Unit cell dimensions	a = 62.039(5) Å	= 90 °.
	b = 62.039(5) Å	= 90°.
	c = 62.039(5) Å	= 90°.
Volume	238775(34) $Å^3$	
Z	48	
Density (calculated)	0.397 Mg/m^3	
Absorption coefficient	0.703 mm^{-1}	
F(000)	28608	
Crystal size	0.40 x 0.40 x 0.30 mm^3	
Theta range for data collection	1.74 to 37.74 °.	
Index ranges	0<=h<=28, 0<=k<=34, 2<=l<=49	
Reflections collected	5235	
Independent reflections	5235 [R(int) = 0.0000]	
Completeness to theta = 37.74 °	99.9 %	
Absorption correction	multi scan (SADABS)	
Max. and min. transmission	0.8167 and 0.7661	
Refinement method	Full-matrix least-squares on F^2	
Data / restraints / parameters	5235 / 348 / 330	
Goodness-of-fit on F^2	1.171	
Final R indices [I>2sigma(I)]	R1 = 0.0536, wR2 = 0.1678	
R indices (all data)	R1 = 0.0660, wR2 = 0.1757	
Largest diff. peak and hole	0.144 and -0.184 $e.Å^{-3}$	

Table A23. Atomic coordinates ($\times 10^4$) and equivalent isotropic displacement parameters ($Å^2 \times 10^3$) for **bio-MOF-101**. U(eq) is defined as one third of the trace of the orthogonalized U^{ij} tensor.

	x	y	z	U(eq)
O(55)	4311(1)	1917(1)	1347(1)	177(2)
C(36)	4160(1)	1880(2)	1474(2)	179(3)
O(45)	4054(1)	2028(1)	1551(1)	238(3)
C(39)	4105(1)	1647(1)	1529(1)	171(3)
C(40)	4212(1)	1483(2)	1433(1)	188(3)
C(42)	4144(1)	1268(2)	1486(1)	171(3)
C(53)	3878(2)	1399(2)	1737(2)	239(5)
C(37)	3945(2)	1601(1)	1681(2)	232(4)
O(15)	4087(1)	2396(1)	1109(1)	179(2)
C(16)	3965(2)	2294(2)	992(2)	210(4)
O(25)	3984(1)	2095(1)	976(1)	284(4)
C(19)	3788(1)	2411(2)	858(1)	225(4)
C(20)	3776(2)	2617(2)	835(2)	251(4)
C(22)	3591(2)	2700(2)	714(2)	271(5)
C(23)	3582(2)	2899(2)	656(2)	352(6)
C(27)	3405(2)	2964(2)	544(2)	328(6)
C(29)	3253(2)	2830(2)	467(2)	278(6)
C(30)	3286(2)	2627(2)	474(2)	341(6)
C(32)	3460(2)	2562(2)	598(3)	321(6)
C(33)	3460(2)	2356(2)	645(3)	391(7)
C(17)	3632(2)	2274(2)	759(2)	360(7)
O(35)	2936(1)	2848(1)	257(2)	278(4)
C(26)	3079(2)	2951(2)	330(2)	240(5)
O(13)	3096(1)	3149(1)	304(1)	253(3)
C(14)	4624(2)	2750(2)	1500(2)	167(3)

N(15)	4703(1)	2962(1)	1485(1)	160(2)
C(11)	4847(1)	2959(1)	1648(2)	161(3)
N(13)	4869(1)	2782(1)	1771(1)	166(2)
C(9)	4730(1)	2642(2)	1683(2)	164(3)
N(7)	4692(1)	2436(1)	1749(1)	159(2)
C(12)	4548(1)	2339(1)	1613(1)	155(3)
N(10)	4442(1)	2420(1)	1449(1)	167(2)
C(6)	4478(2)	2646(2)	1395(2)	176(3)
N(8)	4365(1)	2736(1)	1233(1)	177(2)
Zn(1)	4298(1)	2209(1)	1242(1)	155(1)
Zn(2)	4885(1)	2274(1)	1971(1)	171(1)
O(1)	5000	2500	2150(1)	181(2)

—

Table A24. Bond lengths [Å] and angles [°] for **bio-MOF-101**.

O(55)-C(36)	1.247(8)
O(55)-Zn(1)	1.929(4)
C(36)-O(45)	1.226(8)
C(36)-C(39)	1.522(10)
C(39)-C(40)	1.353(8)
C(39)-C(37)	1.398(9)
C(40)-C(42)	1.440(10)
C(40)-H(40A)	0.9300
C(42)-C(53)#1	1.362(11)
C(42)-C(42)#1	1.399(14)
C(53)-C(42)#1	1.362(11)
C(53)-C(37)	1.363(9)
C(53)-H(53A)	0.9300
C(37)-H(37A)	0.9300
O(15)-C(16)	1.229(8)
O(15)-Zn(1)	1.933(5)
C(16)-O(25)	1.246(8)
C(16)-C(19)	1.555(11)
C(19)-C(20)	1.293(9)
C(19)-C(17)	1.423(11)
C(20)-C(22)	1.462(10)
C(20)-H(20A)	0.9300
C(22)-C(23)	1.287(11)
C(22)-C(32)	1.382(15)
C(23)-C(27)	1.359(11)
C(23)-H(23A)	0.9300
C(27)-C(29)	1.348(12)
C(27)-H(27A)	0.9300
C(29)-C(30)	1.277(12)
C(29)-C(26)	1.567(14)
C(30)-C(32)	1.384(12)

C(30)-H(30A)	0.9300
C(32)-C(33)	1.314(12)
C(33)-C(17)	1.381(11)
C(33)-H(33A)	0.9300
C(17)-H(17A)	0.9300
O(35)-C(26)	1.187(10)
O(35)-Zn(2)#2	1.936(7)
C(26)-O(13)	1.241(10)
C(14)-C(6)	1.287(10)
C(14)-N(15)	1.407(9)
C(14)-C(9)	1.472(11)
N(15)-C(11)	1.351(8)
N(15)-Zn(1)#3	2.044(7)
C(11)-N(13)	1.340(8)
C(11)-H(11A)	0.9300
N(13)-C(9)	1.339(9)
N(13)-Zn(2)#4	1.999(7)
C(9)-N(7)	1.364(10)
N(7)-C(12)	1.371(8)
N(7)-Zn(2)	2.078(7)
C(12)-N(10)	1.312(8)
C(12)-H(12A)	0.9300
N(10)-C(6)	1.463(10)
N(10)-Zn(1)	2.040(7)
C(6)-N(8)	1.349(10)
N(8)-H(8A)	0.8600
N(8)-H(8B)	0.8600
Zn(1)-N(15)#5	2.044(7)
Zn(2)-O(1)	1.926(4)
Zn(2)-O(35)#6	1.936(7)
Zn(2)-N(13)#4	1.999(7)
Zn(2)-Zn(2)#4	3.1440(19)
O(1)-Zn(2)#4	1.926(4)

C(36)-O(55)-Zn(1)	110.8(6)
O(45)-C(36)-O(55)	121.0(10)

O(45)-C(36)-C(39)	120.0(9)
O(55)-C(36)-C(39)	119.0(9)
C(40)-C(39)-C(37)	119.2(7)
C(40)-C(39)-C(36)	120.4(9)
C(37)-C(39)-C(36)	120.5(9)
C(39)-C(40)-C(42)	117.2(9)
C(39)-C(40)-H(40A)	121.4
C(42)-C(40)-H(40A)	121.4
C(53)#1-C(42)-C(42)#1	121.5(13)
C(53)#1-C(42)-C(40)	117.9(9)
C(42)#1-C(42)-C(40)	120.5(10)
C(42)#1-C(53)-C(37)	116.0(10)
C(42)#1-C(53)-H(53A)	122.0
C(37)-C(53)-H(53A)	122.0
C(53)-C(37)-C(39)	125.3(8)
C(53)-C(37)-H(37A)	117.3
C(39)-C(37)-H(37A)	117.3
C(16)-O(15)-Zn(1)	111.0(7)
O(15)-C(16)-O(25)	120.2(11)
O(15)-C(16)-C(19)	120.7(10)
O(25)-C(16)-C(19)	119.1(10)
C(20)-C(19)-C(17)	120.2(8)
C(20)-C(19)-C(16)	124.3(11)
C(17)-C(19)-C(16)	115.5(9)
C(19)-C(20)-C(22)	116.7(10)
C(19)-C(20)-H(20A)	121.6
C(22)-C(20)-H(20A)	121.6
C(23)-C(22)-C(32)	114.7(10)
C(23)-C(22)-C(20)	120.9(12)
C(32)-C(22)-C(20)	120.9(9)
C(22)-C(23)-C(27)	117.8(11)
C(22)-C(23)-H(23A)	121.1
C(27)-C(23)-H(23A)	121.1
C(29)-C(27)-C(23)	124.0(10)
C(29)-C(27)-H(27A)	118.0
C(23)-C(27)-H(27A)	118.0

C(30)-C(29)-C(27)	119.2(10)
C(30)-C(29)-C(26)	127.1(13)
C(27)-C(29)-C(26)	112.0(12)
C(29)-C(30)-C(32)	115.3(11)
C(29)-C(30)-H(30A)	122.4
C(32)-C(30)-H(30A)	122.4
C(33)-C(32)-C(22)	119.1(11)
C(33)-C(32)-C(30)	113.9(13)
C(22)-C(32)-C(30)	124.9(10)
C(32)-C(33)-C(17)	118.2(10)
C(32)-C(33)-H(33A)	120.9
C(17)-C(33)-H(33A)	120.9
C(33)-C(17)-C(19)	121.9(9)
C(33)-C(17)-H(17A)	119.0
C(19)-C(17)-H(17A)	119.0
C(26)-O(35)-Zn(2)#2	111.2(10)
O(35)-C(26)-O(13)	123.2(15)
O(35)-C(26)-C(29)	117.4(13)
O(13)-C(26)-C(29)	119.5(13)
C(6)-C(14)-N(15)	132.6(12)
C(6)-C(14)-C(9)	118.5(12)
N(15)-C(14)-C(9)	108.8(10)
C(11)-N(15)-C(14)	99.4(8)
C(11)-N(15)-Zn(1)#3	121.0(6)
C(14)-N(15)-Zn(1)#3	137.2(7)
N(13)-C(11)-N(15)	120.5(8)
N(13)-C(11)-H(11A)	119.7
N(15)-C(11)-H(11A)	119.7
C(9)-N(13)-C(11)	103.4(9)
C(9)-N(13)-Zn(2)#4	129.2(7)
C(11)-N(13)-Zn(2)#4	125.1(7)
N(13)-C(9)-N(7)	126.6(11)
N(13)-C(9)-C(14)	107.8(10)
N(7)-C(9)-C(14)	125.6(10)
C(9)-N(7)-C(12)	109.9(9)
C(9)-N(7)-Zn(2)	123.6(7)

C(12)-N(7)-Zn(2)	124.8(6)
N(10)-C(12)-N(7)	129.4(8)
N(10)-C(12)-H(12A)	115.3
N(7)-C(12)-H(12A)	115.3
C(12)-N(10)-C(6)	118.1(9)
C(12)-N(10)-Zn(1)	117.5(6)
C(6)-N(10)-Zn(1)	122.5(7)
C(14)-C(6)-N(8)	122.6(12)
C(14)-C(6)-N(10)	118.1(11)
N(8)-C(6)-N(10)	119.2(10)
C(6)-N(8)-H(8A)	120.0
C(6)-N(8)-H(8B)	120.0
H(8A)-N(8)-H(8B)	120.0
O(55)-Zn(1)-O(15)	137.4(2)
O(55)-Zn(1)-N(10)	111.8(3)
O(15)-Zn(1)-N(10)	100.3(3)
O(55)-Zn(1)-N(15)#5	100.6(3)
O(15)-Zn(1)-N(15)#5	102.3(3)
N(10)-Zn(1)-N(15)#5	97.3(2)
O(1)-Zn(2)-O(35)#6	108.8(3)
O(1)-Zn(2)-N(13)#4	101.7(2)
O(35)#6-Zn(2)-N(13)#4	126.1(4)
O(1)-Zn(2)-N(7)	104.2(2)
O(35)#6-Zn(2)-N(7)	116.8(4)
N(13)#4-Zn(2)-N(7)	96.4(2)
O(1)-Zn(2)-Zn(2)#4	35.30(15)
O(35)#6-Zn(2)-Zn(2)#4	143.8(3)
N(13)#4-Zn(2)-Zn(2)#4	78.9(2)
N(7)-Zn(2)-Zn(2)#4	80.3(2)
Zn(2)#4-O(1)-Zn(2)	109.4(3)

Symmetry transformations used to generate equivalent atoms:

#1 z+1/4,-y+1/4,x-1/4 #2 -y+1/2,-z+1/2,-x+1/2

#3 y+1/4,-x+3/4,-z+1/4 #4 -x+1,-y+1/2,z+0 #5 -y+3/4,x-1/4,-z+1/4

#6 -z+1/2,-x+1/2,-y+1/2

Table A25. Anisotropic displacement parameters ($Å^2 \times 10^3$) for **bio-MOF-101**. The anisotropic displacement factor exponent takes the form: $-2\ ^2[\ h^2\ a^{*2}U^{11} + ...\ + 2\ h\ k\ a^*\ b^*\ U^{12}\ ]$

	U^{11}	U^{22}	U^{33}	U^{23}	U^{13}	U^{12}
O(55)	129(4)	136(4)	268(6)	48(3)	-13(3)	-28(3)
C(36)	121(8)	140(7)	275(11)	47(7)	8(6)	-10(6)
O(45)	212(6)	134(5)	367(8)	43(5)	76(5)	6(4)
C(39)	148(7)	133(6)	233(9)	34(6)	6(5)	-21(6)
C(40)	183(8)	138(7)	244(9)	30(7)	15(6)	0(6)
C(42)	193(8)	128(7)	193(8)	8(8)	2(6)	-5(8)
C(53)	299(12)	140(8)	278(11)	19(8)	99(9)	-34(8)
C(37)	258(10)	131(7)	306(11)	26(7)	101(8)	-12(7)
O(15)	122(4)	170(4)	246(6)	28(4)	-12(3)	15(3)
C(16)	159(9)	197(9)	273(12)	27(9)	-46(6)	15(8)
O(25)	245(7)	194(5)	413(9)	-5(7)	-121(6)	17(6)
C(19)	147(7)	238(10)	290(10)	50(9)	-50(6)	37(7)
C(20)	200(9)	240(9)	315(11)	24(9)	-13(7)	67(8)
C(22)	243(11)	282(10)	289(12)	61(10)	-6(7)	134(9)
C(23)	293(13)	308(11)	457(17)	47(13)	-92(10)	100(11)
C(27)	241(14)	359(11)	384(16)	67(12)	-63(11)	150(10)
C(29)	183(10)	377(14)	273(12)	73(12)	10(7)	108(10)
C(30)	263(12)	384(12)	377(15)	73(13)	-42(9)	114(11)
C(32)	250(13)	354(11)	357(16)	96(13)	-60(9)	61(11)
C(33)	321(14)	367(12)	484(17)	85(15)	-198(12)	10(13)
C(17)	260(12)	311(10)	507(17)	58(11)	-207(11)	1(9)
O(35)	231(8)	297(7)	306(9)	49(7)	-57(6)	50(6)
C(26)	255(14)	289(13)	175(10)	27(12)	-3(9)	64(10)
O(13)	209(6)	293(8)	257(7)	47(7)	-28(4)	42(6)
C(14)	158(8)	140(7)	203(8)	-10(6)	4(5)	0(5)
N(15)	132(5)	125(5)	223(6)	1(5)	-2(4)	8(4)
C(11)	128(6)	131(6)	223(9)	17(6)	0(5)	9(5)
N(13)	186(7)	125(6)	186(6)	14(4)	8(5)	-2(5)

C(9)	131(7)	170(8)	190(8)	17(6)	21(5)	-7(6)
N(7)	136(5)	152(5)	188(6)	-1(5)	11(4)	-13(4)
C(12)	117(7)	147(7)	201(8)	-13(5)	24(4)	3(5)
N(10)	129(5)	138(5)	235(7)	20(5)	-10(4)	-10(4)
C(6)	171(9)	150(7)	206(9)	-15(6)	-10(6)	-19(6)
N(8)	175(6)	146(5)	211(6)	8(4)	-28(5)	1(4)
Zn(1)	118(1)	122(1)	224(1)	15(1)	-4(1)	-6(1)
Zn(2)	171(1)	142(1)	199(1)	10(1)	14(1)	-2(1)
O(1)	198(6)	162(5)	182(5)	0	0	-6(4)

Table A26. Hydrogen coordinates ($\times 10^4$) and isotropic displacement parameters ($Å^2 \times 10^3$) for **bio-MOF-101**.

	x	y	z	U(eq)
H(40A)	4324	1508	1337	226
H(53A)	3765	1377	1832	287
H(37A)	3879	1717	1749	278
H(20A)	3880	2709	892	302
H(23A)	3693	2994	689	423
H(27A)	3388	3111	520	394
H(30A)	3199	2529	400	410
H(33A)	3347	2267	602	469
H(17A)	3647	2125	772	431
H(11A)	4931	3079	1676	193
H(12A)	4520	2194	1642	186
H(8A)	4388	2868	1196	212
H(8B)	4268	2662	1166	212

Table A27. Crystal data and structure refinement for **bio-MOF-102**.

Identification code	bio-MOF-102
Empirical formula	C52 H32 N16 O13 Zn4
Formula weight	1350.42
Temperature	296(2) K
Wavelength	1.54178 Å
Crystal system	Cubic
Space group	Ia-3d
Unit cell dimensions	a = 75.2379(13) Å = 90°.
	b = 75.2379(13) Å = 90°.
	c = 75.2379(13) Å = 90°.
Volume	425902(13) $Å^3$
Z	48
Density (calculated)	0.253 Mg/m^3
Absorption coefficient	0.412 mm^{-1}
F(000)	32640
Crystal size	0.24 x 0.15 x 0.15 mm^3
Theta range for data collection	1.44 to 25.41 °.
Index ranges	-41<=h<=41, -41<=k<=41, -41<=l<=41
Reflections collected	994984
Independent reflections	3226 [R(int) = 0.2434]
Completeness to theta = 25.41 °	100.0 %
Absorption correction	multi scan (SADABS)
Max. and min. transmission	0.9408 and 0.9075
Refinement method	Full-matrix least-squares on F^2
Data / restraints / parameters	3226 / 160 / 160
Goodness-of-fit on F^2	2.616
Final R indices [I>2sigma(I)]	R1 = 0.2380, wR2 = 0.5382
R indices (all data)	R1 = 0.2843, wR2 = 0.5803
Largest diff. peak and hole	0.510 and -0.502 $e.Å^{-3}$

Table A28. Atomic coordinates ($\times 10^4$) and equivalent isotropic displacement parameters ($Å^2 \times 10^3$) for **bio-MOF-102**. U(eq) is defined as one third of the trace of the orthogonalized U^{ij} tensor.

	x	y	z	U(eq)
O(44)	4616(4)	6734(4)	4023(3)	258(14)
C(45)	4490(5)	6815(4)	3954(4)	271(19)
O(43)	4541(4)	6915(3)	3833(4)	228(12)
C(46)	4317(5)	6777(7)	4009(7)	283(18)
C(51)	4297(7)	6659(6)	4140(6)	279(19)
C(50)	4120(10)	6624(5)	4201(5)	330(20)
C(49)	3986(6)	6699(8)	4109(8)	323(19)
C(48)	4006(7)	6823(6)	3985(6)	274(18)
C(47)	4185(9)	6862(4)	3928(4)	271(18)
N(8)	3818(5)	6644(6)	4176(6)	360(20)
O(14)	5537(4)	5366(5)	2706(4)	268(14)
C(15)	5608(5)	5507(5)	2758(5)	310(20)
O(13)	5774(4)	5509(3)	2738(3)	247(13)
C(16)	5536(11)	5650(7)	2851(5)	336(19)
C(24)	5357(11)	5631(6)	2877(6)	430(20)
C(22)	5261(5)	5760(11)	2964(7)	460(30)
C(21)	5346(11)	5910(8)	3026(4)	420(20)
C(26)	5525(11)	5929(6)	3001(6)	340(20)
C(19)	5620(4)	5801(11)	2912(7)	330(20)
N(7)	5210(8)	6113(6)	3176(6)	400(20)
O(29)	4925(4)	6754(4)	3653(4)	247(12)
C(30)	4871(5)	6652(5)	3532(5)	310(20)
O(28)	4706(5)	6671(4)	3522(4)	302(16)
C(31)	4946(11)	6508(5)	3443(6)	320(19)
C(39)	5122(11)	6488(7)	3463(5)	310(20)
C(37)	5208(4)	6360(10)	3374(9)	340(20)

C(36)	5119(12)	6252(6)	3264(7)	390(20)
C(34)	4942(11)	6270(7)	3247(5)	410(20)
C(32)	4857(4)	6398(10)	3334(9)	380(20)
N(6)	5275(9)	6057(7)	3119(6)	430(20)
C(1)	5217(2)	7201(2)	3971(2)	236(16)
N(1)	5385(2)	7269(2)	3966(2)	212(13)
C(2)	5383(3)	7383(2)	4098(3)	238(17)
N(2)	5233(4)	7396(2)	4188(2)	230(14)
C(3)	5126(3)	7279(2)	4107(2)	226(15)
N(3)	4959(3)	7241(3)	4153(2)	218(13)
C(4)	4890(2)	7118(3)	4052(3)	216(15)
N(4)	4962(2)	7035(2)	3918(3)	239(14)
C(5)	5129(2)	7074(2)	3872(2)	244(16)
N(5)	5198(3)	6989(2)	3736(2)	209(14)
Zn(1)	4771(1)	6923(1)	3747(1)	227(5)
Zn(2)	4814(1)	7407(1)	4342(1)	234(5)
O(3)	5000	7500	4488(5)	198(14)

—

Table A29. Bond lengths [Å] and angles [°] for **bio-MOF-102**.

O(44)-C(45)	1.24(2)
C(45)-O(43)	1.25(2)
C(45)-C(46)	1.395(10)
O(43)-Zn(1)	1.85(3)
C(46)-C(47)	1.33(5)
C(46)-C(51)	1.33(5)
C(51)-C(50)	1.44(4)
C(51)-H(51A)	0.9300
C(50)-C(49)	1.35(5)
C(50)-H(50A)	0.9300
C(49)-C(48)	1.33(5)
C(49)-N(8)	1.424(19)
C(48)-C(47)	1.45(4)
C(48)-H(48A)	0.9300
C(47)-H(47A)	0.9300
N(8)-N(8)#1	1.08(9)
O(14)-C(15)	1.251(19)
O(14)-Zn(2)#2	1.84(4)
C(15)-O(13)	1.25(2)
C(15)-C(16)	1.397(10)
C(16)-C(24)	1.372(19)
C(16)-C(19)	1.38(2)
C(24)-C(22)	1.38(2)
C(24)-H(24A)	0.9300
C(22)-C(21)	1.38(2)
C(22)-H(22A)	0.9300
C(21)-C(26)	1.37(2)
C(21)-N(6)	1.414(19)
C(26)-C(19)	1.37(2)
C(26)-H(26A)	0.9300
C(19)-H(19A)	0.9300

N(7)-N(6)	0.77(6)
N(7)-C(36)	1.414(19)
O(29)-C(30)	1.25(2)
O(29)-Zn(1)	1.86(3)
C(30)-O(28)	1.25(2)
C(30)-C(31)	1.395(10)
C(31)-C(39)	1.339(18)
C(31)-C(32)	1.340(18)
C(39)-C(37)	1.340(18)
C(39)-H(39A)	0.9300
C(37)-C(36)	1.338(18)
C(37)-H(37A)	0.9300
C(36)-C(34)	1.342(18)
C(34)-C(32)	1.335(18)
C(34)-H(34A)	0.9300
C(32)-H(32A)	0.9300
C(1)-C(3)	1.3588
C(1)-N(1)	1.3679
C(1)-C(5)	1.3789
N(1)-C(2)	1.3111
N(1)-Zn(1)#3	2.16(2)
C(2)-N(2)	1.3238
C(2)-H(2A)	0.9300
N(2)-C(3)	1.3375
N(2)-Zn(2)#4	1.915(16)
C(3)-N(3)	1.3368
N(3)-C(4)	1.3054
N(3)-Zn(2)	2.186(17)
C(4)-N(4)	1.3005
C(4)-H(4A)	0.9300
N(4)-C(5)	1.3329
N(4)-Zn(1)	2.111(17)
C(5)-N(5)	1.3150
N(5)-H(5A)	0.8600
N(5)-H(5B)	0.8600
Zn(1)-N(1)#5	2.16(4)

Zn(2)-O(14)#6	1.84(4)
Zn(2)-O(3)	1.91(2)
Zn(2)-N(2)#4	1.91(3)
Zn(2)-Zn(2)#4	3.132(14)
O(3)-Zn(2)#4	1.91(2)

O(44)-C(45)-O(43)	112(3)
O(44)-C(45)-C(46)	119(4)
O(43)-C(45)-C(46)	129(5)
C(45)-O(43)-Zn(1)	124(3)
C(47)-C(46)-C(51)	126(3)
C(47)-C(46)-C(45)	117(7)
C(51)-C(46)-C(45)	117(6)
C(46)-C(51)-C(50)	117(3)
C(46)-C(51)-H(51A)	121.4
C(50)-C(51)-H(51A)	121.4
C(49)-C(50)-C(51)	117(3)
C(49)-C(50)-H(50A)	121.6
C(51)-C(50)-H(50A)	121.6
C(48)-C(49)-C(50)	125(3)
C(48)-C(49)-N(8)	123(7)
C(50)-C(49)-N(8)	111(7)
C(49)-C(48)-C(47)	117(3)
C(49)-C(48)-H(48A)	121.5
C(47)-C(48)-H(48A)	121.5
C(46)-C(47)-C(48)	117(3)
C(46)-C(47)-H(47A)	121.4
C(48)-C(47)-H(47A)	121.4
N(8)#1-N(8)-C(49)	135(9)
C(15)-O(14)-Zn(2)#2	124(3)
O(13)-C(15)-O(14)	113(4)
O(13)-C(15)-C(16)	116(4)
O(14)-C(15)-C(16)	130(5)
C(24)-C(16)-C(19)	119.6(10)
C(24)-C(16)-C(15)	112(7)
C(19)-C(16)-C(15)	128(7)

C(16)-C(24)-C(22)	120.4(11)
C(16)-C(24)-H(24A)	119.8
C(22)-C(24)-H(24A)	119.8
C(21)-C(22)-C(24)	119.8(11)
C(21)-C(22)-H(22A)	120.1
C(24)-C(22)-H(22A)	120.1
C(26)-C(21)-C(22)	119.8(10)
C(26)-C(21)-N(6)	111(8)
C(22)-C(21)-N(6)	129(8)
C(21)-C(26)-C(19)	120.4(11)
C(21)-C(26)-H(26A)	119.8
C(19)-C(26)-H(26A)	119.8
C(26)-C(19)-C(16)	120.0(10)
C(26)-C(19)-H(19A)	120.0
C(16)-C(19)-H(19A)	120.0
N(6)-N(7)-C(36)	165(10)
C(30)-O(29)-Zn(1)	120(3)
O(29)-C(30)-O(28)	107(3)
O(29)-C(30)-C(31)	134(5)
O(28)-C(30)-C(31)	117(5)
C(39)-C(31)-C(32)	119.6(11)
C(39)-C(31)-C(30)	116(8)
C(32)-C(31)-C(30)	125(8)
C(31)-C(39)-C(37)	120.1(11)
C(31)-C(39)-H(39A)	120.0
C(37)-C(39)-H(39A)	120.0
C(36)-C(37)-C(39)	120.3(11)
C(36)-C(37)-H(37A)	119.9
C(39)-C(37)-H(37A)	119.9
C(37)-C(36)-C(34)	119.6(11)
C(37)-C(36)-N(7)	120(9)
C(34)-C(36)-N(7)	121(9)
C(32)-C(34)-C(36)	120.1(11)
C(32)-C(34)-H(34A)	120.0
C(36)-C(34)-H(34A)	120.0
C(34)-C(32)-C(31)	120.4(11)

C(34)-C(32)-H(32A)	119.8
C(31)-C(32)-H(32A)	119.8
N(7)-N(6)-C(21)	160(10)
C(3)-C(1)-N(1)	108.8
C(3)-C(1)-C(5)	117.6
N(1)-C(1)-C(5)	133.6
C(2)-N(1)-C(1)	102.4
C(2)-N(1)-Zn(1)#3	124.5(8)
C(1)-N(1)-Zn(1)#3	130.0(8)
N(1)-C(2)-N(2)	116.3
N(1)-C(2)-H(2A)	121.8
N(2)-C(2)-H(2A)	121.8
C(2)-N(2)-C(3)	103.3
C(2)-N(2)-Zn(2)#4	121.5(13)
C(3)-N(2)-Zn(2)#4	132.7(12)
N(3)-C(3)-N(2)	125.7
N(3)-C(3)-C(1)	125.1
N(2)-C(3)-C(1)	109.2
C(4)-N(3)-C(3)	111.9
C(4)-N(3)-Zn(2)	125.9(11)
C(3)-N(3)-Zn(2)	121.3(11)
N(4)-C(4)-N(3)	128.6
N(4)-C(4)-H(4A)	115.7
N(3)-C(4)-H(4A)	115.7
C(4)-N(4)-C(5)	119.2
C(4)-N(4)-Zn(1)	112.4(10)
C(5)-N(4)-Zn(1)	124.8(10)
N(5)-C(5)-N(4)	118.0
N(5)-C(5)-C(1)	124.4
N(4)-C(5)-C(1)	117.5
C(5)-N(5)-H(5A)	120.0
C(5)-N(5)-H(5B)	120.0
H(5A)-N(5)-H(5B)	120.0
O(43)-Zn(1)-O(29)	134.2(12)
O(43)-Zn(1)-N(4)	115.9(10)
O(29)-Zn(1)-N(4)	94.8(11)

O(43)-Zn(1)-N(1)#5	106.0(12)
O(29)-Zn(1)-N(1)#5	100.2(10)
N(4)-Zn(1)-N(1)#5	100.7(9)
O(14)#6-Zn(2)-O(3)	115.1(16)
O(14)#6-Zn(2)-N(2)#4	121.6(15)
O(3)-Zn(2)-N(2)#4	101.5(14)
O(14)#6-Zn(2)-N(3)	115.2(11)
O(3)-Zn(2)-N(3)	102.6(10)
N(2)#4-Zn(2)-N(3)	97.8(12)
O(14)#6-Zn(2)-Zn(2)#4	149.9(11)
O(3)-Zn(2)-Zn(2)#4	35.1(10)
N(2)#4-Zn(2)-Zn(2)#4	79.5(13)
N(3)-Zn(2)-Zn(2)#4	78.9(7)
Zn(2)-O(3)-Zn(2)#4	110(2)

Symmetry transformations used to generate equivalent atoms:

#1 -x+3/4,z+1/4,y-1/4 #2 -z+1,-x+1,-y+1 #3 -y+5/4,x+1/4,-z+3/4

#4 -x+1,-y+3/2,z+0 #5 y-1/4,-x+5/4,-z+3/4 #6 -y+1,-z+1,-x+1

Table A30. Anisotropic displacement parameters ($Å^2 \times 10^3$) for **bio-MOF-102**. The anisotropic displacement factor exponent takes the form: $-2^2[h^2 a^{*2} U^{11} + ... + 2 h k a^* b^* U^{12}]$

	U^{11}	U^{22}	U^{33}	U^{23}	U^{13}	U^{12}
Zn(1)	161(8)	187(8)	334(9)	-16(6)	38(6)	8(5)
Zn(2)	173(9)	234(8)	296(10)	17(7)	9(7)	-20(7)
O(3)	160(40)	190(40)	250(50)	0	0	60(20)

Table A31. Hydrogen coordinates ($\times 10^4$) and isotropic displacement parameters ($Å^2 \times 10^3$) for **bio-MOF-102**.

	x	y	z	U(eq)
H(51A)	4395	6602	4190	335
H(50A)	4098	6553	4300	391
H(48A)	3909	6883	3938	329
H(47A)	4208	6944	3837	325
H(24A)	5299	5529	2836	520
H(22A)	5139	5747	2981	553
H(26A)	5583	6030	3043	409
H(19A)	5741	5816	2894	398
H(39A)	5184	6563	3539	375
H(37A)	5330	6346	3389	414
H(34A)	4879	6192	3174	487
H(32A)	4735	6412	3320	451
H(2A)	5482	7451	4127	286
H(4A)	4774	7085	4080	259
H(5A)	5136	6911	3680	251
H(5B)	5306	7011	3704	251

Table A32. Crystal data and structure refinement for **bio-MOF-104**.

Identification code	bio-MOF-104	
Empirical formula	C46 H32 N10 O12.50 Zn4	
Formula weight	1186.30	
Temperature	296(2) K	
Wavelength	0.77490 Å	
Crystal system	Cubic	
Space group	Ia-3d	
Unit cell dimensions	a = 69.615(6) Å	a= 90 °.
	b = 69.615(6) Å	b= 90 °.
	c = 69.615(6) Å	g = 90 °.
Volume	337369(49) $Å^3$	
Z	48	
Density (calculated)	0.280 Mg/m^3	
Absorption coefficient	0.441 mm^{-1}	
F(000)	28704	
Crystal size	0.25 x 0.25 x 0.25 mm^3	
Theta range for data collection	0.78 to 12.79 °.	
Index ranges	-39<=h<=39, -39<=k<=39, -39<=l<=39	
Reflections collected	193379	
Independent reflections	2760 [R(int) = 0.1733]	
Completeness to theta = 12.79 °	100.0 %	
Absorption correction	Multiscan	
Max. and min. transmission	0.8976 and 0.8976	
Refinement method	Full-matrix least-squares on F^2	
Data / restraints / parameters	2760 / 1 / 76	
Goodness-of-fit on F^2	2.798	
Final R indices [I>2sigma(I)]	R1 = 0.2799, wR2 = 0.5731	
R indices (all data)	R1 = 0.3702, wR2 = 0.6341	
Largest diff. peak and hole	0.335 and -0.812 $e.Å^{-3}$	

Table A33. Atomic coordinates ($\times 10^4$) and equivalent isotropic displacement parameters ($Å^2 \times 10^3$) for **bio-MOF-104**. U(eq) is defined as one third of the trace of the orthogonalized U^{ij} tensor.

	x	y	z	U(eq)
O(25)	4181(3)	2432(4)	1100(3)	364(16)
C(13)	4075(3)	2307(3)	1010(3)	420(30)
O(26)	4096(3)	2131(3)	1026(3)	560(30)
C(14)	3917(3)	2377(3)	893(2)	380(30)
C(15)	3891(2)	2563(3)	859(2)	450(30)
C(16)	3725(2)	2637(3)	745(2)	540(40)
C(17)	3699(2)	2825(3)	724(3)	560(50)
C(18)	3591(3)	2514(2)	655(3)	630(60)
O(27)	2938(3)	2974(4)	187(3)	420(20)
C(19)	3054(2)	3093(3)	267(2)	340(20)
O(28)	3032(3)	3273(3)	256(3)	440(20)
C(20)	3209(2)	3026(3)	381(2)	470(40)
C(21)	3247(2)	2846(3)	421(2)	380(30)
C(22)	3409(2)	2777(3)	537(2)	480(40)
C(23)	3440(3)	2583(2)	562(3)	630(60)
C(24)	3545(2)	2902(2)	624(2)	480(40)
O(35)	4370(3)	1973(2)	1330(3)	337(15)
C(29)	4251(3)	1967(2)	1474(3)	360(20)
O(36)	4178(4)	2113(3)	1547(4)	450(20)
C(30)	4191(3)	1781(3)	1546(3)	420(30)
C(31)	4270(3)	1618(2)	1484(3)	400(30)
C(32)	4204(4)	1426(2)	1552(4)	360(30)
C(33)	4279(5)	1267(2)	1477(5)	490(40)
C(34)	4063(5)	1403(4)	1695(4)	440(30)
Zn(2)	4910(1)	2299(1)	1887(1)	372(6)
C(5)	4672(2)	2730(3)	1483(2)	390(30)

N(5)	4748(3)	2916(3)	1485(3)	330(18)
C(3)	4869(3)	2910(4)	1633(4)	360(30)
N(4)	4880(3)	2741(5)	1728(3)	323(18)
C(2)	4753(3)	2627(4)	1632(2)	350(30)
N(1)	4711(4)	2441(4)	1677(3)	353(19)
C(4)	4578(4)	2369(3)	1561(4)	320(20)
N(3)	4491(3)	2452(3)	1413(4)	410(20)
C(1)	4535(2)	2637(3)	1369(3)	380(30)
N(2)	4445(3)	2717(4)	1219(3)	331(18)
Zn(1)	4371(1)	2247(1)	1250(1)	362(6)
O(1)	5000	2500	2054(8)	150(20)

—

Table A34. Bond lengths [Å] and angles [°] for **bio-MOF-104**.

O(25)-C(13)	1.3042
O(25)-Zn(1)	2.118(19)
C(13)-O(26)	1.2382
C(13)-C(14)	1.4540
C(14)-C(15)	1.3283
C(14)-H(14A)	0.9300
C(15)-C(16)	1.4904
C(15)-H(15A)	0.9300
C(16)-C(17)	1.3300
C(16)-C(18)	1.4114
C(17)-C(24)	1.3878
C(17)-H(17A)	0.9300
C(18)-C(23)	1.3266
C(18)-H(18A)	0.9300
O(27)-C(19)	1.2859
O(27)-Zn(2)#1	2.026(19)
C(19)-O(28)	1.2598
C(19)-C(20)	1.4184
C(20)-C(21)	1.3081
C(20)-H(20A)	0.9300
C(21)-C(22)	1.4631
C(21)-H(21A)	0.9300
C(22)-C(23)	1.3812
C(22)-C(24)	1.4209
C(23)-H(23A)	0.9300
C(24)-H(24A)	0.9300
O(35)-C(29)	1.3040
O(35)-Zn(1)	1.987(9)
C(29)-O(36)	1.2380
C(29)-C(30)	1.4533
C(30)-C(31)	1.3290

C(30)-H(30A)	0.9300
C(31)-C(32)	1.4903
C(31)-H(31A)	0.9300
C(32)-C(33)	1.3299
C(32)-C(34)	1.4112
C(33)-C(34)#2	1.45(4)
C(33)-H(33A)	0.9300
C(34)-C(33)#2	1.45(3)
C(34)-H(34A)	0.9300
Zn(2)-N(4)#3	1.85(3)
Zn(2)-O(1)	1.92(3)
Zn(2)-O(27)#4	2.03(2)
Zn(2)-N(1)	2.25(2)
Zn(2)-Zn(2)#3	3.069(16)
C(5)-C(2)	1.3845
C(5)-N(5)	1.3937
C(5)-C(1)	1.4042
N(5)-C(3)	1.3330
N(5)-Zn(1)#5	2.21(2)
C(3)-N(4)	1.3495
C(3)-H(3A)	0.9300
N(4)-C(2)	1.3600
N(4)-Zn(2)#3	1.853(19)
C(2)-N(1)	1.3593
N(1)-C(4)	1.3288
C(4)-N(3)	1.3249
C(4)-H(4A)	0.9300
N(3)-C(1)	1.3560
N(3)-Zn(1)	2.01(2)
C(1)-N(2)	1.3373
N(2)-H(2A)	0.8600
N(2)-H(2B)	0.8600
Zn(1)-N(5)#6	2.21(5)
O(1)-Zn(2)#3	1.92(3)

C(13)-O(25)-Zn(1)	100.7(9)

O(26)-C(13)-O(25)	123.3
O(26)-C(13)-C(14)	118.4
O(25)-C(13)-C(14)	118.3
C(15)-C(14)-C(13)	122.1
C(15)-C(14)-H(14A)	118.9
C(13)-C(14)-H(14A)	118.9
C(14)-C(15)-C(16)	122.3
C(14)-C(15)-H(15A)	118.8
C(16)-C(15)-H(15A)	118.8
C(17)-C(16)-C(18)	116.9
C(17)-C(16)-C(15)	120.4
C(18)-C(16)-C(15)	122.7
C(16)-C(17)-C(24)	123.0
C(16)-C(17)-H(17A)	118.5
C(24)-C(17)-H(17A)	118.5
C(23)-C(18)-C(16)	121.8
C(23)-C(18)-H(18A)	119.1
C(16)-C(18)-H(18A)	119.1
C(19)-O(27)-Zn(2)#1	110.4(9)
O(28)-C(19)-O(27)	122.4
O(28)-C(19)-C(20)	117.2
O(27)-C(19)-C(20)	120.3
C(21)-C(20)-C(19)	126.3
C(21)-C(20)-H(20A)	116.8
C(19)-C(20)-H(20A)	116.8
C(20)-C(21)-C(22)	125.9
C(20)-C(21)-H(21A)	117.0
C(22)-C(21)-H(21A)	117.0
C(23)-C(22)-C(24)	116.2
C(23)-C(22)-C(21)	120.7
C(24)-C(22)-C(21)	123.0
C(18)-C(23)-C(22)	122.5
C(18)-C(23)-H(23A)	118.7
C(22)-C(23)-H(23A)	118.7
C(17)-C(24)-C(22)	119.5
C(17)-C(24)-H(24A)	120.3

C(22)-C(24)-H(24A)	120.3
C(29)-O(35)-Zn(1)	104.1(10)
O(36)-C(29)-O(35)	123.3
O(36)-C(29)-C(30)	118.4
O(35)-C(29)-C(30)	118.2
C(31)-C(30)-C(29)	122.2
C(31)-C(30)-H(30A)	118.9
C(29)-C(30)-H(30A)	118.9
C(30)-C(31)-C(32)	122.4
C(30)-C(31)-H(31A)	118.8
C(32)-C(31)-H(31A)	118.8
C(33)-C(32)-C(34)	117.0
C(33)-C(32)-C(31)	120.4
C(34)-C(32)-C(31)	122.6
C(32)-C(33)-C(34)#2	111(4)
C(32)-C(33)-H(33A)	124.3
C(34)#2-C(33)-H(33A)	124.3
C(32)-C(34)-C(33)#2	132(4)
C(32)-C(34)-H(34A)	114.2
C(33)#2-C(34)-H(34A)	114.2
N(4)#3-Zn(2)-O(1)	102.3(19)
N(4)#3-Zn(2)-O(27)#4	115(2)
O(1)-Zn(2)-O(27)#4	114(2)
N(4)#3-Zn(2)-N(1)	99.3(16)
O(1)-Zn(2)-N(1)	105.7(12)
O(27)#4-Zn(2)-N(1)	117.6(14)
N(4)#3-Zn(2)-Zn(2)#3	79.4(17)
O(1)-Zn(2)-Zn(2)#3	37.1(13)
O(27)#4-Zn(2)-Zn(2)#3	151.5(17)
N(1)-Zn(2)-Zn(2)#3	81.2(9)
C(2)-C(5)-N(5)	108.7
C(2)-C(5)-C(1)	117.6
N(5)-C(5)-C(1)	133.6
C(3)-N(5)-C(5)	102.5
C(3)-N(5)-Zn(1)#5	126.5(10)
C(5)-N(5)-Zn(1)#5	128.1(10)

N(5)-C(3)-N(4)	116.3
N(5)-C(3)-H(3A)	121.8
N(4)-C(3)-H(3A)	121.8
C(3)-N(4)-C(2)	103.3
C(3)-N(4)-Zn(2)#3	117.9(17)
C(2)-N(4)-Zn(2)#3	135.7(17)
N(1)-C(2)-N(4)	125.7
N(1)-C(2)-C(5)	125.1
N(4)-C(2)-C(5)	109.2
C(4)-N(1)-C(2)	112.0
C(4)-N(1)-Zn(2)	131.1(14)
C(2)-N(1)-Zn(2)	115.7(14)
N(3)-C(4)-N(1)	128.5
N(3)-C(4)-H(4A)	115.7
N(1)-C(4)-H(4A)	115.7
C(4)-N(3)-C(1)	119.3
C(4)-N(3)-Zn(1)	108.5(14)
C(1)-N(3)-Zn(1)	129.6(13)
N(2)-C(1)-N(3)	118.1
N(2)-C(1)-C(5)	124.5
N(3)-C(1)-C(5)	117.5
C(1)-N(2)-H(2A)	120.0
C(1)-N(2)-H(2B)	120.0
H(2A)-N(2)-H(2B)	120.0
O(35)-Zn(1)-N(3)	121.7(12)
O(35)-Zn(1)-O(25)	136.1(10)
N(3)-Zn(1)-O(25)	96.1(11)
O(35)-Zn(1)-N(5)#6	102.1(12)
N(3)-Zn(1)-N(5)#6	97.8(12)
O(25)-Zn(1)-N(5)#6	93.0(9)
Zn(2)#3-O(1)-Zn(2)	106(3)

Symmetry transformations used to generate equivalent atoms:

#1 -y+1/2,-z+1/2,-x+1/2 #2 z+1/4,-y+1/4,x-1/4

#3 -x+1,-y+1/2,z+0 #4 -z+1/2,-x+1/2,-y+1/2 #5 y+1/4,-x+3/4,-z+1/4

#6 -y+3/4,x-1/4,-z+1/4

Table A35. Anisotropic displacement parameters ($Å^2 \times 10^3$) for **bio-MOF-104**. The anisotropic displacement factor exponent takes the form: $-2p^2[h^2 a^{*2} U^{11} + ... + 2 h k a^* b^* U^{12}]$

	U^{11}	U^{22}	U^{33}	U^{23}	U^{13}	U^{12}
Zn(2)	330(10)	277(10)	507(13)	35(9)	51(9)	35(7)
Zn(1)	273(8)	256(8)	557(13)	53(7)	6(8)	-12(5)
O(1)	270(70)	10(40)	180(60)	0	0	-10(40)

Table A36. Hydrogen coordinates ($\times 10^4$) and isotropic displacement parameters ($Å^2 \times 10^3$) for **bio-MOF-104**.

	x	y	z	U(eq)
H(14A)	3831	2290	840	461
H(15A)	3980	2651	907	540
H(17A)	3787	2909	780	675
H(18A)	3610	2382	661	760
H(20A)	3291	3118	432	568
H(21A)	3164	2754	372	455
H(23A)	3351	2497	512	760
H(24A)	3531	3035	613	581
H(30A)	4094	1775	1638	509
H(31A)	4370	1625	1396	477
H(33A)	4373	1265	1383	586
H(34A)	4016	1518	1745	525
H(3A)	4941	3016	1669	437
H(4A)	4541	2243	1587	380
H(2A)	4362	2652	1155	397
H(2B)	4470	2834	1187	397

Table A37. Crystal data and structure refinement for **bio-MOF-105**.

Identification code	bio-MOF-105	
Empirical formula	C58 H38 N10 O13 Zn4	
Formula weight	1344.46	
Temperature	296(2) K	
Wavelength	0.77490 Å	
Crystal system	Cubic	
Space group	Ia-3d	
Unit cell dimensions	a = 76.615(9) Å	a= 90 °.
	b = 76.615(9) Å	b= 90 °.
	c = 76.615(9) Å	g = 90 °.
Volume	449726(90) $Å^3$	
Z	48	
Density (calculated)	0.238 Mg/m^3	
Absorption coefficient	0.333 mm^{-1}	
F(000)	32640	
Crystal size	0.40 x 0.40 x 0.30 mm^3	
Theta range for data collection	0.71 to 11.16 °.	
Index ranges	-38<=h<=38, -38<=k<=38, -38<=l<=38	
Reflections collected	182689	
Independent reflections	2468 [R(int) = 0.1370]	
Completeness to theta = 11.16 °	99.9 %	
Absorption correction	Multiscan	
Max. and min. transmission	0.9067 and 0.8783	
Refinement method	Full-matrix least-squares on F^2	
Data / restraints / parameters	2468 / 101 / 160	
Goodness-of-fit on F^2	2.840	
Final R indices [I>2sigma(I)]	R1 = 0.2283, wR2 = 0.5252	
R indices (all data)	R1 = 0.2693, wR2 = 0.5668	
Largest diff. peak and hole	0.442 and -0.520 $e.Å^{-3}$	

Table A38. Atomic coordinates ($\times 10^4$) and equivalent isotropic displacement parameters ($Å^2 \times 10^3$) for **bio-MOF-105**. U(eq) is defined as one third of the trace of the orthogonalized U^{ij} tensor.

	x	y	z	U(eq)
O(44)	4624(5)	6737(5)	4012(5)	277(18)
C(45)	4535(9)	6836(4)	3940(5)	240(40)
O(43)	4536(6)	6930(4)	3821(5)	233(17)
C(46)	4334(6)	6782(8)	4010(8)	230(20)
C(51)	4302(9)	6658(7)	4140(8)	300(30)
C(50)	4126(12)	6630(5)	4186(5)	330(30)
C(49)	3998(7)	6717(10)	4102(10)	310(30)
C(48)	4029(8)	6840(6)	3977(7)	290(30)
C(47)	4210(13)	6868(5)	3929(5)	330(30)
C(52)	3820(8)	6685(9)	4145(9)	380(40)
O(14)	5539(5)	5339(7)	2692(5)	241(17)
C(15)	5588(13)	5485(8)	2748(8)	360(40)
O(13)	5763(5)	5491(4)	2741(4)	235(17)
C(16)	5538(11)	5633(8)	2841(6)	310(30)
C(24)	5358(12)	5616(7)	2851(7)	450(40)
C(22)	5258(6)	5741(11)	2937(8)	460(40)
C(21)	5339(11)	5885(8)	3014(6)	440(40)
C(26)	5520(11)	5902(6)	3004(6)	320(30)
C(19)	5620(5)	5779(11)	2915(8)	310(30)
C(17)	5237(7)	6136(7)	3194(9)	350(30)
O(29)	4916(5)	6766(5)	3657(5)	209(15)
C(30)	4883(12)	6683(8)	3522(11)	400(50)
O(28)	4708(5)	6676(4)	3530(5)	300(20)
C(31)	4944(11)	6529(8)	3447(8)	290(30)

C(39)	5128(11)	6521(8)	3461(7)	330(30)
C(37)	5221(5)	6386(11)	3377(10)	360(30)
C(36)	5133(12)	6268(8)	3265(9)	350(30)
C(34)	4949(12)	6270(9)	3260(8)	420(40)
C(32)	4856(5)	6408(12)	3338(10)	420(40)
C(41)	5255(9)	6026(8)	3093(9)	400(40)
C(1)	5211(2)	7206(2)	3967(2)	280(20)
N(1)	5379(3)	7274(2)	3969(3)	206(16)
C(2)	5372(4)	7386(2)	4103(3)	210(20)
N(2)	5218(5)	7397(2)	4188(2)	240(19)
C(3)	5116(3)	7281(2)	4101(2)	230(20)
N(3)	4947(3)	7242(4)	4141(3)	241(17)
C(4)	4882(2)	7120(4)	4036(4)	197(19)
N(4)	4959(2)	7039(3)	3903(3)	273(19)
C(5)	5127(2)	7080(2)	3864(2)	270(20)
N(5)	5202(4)	6997(3)	3729(3)	253(19)
Zn(1)	4772(1)	6933(1)	3746(1)	229(6)
Zn(2)	4821(1)	7409(1)	4331(1)	242(6)
O(3)	5000	7500	4474(7)	210(20)

—

Table A39. Bond lengths [Å] and angles [°] for **bio-MOF-105**.

O(44)-C(45)	1.16(3)
C(45)-O(43)	1.16(3)
C(45)-C(46)	1.68(6)
C(45)-Zn(1)	2.46(7)
O(43)-Zn(1)	1.90(4)
C(46)-C(47)	1.31(5)
C(46)-C(51)	1.40(5)
C(51)-C(50)	1.41(5)
C(51)-H(51A)	0.9300
C(50)-C(49)	1.35(6)
C(50)-H(50A)	0.9300
C(49)-C(48)	1.36(6)
C(49)-C(52)	1.43(2)
C(48)-C(47)	1.45(6)
C(48)-H(48A)	0.9300
C(47)-H(47A)	0.9300
C(52)-C(52)#1	1.15(11)
O(14)-C(15)	1.25(6)
O(14)-Zn(2)#2	1.76(5)
C(15)-O(13)	1.35(9)
C(15)-C(16)	1.393(10)
C(16)-C(24)	1.39(2)
C(16)-C(19)	1.40(2)
C(24)-C(22)	1.39(2)
C(24)-H(24A)	0.9300
C(22)-C(21)	1.40(2)
C(22)-H(22A)	0.9300
C(21)-C(26)	1.39(2)
C(21)-C(41)	1.395(10)
C(26)-C(19)	1.40(2)
C(26)-H(26A)	0.9300
C(19)-H(19A)	0.9300
C(17)-C(41)	1.15(7)

C(17)-C(36)	1.396(10)
O(29)-C(30)	1.24(7)
O(29)-Zn(1)	1.82(4)
C(30)-O(28)	1.34(9)
C(30)-C(31)	1.393(10)
C(31)-C(39)	1.42(2)
C(31)-C(32)	1.42(2)
C(39)-C(37)	1.41(2)
C(39)-H(39A)	0.9300
C(37)-C(36)	1.42(2)
C(37)-H(37A)	0.9300
C(36)-C(34)	1.42(2)
C(34)-C(32)	1.41(2)
C(34)-H(34A)	0.9300
C(32)-H(32A)	0.9300
C(1)-C(3)	1.3839
C(1)-N(1)	1.3929
C(1)-C(5)	1.4041
N(1)-C(2)	1.3352
N(1)-Zn(1)#3	2.19(2)
C(2)-N(2)	1.3480
C(2)-H(2A)	0.9300
N(2)-C(3)	1.3620
N(2)-Zn(2)#4	1.869(18)
C(3)-N(3)	1.3611
N(3)-C(4)	1.3294
N(3)-Zn(2)	2.17(2)
C(4)-N(4)	1.3242
C(4)-H(4A)	0.9300
N(4)-C(5)	1.3573
N(4)-Zn(1)	2.04(2)
C(5)-N(5)	1.3391
N(5)-H(5A)	0.8600
N(5)-H(5B)	0.8600
Zn(1)-N(1)#5	2.19(5)
Zn(2)-O(14)#6	1.76(5)

Zn(2)-N(2)#4	1.87(3)
Zn(2)-O(3)	1.89(3)
Zn(2)-Zn(2)#4	3.08(2)
O(3)-Zn(2)#4	1.89(3)

O(44)-C(45)-O(43)	141(9)
O(44)-C(45)-C(46)	103(5)
O(43)-C(45)-C(46)	114(6)
O(44)-C(45)-Zn(1)	93(5)
O(43)-C(45)-Zn(1)	48(4)
C(46)-C(45)-Zn(1)	160(3)
C(45)-O(43)-Zn(1)	105(5)
C(47)-C(46)-C(51)	124(4)
C(47)-C(46)-C(45)	113(7)
C(51)-C(46)-C(45)	124(6)
C(46)-C(51)-C(50)	117(3)
C(46)-C(51)-H(51A)	121.7
C(50)-C(51)-H(51A)	121.7
C(49)-C(50)-C(51)	120(4)
C(49)-C(50)-H(50A)	119.9
C(51)-C(50)-H(50A)	119.9
C(50)-C(49)-C(48)	123(4)
C(50)-C(49)-C(52)	120(10)
C(48)-C(49)-C(52)	116(10)
C(49)-C(48)-C(47)	116(3)
C(49)-C(48)-H(48A)	121.8
C(47)-C(48)-H(48A)	121.8
C(46)-C(47)-C(48)	120(4)
C(46)-C(47)-H(47A)	120.1
C(48)-C(47)-H(47A)	120.1
C(52)#1-C(52)-C(49)	174(10)
C(15)-O(14)-Zn(2)#2	127(6)
O(14)-C(15)-O(13)	108(6)
O(14)-C(15)-C(16)	145(10)
O(13)-C(15)-C(16)	105(7)
C(15)-C(16)-C(24)	103(9)

C(15)-C(16)-C(19)	138(9)
C(24)-C(16)-C(19)	119.7(10)
C(22)-C(24)-C(16)	120.3(11)
C(22)-C(24)-H(24A)	119.8
C(16)-C(24)-H(24A)	119.8
C(24)-C(22)-C(21)	120.0(10)
C(24)-C(22)-H(22A)	120.0
C(21)-C(22)-H(22A)	120.0
C(26)-C(21)-C(41)	114(8)
C(26)-C(21)-C(22)	119.6(10)
C(41)-C(21)-C(22)	126(8)
C(21)-C(26)-C(19)	120.4(10)
C(21)-C(26)-H(26A)	119.8
C(19)-C(26)-H(26A)	119.8
C(26)-C(19)-C(16)	119.8(10)
C(26)-C(19)-H(19A)	120.1
C(16)-C(19)-H(19A)	120.1
C(41)-C(17)-C(36)	149(9)
C(30)-O(29)-Zn(1)	123(5)
O(29)-C(30)-O(28)	101(5)
O(29)-C(30)-C(31)	135(10)
O(28)-C(30)-C(31)	109(7)
C(30)-C(31)-C(39)	110(9)
C(30)-C(31)-C(32)	129(9)
C(39)-C(31)-C(32)	119.3(11)
C(37)-C(39)-C(31)	120.1(11)
C(37)-C(39)-H(39A)	120.0
C(31)-C(39)-H(39A)	120.0
C(39)-C(37)-C(36)	120.3(12)
C(39)-C(37)-H(37A)	119.8
C(36)-C(37)-H(37A)	119.8
C(17)-C(36)-C(37)	115(9)
C(17)-C(36)-C(34)	125(9)
C(37)-C(36)-C(34)	119.0(12)
C(32)-C(34)-C(36)	119.9(13)
C(32)-C(34)-H(34A)	120.0

C(36)-C(34)-H(34A)	120.0
C(34)-C(32)-C(31)	120.1(12)
C(34)-C(32)-H(32A)	119.9
C(31)-C(32)-H(32A)	119.9
C(17)-C(41)-C(21)	156(9)
C(3)-C(1)-N(1)	108.8
C(3)-C(1)-C(5)	117.6
N(1)-C(1)-C(5)	133.6
C(2)-N(1)-C(1)	102.4
C(2)-N(1)-Zn(1)#3	127.5(10)
C(1)-N(1)-Zn(1)#3	126.6(10)
N(1)-C(2)-N(2)	116.3
N(1)-C(2)-H(2A)	121.8
N(2)-C(2)-H(2A)	121.8
C(2)-N(2)-C(3)	103.3
C(2)-N(2)-Zn(2)#4	118.1(18)
C(3)-N(2)-Zn(2)#4	135.5(17)
N(3)-C(3)-N(2)	125.7
N(3)-C(3)-C(1)	125.1
N(2)-C(3)-C(1)	109.2
C(4)-N(3)-C(3)	111.9
C(4)-N(3)-Zn(2)	131.0(16)
C(3)-N(3)-Zn(2)	116.4(16)
N(4)-C(4)-N(3)	128.6
N(4)-C(4)-H(4A)	115.7
N(3)-C(4)-H(4A)	115.7
C(4)-N(4)-C(5)	119.2
C(4)-N(4)-Zn(1)	109.0(14)
C(5)-N(4)-Zn(1)	128.5(13)
N(5)-C(5)-N(4)	118.0
N(5)-C(5)-C(1)	124.4
N(4)-C(5)-C(1)	117.5
C(5)-N(5)-H(5A)	120.0
C(5)-N(5)-H(5B)	120.0
H(5A)-N(5)-H(5B)	120.0
O(29)-Zn(1)-O(43)	133.0(14)

O(29)-Zn(1)-N(4)	94.3(14)
O(43)-Zn(1)-N(4)	119.7(12)
O(29)-Zn(1)-N(1)#5	100.1(12)
O(43)-Zn(1)-N(1)#5	104.1(15)
N(4)-Zn(1)-N(1)#5	100.2(10)
O(29)-Zn(1)-C(45)	117.3(13)
O(43)-Zn(1)-C(45)	27.2(15)
N(4)-Zn(1)-C(45)	106.4(12)
N(1)#5-Zn(1)-C(45)	131.3(14)
O(14)#6-Zn(2)-N(2)#4	125(2)
O(14)#6-Zn(2)-O(3)	110(2)
N(2)#4-Zn(2)-O(3)	99.5(19)
O(14)#6-Zn(2)-N(3)	115.7(14)
N(2)#4-Zn(2)-N(3)	98.4(14)
O(3)-Zn(2)-N(3)	106.4(14)
O(14)#6-Zn(2)-Zn(2)#4	145.0(13)
N(2)#4-Zn(2)-Zn(2)#4	77.5(17)
O(3)-Zn(2)-Zn(2)#4	35.5(14)
N(3)-Zn(2)-Zn(2)#4	82.5(10)
Zn(2)-O(3)-Zn(2)#4	109(3)

Symmetry transformations used to generate equivalent atoms:

#1 -x+3/4,z+1/4,y-1/4 #2 -z+1,-x+1,-y+1 #3 -y+5/4,x+1/4,-z+3/4

#4 -x+1,-y+3/2,z+0 #5 y-1/4,-x+5/4,-z+3/4 #6 -y+1,-z+1,-x+1

Table A40. Anisotropic displacement parameters ($Å^2 \times 10^3$) for **bio-MOF-105**. The anisotropic displacement factor exponent takes the form: $-2p^2[h^2 a^{*2} U^{11} + ... + 2 h k a^* b^* U^{12}]$

	U^{11}	U^{22}	U^{33}	U^{23}	U^{13}	U^{12}
Zn(1)	165(10)	181(9)	341(11)	-25(7)	39(7)	9(6)
Zn(2)	191(12)	243(10)	291(14)	35(9)	14(9)	-29(8)
O(3)	200(70)	240(60)	190(60)	0	0	150(60)

Table A41. Hydrogen coordinates ($\times 10^4$) and isotropic displacement parameters ($Å^2 \times 10^3$) for **bio-MOF-105**.

	x	y	z	U(eq)
H(51A)	4393	6597	4194	363
H(50A)	4098	6551	4274	392
H(48A)	3938	6902	3925	353
H(47A)	4238	6946	3841	393
H(24A)	5303	5520	2800	541
H(22A)	5138	5729	2944	550
H(26A)	5575	5997	3057	390
H(19A)	5740	5793	2904	372
H(39A)	5187	6604	3526	396
H(37A)	5341	6375	3395	432
H(34A)	4888	6180	3205	500
H(32A)	4737	6421	3317	503
H(2A)	5468	7453	4136	257
H(4A)	4768	7086	4058	237
H(5A)	5144	6921	3671	304
H(5B)	5308	7019	3701	304

BIBLIOGRAPHY

(1) Kitagawa, S.; Kitaura, R.; Noro, S. *Angew. Chem., Int. Ed.* **2004**, *43*, 2334.

(2) Eddaoudi, M.; Moler, D. B.; Li, H.; Chen, B.; Reineke, T. M.; O'Keeffe, M.; Yaghi, O. M. *Acc. Chem. Res.* **2001**, *34*, 319.

(3) Furukawa, H.; Cordova, K. E.; O'Keeffe, M.; Yaghi, O. M. *Science* **2013**, *341*, 1230444.

(4) Eddaoudi, M.; Kim, J.; Rosi, N.; Vodak, D.; Wachter, J.; O'Keeffe, M.; Yaghi, O. M. *Science* **2002**, *295*, 469.

(5) Chae, H. K.; Siberio-Perez, D. Y.; Kim, J.; Go, Y.; Eddaoudi, M.; Matzger, A. J.; O'Keeffe, M.; Yaghi, O. M. *Nature* **2004**, *427*, 523.

(6) Deng, H.; Doonan, C. J.; Furukawa, H.; Ferreira, R. B.; Towne, J.; Knobler, C. B.; Wang, B.; Yaghi, O. M. *Science* **2010**, *327*, 846.

(7) Cohen, S. M. *Chem. Rev.* **2012**, *112*, 970.

(8) Wang, Z.; Cohen, S. M. *J. Am. Chem. Soc.* **2007**, *129*, 12368.

(9) Farha, O. K.; Eryazici, I.; Jeong, N. C.; Hauser, B. G.; Wilmer, C. E.; Sarjeant, A. A.; Snurr, R. Q.; Nguyen, S. T.; Yazaydin, A. O.; Hupp, J. T. *J. Am. Chem. Soc.* **2012**, *134*, 15016.

(10) Li, T.; Kozlowski, M. T.; Doud, E. A.; Blakely, M. N.; Rosi, N. L. *J. Am. Chem. Soc.* **2013**, *135*, 11688.

(11) An, J.; Farha, O. K.; Hupp, J. T.; Pohl, E.; Yeh, J. I.; Rosi, N. L. *Nat. Commun.* **2012**, *3*, 604.

(12) Deng, H.; Grunder, S.; Cordova, K. E.; Valente, C.; Furukawa, H.; Hmadeh, M.; Gandara, F.; Whalley, A. C.; Liu, Z.; Asahina, S.; Kazumori, H.; O'Keeffe, M.; Terasaki, O.; Stoddart, J. F.; Yaghi, O. M. *Science* **2012**, *336*, 1018.

(13) Sumida, K.; Rogow, D. L.; Mason, J. A.; McDonald, T. M.; Bloch, E. D.; Herm, Z. R.; Bae, T. H.; Long, J. R. *Chem. Rev.* **2012**, *112*, 724.

(14) Suh, M. P.; Park, H. J.; Prasad, T. K.; Lim, D. W. *Chem. Rev.* **2012**, *112*, 782.

(15) Konstas, K.; Osl, T.; Yang, Y.; Batten, M.; Burke, N.; Hill, A. J.; Hill, M. R. *J. Mater. Chem.* **2012**, *22*, 16698.

(16) Li, J. R.; Sculley, J.; Zhou, H. C. *Chem. Rev.* **2012**, *112*, 869.

(17) Lee, J.; Farha, O. K.; Roberts, J.; Scheidt, K. A.; Nguyen, S. T.; Hupp, J. T. *Chem. Soc. Rev.* **2009**, *38*, 1450.

(18) Wang, Z.; Chen, G.; Ding, K. *Chem. Rev.* **2008**, *109*, 322.

(19) Ma, L.; Abney, C.; Lin, W. *Chem. Soc. Rev.* **2009**, *38*, 1248.

(20) Corma, A.; Garc á, H.; Llabr és i Xamena, F. X. *Chem. Rev.* **2010**, *110*, 4606.

(21) Della Rocca, J.; Liu, D.; Lin, W. *Acc. Chem. Res.* **2011**, *44*, 957.

(22) Chen, B.; Xiang, S.; Qian, G. *Acc. Chem. Res.* **2010**, *43*, 1115.

(23) Horcajada, P.; Serre, C.; Vallet-Reg í M.; Sebban, M.; Taulelle, F.; F érey, G. *Angew. Chem., Int. Ed.* **2006**, *45*, 5974.

(24) An, J.; Geib, S. J.; Rosi, N. L. *J. Am. Chem. Soc.* **2009**, *131*, 8376.

(25) Song, L.; Zhang, J.; Sun, L.; Xu, F.; Li, F.; Zhang, H.; Si, X.; Jiao, C.; Li, Z.; Liu, S.; Liu, Y.; Zhou, H.; Sun, D.; Du, Y.; Cao, Z.; Gabelica, Z. *Energy Environ. Sci.* **2012**, *5*, 7508.

(26) Feng, D.; Gu, Z. Y.; Li, J. R.; Jiang, H. L.; Wei, Z.; Zhou, H. C. *Angew. Chem., Int. Ed.* **2012**, *51*, 10307.

(27) White, C. M.; Strazisar, B. R.; Granite, E. J.; Hoffman, J. S.; Pennline, H. W. *J. Air Waste Manage. Assoc.* **2003**, *53*, 645.

(28) Haszeldine, R. S. *Science* **2009**, *325*, 1647.

(29) Gassensmith, J. J.; Furukawa, H.; Smaldone, R. A.; Forgan, R. S.; Botros, Y. Y.; Yaghi, O. M.; Stoddart, J. F. *J. Am. Chem. Soc.* **2011**, *133*, 15312.

(30) McDonald, T. M.; Lee, W. R.; Mason, J. A.; Wiers, B. M.; Hong, C. S.; Long, J. R. *J. Am. Chem. Soc.* **2012**, *134*, 7056.

(31) An, J.; Rosi, N. L. *J. Am. Chem. Soc.* **2010**, *132*, 5578.

(32) Imaz, I.; Rubio-Martinez, M.; An, J.; Sole-Font, I.; Rosi, N. L.; Maspoch, D. *Chem. Commun.* **2011**, *47*, 7287.

(33) An, J.; Shade, C. M.; Chengelis-Czegan, D. A.; Petoud, S.; Rosi, N. L. *J. Am. Chem. Soc.* **2011**, *133*, 1220.

(34) Saunders, C. D. L.; Burford, N.; Werner-Zwanziger, U.; McDonald, R. *Inorg. Chem.* **2008**, *47*, 3693.

(35) An, J.; Fiorella, R. P.; Geib, S. J.; Rosi, N. L. *J. Am. Chem. Soc.* **2009**, *131*, 8401.

(36) An, J.; Geib, S. J.; Rosi, N. L. *J. Am. Chem. Soc.* **2010**, *132*, 38.

(37) Liu, C.; Li, T.; Rosi, N. L. *J. Am. Chem. Soc.* **2012**, *134*, 18886.

(38) Li, T.; Sullivan, J. E.; Rosi, N. L. *J. Am. Chem. Soc.* **2013**, *135*, 9984

(39) Li, T.; Rosi, N. L. *Chem. Commun.* **2013**, *49*, 11385.

(40) Vogiatzis, K. D.; Mavrandonakis, A.; Klopper, W.; Froudakis, G. E. *ChemPhysChem* **2009**, *10*, 374.

(41) Delgado Friedrichs, O.; O'Keeffe, M.; Yaghi, O. M. *Acta Crystallogr., Sect. A: Found. Crystallogr.* **2003**, *59*, 515.

(42) Li, T.; Chen, D.-L.; Sullivan, J. E.; Kozlowski, M. T.; Johnson, J. K.; Rosi, N. L. *Chem. Sci.* **2013**, *4*, 1746

(43) Pennline, H. W.; Luebke, D. R.; Jones, K. L.; Myers, C. R.; Morsi, B. I.; Heintz, Y. J.; Ilconich, J. B. *Fuel Process. Technol.* **2008**, *89*, 897.

(44) Drage, T. C.; Snape, C. E.; Stevens, L. A.; Wood, J.; Wang, J.; Cooper, A. I.; Dawson, R.; Guo, X.; Satterley, C.; Irons, R. *J. Mater. Chem.* **2012**, *22*, 2815.

(45) Keskin, S.; van Heest, T. M.; Sholl, D. S. *ChemSusChem* **2010**, *3*, 879.

(46) Britt, D.; Furukawa, H.; Wang, B.; Glover, T. G.; Yaghi, O. M. *Proc. Natl. Acad. Sci. U. S. A.* **2009**, *106*, 20637.

(47) Banerjee, R.; Furukawa, H.; Britt, D.; Knobler, C.; O'Keeffe, M.; Yaghi, O. M. *J. Am. Chem. Soc.* **2009**, *131*, 3875.

(48) Demessence, A.; D'Alessandro, D. M.; Foo, M. L.; Long, J. R. *J. Am. Chem. Soc.* **2009**, *131*, 8784.

(49) Caskey, S. R.; Wong-Foy, A. G.; Matzger, A. J. *J. Am. Chem. Soc.* **2008**, *130*, 10870.

(50) Vaidhyanathan, R.; Iremonger, S. S.; Dawson, K. W.; Shimizu, G. K. *Chem. Commun.* **2009**, 5230.

(51) Iremonger, S. S.; Liang, J.; Vaidhyanathan, R.; Martens, I.; Shimizu, G. K. H.; Daff, T. D.; Aghaji, M. Z.; Yeganegi, S.; Woo, T. K. *J. Am. Chem. Soc.* **2011**, *133*, 20048.

(52) Xiang, S.; He, Y.; Zhang, Z.; Wu, H.; Zhou, W.; Krishna, R.; Chen, B. *Nat. Commun.* **2012**, *3*, 954.

(53) Burd, S. D.; Ma, S.; Perman, J. A.; Sikora, B. J.; Snurr, R. Q.; Thallapally, P. K.; Tian, J.; Wojtas, L.; Zaworotko, M. J. *J. Am. Chem. Soc.* **2012**, *134*, 3663.

(54) Bae, Y.-S.; Farha, O. K.; Hupp, J. T.; Snurr, R. Q. *J. Mater. Chem.* **2009**, *19*, 2131.

(55) Yang, S.; Lin, X.; Lewis, W.; Suyetin, M.; Bichoutskaia, E.; Parker, J. E.; Tang, C. C.; Allan, D. R.; Rizkallah, P. J.; Hubberstey, P.; Champness, N. R.; Mark Thomas, K.; Blake, A. J.; Schröder, M. *Nat. Mater.* **2012**, *11*, 710.

(56) Thallapally, P. K.; Tian, J.; Radha Kishan, M.; Fernandez, C. A.; Dalgarno, S. J.; McGrail, P. B.; Warren, J. E.; Atwood, J. L. *J. Am. Chem. Soc.* **2008**, *130*, 16842.

(57) Lin, Q.; Wu, T.; Zheng, S.-T.; Bu, X.; Feng, P. *J. Am. Chem. Soc.* **2011**, *134*, 784.

(58) Kauffman, K. L.; Culp, J. T.; Allen, A. J.; Espinal, L.; Wong-Ng, W.; Brown, T. D.; Goodman, A.; Bernardo, M. P.; Pancoast, R. J.; Chirdon, D.; Matranga, C. *Angew. Chem., Int. Ed.* **2011**, *50*, 10888.

(59) Luebke, R.; Eubank, J. F.; Cairns, A. J.; Belmabkhout, Y.; Wojtas, L.; Eddaoudi, M. *Chem. Commun.* **2012**, *48*, 1455.

(60) Li, J.-R.; Ma, Y.; McCarthy, M. C.; Sculley, J.; Yu, J.; Jeong, H.-K.; Balbuena, P. B.; Zhou, H.-C. *Coord. Chem. Rev.* **2011**, *255*, 1791.

(61) Pérez-Yáñez, S.; Beobide, G.; Castillo, O.; Cepeda, J.; Luque, A.; Aguayo, A. s. T.; Román, P. *Inorg. Chem.* **2011**, *50*, 5330.

(62) Pérez-Yáñez, S.; Beobide, G.; Castillo, O.; Cepeda, J.; Luque, A.; Román, P. *Cryst. Growth Des.* **2012**, *12*, 3324.

(63) Wu, H.; Reali, R. S.; Smith, D. A.; Trachtenberg, M. C.; Li, J. *Chem. Eur. J.* **2010**, *16*, 13951.

(64) Ghoufi, A.; Subercaze, A.; Ma, Q.; Yot, P. G.; Ke, Y.; Puente-Orench, I.; Devic, T.; Guillerm, V.; Zhong, C.; Serre, C.; Férey, G.; Maurin, G. *J. Phys. Chem. C* **2012**, *116*, 13289.

(65) Li, D.; Kaneko, K. *Chem. Phys. Lett.* **2001**, *335*, 50.

(66) Millward, A. R.; Yaghi, O. M. *J. Am. Chem. Soc.* **2005**, *127*, 17998.

(67) Henke, S.; Fischer, R. A. *J. Am. Chem. Soc.* **2011**, *133*, 2064.

(68) Park, H. J.; Suh, M. P. *Chem. Commun.* **2010**, *46*, 610.

(69) Choi, H.-S.; Suh, M. P. *Angew. Chem., Int. Ed.* **2009**, *48*, 6865.

(70) Myers, A. L.; Prausnitz, J. M. *AIChE J.* **1965**, *11*, 121.

(71) Seo, J.; Matsuda, R.; Sakamoto, H.; Bonneau, C.; Kitagawa, S. *J. Am. Chem. Soc.* **2009**, *131*, 12792.

(72) Wang, Y.; Hong, L.; Tapriyal, D.; Kim, I. C.; Paik, I.-H.; Crosthwaite, J. M.; Hamilton, A. D.; Thies, M. C.; Beckman, E. J.; Enick, R. M.; Johnson, J. K. *J. Phys. Chem. B* **2009**, *113*, 14971.

(73) Keskin, S.; Liu, J.; Johnson, J. K.; Sholl, D. S. *Langmuir* **2008**, *24*, 8254.

(74) Sheldrick, G. *Acta Crystallogr., A* **2008**, *64*, 112.

(75) Kresse, G.; Hafner, J. *Phys. Rev. B* **1993**, *47*, 558.

(76) Kresse, G.; Hafner, J. *Phys. Rev. B* **1994**, *49*, 14251.

(77) Kresse, G.; Furthmüller, J. *Comput. Mater. Sci.* **1996**, *6*, 15.

(78) Kresse, G.; Furthmüller, J. *Phys. Rev. B* **1996**, *54*, 11169.

(79) Perdew, J. P.; Burke, K.; Ernzerhof, M. *Phys. Rev. Lett.* **1996**, *77*, 3865.

(80) Grimme, S. *J. Comput. Chem.* **2006**, *27*, 1787.

(81) García-Sánchez, A.; Ania, C. O.; Parra, J. B.; Dubbeldam, D.; Vlugt, T. J. H.; Krishna, R.; Calero, S. a. *J. Phys. Chem. C* **2009**, *113*, 8814.

(82) Rappe, A. K.; Casewit, C. J.; Colwell, K. S.; Goddard, W. A.; Skiff, W. M. *J. Am. Chem. Soc.* **1992**, *114*, 10024.

(83) Chen, D.-L.; Stern, A. C.; Space, B.; Johnson, J. K. *J. Phys. Chem. A* **2010**, *114*, 10225.

(84) Lakes, R. *Nature* **1993**, *361*, 511.

(85) Fratzl, P.; Weinkamer, R. *Prog. Mater. Sci.* **2007**, *52*, 1263.

(86) Long, J. R.; Yaghi, O. M. *Chem. Soc. Rev.* **2009**, *38*, 1213.

(87) Zhou, H. C.; Long, J. R.; Yaghi, O. M. *Chem. Rev.* **2012**, *112*, 673.

(88) Rowsell, J. L. C.; Yaghi, O. M. *Microporous Mesoporous Mater.* **2004**, *73*, 3.

(89) Ferey, G. *Chem. Soc. Rev.* **2008**, *37*, 191.

(90) Cook, T. R.; Zheng, Y. R.; Stang, P. J. *Chem. Rev.* **2013**, *113*, 734.

(91) Yaghi, O. M.; O'Keeffe, M.; Ockwig, N. W.; Chae, H. K.; Eddaoudi, M.; Kim, J. *Nature* **2003**, *423*, 705.

(92) Chun, H.; Dybtsev, D. N.; Kim, H.; Kim, K. *Chem. Eur. J.* **2005**, *11*, 3521.

(93) Kleist, W.; Jutz, F.; Maciejewski, M.; Baiker, A. *Eur. J. Inorg. Chem.*. **2009**, *2009*, 3552.

(94) Fukushima, T.; Horike, S.; Inubushi, Y.; Nakagawa, K.; Kubota, Y.; Takata, M.; Kitagawa, S. *Angew. Chem., Int. Ed.* **2010**, *49*, 4820.

(95) Burrows, A. D. *CrystEngComm* **2011**, *13*, 3623.

(96) Hirai, K.; Furukawa, S.; Kondo, M.; Uehara, H.; Sakata, O.; Kitagawa, S. *Angew. Chem., Int. Ed.* **2011**, *50*, 8057.

(97) Ferlay, S.; Hosseini, W. *Chem. Commun.* **2004**, 788.

(98) Brès, E. F.; Ferlay, S.; Dechambenoit, P.; Leroux, H.; Hosseini, M. W.; Reyntjens, S. *J. Mater. Chem.* **2007**, *17*, 1559.

(99) Koh, K.; Wong-Foy, A. G.; Matzger, A. J. *Chem. Commun.* **2009**, 6162.

(100) Furukawa, S.; Hirai, K.; Nakagawa, K.; Takashima, Y.; Matsuda, R.; Tsuruoka, T.; Kondo, M.; Haruki, R.; Tanaka, D.; Sakamoto, H.; Shimomura, S.; Sakata, O.; Kitagawa, S. *Angew. Chem., Int. Ed.* **2009**, *48*, 1766.

(101) Yoo, Y.; Jeong, H.-K. *Cryst. Growth Des.* **2010**, *10*, 1283.

(102) Fukushima, T.; Horike, S.; Kobayashi, H.; Tsujimoto, M.; Isoda, S.; Foo, M. L.; Kubota, Y.; Takata, M.; Kitagawa, S. *J. Am. Chem. Soc.* **2012**, *134*, 13341.

(103) Hirai, K.; Furukawa, S.; Kondo, M.; Meilikhov, M.; Sakata, Y.; Sakata, O.; Kitagawa, S. *Chem. Commun.* **2012**, *48*, 6472.

(104) Song, X.; Kim, T. K.; Kim, H.; Kim, D.; Jeong, S.; Moon, H. R.; Lah, M. S. *Chem. Mater.* **2012**, *24*, 3065.

(105) Delgado Friedrichs, O.; O'Keeffe, M.; Yaghi, O. M. *Acta Crystallogr., A* **2003**, *59*, 515.

(106) Furukawa, S.; Hirai, K.; Takashima, Y.; Nakagawa, K.; Kondo, M.; Tsuruoka, T.; Sakata, O.; Kitagawa, S. *Chem. Commun.* **2009**, 5097.

(107) Wang, X.-S.; Ma, S.; Sun, D.; Parkin, S.; Zhou, H.-C. *J. Am. Chem. Soc.* **2006**, *128*, 16474.

(108) Fang, Q.-R.; Makal, T.; Young, M.; Zhou, H.-C. *Comments on Inorg. Chem.* **2010**, *31*, 165.

(109) Xuan, W.; Zhu, C.; Liu, Y.; Cui, Y. *Chem. Soc. Rev.* **2012**, *41*, 1677.

(110) Morris, W.; Volosskiy, B.; Demir, S.; Gandara, F.; McGrier, P. L.; Furukawa, H.; Cascio, D.; Stoddart, J. F.; Yaghi, O. M. *Inorg. Chem.* **2012**, *51*, 6443.

(111) Chen, Y.; Hoang, T.; Ma, S. *Inorg. Chem.* **2012**, *51*, 12600.

(112) Kondo, M.; Furukawa, S.; Hirai, K.; Kitagawa, S. *Angew. Chem., Int. Ed.* **2010**, *49*, 5327.

(113) Park, H. J.; Cheon, Y. E.; Suh, M. P. *Chem. Eur. J.* **2010**, *16*, 11662.

(114) Li, J.-R.; Zhou, H.-C. *Nat. Chem.* **2010**, *2*, 893.

(115) Burnett, B. J.; Barron, P. M.; Hu, C.; Choe, W. *J. Am. Chem. Soc.* **2011**, *133*, 9984.

(116) Burnett, B. J.; Choe, W. *Dalton Trans.* **2012**, *41*, 3889.

(117) Kim, M.; Cahill, J. F.; Fei, H.; Prather, K. A.; Cohen, S. M. *J. Am. Chem. Soc.* **2012**, *134*, 18082.

(118) Park, J.; Wang, Z. U.; Sun, L. B.; Chen, Y. P.; Zhou, H. C. *J. Am. Chem. Soc.* **2012**, *134*, 20110.

(119) Kim, M.; Cahill, J. F.; Su, Y.; Prather, K. A.; Cohen, S. M. *Chem. Sci.* **2012**, *3*, 126.

(120) Karagiaridi, O.; Bury, W.; Sarjeant, A. A.; Stern, C. L.; Farha, O. K.; Hupp, J. T. *Chem. Sci.* **2012**, *3*, 3256.

(121) Nelson, A. P.; Farha, O. K.; Mulfort, K. L.; Hupp, J. T. *J. Am. Chem. Soc.* **2008**, *131*, 458.

(122) Ravikovitch, P. I.; Neimark, A. V. *Langmuir* **2006**, *22*, 11171.

(123) Schaate, A.; Roy, P.; Godt, A.; Lippke, J.; Waltz, F.; Wiebcke, M.; Behrens, P. *Chem. Eur. J* **2011**, *17*, 6643.

(124) Sheldrick, G. M. *Acta Crystallogr., A* **2008**, *64*.

(125) Spek, A. L. *Acta crystallogr., D* **2009**, *65*, 148.

(126) Dolomanov, O. V.; Bourhis, L. J.; Gildea, R. J.; Howard, J. A. K.; Puschmann, H. *J. Appl. Crystallogr.* **2009**, *42*, 339.

(127) Emsley, P.; Lohkamp, B.; Scott, W. G.; Cowtan, K. *Acta crystallogr., D* **2010**, *66*, 486.

(128) Walton, K. S.; Snurr, R. Q. *J. Am. Chem. Soc.* **2007**, *129*, 8552.

(129) Qian, H.; Zhu, M.; Wu, Z.; Jin, R. *Acc. Chem. Res.* **2012**, *45*, 1470.

(130) Das, A.; Li, T.; Nobusada, K.; Zeng, Q.; Rosi, N. L.; Jin, R. *J. Am. Chem. Soc.* **2012**, *134*, 20286.

(131) Zeng, C.; Li, T.; Das, A.; Rosi, N. L.; Jin, R. *J. Am. Chem. Soc.* **2013**, *135*, 10011.

(132) Zeng, C.; Qian, H.; Li, T.; Li, G.; Rosi, N. L.; Yoon, B.; Barnett, R. N.; Whetten, R. L.; Landman, U.; Jin, R. *Angew. Chem., Int. Ed.* **2012**, *51*, 13114.

(133) Lopez-Acevedo, O.; Akola, J.; Whetten, R. L.; Grönbeck, H.; Häkkinen, H. *J. Phys. Chem. C* **2009**, *113*, 5035.

(134) Qian, H.; Eckenhoff, W. T.; Zhu, Y.; Pintauer, T.; Jin, R. *J. Am. Chem. Soc.* **2010**, *132*, 8280.

(135) Zhu, M.; Aikens, C. M.; Hollander, F. J.; Schatz, G. C.; Jin, R. *J. Am. Chem. Soc.* **2008**, *130*, 5883.

(136) Das, A.; Li, T.; Nobusada, K.; Zeng, C.; Rosi, N. L.; Jin, R. *J. Am. Chem. Soc.* **2013**. DOI: 10.1021/ja409177s

(137) Jin, R.; Qian, H.; Wu, Z.; Zhu, Y.; Zhu, M.; Mohanty, A.; Garg, N. *J. Phys. Chem. Lett.* **2010**, *1*, 2903.

(138) Brust, M.; Walker, M.; Bethell, D.; Schiffrin, D. J.; Whyman, R. *J. Chem. Soc., Chem. Commun.* **1994**, 801.

(139) Whetten, R. L.; Khoury, J. T.; Alvarez, M. M.; Murthy, S.; Vezmar, I.; Wang, Z. L.; Stephens, P. W.; Cleveland, C. L.; Luedtke, W. D.; Landman, U. *Adv. Mater.* **1996**, *8*, 428.

(140) Price, R. C.; Whetten, R. L. *J. Am. Chem. Soc.* **2005**, *127*, 13750.

(141) Siebrands, T.; Giersig, M.; Mulvaney, P.; Fischer, C. H. *Langmuir* **1993**, *9*, 2297.

(142) Jimenez, V. L.; Leopold, M. C.; Mazzitelli, C.; Jorgenson, J. W.; Murray, R. W. *Anal. Chem.* **2002**, *75*, 199.

(143) Schaaff, T. G.; Knight, G.; Shafigullin, M. N.; Borkman, R. F.; Whetten, R. L. *J. Phys. Chem. B* **1998**, *102*, 10643.

(144) Knoppe, S.; Boudon, J.; Dolamic, I.; Dass, A.; Burgi, T. *Anal. Chem.* **2011**, *83*, 5056.

(145) Qian, H.; Jin, R. *Nano Lett.* **2009**, *9*, 4083.

(146) Qian, H.; Zhu, Y.; Jin, R. *ACS Nano* **2009**, *3*, 3795.

(147) Wu, Z.; Jin, R. *Nano Lett.* **2010**, *10*, 2568.

(148) Hubschle, C. B.; Sheldrick, G. M.; Dittrich, B. *J. Appl. Crystallogr.* **2011**, *44*, 1281.